REPUBLIQUE DU CAMEROUN
Paix - Travail - Patrie

UNIVERSITE DE YAOUNDE I

CENTRE DE RECHERCHE ET DE FORMATION DOCTORALE EN SCIENCES, TECHNOLOGIES ET GEOSCIENCES

UNITE DE RECHERCHE ET DE FORMATION DOCTORALE EN PHYSIQUES ET APPLICATIONS

FACULTE DES SCIENCES

B.P 812 Yaoundé
Email: crfd_stg@uy1.uninet.cm

REPUBLIC OF CAMEROON
Peace - Work - Fatherland

UNIVERSITY OF YAOUNDE I

POSTGRADUATE SCHOOL FOR SCIENCES, TECHNOLOGY AND GEOSCIENCES

RESEARCH AND POSTGRADUATE TRAINING UNIT FOR PHYSICS AND APPLICATIONS

FACULTY OF SCIENCES

P.O. Box 812 Yaoundé
Email: crfd_stg@uy1.uninet.cm

DÉPARTEMENT DE PHYSIQUE
DEPARTMENT OF PHYSICS

LABORATOIRE DE MÉCANIQUE, MATÉRIAUX ET STRUCTURES
LABORATORY OF MECHANICS, MATERIALS AND STRUCTURES

NONLINEAR DYNAMICS OF PARITY-TIME SYMMETRY MECHANICAL OSCILLATORS

Thesis submitted and defended in partial fulfillment of the requirements for the awards of the degree of **Doctor of Philosophy** (Ph.D) in Physics

Speciality : **Mechanics, Materials and Structures**

Option : **Fundamental Mechanics and Complex Systems**

By

AZEGHAP SIMO Ibrahim

Registration number: 08W0039
Master in Physics

Under the supervision of:

KENFACK JIOTSA Aurélien
Professor
University of Yaounde I

FOTSA NGAFFO Fernande
Associate Professor
University of Yaounde I

REPUBLIQUE DU CAMEROUN
Paix - Travail - Patrie

UNIVERSITE DE YAOUNDE I

CENTRE DE RECHERCHE ET DE FORMATION DOCTORALE EN SCIENCES, TECHNOLOGIES ET GEOSCIENCES

UNITE DE RECHERCHE ET DE FORMATION DOCTORALE EN PHYSIQUES ET APPLICATIONS

FACULTE DES SCIENCES

B.P 812 Yaoundé
Email: crfd_stg@uy1.uninet.cm

REPUBLIC OF CAMEROON
Peace - Work - Fatherland

UNIVERSITY OF YAOUNDE I

POSTGRADUATE SCHOOL FOR SCIENCES, TECHNOLOGY AND GEOSCIENCES

RESEARCH AND POSTGRADUATE TRAINING UNIT FOR PHYSICS AND APPLICATIONS

FACULTY OF SCIENCES

P.O. Box 812 Yaoundé
Email: crfd_stg@uy1.uninet.cm

DÉPARTEMENT DE PHYSIQUE
DEPARTMENT OF PHYSICS

LABORATOIRE DE MÉCANIQUE, MATÉRIAUX ET STRUCTURES
LABORATORY OF MECHANICS, MATERIALS AND STRUCTURES

NONLINEAR DYNAMICS OF PARITY-TIME SYMMETRY MECHANICAL OSCILLATORS

Thesis submitted and defended in partial fulfillment of the requirements for the awards of the degree of ***Doctor of Philosophy*** *(Ph.D) in Physics*

Speciality : **Mechanics, Materials and Structures**
Option : **Fundamental Mechanics and Complex Systems**

By
AZEGHAP SIMO Ibrahim
Registration number: 08W0039
Master in Physics

Defended on 02 May 2025

The thesis Jury composed of :

President:	**KOFANE Timoléon Crépin, Professor**	**University of Yaoundé I**
Supervisors:	**KENFACK JIOTSA Aurélien, Professor**	**University of Yaoundé I**
	FOTSA NGAFFO Fernande, Associate Professor	**University of Yaoundé I**
Members:	**YAMGOUE Serge Bruno, Associate Professor**	**University of Bamenda**
	FEWO Serge Ibraïd, Professor	**University of Yaoundé I**

UNIVERSITÉ DE YAOUNDÉ I
THE UNIVERSITY OF YAOUNDE I

FACULTÉ DES SCIENCES
FACULTY OF SCIENCES

DÉPARTEMENT DE PHYSIQUE
DEPARTMENT OF PHYSICS

ATTESTATION DE CORRECTION DE LA THÈSE DE DOCTORAT/Ph.D

Nous, Professeur **FEWO Serge Ibraïd** et Professeur **KOFANE Timoléon Crépin**, respectivement Examinateur et Président du jury de la Thèse de Doctorat/Ph.D. de Monsieur **AZEGHAP SIMO Ibrahim**, Matricule **08W0039**, préparée sous la direction des Professeurs **KENFACK JIOTSA Aurélien** (Université de Yaoundé I) et **FOTSA NGAFFO Fernande** (Université de Yaoundé I), intitulée : « **NONLINEAR DYNAMICS OF PARITY-TIME SYMMETRY MECHANICAL OSCILLATORS** », soutenue le vendredi, **02 Mai 2025**, en vue de l'obtention du grade de Docteur/Ph.D. en Physique, Spécialité **Mécanique, Matériaux et Structures,** option **Mécanique Fondamentale et Systèmes Complexes,** attestons que toutes les corrections demandées par le jury de soutenance ont été effectuées.

En foi de quoi, la présente attestation lui est délivrée pour servir et valoir ce que de droit.

Fait à Yaoundé, le 23 MAI 2025

Examinateur	Le Président du jury	Le Chef du Département de Physique
Pr. FEWO Serge Ibraïd	Pr. KOFANE Timoléon Crépin	Pr. NDJAKA Jean Marie B.

Nonlinear Dynamics of Parity-Time Symmetry Mechanical Oscillators

THESIS

Thesis is submitted to the Department of Physics
in partial fulfillment of the requirements for the degree of Doctor
of Philosophy in field of Fundamental Mechanics and Complex Systems

By

AZEGHAP SIMO Ibrahim
Master in Physics

Ph.D candidate

Specialty: Mechanics, Materials and Structures

Option : Fundamental Mechanics and Complex Systems

Co-Directors:

KENFACK JIOTSA Aurélien
Professor
University of Yaounde I

FOTSA NGAFFO Fernande
Associate Professor
University of Yaounde I

University of Yaounde I
Centre de Recherche et de Formation Doctorale en Sciences, Technologie et Geosciences
P.O. Box 812 Yaoundé, Cameroon

Citation

"It's not that I'm so smart,
it's just that I stay with problems longer."

Albert Einstein

Dedications

♡ *To my lovely mother* ***DEMGNE Jacqueline***,

♡ *To my sister,*
TCHUENDEM SIMO Else Daykon,

♡ *To my late beloved father,*
peace to his soul ***SIMO TENKUE Z. Jean-Marie***
1950-2020

Declaration

I, undersigned, **AZEGHAP SIMO Ibrahim**, Registration Number : **08W0039**, hereby declare that the work contained in this thesis entitled **"Nonlinear Dynamics of Parity-Time Symmetry Mechanical Oscillators"** is my original work and that any work done by others or by myself previously has been acknowledged and referenced accordingly.

The author :

AZEGHAP SIMO Ibrahim
Ph.D candidate
University of Yaounde 1

The supervisors :

KENFACK JIOTSA Aurélien
Professor
University of Yaounde 1

FOTSA NGAFFO Fernande
Associate Professor
University of Yaounde 1

Acknowledgments

This thesis would have been impossible without the help and support from several people. Here, I would like to express my sincere gratitude to them.

• First of all, I would like to thank **God, the Almighty** for giving me the patience, the strength and the mercy to accomplish this modest work, despite the difficulties encountered.

• I would like to express my deepest gratitude and unwavering attachment to my thesis supervisor, **Prof. Aurélien KENFACK JIOTSA**, who welcomed me into his laboratory from the Master's level to this doctoral thesis. His sympathetic attitude, cordiality, know-how and encouragement have enabled me to broaden my knowledge and improve my research skills and capability. Thank you for your multifaceted support, both scientific and moral. I hope that I have been worthy of the trust you have placed in me.

• Secondly, I would like to express my thankfulness to my advisor, **Prof. Fernande FOTSA NGAFFO**. It has been an honour to work with you throughout my thesis training. It has not always been easy to integrate and accept your rigorous approach to research, but it edified my scientific mind. I learnt a lot from you, about discipline and a job well done, thanks to your research experience. Many thanks for our long hours of discussion, which awakened my spirit of research.

• I would like to thank each member of jury who has accepted to evaluate the present work.

• I would also like to thank all those who dedicated their time to teach me a part of what they know, from primary school to University, with a particular emphasis on the teaching staff of the Department of Physics of the University of Yaounde I; I am particularly grateful to **Prof. Paul WOAFO, Prof. Jean-Marie Bienvenu NDJAKA, Prof. Timoléon Crépin KOFANE, Prof. DJUIDJE KENMOE Germaine, Prof. Clement TCHAWOUA, Prof. Serge ZEKENG, Prof. Blaise Romeo NANA NBENDJO, Prof. Martin SIEWE SIEWE, Prof. Bernard ESSIMBI ZOBO, Prof. Serge Ibraïd FEWO, Prof. Debertini Apollinaire VONDOU, Prof. Alain MVOGO**.

• Many thanks to **Dr. Emmanuel FENDZI**, **Dr. Senghor TAGOUEGNI** and **Dr. Marcial BADUIDANA**, for all our many fruitful exchanges on different aspects of physics. Without forgetting their availability and unconditional help.

• I express my gratitude to **Prof. Bruno LENTA**, **Prof. Eric TALA TEBUE, Dr. Zacharie DJOUFACK, Dr. Deschances TSOBGNI, Dr. Hervé KAMDOUM, Dr. Hervé BONSOU, Dr. Jean Paul DJIOKO, Dr. Arnaud TIKENG MANFOUO, Dr. Joel NKOUAGNOU**, **Dr. Evariste NGATCHOU**, **Dr. Anne Justine ETINDELE** and **M. Stéphane Boris TABEU** for their permanent encouragements.

• Special thanks go to my wonderful friends **Dr. Camile R. TCHUENGUEM KAMTO, Dr. Thomas B. DJUITCHOU YALEU, Dr. Gabin T. OUMBE TEKAM** for their fruitful and stimulating discussions during this work and also about research questions in general.

• My gratitude also goes to all my lab mates from the ANALOGICAL SIMULATION LAB under the supervision of **Prof. Aurélien KENFACK JIOTSA**, **Landry SILATCHOM, Idriss NJIKE NJIKE, Junior MBA NDEDA, Daniel BANG, Jean Paul TEUGUIA, Stephane NOUPEYI, Romuald TATSITSA, Landry NYAPA**, for the sincere collaboration, solidarity, spirit of group and the uplifting debates that elucidated me.

• I also give special thanks to late grand father **Joseph KOUAM** and my late grand-mother **Anne MAKOUMBE** for their multiple encouragements and prayers.

• My deepest gratitude goes to my entire family for their support throughout my life. I want to thank my sister and my mother: **Else D. TCHUENDEM SIMO**, and **Jacqueline DEMGNE**, who have always appreciated me and for the affection, the tenderness, the support, the advice and above all for the immeasurable love that they have always shown me. To my uncles **Denis KAMGAING, Réné Iwago TAHATE, Elie MBA** and my aunts **Clarisse DJOUKOUO, Rébecca MAKAM, Nathalie FOTSO, Cathy DJOUONTSO**: Thank you for the education you gave me. To my cousins, nieces and nephews **Ilan** and **Hilona NZEUTAM, Aurel, Baresi, Archange, Renata** and **Warren TAHATE, Josué SIGHA, Joel TAKAMTE** and all of other members of **KOUAM** family.

• A special thanks to my loving fiancee **Brinda Laurelle TSAGUE MOUGANG**. Thank you for being the most loving, caring, and comprehensive companion, I could ever dream of. Thank you for making my happiness grow, and my disappointments fade. Thank you also for giving a sense to my life.

• I can't forget the **NZEUTAM, NGUEFACK, NEOSSI** and **FOMETEU** families, for their support and multiple encouragements.

• I also give special thanks to **Rev. Hervé BITOMO TSALLA** for his multiple encouragements and prayers.

• A special thanks to my friends **Gladys-Laure GUEGUIM** and **Stève ESSONO**.

• To all the members of the **High Tech and Slow Technology Club (HITASTEC)**, I am grateful for your instructive exchanges on the experimental level.

• I must remember the particular group of special persons on which I am extremely happy to be a member. I think of **AEEAB**, thank you for your support.

• To all those who have contributed directly or indirectly to this work, and whose names do not appear on this list, please feel not forgotten, we are together!

To all of you, thank you.
Ibrahim.

Abstract

This thesis deals with the nonlinear dynamics of a parity-time symmetry mechanical system and the study of wave transport phenomena in a conservative mechanical transmission line. It entends to be a contribution to the characterisation of the dynamics of $\mathcal{PTS}$ systems governed by Duffing nonlinearity with catastrophic and/or bounded ϕ^4 and ϕ^6 potentials. Starting from a general modelling of the system, a study of the linear case is carried out. In a first step, and under different configurations of initial conditions, we analytically established the stability diagrams giving the non-Hermiticity parameter as a function of the different types of coupling (elastic and inertial, respectively). The effect of each coupling is then described by analysing the system dynamics. The dynamic behaviour in the region of stability shows that the elastic and inertial effects are felt on the amplitude and frequency of the oscillations respectively. And at the point of zero effective coupling, it appears that each monomer oscillates independently like a harmonic oscillator, regardless of the initial excitation. In the nonlinear regime, mathematical and numerical tools have been used to show that nonlinearity and initial conditions modify the transition point or $\mathcal{PT}$ symmetry breaking point and can lead to catastrophe or large amplitude oscillations in the system. Indeed, for a soft potential system, the stability domain is less extended than in the linear case, in contrast to hard potential systems where the stability domain is more extensive. We also showed that the averaging method is suitable for analytically approximating the transition point or breaking point. An improvement in the stability as well as the oscillation time of the system is observed for high values of the inertial coupling parameter. Stability diagrams are also produced for the soft cubic and hard quintic systems. The second part of this research topic is devoted to the study of wave propagation phenomena in the linear regime. To this end, the $\mathcal{PTS}$ mechanical dimer is introduced as an impurity in a Hermitian conservative mass-spring transmission line. The propagation results revealed the presence of exceptional points (EPs) where unidirectional and bidirectional invisibility behaviour can be observed. Laser emission modes are also observed for real and imaginary values of the wavenumber, corresponding to real values of the non-Hermiticity parameter, demonstrating the possibility of controlling forbidden waves.

Keywords: Parity-time symmetry, $\mathcal{PT}$ breaking point, diagram of stability, non-hermiticity, unidirectional invisibility and bidirectional invisibility.

Résumé

Cette thèse traitant de la dynamique nonlinéaire d'un système mécanique à symétrie parité-temps et de l'étude des phénomènes de transport d'ondes dans une ligne de transmission mécanique conservative, se veut être une contribution à la caractérisation de la dynamique des systèmes $\mathcal{PTS}$ régis par la nonlinéarité de type Duffing, à potentiel ϕ^4 et ϕ^6 catastrophiques et/ou bornés. Partant de la modélisation du système de manière générale, une étude du cas linéaire est d'abord effectuée. Dans un premier temps et sous différentes configurations des conditions initiales, nous avons établi analytiquement les diagrammes de stabilité donnant le paramètre de non-Hermiticité en fonction des différents types de couplage (élastique et inertiel respectivement). Ensuite, L'effet de chaque couplage est décrit en analysant la dynamique du système. Le comportement dynamique dans la région de stabilité révèle que les effets élastique et inertiel sont ressentis respectivement sur l'amplitude et la fréquence des oscillations. Et, au point de couplage effectif nul, il apparaît que chaque monomère oscille indépendemment de l'autre comme un oscillateur harmonique quelle que soit l'excitation initiale. En régime nonlinéaire, les outils mathématique et numérique permettent de montrer que la nonlinéarité ainsi que les conditions initiales modifient le point de transition ou point de rupture de symétrie $\mathcal{PT}$ et peut conduire à une catastrophe ou à des oscillations de grandes amplitudes dans le système. En effet, pour un système à potentiel mou, le domaine de stabilité est moins étendu par rapport à celui du cas linéaire, à l'opposé des systèmes à potentiel dur où, le domaine de stabilité est plus étendu. Nous montrons également que la méthode de la moyenne est adaptée pour approximer analytiquement le point de transition ou le point de rupture. Une amélioration de la stabilité ainsi que du temps des oscillations du système est observée pour des valeurs élevées du paramètre de couplage inertiel. Des diagrammes de stabilité sont également établis pour le système cubique mou et le système quintique dur. La deuxième partie de ce thème de recherche est consacrée à l'étude des propriétés de diffusion des phénomènes de propagation des ondes en régime linéaire. Et pour ce faire, le dimère mécanique $\mathcal{PTS}$ est introduite comme impureté dans une ligne de transmission Hermitienne masse-ressort conservative. Les résultats lors de la propagation ont révélé la présence des points exceptionnels (EPs), où on peut observer des comportements d'invisibilité unidirectionnelle et bidirectionnelle. Egalement, les modes émission laser sont observés pour des valeurs réelles et imaginaires du nombre d'onde, correspondant à des valeurs réelles du paramètre de non-Hermiticité, ce qui démontre la possibilité de contrôler les ondes interdites.

Mots clés : Symétrie parité-temps, point de rupture $\mathcal{PT}$, diagramme de stabilité, non-Hermiticité, invisibilité unidirectionnelle et bidirectionnelle.

Contents

List of Tables

List of Figures

List of Abbreviations

$\mathcal{P}$: Parity

$\mathcal{T}$: Time

$\mathcal{PT}$: Parity Time

$\mathcal{PTS}$: Parity Time Symmetric

EP: Exceptional Point

BP: Breaking Point

FP: Fixed Point

RK4: 4^{th} order Runge-Kutta

NCQP: Nonlinear Cubic Quintic Potential

TL: Transmission Line

MTL: Mechanical Transmission Line

MMS: Method of Multiple Scale

NSMS: Nonlinear scattering Mechanical System

NHH: Non-Hermitian Hamiltonian

TH: Threshold

THL: Thresholdless

THLP: Thresholdless Point

General Introduction

In the light of the dispositions implemented to regulate in a balanced and sustainable way the consumption and exploitation of the natural resources of our planet Earth, considered as a system, it is logical to think that energy dissipation and energy gain mechanisms are ubiquitous phenomena in nature. In fact, nature itself is a permanent source of energy, while the loss of energy to the environment is induced by the consumption of these resources by Human. These two opposing and simultaneously present phenomena require a rational management of these resources between man and nature in order to maintain the system in balance. This clearly illustrates the importance of the existence of loss and gain mechanisms in the same system.

The idea of designing a system in which losses and gains coexist at the same time dates back to 1998, in the context of quantum mechanics, and was proposed by Carl Bender and his colleagues [1–3]. These types of systems are called: *the* $\mathcal{PTS}$ systems, and they are nowadays intensively studied in various fields of science such as acoustics [4,5], atomic physics [6], optics [7,8], electronics [9–12] and even mechanics [8,13–21]. In fact, these systems are described by a non-Hermitian Hamiltonian $\mathcal{H}$ (NHH) which, under the condition of commuting simultaneously with the parity operator $\mathcal{P}$ and the time operator $\mathcal{T}$, can admit an entirely real spectrum. And if this is the case, the system can be said to be stable. Our understanding of the interest in this type of system goes back several years, when it was accepted that only Hermitian Hamiltonians, i.e. those with entirely real energy spectra, could describe physical phenomena. At that time, systems with NHHs were of no interest to researchers. However, despite the lack of attention paid to this class of Hamiltonians, they allowed us to describe dissipative processes such as radioactive decay in an approximate (rather than fundamental) way, because they did not respect the unitarity requirement. In 1963, Barton showed that if a NHH cannot provide a fundamental description of the nature of [22], it is partly because the measurement of its energy spectrum can produce complex values. Over time, the work of Bender and Boettcher showed that the reality of the spectrum was due to the reflection symmetry principle of space-time $\mathcal{H} = \mathcal{H}^{\mathcal{PT}}$ ($\mathcal{H}^{\mathcal{PT}}$). At the same time, it was found that the Dirac Hermiticity condition $\mathcal{H} = \mathcal{H}^{+}$ ($\mathcal{H}^{+}$ denotes the transpose of the matrix $\mathcal{H}$), which is often stated as an axiom of quantum mechanics, is not a necessary condition, while the symmetry condition is a sufficient condition to guarantee that the energy spectrum is real.

In addition, thanks to the isomorphism between the quantum Schrödinger and the paraxial optical wave equation in which the refractive index plays the role of the potential, the optics field has provided valuable insights into this initial fairly abstract mathematical demonstration. It is now understood that the $\mathcal{PT}$ symmetry phase is the results of a net compensation between

the losses (drain) and the gain (source) in the dynamic of a coupled system [7, 23–29]. In 2007, following on from Bender's work, El Ganainy and co-workers demonstrated in optics [7, 24, 28] that a symmetric $\mathcal{PT}$ system is obtained by linearly coupling two waveguides, one of which acts as a wave amplifier and is called the gain, while the second is the seat of attenuation and is called the loss. They also presented the first experimental optical device for highlighting the exact phase and broken phase regions separated by the EP. In electronics [9, 10, 33], Schindler and his colleagues proposed an electronic circuit based on negative and positive resistors, which implement the gain and loss respectively. Similarly, in mechanics [13], Carl Bender and his collaborators showed that the concept of $\mathcal{PTS}$ could be observed experimentally in a dimer of coupled pendulums whose suspensions were subjected to an adjustable tension. One of the characteristics of non-Hermitian systems is that they have remarkable points in parameter space, called exceptional points (EPs), where the Hamiltonian loses its dimensionality. This means that the number of independent degrees of freedom in the system described by the Hamiltonian is reduced. These EPs correspond to the points in the parameter space of a non-Hermitian system at which the eigenvalues and corresponding eigenvectors simultaneously coalesce, resulting in their degeneracy. At the EP, many unconventional properties such as unidirectional invisibility [24, 26], non-reciprocal Bloch oscillations [28], chiral behaviour [30], mode selection in lasers [31] and enhanced sensor [32] have been realised. In symmetric $\mathcal{PT}$ systems, EPs mark the spontaneous breaking of the parity-time symmetry and can be regarded as phase transition points where the eigenvalues change from real to complex values when the Hermiticity control parameter (which refers to a real-valued parameter governing the balance between gain and loss) increases. In other words, the hermiticity control parameter goes from a stable region called the unbroken or $\mathcal{PT}$ exact phase to a region of instability called the $\mathcal{PT}$ broken phase. As a result, when the EP is crossed, the system loses its stability and goes into resonance i.e., the system vibrates with the high amplitudes, which can lead to its destruction. Resonance in a physical system, particularly a mechanical system, is a phenomenon that occurs when the frequency of an excitation force matches the natural frequency of the system, amplifying vibrations. This can lead to excessive vibration and potential deformation. Techniques such as vibration damping and absorption [35] are often used to mitigate the effects of resonance in mechanical systems. Although resonance is generally undesirable in most mechanical applications as it can lead to structural failure, it can be beneficial in certain specific contexts such as radio receivers, nuclear magnetic resonance and magnetic resonance imaging.

The EP is a critical point which, once reached, can cause irreversible damage to the system. In a linear framework, however, it is quite easy, both analytically and experimentally, to predict the position of this point [9–16, 30, 32, 35–39], i.e. the value of the gain-loss parameter at which the symmetry is broken. For example, the authors in [13] observed the phase transition on a mechanical experimental device consisting of two coupled pendula. They showed that by adjusting the tension applied on the pendula, one can vary the coupling of the two pendula, and so, increase or decrease the damping or anti-damping parameter. Through the systems exhibing the EP, some phenomena such as robust wireless power transfer [12], laser linewidth broadening

[40], ultralow $\mathcal{PT}$ breaking chaos [21], reduced fluctuations due to nonlinear saturation effects and quantum noise combination [22], slow to fast light switching modulation [41] have been predicted. However, when nonlinearity comes into play [21, 23, 24, 42], particular phenomena can arise. It was reported that integrable $\mathcal{PT}$-symmetric Kerr nonlinear structures (structures in which the refractive index of a medium becomes intensity-dependent) involving a balanced gain–loss can act as unidirectional optical valves above a critical value of the nonlinearity strength [43]. It was also mentioned that solitons evolving in a $\mathcal{PT}$-symmetric nonlinear chain develop an instability, leading to blow-up when their amplitudes exceed a critical value [44]. On the other hand, it was rather demonstrated that cubic nonlinear terms can soften the $\mathcal{PT}$-symmetry transition and, thus, enable the existence of stable periodic and/or quasi-periodic states at any arbitrary value of the gain–loss parameter [21, 23]. Moreover, it has been shown that the nonlinear $\mathcal{PT}$ transition can be observed in ultracompact nonlinear couplers consisting of one or two $\mathcal{PT}$-symmetric waveguides [45] and, also shown that the nonlinearity can trigger a $\mathcal{PT}$ transition in an infinite periodic array of $\mathcal{PT}$-symmetric waveguides described by cosine-like permittivity distribution [46].

Although numerous studies have been carried out on EP in nonlinear systems with $\mathcal{PT}$ symmetry, they have only highlighted the existence of a transition point. To date, no study has addressed the question of how the $\mathcal{PT}$ phase transition point is modified in the nonlinear regime. Given the importance of knowing the stable oscillation range of a system, is it possible to characterise its stability threshold ? Furthermore, in view of the results obtained and the phenomena observed on the scattering properties in the field of optics and electronics when the dimer is inserted as a defect in a Hermitian transmission line, would it not be possible to observe new phenomena in a mechanical context ?

This dissertation work is organised into three chapters, followed by the list of references cited and articles published.

∗ **Chapter 1**, reviews the literature on the origins of the concept of parity-time symmetry. The notions of hermiticity and pseudo-Hermiticity are introduced. Next, generalities about mechanical systems, focusing on parity-time symmetric mechanical systems are presented. Finally, a reminder of resonance phenomena is given.

∗ **Chapter 2**, introduces the methodology used in our research. First, the equations of motion of the system under study are established, and then the different numerical (RK4, dichotomy) and analytical (averaging method, multiple time scale and Stokes parametrisation) methods are used to solve the problem posed.

∗ Finally, **chapter 3**, is devoted to the presentation of the results obtained. The first part presents the expressions for the eigenmodes and the Hermiticity parameter in a linear framework. The different stability diagrams are obtained and the effects of the different couplings involved are highlighted. In the second part, the various results obtained on the effects of coupling and nonlinearity on the dynamics of the system are elucidated. The last part illustrates the diffusion properties of the parity-time symmetry when the dimer is inserted as an impurity in a Hermitian conservative mechanical transmission line.

This thesis ends with a general conclusion in which main results that have been the subject of publications are summarised. However, on the basis of a detailed analysis of the results presented, a number of perspectives are to be considered.

Chapter 1

Literature Review

Introduction

Originally introduced in the framework of quantum mechanics, non-Hermitian systems in general or $\mathcal{PT}$ symmetry systems in particular, have been intensively investigated in several domains of physics since this last quarter of century. Indeed, since 1998, the $\mathcal{PT}$ symmetry concept [1,2] has been one of the most important subject of the physics. Through this concept, significant progresses have been done in diverse areas of sciences, in theoretical as well as in experimental levels.

In addition to provide the background on the basic concepts concerning $\mathcal{PT}$ symmetric systems, an overview is made on the different components included in the constitution of a mechanical system. On the other hand, a brief literature review of the scattering formalism is presented.

1.1 On the origins of the $\mathcal{PT}$ Symmetry concept

1.1.1 Notion of Hermiticity/Hermitian theory

The notion of hermiticity dates back to the early days of quantum mechanics and, it remains a worrying topic to this day. The fundamental interest in this aspect of physics lies in its property of the energy preservation in physical systems. From the point of view of the classical physics, observables are generally represented by real-valued functions defined on the state space of the system. By analogy with the quantum theory, these observables can be seen as mapping from the space of states of the system onto the real numbers [47]. Thus, these operators are usually taken to be Hermitian in order to ensure that they are real-valued. The notion of Hermiticity of a system refers to wether the operator reflecting the dynamics of the system is Hermitian. The Hermitian operator is defined as [48]:

Definition : Let $\mathcal{B}(\mathcal{H})$ (H) denotes the set of bounded linear operators on a complex Hilbert space $\mathcal{H}$ equipped with the Dirac norm $\langle\cdot|\cdot\rangle$ Then any operator $A \in \mathcal{B}(\mathcal{H})$ is Hermitian iff

$$A = A^{\dagger}$$

where $A^{\dagger}$ denotes the adjoint operator.

At the quantum level, physics focuses on the study of behaviour of the atomic particles [49]. It was by carrying out work on the behaviour of systems at the microscopic scale that Schrödinger, Heisenberg and Dirac formulated the quantum theory in $1925-1930$. According to the fundamental postulate of quantum physics, every measurable dynamic quantity is represented by a Hermitian linear operator acting on the wave function. This postulate results from another postulate in quantum physics stating that: the quantities we observe are the eigenvalues of the operators which represent the measurable quantities [50]. In other words, this means that, the operators which represent these real measurable quantities should be Hermitian. As already known, the fundamental time-dependent Schrödinger equation in quantum mechanics is written as:

$$i\hbar\frac{\partial\psi\left(t\right)}{\partial t}=\mathcal{H}\psi\left(t\right)\,, \tag{1.1}$$

where $\psi\left(t\right)$ is the state of the system and $\mathcal{H}$ the Hamiltonian and its eigenvalues represent the energies.

In conventional quantum mechanics such a system evolves according to a Hermitian Hamiltonian. The term Hermitian Hamiltonian is used to mean that if the Hamiltonian $\mathcal{H}$ is in matrix form, then $\mathcal{H}$ remains invariant under the combined operations of matrix transposition and complex conjugation. The symbol $\dagger$ is used to represent these combined operations and to indicate that a Hamiltonian is Hermitian with respect to the Hermiticity condition given as follows

$$\mathcal{H}=\mathcal{H}^{\dagger}. \tag{1.2}$$

The eigenvalues of a Hermitian Hamiltonian are always real. Moreover, a Hermitian Hamiltonian conserves probability (the norm of a state). When the probability is constant in time, the time evolution is said to be unitary [51].

1.1.2 Non-Hermitian systems

In both quantum and classical mechanics, a physical system is often qualified as Hermitian if the Hamiltonian $\mathcal{H}$ of the system is Hermitian. Although nature is rich in physical systems characterised by Hermitian Hamiltonians−allowing for the description and explanation of various natural phenomena−there also exist systems whose Hamiltonians are not Hermitian. Indeed, Hermitian Hamiltonians guarantee the reality of observables, which means that they can be measured in physical experiments. However, there is also an another class of Hamiltonians which are not Hermitian but, can possess real spectra: non-Hermitian Hamiltonians.

1.1.2.1 Background

Nature is essentially full of dissipative systems. This is because dissipative systems possess non-Hermitian Hamiltonians, which has led to less interest from scientists, by virtue of certain fundamental properties which are inherent to physical systems although, these kind of

systems can be used to describe dissipative processes such as, the phenomenon of radioactive decay [28, 52, 53]. However, such non-Hermitian Hamiltonians are only approximate, descriptions of physical processes. They cannot be regarded as fundamental because they violate the requirement of unitarity [54]. Indeed, talking about dissipative systems refer to the energy losses in the systems. And where there are energy losses in a system, this could mean that the power of a transmitted information through that system will be loss after a short time, which would be undesirable. In other words, losses in a system would be a minor importance for the science and should not aroused any interest. In the opposite of losses, there are also gain systems whose importance is no longer to put again in question. In the literature, we can find a lot of applications of the gain in physical systems, such as amplification of signals. However, there are no systems in which loss and gain can simultaneously coexist. So, from the above, it can be deduce that the losses in a system are as important as the gains. It from this observation that a new class of systems called $\mathcal{PT}$ symmetric systems was born.

Inspired by the relevance of the spatially symmetric harmonic oscillator (an oscillator with a potential invariant under spatial reflection symmetry), Carl Bender and Stefan Boettcher [1] demonstrated the weakness requirement of the essentially self-adjoint Hamiltonian as the unique possibility for the operator associated to have a real observable. Without violating any of the physical axioms of quantum physics, they showed that the axiom of hermiticity can be replaced by the condition that a Hamiltonian $\mathcal{H}$ have real spectra and still satisfy the requirements of the quantum theory i.e., the Hamiltonian must simultaneously commutes with the parity inversion ($\mathcal{P}$: $x \to -x, p \to -p$) and time reversal ($\mathcal{T}$: $p \to -p, i \to -i$) operators where, p and x are the momentum and the position operators, respectively. Under the $\mathcal{PT}$ symmetry condition, the non-Hermitian Hamiltonian share the same eigenfunctions with the $\mathcal{PT}$ operator. This quantum theory introduced by the latter offered a large class of non-Hermitian Hamiltonians which possess real spectra [1, 2, 55–62] and allowed scientists to study numerous phenomena in different fields of physics. Morever, this Hamiltonian exhibits at least a region in which all the eigenvalues are completely real and then the energy is conserved. However, there exists a critical parameter so-called exceptional point (EP) [13], also referenced as a branch point singularity [63–65] at which all the eigenvalues and their corresponding eigenvectors coalesce (i.e., modes become completely non-orthogonal or parallel). EP was also observed both at the theoretical level and at the experimental level. It makes the Hamiltonian describing the system non-Hermitian [66, 67] likewise EPs exist only in non-Hermitian Hamiltonians. Above the EP, some of the Hamiltonian eigenvalues become complex and the system symmetry is broken, i.e., the Hamiltonian still commutes with the $\mathcal{PT}$ operator but no longer shares the same eigenfunctions. Thus, EP marks the boundary between broken and unbroken $\mathcal{PT}$ symmetric phases. By relying on the paraxial approximation which maps the scalar wave equation to the Schrodinger equation, most of the studies on optical realisations of $\mathcal{PT}$ synthetic media have shown that refractive index must satisfy the condition $n(z) = n^*(-z)$ (z represents the spatial coordinate along the direction of wave propagation, $n(z)$ denotes the complex refractive index at position z and $n^*(-z)$ is the complex conjugate of $n(z)$), so that, creation and absorption

of photons occur in a balanced manner. From these observations one can now understand that a $\mathcal{PT}$ symmetric system can be realised by coupling two elements (one with losses and the other with gains) so that the gains and losses are zero. Consequently, optics has become a fertile branch of physics for the creation of $\mathcal{PT}$ symmetric systems. The study of the phase transition in the latter field has led to the extension of work on the exceptional point into various areas of classical physics such as acoustics [4, 5], electronics [9–12], whispery gallery micro cavities [68], phonon laser [14, 40, 41, 69], Bose condensates [70], optomechanics [19, 71], metamaterials [72–75], plasmonics [76], microwaves [39] and mechanics [8, 13, 15–21].

Through the different properties contained in the EP, several achievements such as unidirectional invisibility [24, 26], non-reciprocal Bloch oscillations [28], chiral behaviour [30], mode selection in lasers [31], enhanced sensor [32], double refraction [77], spectral singularities [78, 79], non-linearity induced $\mathcal{PT}$-symmetry breaking [46, 80], perfect optical absorption [81], thresholdless $\mathcal{PT}$-symmetry breaking [82], resonant mode conversion [83] and $\mathcal{PT}$ Symmetric wave chaos [84], have been made. Furthermore, certains phenomena such as robust wireless power transfer [12], laser linewidth broadening [40], ultralow $\mathcal{PT}$ breaking chaos [19], reduced fluctuations due to nonlinear saturation effects and quantum noise combination [20] and slow to fast light switching modulation [41] have been successfully predicted.

1.1.2.2 Pseudo Hermiticity

Although Hermiticity guarantees the reality of the Hamiltonian's spectrum, it constitutes a necessary but not sufficient condition. This limitation was first brought to light in 1959 in the context of investigations on the hard-core Bose gas where the Fermi pseudo-potential was employed [85]. Furthermore, after been found that the spectrum of a non-Hermitian variant of the Toda lattice is real [86], it was shown that there are certain classes of Hamiltonians whose spectra can be real even though they are non-Hermitians. Among these classes of Hamiltonians are the pseudo-Hermitians, whose subclass, the $\mathcal{PT}-$symmetry, is a special feature of pseudo$-$Hermitian systems.

The pseudo$-$Hermiticity is the generalisation of $\mathcal{PT}-$symmetry. In other words, the $\mathcal{PT}-$symmetry concept is a particular case of the pseudo-Hermiticity. The concept of pseudo-Hermiticity was first introduced in the 1940s by Dirac and Pauli, and later questioned by Lee, Wick, and Sudarshan, who were trying to resolve the problems that arise in quantizing electrodynamics and other quantum field theories in which negative norm states appear as a consequence of renormalisation [87–91]. In 2002, Ali Mostafazadeh constructed an alternative theory, to conventional quantum mechanics and $\mathcal{PT}-$symmetric quantum theory, for non-Hermitian Hamiltonians whose spectrum is real. He showed that any Hamiltonian with a real spectrum is pseudo-Hermitian, and in particular $\mathcal{PT}-$symmetric Hamiltonians belong to the class of pseudo$-$Hermitian Hamiltonians [92–94].

By definition, a linear operator $\mathcal{H}$ is pseudo-Hermitian if there is a Hermitian operator η such that

$$\mathcal{H}^{\dagger} = \eta \mathcal{H} \eta^{-1} \tag{1.3}$$

where η is an invertible linear operator and $\dagger$ is the transpose and complex conjugation operation. We can observe that if we take the identity operator as $\eta = I$, η-pseudo Hermiticity reduces to an ordinary Hermiticity $\mathcal{H}^{\dagger} = \mathcal{H}$.

1.1.3 $\mathcal{PT}-$ Symmetry concept

When a system remains unvariant under effet of the transformation (translation, rotation,..), this means that it possesses a symmetry. Symmetry is a fundamental concept that is widely used by mathematicians and physicists alike. In physics, and in particular in quantum mechanics, this concept is associated with the operators of parity $\mathcal{P}$ and of time $\mathcal{T}$.

1.1.3.1 $\mathcal{P}$ and $\mathcal{T}$ operators

The Parity ($\mathcal{P}$) and Time reversal ($\mathcal{T}$) transformations are defined by their actions on the position operator $\hat{x}$ and the momentum operator $\hat{p}$ as well as the time parameter t [1]. ($\mathcal{P}$) is a linear operator which inverses space and momentum. In a one dimensional system, this corresponds to the reflection $x \to -x$ around a point of origin. Similarly, physical quantities that depend on odd powers of x, such as momentum p_x, are also inverted. In quantum mechanics, the action of the operator $\mathcal{P}$ is described by the relation (1.4) below

$$\mathcal{P}: \ \hat{x} \to -\hat{x}; \ \ \hat{p} \to -\hat{p} \tag{1.4}$$

For example, in electronic circuits or mechanical systems, applying spatial reflection means inverting the left and right elements of the device.

On the other hand, the anti-linear $\mathcal{T}$ operator reverses the time $t \to -t$. Any physical quantity dependent on odd powers of t such as momentum or is reversed. In the framework of wave theories, the action of $\mathcal{T}$ operator is equivalent to the transformation $i \to -i$. Its action is given by

$$\mathcal{T}: \ i \to -i; \ \ \hat{x} \to \hat{x}; \ \ \hat{p} \to -\hat{p} \tag{1.5}$$

1.1.3.2 $\mathcal{PT}$ operator

Although systems obeying parity ($\mathcal{P}$) and time ($\mathcal{T}$) symmetry are ubiquitous and have been well studied, systems which do not obey $\mathcal{P}$ or $\mathcal{T}$ symmetry individually, but are invariant to combined parity-time ($\mathcal{PT}$) reversal, have attracted a great deal of interest. These systems are so-called $\mathcal{PT}$ symmetric systems. They are systems having non-Hermitian Hamiltonians but, can have real energy eigenvalues under a certain condition. Indeed, it was demonstrated by Carl Bender and Stefan Boettcher that a Hamiltonian $\mathcal{H}$ of a system do not need to be

Hermitian i.e., it does not need to satisfy the Hermiticity symmetry condition (1.2). But only the condition of space-time reflection symmetry or $\mathcal{PT}$ symmetry expressed as

$$\mathcal{H} = \mathcal{H}^{\mathcal{PT}} \tag{1.6}$$

where the $\mathcal{PT}$-reflected Hamiltonian $\mathcal{H}^{\mathcal{PT}}$ is defined in terms of $\mathcal{P}$ and $\mathcal{T}$ operators as $\mathcal{H}^{\mathcal{PT}} \equiv (\mathcal{PT})\mathcal{H}(\mathcal{PT})$. This supposes that the $\mathcal{PT}$ operator must commute with $\mathcal{H}$

$$[\mathcal{H}, \mathcal{PT}] = \mathcal{HPT} - \mathcal{PTH} = 0 \tag{1.7}$$

So, if $\mathcal{H}$ satisfies (1.6), it is said to be $\mathcal{PT}$ symmetric. In their works, C. M. Bender and S. Boettcher have proposed a general parametric family of $\mathcal{PT}$ symmetric Hamiltonians and demonstrated that the reality of the spectrum is a consequence of the system obeying $\mathcal{PT}$ symmetry in (1.7). The expression for the Hamiltonian of this family is given by the formula

$$\mathcal{H} = \hat{p} + \hat{x}^2(i\hat{x})^{\varepsilon} \tag{1.8}$$

where the parameter ε is real. It was shown in 1998 in [1] that when $\varepsilon \geq 0$ all of the eigenvalues of these Hamiltonians are entirely real and positive, but when $\varepsilon < 0$ there are complex eigenvalues. We say that $\varepsilon \geq 0$ is the parametric region of unbroken $\mathcal{PT}$ symmetry and that $\varepsilon < 0$ is the parametric region of broken $\mathcal{PT}$ symmetry (see Fig.**??**).

No mathematical formulation shows that the individual action of either the $\mathcal{P}$ or $\mathcal{T}$ operator on a non-Hermitian Hamiltonian would make any real physical sense. However, Bender and Boettcher proved that it is possible for a non-Hermitian Hamiltonian to admit real eigenvalues under the condition that it commutes simultaneously with the parity $\mathcal{P}$ and time $\mathcal{T}$ operators. With this new formulation of hermeticity, the relevance of systems gorvend by non-Hermitian Hamiltonians becomes evident. These systems were long dismissed, as they appeared to contradict the standard postulates of quantum mechanics and were therefore considered incapable of describing physical phenomena.

1.1.3.3 $\mathcal{PT}-$symmetric systems

Using the language of quantum mechanics, $\mathcal{PT}$ symmetric systems are those described by a Hamiltonian $\mathcal{H}$ which commutes with the $\mathcal{PT}$ operator, i.e. $[\mathcal{H}, \mathcal{PT}] = 0$. In general, such Hamiltonians can be non-Hermitian, with some parameter called γ or gain/loss parameter, that controls the non-Hermiticity. These systems are specifically constructed by combining balanced pairwise energy gain and loss mechanisms linked by parity to an otherwise symmetric system. In general, these systems taken individually are non-conservative, but the gain and loss mechanisms present in the environment allow for the possibility of a net compensation of energy between these gains and losses (when they are equal and opposite). Such systems are achieved by mean of a coupling mechanism between the two sub-systems as shown in Fig.1.2.

As illustrated on 1.2(a) and 1.2(b), there are two non-concervative subsystems which represent the gain and loss respectively. From Fig.1.2(a), a system with a gain is unstable, in

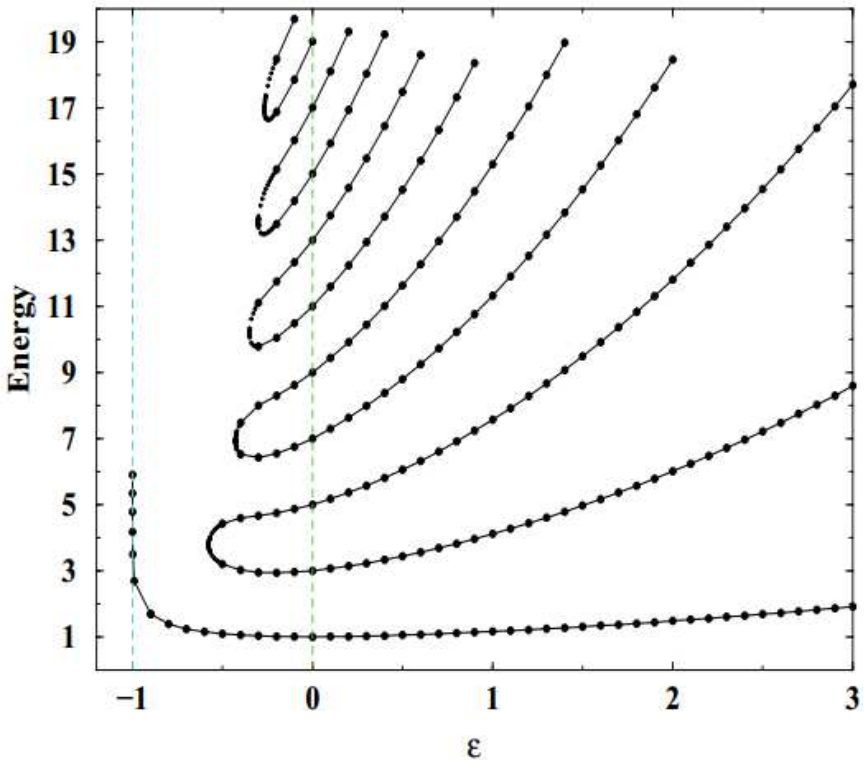

Figure 1.1: Energy eigenvalues of the Hamiltonian $\mathcal{H}= \hat{p}+\hat{x}^2(i\hat{x})^{\varepsilon}$ with respect to the real parameter ε. There are three regions: when $\varepsilon \geq 0$, the spectrum is real, positive and the energy levels rise with increasing ε. The lower bound of this region, $\varepsilon = 0$, corresponds to the harmonic oscillator, whose energy levels are $E_n = 2n + 1$. When $-1 < \varepsilon < 0$, there are a finite number of real positive eigenvalues and an infinite number of complex conjugate pairs of eigenvalues. As ε decreases from 0 to -1, the number of real eigenvalues decreases; when $\varepsilon \leq -0.57793$, the only real eigenvalue is the ground-state energy. As ε approaches -1^+, the ground-state energy diverges. For $\varepsilon \leq -1$ there are no real eigenvalues. When $\varepsilon \geq 0$, the $\mathcal{PT}$ symmetry is unbroken, but when $\varepsilon < 0$ the $\mathcal{PT}$ symmetry is broken. [57]

the same way as for a system with a loss, portrayed in Fig.1.2(b); the system with a gain has a growing state while the system with a loss has a decaying state. It is, however, through the coupling of these subsystems that a system exhibiting energy growth can be stabilised by interaction with a dissipating subsystem, ultimately leading to a globally stable system, as illustrated in Fig.1.2(c).

A peculiar feature of this type of system is that it exhibits a dynamic bifurcation as the strength of the γ control parameter increases. Indeed, as this gain/loss parameter γ that controls the degree of non-Hermiticity of $\mathcal{H}$ gets a critical value $\gamma_{\mathcal{PT}}$ (also known as the Exceptional Point), a spontaneous transition from net conservation of energy to net non-conservation can occurs. This also corresponds to a spontaneous breaking of the $\mathcal{PT}$ symmetry of the solutions of the symmetric system. For low but non-zero γ, the spectrum can be entirely real with $\mathcal{H}$ and $\mathcal{PT}$ sharing the same eigenvectors. In this case, the system is considered in the *exact phase*. However, as γ is increased past a critical point $\gamma_{\mathcal{PT}}$, the eigenvectors of $\mathcal{H}$ cease to be eigenvectors of $\mathcal{PT}$ and the spectrum becomes complex; the system is in the *broken phase*. Fig.1.3 shows the eigenvalues as a function of the gain/loss parameter. Three regions can be

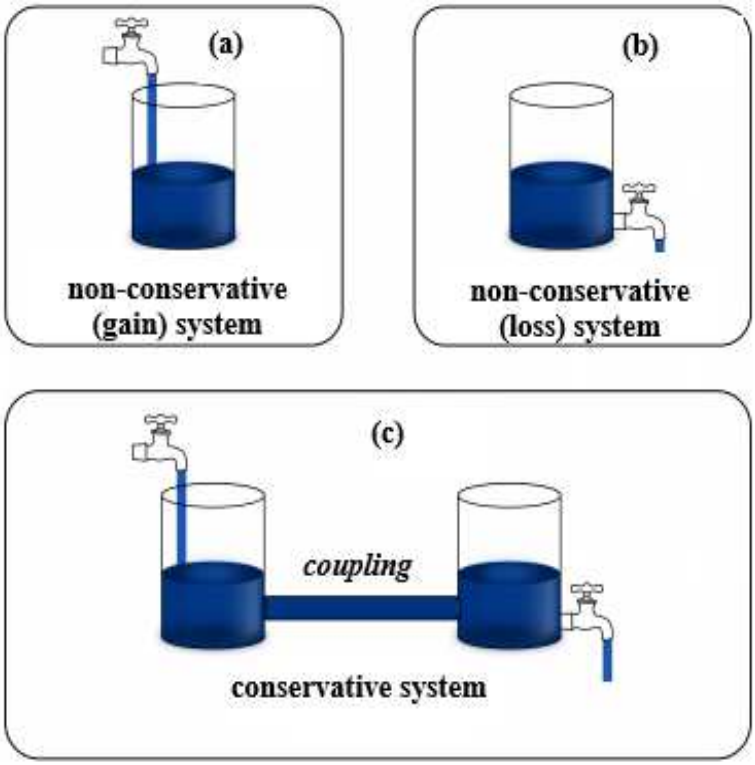

Figure 1.2: Illustration of gain-loss system. (a) represents a non-conservative isolated subsystem with gain, (b) a non-conservative isolated subsystem with loss and (c) the conservative coupled system, one with gain and the other with loss. The figure is modified from [95]

clearly distinguished: the exact or unbroken phase, the broken phase and the exponential phase.

When $0 < \gamma < \gamma_{\mathcal{PT}}$ (in the exact phase), the $\mathcal{PT}$ symmetric system has four real eigenvalues, i.e. a positive pair and a negative pair. In this region, the system is characterised by bounded oscillations and is in the stable regime. Between the symmetry breaking point and the critical point $\gamma_{\mathcal{PT}} < \gamma < \gamma_{cr}$ (in the broken phase), the different pairs of eigenvalues become complex conjugates, which imposes unstable dynamics on the system with the energy increasing exponentially [9, 10]. Moreover, when $\gamma = \gamma_{\mathcal{PT}}$ (at the exceptional point), the eigenvalues coalesce. Finally, when $\gamma > \gamma_{cr}$, the values become purely imaginary. In this last case, there are no oscillations in the system since the energy can either blow up or decays away exponentially. This exponential region corresponds to the overdamped modes of a single oscillator, and is therefore of no interest.

$\mathcal{PT}$ symmetric systems have not only been studied in quantum mechanics. They have also been implemented in many other areas of physics, including optics-photonics [23, 26, 43, 97–105, 117], electronics [9, 10, 106], acoustics [4, 5] and even mechanics [8, 13, 15–21], to name but a few. In this work, particular attention is given to the mechanical domain; however, a general overview will first be provided on optical and electronic $\mathcal{PT}$ symmetric systems, followed by a focus on mechanical $\mathcal{PT}$ symmetric systems.

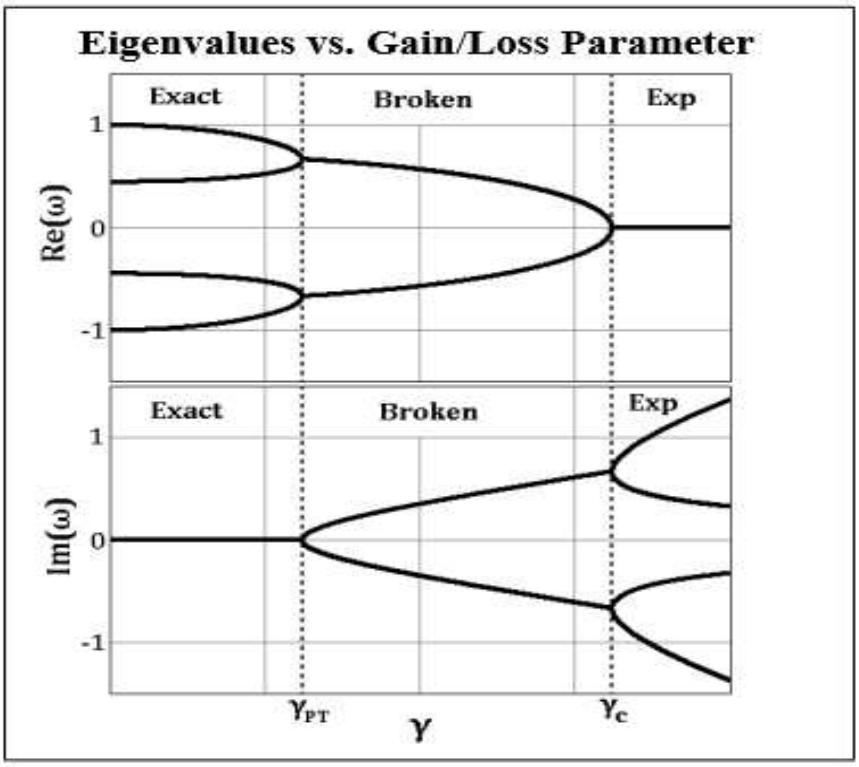

Figure 1.3: Real and imaginary parts of the eigenvalues. Frequencies are defined by the $e^{i\omega t}$ convention. The exact phase is characterized by four purely real oscillating frequencies. The broken phase has exponentially growing and decaying oscillations. The exponential phase has purely exponential non-oscillating solutions. [96]

a) In electronics

Due to its theoretical and experimental simplicity, the field of electronics is very opened to the implementation of $\mathcal{PT}$ symmetry in electronic circuits. The pair of coupled LRC oscillators are shown in Fig.1.4, one with the resistor component $-R$ (negative resistance) providing linear amplification and the other with the resistor component R providing linear attenuation of equal intensity, form a system called $\mathcal{PT}$ dimer.

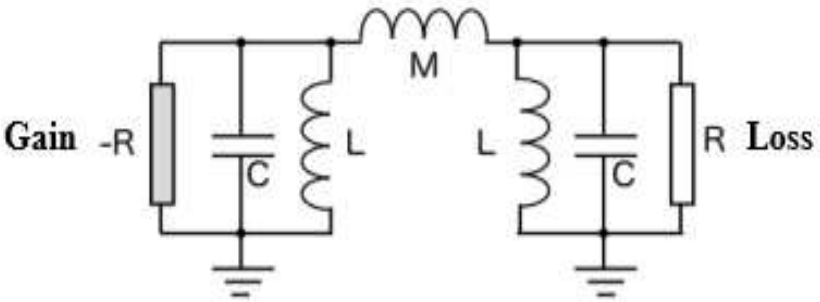

Figure 1.4: $\mathcal{PT}$ symmetric electronic dimer. The gain (amplification) is realised by the negative resistance $-R$ while the loss (attenuation) is achieved by the resistance R. [10]

The Fig.1.4 was first proposed first by J. Schindler et *al* in 1998 to demonstrate that a pair of

coupled LRC circuits, with gain and loss mechanisms, can provide an experimental realisation of a $\mathcal{PT}$ symmetry system.

From Kirchhoffs laws, the set of coupled second order differential equations modeling this system are given by Eq.(1.9)

$$\begin{aligned} \frac{d^2Q_1^C}{d\tau^2} &= -\alpha Q_1^C + \mu\alpha Q_2^C + \gamma\frac{dQ_1^C}{d\tau} \\ \frac{d^2Q_2^C}{d\tau^2} &= \mu\alpha Q_1^C - \alpha Q_2^C - \gamma\frac{dQ_2^C}{d\tau} \end{aligned} \quad . \tag{1.9}$$

where $Q_i^C, i = 1, 2$ are the dimensionless charges through the capacitors, with $\tau = \omega_0 t$, $\omega_0 = 1/\sqrt{LC}$; $\gamma = \frac{1}{R}\sqrt{\frac{L}{C}}$; $\mu = \frac{M}{L}$; $\alpha = \frac{1}{1-\mu^2}$. γ is the symmetric gain/loss strength parameter associated with the resistance, while μ is the inductive coupling term.

The $\mathcal{PT}$-symmetry of the equations of motion is easily confirmed. In the framework of Eq. (1.9), the $\mathcal{PT}$ operation swaps the indices 1 and 2, and reverses the sign of τ. These operations in conjunction leave the equations unaltered. The symmetry of the equations of motion correspond to the physical symmetry of the system. Fig.1.5 illustrates the presence of physical symmetry.

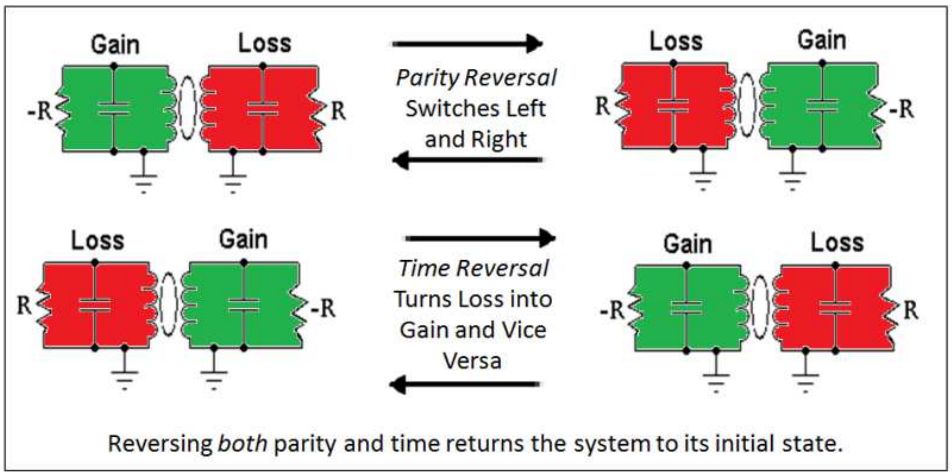

Figure 1.5: The physical symmetry of the system corresponds to its symmetric equations of motion. The figure is adapted from [107].

Applying the steady state solution, $Q_{1,2}^C = Q_{1,2}e^{i\omega\tau}$ to Eq.(1.9), and solving for the eigenvalues ω, four expressions of eigenfrequencies are obtained with positive ones given by Eq.(1.10):

$$\omega_{1,2} = \omega_0\sqrt{\frac{2+\gamma^2\left(\mu^2-1\right) \pm \sqrt{4\left(\mu^2-1\right)+\left[2+\gamma^2\left(\mu^2-1\right)\right]^2}}{2\left(1-\mu^2\right)}} \tag{1.10}$$

These two eigenvalues coalesce at the exceptional point (EP) below [7], marking the transition between real eigenvalues and complex eigenvalues.

$$\gamma_{\mathcal{PT}} = \frac{1}{\sqrt{1-\mu}} - \frac{1}{\sqrt{1+\mu}} \tag{1.11}$$

The critical point γ_{cr}, marking the transition between complex eigenvalues and purely imaginary eigenvalues [9] is given as

$$\gamma_{cr} = \frac{1}{\sqrt{1-\mu}} + \frac{1}{\sqrt{1+\mu}} \tag{1.12}$$

The solutions have several regimes of behaviour, as described by the Fig.1.3. These theoretical results together with the experimental results [9, 10], as depicted in Fig.1.6 shows that this "active" dimer allows for a direct observation of all the characteristics of $\mathcal{PT}$ systems such as power oscillation in the exact phase, power law behaviour at the exceptional point and exponential growth of the total energy in the capacitors in the broken phase.

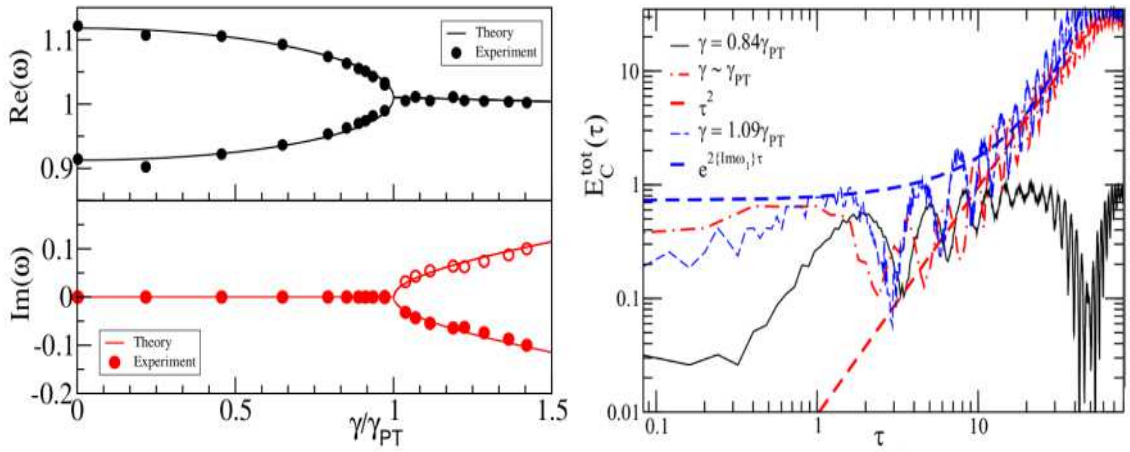

Figure 1.6: (Left) Parametric evolution of the experimentally measured eigenfrequencies vs the normalised gain and loss parameter $\gamma/\gamma_{\mathcal{PT}}$. The dots show the experimental results while the solid curve show the theoretical results. (Right) Experimentally measured temporal dynamics of the capacitance energy $E_C^{tot}(\tau)$ of the total system for various γ-values. As $\gamma \to \gamma_{\mathcal{PT}}$ the τ^2 behaviour, a signature of the spontaneous $\mathcal{PT}$-symmetry breaking, is observed. The figure is adapted from [10].

b) In optics

An optical $\mathcal{PT}$ symmetric dimer can be realised by associating two coupled $\mathcal{PT}$ symmetric waveguides, one with amplification and the other one with attenuation. If so, the medium has two regions with only one of the two parallel channels being optically pumped to provide gain γ for the guided light, whereas the neighbour arm experiences equal amount of loss see Fig.1.7. Light is transferred from one waveguide to the other via optical tunneling.

After paraxial approximation [7, 24], the beam dynamics of the optical dimer along the waveguides (z-axis) is given by a Schrödinger-like differential equation,

$$i\frac{d\Psi}{dz} = \mathcal{H}\Psi \tag{1.13}$$

where $\Psi = (a(z), b(z))^T$ (with T denoting the transpose), describes the optical mode electric field amplitudes $a(z)$,$b(z)$ in the two waveguides and the paraxial distance z plays an analogous

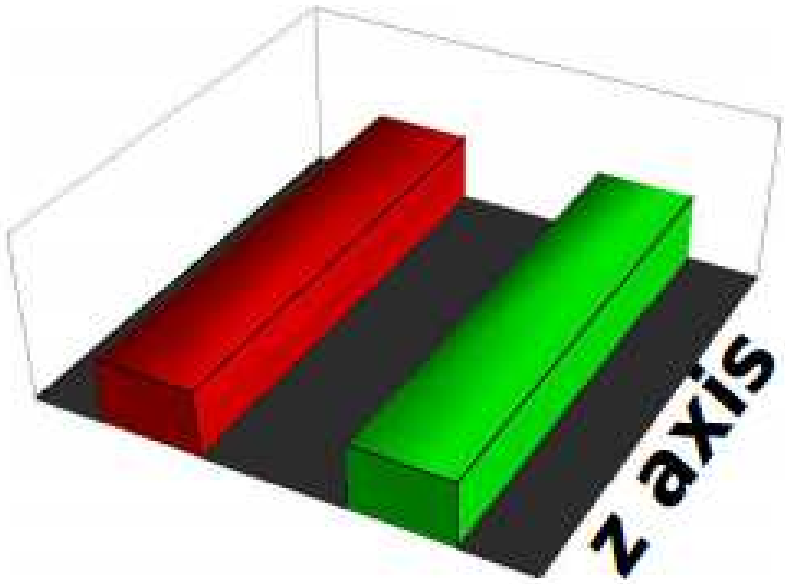

Figure 1.7: An illustration of $\mathcal{PT}$ symmetric dimer waveguide. The green waveguide indicates associated optical loss γ while the red waveguide involves an equivalent amount of optical gain $-\gamma$. Light is transferred from one waveguide to the other via evanescent coupling κ. The figure is adapted from [109].

role of time t in the Schrödinger picture. The Hamiltonian $\mathcal{H}$ of the dimer is given by a simple 2×2 matrix [108] :

$$\mathcal{H} = \begin{pmatrix} \epsilon_0 + i\gamma & \kappa \\ \kappa & \epsilon_0 - i\gamma \end{pmatrix}. \tag{1.14}$$

in which κ is the evanescent coupling between the two waveguides, γ is the gain/loss coefficient, and ϵ_0 is the real part of the index of refraction (which we will set to zero without loss of generality). It is easy to see that the dimer is $\mathcal{PT}$-invariant; parity switches between the two waveguides (the diagonal terms in $\mathcal{H}$) while time reversal transforms them back by complex conjugation so that the combined action of $\mathcal{PT}$ leaves the Hamiltonian unchanged. The eigenvalues of this system is given by Eq.(1.15)

$$\varepsilon_{\pm} = \pm\sqrt{\kappa^2 - \gamma^2} \tag{1.15}$$

From the above equation, one can see that ε is real for $\gamma < \kappa$ and becomes imaginary for $\gamma > \kappa$. The sharp transition from a real to a complex spectrum that takes place at $\gamma_{\mathcal{PT}} = \kappa$ is coined spontaneous $\mathcal{PT}$ symmetry breaking, depicted in Fig.1.8.

c) In mechanics

Just as one can transfer the formalism of $\mathcal{PT}$ symmetry from quantum mechanics to optics and to electronics, it is possible to map $\mathcal{PT}$ symmetry onto the framework of mechanical

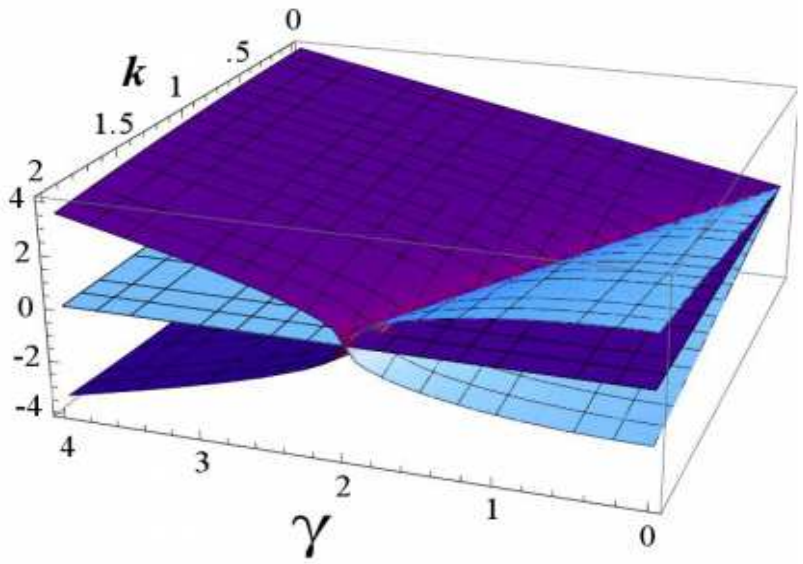

Figure 1.8: The plot of the eigenvalues ε. The z-axis represents the value of $\Re(\varepsilon_\pm)$ or $Im(\varepsilon_\pm)$. The blue curve represents $\Re(\varepsilon_\pm)$ and the purple curve represents $\Im(\varepsilon_\pm)$. The eigenvalues become degenerate when the curves coalesce along the line $\gamma_{\mathcal{PT}} = \kappa$. The figure is adapted from [110].

systems. It was demonstrated by Bender et *al.* [13] that the $\mathcal{PT}$ phase transition can occur in a simple $\mathcal{PT}$ symmetric classical-mechanical system as a coupled pair of two oscillators. To this end, they have proposed a $\mathcal{PT}$ mechanical dimer shown in Fig.1.9, and formed by a pair of coupled and driven pendulums such that one of them is damped, while the other is anti-damped (i.e. driven). In the other words, one of the pendula has energy gain, while the other has energy loss. This simple physical system exhibits the features of $\mathcal{PT}$-symmetric systems, as described in Sec.1.1.3.3, and exhibits also two $\mathcal{PT}$ transitions: a transition from broken to unbroken $\mathcal{PT}$ symmetry when the parameter of control of the Hermiticity is small, and a second transition from unbroken to broken $\mathcal{PT}$ symmetry when that parameter is large.

Thus the classical equations of motion of the coupled pendulum system [13] for small displacements $x(t)$ and $y(t)$ are given by :

$$\begin{aligned} \ddot{x}(t) &= -x(t) - \varepsilon y(t) \\ \ddot{y}(t) &= -y(t) - \varepsilon x(t) \end{aligned} \tag{1.16}$$

where $x(t)$ and $y(t)$ are the displacements of the pendula. The real and positive parameter ε represents the coupling of the two pendula. The $\mathcal{PT}$ phase transition is introduced by inserting a damping (loss) term in the x-equation and an anti-damping (gain) term in the y-equation such that Eq.(1.16) becomes

$$\begin{cases} \ddot{x}(t) + b\dot{x}(t) + x(t) + \varepsilon y(t) = 0 \\ \ddot{y}(t) - b\dot{y}(t) + y(t) + \varepsilon x(t) = 0 \end{cases} \tag{1.17}$$

where the real and positive coefficient b represents the gain/loss parameter. If we simultaneously apply the $\mathcal{P}$ and $\mathcal{T}$ operators to this system, it will be easy to verify that it is a $\mathcal{PT}$ symmetric

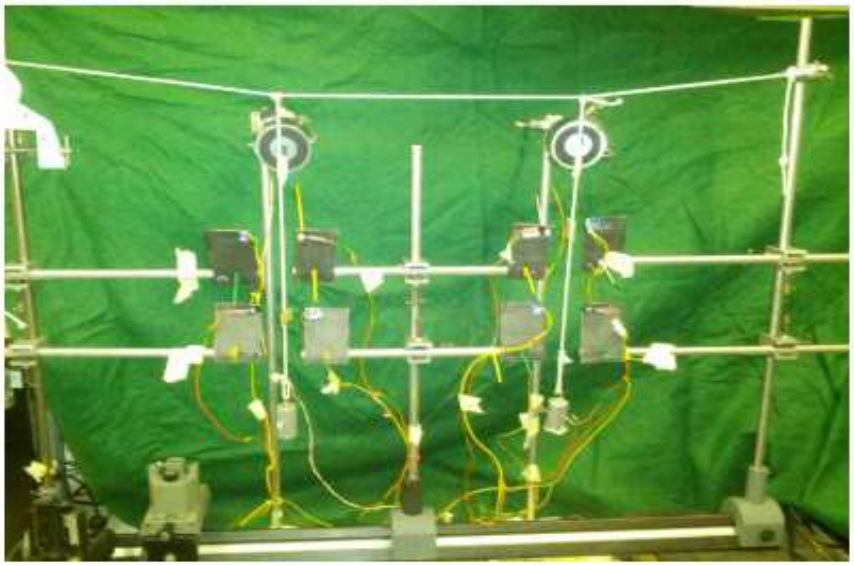

Figure 1.9: The mechanical experimental device of two coupled pendulums. The two pendula are suspended from a horizontal rope and the tension in the rope is adjusted to increase or decrease the coupling of the pendula. The figure is taken from [13].

system. This is because, the dynamical variables x and y will be interchanged under the $\mathcal{P}$ action and the signs of the damping and anti-damping terms will be reversed under the time reversal $\mathcal{T}$ action. The coupled system in (1.17) is an instance of the generic balanced loss-gain system illustrated in Fig.1.2(c). This system is not just $\mathcal{PT}$ symmetric; it is also called Hamiltonian system, and the equations of motion can be derived from the Hamiltonian

$$\mathcal{H} = \frac{1}{2}p^2 + \frac{1}{2}x^2 + \frac{1}{2}q^2 + \frac{1}{2}y^2 + \varepsilon xy \tag{1.18}$$

where $p(t)$ and $q(t)$ are the corresponding conjugate momenta. The Hamiltonian (1.18) is $\mathcal{PT}$ symmetric because under parity reflection $\mathcal{P}$ the loss and gain oscillators are interchanged,

$$x \to y, \quad y \to x, \quad p \to q, \quad q \to p,$$

and under time reversal $\mathcal{T}$ the signs of the momenta are reversed,

$$x \to x, \quad y \to y, \quad p \to -p, \quad q \to -q,$$

To solve analytically the system (1.17), we seek a solution of the form $x(t) = Ae^{i\lambda t}$ and $y(t) = Be^{i\lambda t}$, where A and B are constants. Substituting these expressions into Eq.(1.17), the system below is obtained:

$$\begin{cases} (-\lambda^2 + ib\lambda + 1)A + \varepsilon B = 0 \\ \varepsilon A + (-\lambda^2 - ib\lambda + 1)B = 0 \end{cases} \tag{1.19}$$

Solving this system for λ, the following fourth-degree polynomial equation is obtain

$$P(\lambda) = \lambda^4 + (b^2 - 2)\lambda^2 + 1 - \varepsilon^2 = 0 \tag{1.20}$$

which has zeros when,

$$\lambda^2 = \frac{1}{2}\left(2 - b^2 \pm \sqrt{b^4 - 4b^2 + 4\varepsilon^2}\right) \tag{1.21}$$

The system (1.17) admits oscillatory solutions if $\lambda^2 > 0$. The $\mathcal{PT}$ breaking point given in Eq.(1.22) is obtained by solving $b^4 - 4b^2 + 4\varepsilon^2 = 0$

$$b_{\mathcal{PT}} = \sqrt{2(1 - \sqrt{1 - \varepsilon^2})} \tag{1.22}$$

Therefore, if the damping/anti-damping parameter b is below this $\mathcal{PT}$ breaking point, the eigenvalues are real and the system is in the unbroken $\mathcal{PT}$ symmetric region. after this point, the eigenvalues are complex. There is also a critical point above which the eigenvalues pass from complex to purely imaginary, its expression is as follows:

$$b_{cr} = \sqrt{2(1 + \sqrt{1 - \varepsilon^2})} \tag{1.23}$$

The dynamics of the eigenvalues as a function of the damping/anti-damping parameter b is the same as shown in Fig.1.3, with the same interpretation. A simple analysis of Eq.(1.22) reveals that the system will remain stable if $\varepsilon < 1$. Fig.1.10 illustrates the various behaviours of the solutions to Eq.(1.17) accross the weak-, intermediate-, and strong-coupling regimes, indicates the presence of two $\mathcal{PT}$-symmetry transitions. The solutions $x(t)$ and $y(t)$ are plotted accroding to the time t.

In the weak-coupling regime the solutions oscillate and grow exponentially in time. In the intermediate-coupling (unbroken-$\mathcal{PT}$) regime the solutions oscillate and remain bounded. and remain bounded. In this regime the envelopes of the $x(t)$ and the $y(t)$ solutions grow and decay periodically and there is a lag time between the maxima. These long-time vibrations are power oscillations also called *Rabi oscillations* [111]. The behavior in the strong-coupling (broken-$\mathcal{PT}$) regime is different from the behavior in the weak-coupling (broken-$\mathcal{PT}$) regime. In both cases, the solutions grow exponentially, but in the strong-coupling regime, the solutions grow so rapidly that they do not oscillate about the horizontal axes.

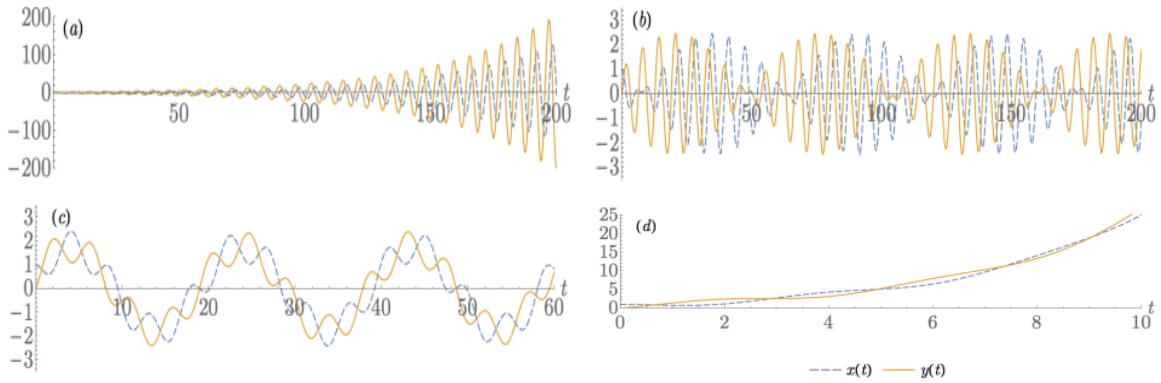

Figure 1.10: Dynamical evolution of the solutions $x(t)$ (dashed blue line) and $y(t)$ (solid orange line) of the system Eq.(1.17) plotted as functions of t. For all plots $\gamma = 0.1$ has been used. Plots are shown for four different values of the coupling strength ε: (a) $\varepsilon = 0.09$ (in the weak-coupling region of broken $\mathcal{PT}$ symmetry), (b) $\varepsilon = 0.15$ (in the lower range of the intermediate-coupling region of unbroken $\mathcal{PT}$ symmetry), (c) $\varepsilon = 0.9$ (in the upper range of the intermediate-coupling region), (d) $\varepsilon = 1.1$ (in the strong-coupling region of broken $\mathcal{PT}$ symmetry). The figure is taken from [118].

1.2 Generalities on the mechanical systems

1.2.1 Examples of mechanical systems

A mechanical system refers to a set of mechanical elements (coupled or not), that are arranged to perform a specific function or task. Mechanical systems play an essential role in our daily lives, whether in vehicles within the infrastructure we rely upon, and may range from simple to highly complex. Naturally, the term "mechanical systems" often refers to oscillatory systems, i.e. any mechanical system that periodically moves about its stable equilibrium position. A wide range of mechanical systems can be found in the literature, including: beams, pendulums and solid-spring systems.

1.2.1.1 Beam systems

A beam is an elongated member formed by a flat surface with a constant or variable cross-section along its length. Beams can be made of metal, concrete or wood and are generally used in the following areas: civil engineering, where they are used in the construction of buildings as framing elements, floors and transverse structures such as bridges and viaducts; industry, where they are used as rails on which robots run: and even ports, where they are used as supports on which trolleys run to load ships. The Fig.1.11 below show a model of beam under transversal excitation P, widely found in civil and mechanical engineering [119]. This model is strongly non-linear and the transversal excitation can be the movement of vehicles or people on the bridge, the movement of robots or vibrating machines on the floor-plates (for example in industries), etc.

It has been demonstrated that the equation goverving the dynamics of such structure are

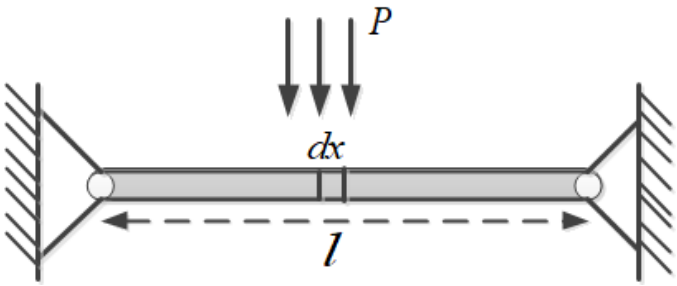

Figure 1.11: Articulated beam under transversal excitation. The figure is taken from [119].

given as

$$\frac{d^2q}{d\tau^2} + \lambda\frac{dq}{d\tau} + \pi^4 q + cq^3 + dq^5 = F_0\cos(\Omega\tau) \tag{1.24}$$

where q is the dimensionless tranversal displacement and τ the dimensionless time. The other dimensionless coefficients are: F_0 the amplitude of the external excitation, λ the coefficient of the viscous damping, π^4 the natural frequency, c and d the cubic and quintic nonlinearity coefficients respectively.

1.2.1.2 Double pendulum systems

Nature abounds with remarkable phenomena that warrant thorough investigation. One of such occur in pendulums. A pendulum can be defined as a weight suspended from a pivot so that it can swing freely [112]. Examples of pendulums include simple pendulums, double pendulums and many other "real life" examples of pendulums [113, 114]. A double pendulum is a simple mechanical system composed of two pendulums connected in series, which exhibits significantly more complex dynamics. The double pendulum has a rich dynamics making it a so called miracle of nature. On one hand, when subjected to small oscillations, the system displays the beat phenomenon. On the other hand, when a large amount of energy is supplied to the system, a chaotic behaviour is observed [115].

Dynamic systems with double elements have important applications in engineering sciences. In addition, pendulum systems are widely used in nature for the description of the movement of certain mechanical structures, particularly robot arms (see Fig.1.12(b) below). These systems are essentially used to solve the problems related to the systems control since they are systems that have both stable and unstable equilibria, and can exhibit chaotic behavior [116]. Two interesting control problems with pendulum systems are the stabilisation around an unstable equilibrium, and the swing-up maneuver.

A double pendulum can be described as a pendulum with another pendulum attached to its end as illustrated in Fig.1.12(a). In terms of the generalised coordinates, θ_1 and θ_2, the general differential equations governing the dynamics of the system (for small oscillations) can be derived using Lagrange formalism and expressed as

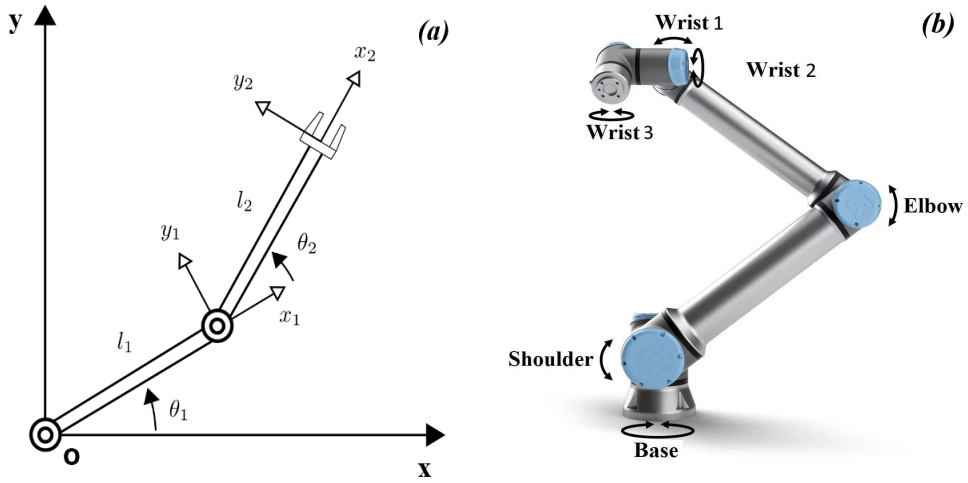

Figure 1.12: Model of double pendulum system.

$$\begin{aligned}(m_1+m_2)l_1\ddot{\theta}_1 + m_2 l_2\ddot{\theta}_2 + (m_1+m_2)g\theta_1 - \frac{1}{6}(m_1+m_2)g\theta_1^3 = 0\\ l_2\ddot{\theta}_2 + l_1\ddot{\theta}_1 + g\theta_2 - \frac{1}{6}g\theta_2^3 = 0\end{aligned} \tag{1.25}$$

where m_1 and m_2 are the masses of the pendulums of lengths l_1 and l_2 respectively. The overdots indicate the differentiation with respect to time t.

1.2.1.3 Mass-spring-damper systems

A simple mass-spring-damper (MSD) system is a mechanical system with one degree of freedom as presented in Fig.1.13(a) below. It consists of a mass attached to a spring which is forced to move in a single direction. Its movement is due to three forces: a restoring force $\overrightarrow{T}$, a damping force $\overrightarrow{f}$ and an exerted force $\overrightarrow{F}$. There are also MSD systems with two or more degree-of-freedom (see Fig.1.13(c)), nonlinear or not which have been intensively investigated in the past few years [117, 120–126]. MSD systems are important in engineering because many practical engineering components consist of vibrating systems that can be modeled using one or two-degree-of-freedom systems such as elastic beams supported by two springs and vibration of a milling machine [127], in watchmaking to create precise movements in watches and clocks. Springs have also been used in vehicle suspensions (Fig.1.13(b)) to absorb shock and vibration.

In addition, these MSD systems have allowed us to better understand the dynamic behaviour of certain mechanisms, study their stability, optimise them for energy harvesting applications and even control certain structures. These systems can be mathematically modeled using Newton's second law of motion. By applying this to the mechanical system depicted in Fig.1.13(c), and assuming that the end springs possess nonlinear stiffness, the resulting second-order differential equations expressed as

$$\begin{aligned}m_1\ddot{x}_1 + b\dot{x}_1 + (k_1+K)x_1 - k_2x_1^3 - Kx_2 = 0\\ m_2\ddot{x}_2 + b\dot{x}_2 + (k_1+K)x_2 - k_2x_2^3 - Kx_1 = F_0 cos(\omega t)\end{aligned} \tag{1.26}$$

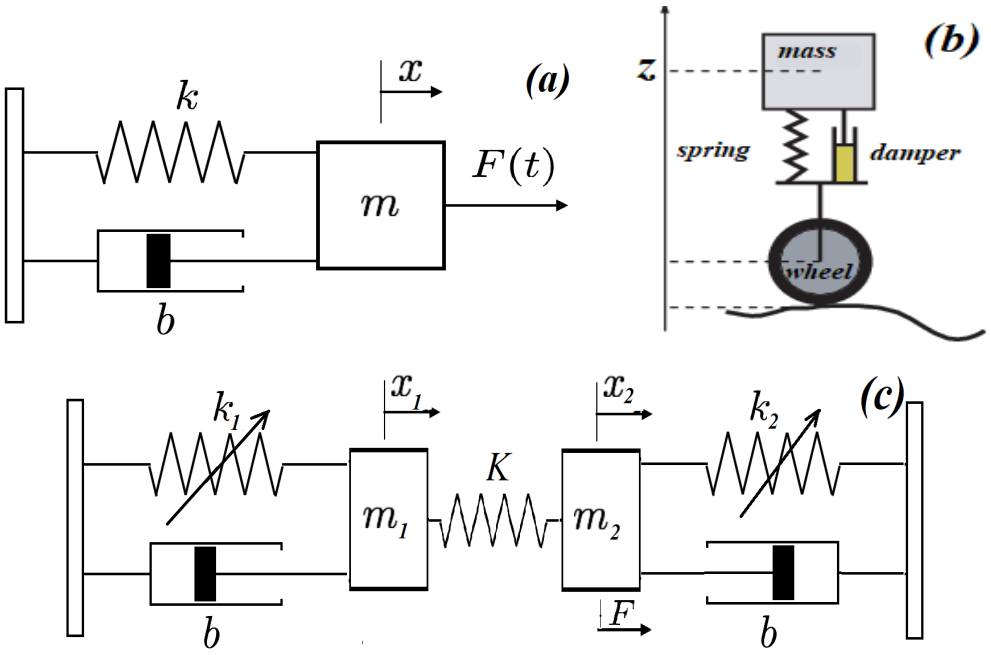

Figure 1.13: Models of mass-spring systems with one (a and b) and two (c) degrees of freedom.

where m_1 denotes the mass of the first nonlinear system and m_2 the mass of the second nonlinear system. k_1 , k_2 and b (with $k = (k_1, k_2)$) represent the linear, nonlinear stiffness and damping coefficient in relation to mass m_1 and m_2 respectively. The displacements of the masses are denoted by x_1 and x_2. F_0 represents the amplitude of the external excitation and ω its frequency. An overdot indicates the differentiation with respect to time t.

1.2.2 Nonlinearity and Coupling in mechanical systems

1.2.2.1 Nonlinearity in mechanical systems

Most physical systems are inherently nonlinear in nature. Some of the interesting physical phenomena observed in these systems are only possible if the mathematical model of the system includes nonlinearities, as opposed to linear models, which are very often limited. For example, phenomena such as jumps, hysteresis, subharmonic, superharmonic and combined resonances, self-excited oscillations, modal interactions and chaos can only be observed and explained if there are nonlinear terms in a system. In other words, linear models of physical systems are limited and only applicable in a restrictive domain where the amplitude of oscillations is generally considered to be very small. Thus, in order to accurately characterise the dynamic behaviour of systems, it is therefore essential to consider the study of the nonlinearities present in the systems. To achieve this, it would be useful to have knowledge of the origin and nature of the nonlinearities particularly in mechanical systems under investigation.

a) Source of nonlinearity

Nonlinearities in mechanical systems can be divided into three main categories.

Contact nonlinearities. This category covers all nonlinearities associated with contact between solids :

– The contact between solids across a surface of reduced dimensions, for which the model associated with Hertz's law is generally used.

– Dry friction, which produces a highly non-regular relationship between contact forces and sliding speed.

– Intermittent contacts.

Material nonlinearities. These arise from the nonlinear behaviour of the material: the relationship between stresses and strains in the material is nonlinear, and can be list as :

– Elasto-plastic materials, this is the usual case of a non-linear behaviour law, which will only be mentioned here because it has few applications in vibration due to its irreversibility.

– Elastomer-type materials, which are generally highly dissipative.

–Shape memory alloys, which are beginning to be studied and used in vibration control, in particular because of the hysteresis associated with their behaviour, which produces damping.

Geometric nonlinearities. They appear in structures or mechanisms subjected to large amplitude movements. Their physical basis and their main manifestations will be recalled both in the case of mechanisms composed of rigid solids and for thin deformable structures. For example

– a bi-articulated pendulum,

– a system of two articulated bars forming a purely nonlinear spring used in nonlinear vibration absorbers. The elastic potential of the spring of this system can be modelled in the following way:

$$V(x) \approx \frac{1}{2}\left(k_1 \pm \frac{1}{2}k_2x^2 \pm \frac{1}{3}k_3x^4 \pm ...\right)x^2 \tag{1.27}$$

where $K \approx k_1 \pm \frac{1}{2}k_2x^2 \pm \frac{1}{3}k_3x^4 \pm ...$ represents the nonlinear stiffness, with k_1, k_2 and k_3 being all positive parameters.

b) Nature or type of nonlinearity

Generally, in mechanics, most nonlinear physical systems can be modelled by a set of masses and springs arranged in an appropriate way. In such systems the nonlinearity is geometric. In a classical mass-spring system, the vibration of the mass is caused by the spring force F. Indeed, if the spring is extended, a force appears which has the tendency to relax and to put the spring in the previous state. The same happens when the spring is pressed. This force depends on the deformation x of the spring. In the first case the deformation is positive,

and in the second case it is negative. If for small deformation, the relation force–deformation is approximately linear, the spring is said to be linear. The experiments done on the springs made of aluminum, titanium, copper and their alloys [128] and also of wooden materials [129] show that the force–deformation characteristics are nonlinear and can be divided into two types: *hard* and *soft*. For the soft spring nonlinearity decreases the force faster than in the linear spring. For the hard spring the increase of the force is faster than in the linear spring. In other words, nonlinearity in a mechanical system (such as a mass-spring system) is related to the stiffness of the spring. For the case considered in the Eq.(1.27), and assuming that the system is symmetric, i.e., the stiffness characteristic is the same when the spring is in compression or in tension, the nonlinear relationship between the force applied to the spring F and the resulting displacement if we consider only is given as

$$F = k_1 x \pm k_3 x^3 \pm k_5 x^5 \tag{1.28}$$

It is assume here that, the restoring force above is approximated as a series in x and truncated after the first three terms.

Soft nonlinearity, the system is considered to be softening if the quintic term is negative. When this is the case, it is referred to as a soft nonlinearity because the spring becomes softer as the displacement increases. In these systems, the curve of the Force versus the deformation is concave downward as presented in Fig.1.14 below.

Hard nonlinearity, in the opposite, the system is considered to be hardening if the quintic term is positive. And when this happens, it is referred to as a hard nonlinearity because the spring becomes stiffer as the displacement increases, see Fig.1.14. The characteristic of the force versus the deformation is concave towards the up.

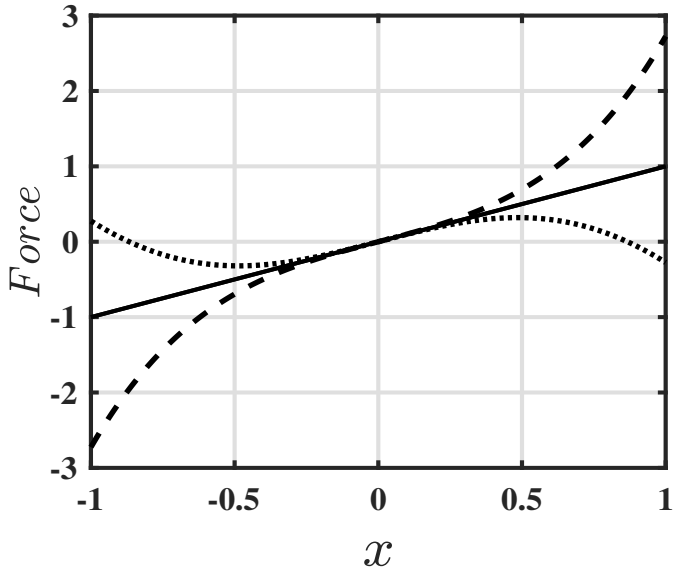

Figure 1.14: Characteristics of a nonlinear hardening and softening spring described by Eq.(1.28). Force-deflection characteristics for a linear spring (solid line), hardening spring with (dashed line) and softening spring (dotted line).

1.2.2.2 Coupling in mechanical systems

In physics, when two objects are in interaction with each other, they are said to be coupled. In Newtonian mechanics, coupling is an interaction between two oscillating systems, such as pendulums linked by a chain. These interactions affect the oscillatory behaviour of the two objects. When two harmonic oscillators can exchange energy, they are said to be coupled. This happens when the two oscillators are receptive to each other's excitations. However, the interaction between these two systems can be of a different nature. Three main types of coupling in mechanics are distinguished :

a) Elastic coupling

Elastic coupling between two mechanical oscillators occurs when the coupling term is proportional to the dynamic variable (displacement). Such a coupling is achieved by a spring characterised by an elastic force. As an example of systems coupled by elasticity, we can cite two pendulums connected by a spring as shown in Fig.1.15.

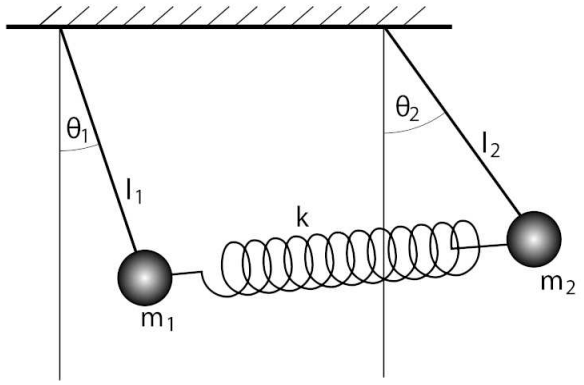

Figure 1.15: pendulums coupled by a spring.

The corresponding differential equations are expressed as

$$\begin{aligned} m\ddot{x} &= -\frac{mg}{l_1}x - k(x_1 - x_2) \\ m\ddot{x} &= -\frac{mg}{l_2}x + k(x_1 - x_2) \end{aligned} \tag{1.29}$$

with $x_i = l\theta_i$ $(i = 1, 2)$ and $l_1 = l_2 = l$

b) Dissipative coupling

In this case, the coupling is ensured by means of viscous damping (or friction, see Fig.1.16) and is expressed in terms proportional to speed in the differential equations.

Assuming that the masses are identical, the corresponding differential equations are expressed as

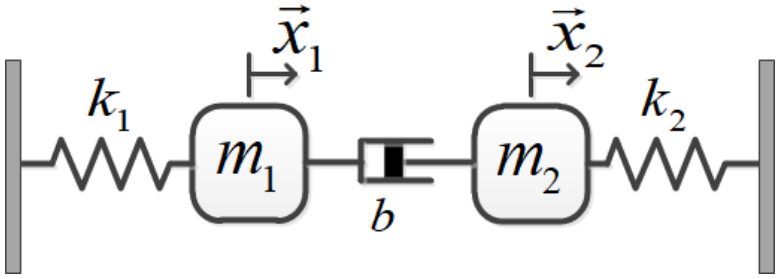

Figure 1.16: Oscillators coupled through viscous damping.

$$\begin{aligned} \ddot{x}_1 + \frac{b}{m_1}\dot{x}_1 + \frac{k_1}{m_1}x_1 - \frac{b}{m_1}\dot{x}_2 = 0 \\ \ddot{x}_2 + \frac{b}{m_2}\dot{x}_2 + \frac{k_2}{m_2}x_2 - \frac{b}{m_2}\dot{x}_1 = 0 \end{aligned} \tag{1.30}$$

c) Inertial coupling

An inertial coupling appears through the second time derivative of the variables (acceleration). A simple example of inertial coupling is the double pendulum (see Eq.(1.25)). It is also possible to create inertial coupling using a mechanical element called an "*inerter*". The inerter is a mechanical device with the property that the force applied to its two terminals is proportional to the relative acceleration between them [34, 130]. As a new passive mechanical element, the performance benefits of using inerters in various mechanical systems have been well demonstrated [130].

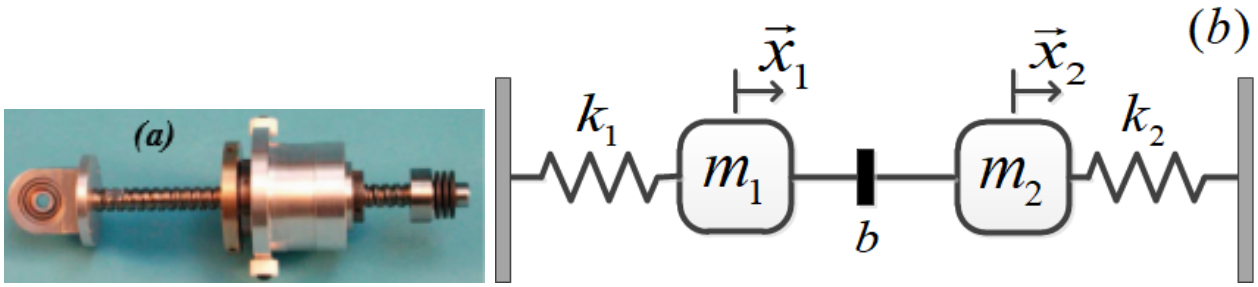

Figure 1.17: (a) an inerter device, (b) oscillators coupled through inertia.

The corresponding differential equations are given as follows :

$$\begin{aligned} \ddot{x}_1 + \frac{k_1}{m_1}x_1 - \frac{b}{m_1}\ddot{x}_2 = 0 \\ \ddot{x}_2 + \frac{k_2}{m_2}x_2 - \frac{b}{m_2}\ddot{x}_1 = 0 \end{aligned} \tag{1.31}$$

1.2.3 $\mathcal{PT}$ symmetric mechanical systems

As mentioned above, the design of a balanced $\mathcal{PT}$ symmetric system requires the presence of two oscillators, one attenuating the energy and the other amplifying it. In other words, it means bringing into play two systems with opposite characteristics (loss and gain respectively) that interact with each other.

1.2.3.1 Loss oscillator

It is a non-conservative system that oscillates with friction, i.e. with a frictional force proportional to the velocity $\dot{x}$ of the oscillations. This is referred to as a system with viscous damping and is closely approximated for small velocities in air and in liquids. The physical system associated with this type of behaviour is similar to that shown in Fig.1.13(a) (with no external force) and, in the linear regime, the equation of its motion is given by

$$m\ddot{x} + b\dot{x} + kx = 0 \tag{1.32}$$

where b (positive) is the friction coefficient, i.e. the frictional force per unit of velocity. If $\frac{b}{m} = 2\gamma$ and $\frac{k}{m} = \omega_0^2$, Eq.(1.32) can be reduced to the usual form expressed as follows :

$$\ddot{x} + 2\gamma\dot{x} + \omega_0^2 x = 0 \tag{1.33}$$

If the parameters γ and ω_0^2 are chosen appropriately (such that $\gamma^2 = \omega_0^2$), the system will perform a damped oscillatory motion. The temporal evolution of a such system is illustrated in the Fig.1.18.

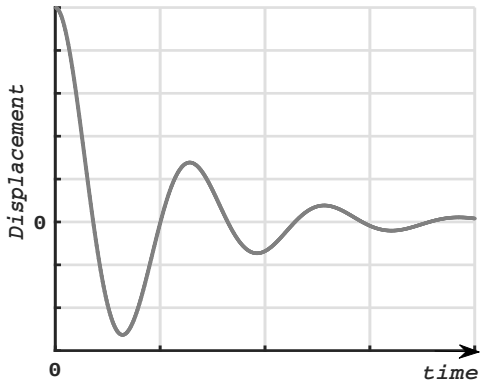

Figure 1.18: Typical temporal evolution of an underdamped oscillatory system.

1.2.3.2 Gain oscillator: negative friction

A gain oscillator is an oscillator where the energy increases over time. In other words, it is also a non-conservative system that is subject to energy amplification due to a negative friction. In ordinary systems with friction, the coefficient $\gamma = b/2m$ (in Eq.(1.33) is always positive since friction always resists the motion and $b > 0$. A positive coefficient of friction means that the

overcoming of friction requires energy. If b and hence γ were negative, the energy of the system would increase and friction would be a source of energy. It is clear that this is impossible in a system without a source of energy, since b as well as γ is always positive. If the system possesses a reservoir of energy, then one can allow $\gamma < 0$ and the energy of the system increases on account of friction. Of course, this can no longer be regarded as friction in the conventional sense. However, if it is represented by the same term in the differential equations as ordinary friction–namely the term involving $\dot{x}$– one shall also refer to it as friction in the case of negative γ, and thus speak of *negative friction*.

To achieve negative friction, the mechanical system in Fig.1.19 can be considered. It consists of a mass m attached to one end of a spring k, the other end of which is fixed to a stationary support [131]. The assembly is placed on a conveyor belt moving uniformly with a velocity v_0.

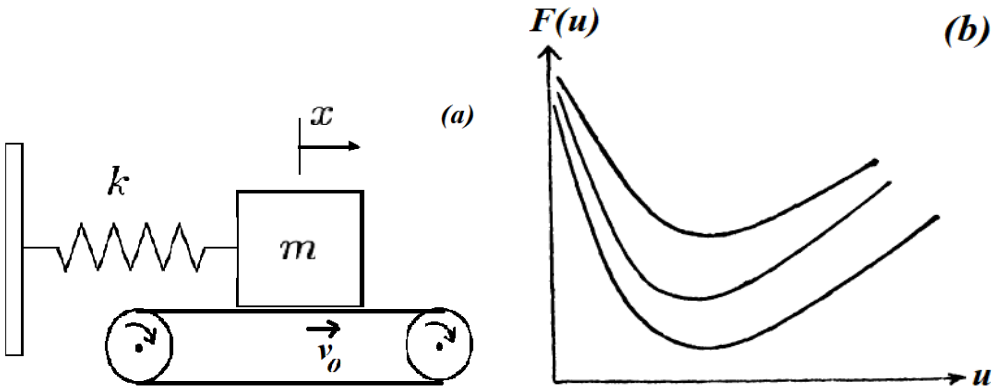

Figure 1.19: (a) Mechanical system with negative friction, (b) frictional characteristics $F(u)$, with $u = v_0 - \dot{x}$ stands for the relative velocity between the conveyor and the mass. [131]

The friction of the conveyor belt on the mass is a function of their relative velocity u expressed by $F(u) = F(v_0 - \dot{x})$. Assuming that all the other frictional forces (for example, air resistance or internal friction of the springs) are proportional to the first power of the velocity, the equation of motion of the mass m is of the form

$$m\ddot{x} + b\dot{x} + kx = F(v_0 - \dot{x}) \tag{1.34}$$

Considering the region where $\dot{x} << v_0$ (small $\dot{x}$), $F(v_0 - \dot{x})$ can be expanded in powers of $\dot{x}$

$$F(v_0 - \dot{x}) = F(v_0) - \dot{x}F'(v_0) + ... \tag{1.35}$$

Inserting it into Eq.(1.34) and taking into account the position of equilibrium, we obtain

$$m\ddot{x} + (b + F'(v_0))\dot{x} + kx = 0 \tag{1.36}$$

As to the coefficient $b + F'(v_0)$ of $\dot{x}$ its value and sign depend on the form of the characteristic of friction (see Fig.1.19(b)); $F'(v_0)$ represents the slope of the frictional characteristic $F(u)$ at the point v_0. If the frictional characteristic decreases, $F'(v_0) < 0$. If the frictional characteristic decreases very rapidly about v_0, then $b + F'(v_0) < 0$ and Eq.(1.36) describes a system with

negative friction. When this occurs, the system will act as source of energy and its energy increases with the time such it is presented in the Fig.1.20

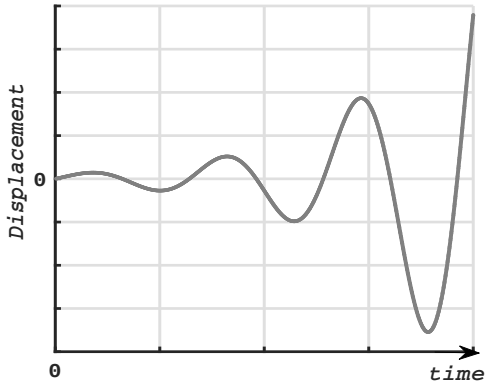

Figure 1.20: Temporal evolution of an anti-damped system.

1.2.3.3 $\mathcal{PT}$ symmetric mechanical oscillator: Conception

By making coupling (elastic coupling for example such in Fig.1.21 [15]) between the loss and gain oscillators, one can realise under certain conditions, a system that conserves the energy. In fact, since the anti-damping and damping of the masses m_1 and m_2 respectively are all proportional to their velocities, and if the rate of growth of the displacement of mass m_1 and the rate of decay of the displacement of m_2 are balanced, the energy in the gain oscillator will be transfer to the loss oscillator and the energy of the system is conserved. And in this case the system is called $\mathcal{PT}$ symmetric mechanical oscillator. In other words, if the rate of the growth of the gain oscillator and the rate of the decay of the loss oscillator are not balanced, the system will be non-conservative and one can observe either a growth or a decay of the energy in the system.

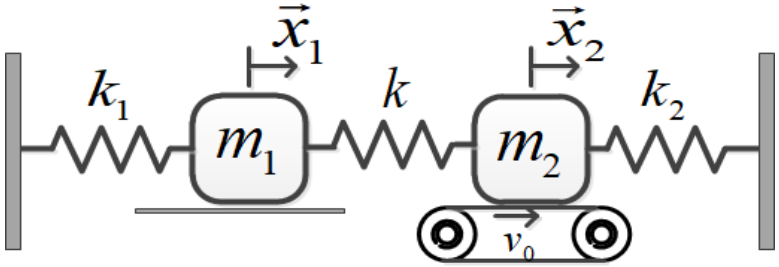

Figure 1.21: Mechanical system model with $\mathcal{PT}$-symmetry. Figure is adapted from [15]

The differential equations gorverning the dynamics of this coupled system can be written as

$$\begin{aligned} m_1\ddot{x}_1 + b_1\dot{x}_1 + k_1x_1 &= (k_1 + k)x_2 \\ m_2\ddot{x}_2 + b_2\dot{x}_2 + k_2x_2 &= (k_2 + k)x_1 \end{aligned} \tag{1.37}$$

with $b_2 = b + F'(v_0) < 0$ and $b_1 > 0$. The term in the second member represents the coupling term.

1.3 Resonance phenomenon

1.3.1 Definition and description

The phenomenon of resonance is an inherent property of certain physical objects or systems that preferentially absorb energy, generally in mechanical, electrical, electromagnetic or other form, when subjected to forces that vary periodically over time. Resonance corresponds to an energy maximum. It occurs when the amplitude of the oscillations of the system increases under the influence of regular pulses until it reaches a state of equilibrium, which depends on the dissipative elements of the system, or until a component of the system fails. This failure occurs when the excitation frequency is close to the natural frequency of the system (also known as the resonant frequency). When a resonant system is subjected not to periodic excitation, but to percussion (in the case of mechanical systems), or to an impulse (in the case of electrical systems), then it becomes the seat of damped oscillations, at a frequency close to its natural frequency, and will gradually returns to its stable state. Resonance is a concept that exists on many different scales in nature, and is involved in a wide range of fields including acoustics (the voice and musical instruments), the movement of seas and oceans (tidal resonance), astronomy, electronics, mechanics, civil engineering, etc.

A resonant system, i.e. a system capable of amplifying its response under the effect of certain sustained cyclic constraints, is an oscillator. The peculiarity of such a system is that it can temporarily store energy in two forms: potential or kinetic. From this point of view, oscillation is the phenomenon by which the energy of the system periodically changes from one form to the other. In a mechanical system, for example, energy alternates between potential and kinetic forms: to illustrate, let's consider a mass-spring system that is compressed (moved away from its equilibrium position). It acquires potential energy, which is then converted into kinetic energy when it relaxes. When the mass reaches its highest point, the spring is at its maximum extension and the accumulated kinetic energy is completely converted into potential energy, and so on. This more or less damped repetitive motion is an oscillatory motion in which the velocity (and therefore the kinetic energy) is maximum at the point of equilibrium and the potential energy is maximum at the extremes of extension. Due to dissipative phenomena (damping), the system will come to rest when all forms of energy have been completely dissipated.

By injecting additional potential or kinetic energy at the moment when the potential (or kinetic) energy already stored is at its maximum, the energy thus injected will be added to the energy already stored and the amplitude of the oscillation will increase, as will the total energy of the system. If energy is injected in this way with a periodicity equal to (or close to) the periodicity of the system, the total energy will increase steadily. As a consequence, the amplitude of the oscillations will increase until it reaches a peak amplitude, at which point the system is said to be in resonance. An experiment like this allows to understand that the

phenomenon of resonance is nothing more than this effect of accumulating energy by injecting it at the moment when it can be added (i.e. in phase) to the energy already accumulated.

1.3.2 Applications of the resonance

Resonance eliminates certain frequencies, but has no effect on energy production. The resonator simply stores energy. However, it has a number of advantages, such as :

a) Radio receivers

Radio transmissions are low-amplitude oscillatory systems. For a given radio station, there is a corresponding electromagnetic wave with a very specific frequency. To pick it up, the *RLC* circuit (resistance, inductance, capacitance) is forced to vibrate via an antenna that picks up all the electromagnetic waves that reach it. To listen to a single station, the natural frequency of the RLC circuit must be tuned to the frequency of the desired station by varying the capacitance of a variable capacitor.

b) Nuclear magnetic resonance (NMR) and magnetic resonance imaging (MRI)

Working independently in 1946, two Americans, Felix Bloch and Edward Mills Purcell, discovered the phenomenon of nuclear magnetic resonance [132–134], also known as NMR. Their experiments consisted of placing an object in a magnetic field and exciting it with a radio frequency wave at the appropriate (resonance) frequency, in order to obtain details of its chemical composition from a signal emitted by the object in response.

In 1971, Raymond Damadian realised that the signal emitted by cancerous organic tissue was different from that emitted by healthy tissue in the same organ [135]. Two years later, Paul Lauterbur translated the signal into two-dimensional images. This was the beginning of magnetic resonance imaging.

The British scientist Peter Mansfield applied NMR to objects with complex internal structures. His extensive experiments made him one of the pioneers of magnetic resonance imaging for medical applications.

c) Musical instruments

Sound is usually produced by exciting an oscillating system (string, air column) to resonance in stringed and wind instruments.

d) Two-stroke engine

The exhaust pipe of a two-stroke engine has a very specific shape, designed to create a resonance phenomenon that improves engine performance by reducing fuel consumption and pollution. This resonance partially reduces unburned gases and increases compression in the cylinder.

1.3.3 Disadvantages of the resonance

a) Civil engineering

In civil engineering, a structure such as a bridge (generally assimilated to a beam) can vibrate vertically, transversely or torsionally. Each of these types of vibration has its own period; if the deck is suspended (held in place by cables attached to the pillars), the system will have a very different resonant frequency.

It is still remembered today that on April 16, 1850, a troop crossing in close order the bridge of the Basse-Chaîne, suspension bridge over the Maine at Angers, caused by resonance the rupture of the bridge and the death of 226 soldiers.

In the case of the Tacoma Narrows Bridge (USA, in 1940), transverse bending vibrations caused by high forces led to the failure of a cable, and the rest of the structure. The first explanation given was based on the excitation of a resonance by the periodic detachment of vortices in a Karman alley. In fact, the observed frequency of the oscillations was much lower than the detachment frequency that could be calculated. In this case, therefore, it seemed necessary to abandon the resonance explanation and replace it with one based on the notion of aeroelastic instability. When such a structure is coupled to a light fluid, the aeroelastic forces are negligible compared to the inertial forces or elastic forces of the structure, except in the vicinity of frequencies, where they compensate. The quadrature component, when it opposes the damping, reflects the wind energy input to the structure, which is the cause of the aeroelastic instability. The torsion mode becomes unstable, corresponding to oscillations of increasing amplitude. Breakage may then occur. Instability always occurs in the vicinity of a natural mode and therefore a natural frequency in the light fluid-structure coupling.

b) Buildings

Buildings are very sensitive to earthquakes. They can be protected by certain passive control devices: these are oscillators (a large pendulum suspended from the top of the building) whose natural frequency is close to that of the building itself. The energy is thus absorbed by the pendulum, preventing the building from collapsing.

c) Automobile

Motorists are often irritated by the parasitic noises that appear at a certain vehicle speeds or engine rotation. Certain poorly damped parts of the engine or bodywork resonate and emit sound vibrations. The car itself, with its suspension system, is an oscillator equipped with effective dampers that prevent the vehicle from entering into high frequency resonance.

d) Railways

There are also resonance problems in railway engineering. The wires suspended from the catenary wires form interconnected oscillators. To prevent them from transmitting the wave

caused by contact with the trains, the catenary wires are not laid at equal intervals. The same applies to the rails laid on the sleepers, but the phenomenon can be observed at higher frequencies.

1.4 Scattering

Scattering is a term used in physics to describe a wide range of physical processes where moving waves, are forced to deviate from a straight trajectory by localised non-uniformities (including particles and radiation) in the medium through which they pass. In other words, it is the phenomenon that describes the collision and subsequent interaction between propagating waves and the medium. It is a phenomenon that is widely studied in many fields: acoustics, electromagnetics and quantum waves, optics, electronics, etc. Despite the different languages, the fundamental process and the underlying physics coincide.

In electronics, the authors in [33,136] have experimentally investigated $\mathcal{PT}$ symmetric scattering using LRC circuits in an inductively coupled $\mathcal{PT}$-symmetric pair connected to transmission line leads. They have shown that, in the single-lead case, the $\mathcal{PT}$-symmetric circuit acts as a simple dual device—an amplifier or an absorber depending on the orientation of the lead. However, when a second lead is attached, the system exhibits unidirectional transparency for some characteristic frequencies.

For the single port scattering, they distinguished two cases: the first is when a transmission line (TL) is attached to the left (amplifying) circuit of the dimer load while in the second case, the TL is connected to the right (lossy) circuit of the load (see lower right and left insets of Fig.1.22 respectively).

The authors of ref. [136] were interested in the behaviour of the reflectance and the spatial profile of the potential inside the scattering domain were analysed as the gain/loss parameter γ and the frequency ω changes. For $\mathcal{PTS}$ structures, the corresponding scattering signals satisfy generalised unitarity relations which reveal the symmetries of the scattering target. Specifically, in the single-port configuration, this information is entirely encoded in the reflection. It may be observed that the lower-left setup in Fig.1.22 is the $\mathcal{PTS}$ counterpart of the one shown in the lower-right. As illustrated in the main panel of Fig.1.22, a representative measurement of the reflection signals corresponding to the two scattering configurations are presented and the results indicate that, the measured reflectances R_L and R_R satisfy the generalized conservation relation $R_L R_R = 1$.

For the double port scattering, the results found in this case have demonstrated that at specific ω-values (marked with vertical dashed lines in Fig.1.23 below), the transmittance becomes $T = 1$, while at the same time one and only one of the reflectances vanishes. This implies that, the scattering for this direction of incidence is flux conserving and the structure is unidirectionally transparent.

Another interesting feature exhibited by the two-port $\mathcal{PTS}$ scattering is a so-called simultaneous coherent perfect absorber-amplifier, or CPA laser [121], as illustrated in Fig.1.24. This

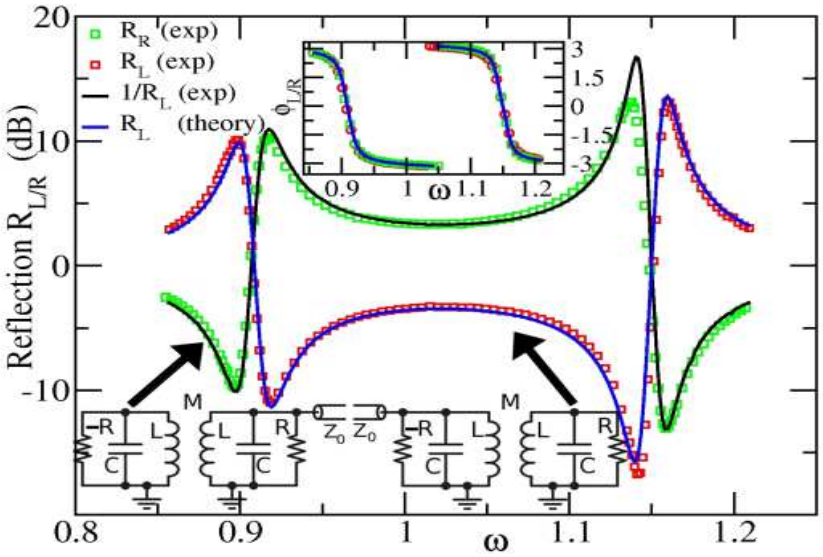

Figure 1.22: Experimental reflectances for a single TL attached to the lossy (R_R) or the gain (R_L) side of the dimer (see lower insets) for $\mu = 0.29$; $\gamma = 0.188875$; $\eta = 0.0305$. The black line corresponds to R_L^{-1} and confirms the non-reciprocal nature $R_L R_R = 1$ of the $\mathcal{PT}$-scattering The upper inset shows the measurements for the left (right) reflection phases ϕ_L (ϕ_R). The blue lines are the theoretical results. The figure is adapted from ref. [33].

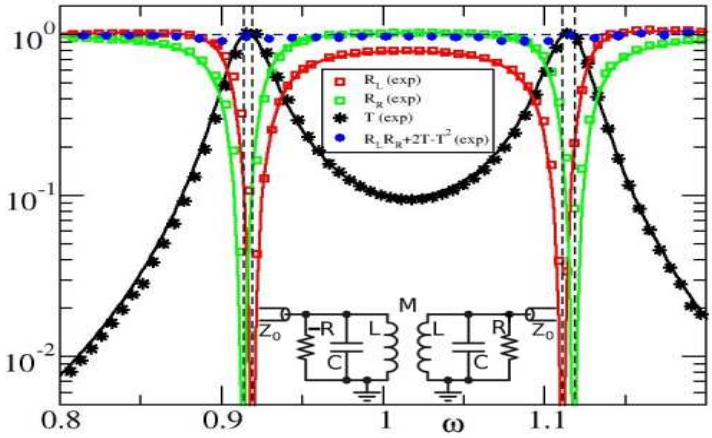

Figure 1.23: Measurements (symbols) and numerics (lines of corresponding color) of T , $R_{L/R}$ for the two-port scattering set-up. The vertical black dashed lines indicate the frequencies where unidirectional transparency occurs. The conservation relation is also evaluated using the experimental data. The horizontal dashed blue line is drawn for the eye and indicates the value 1. The parameters used are the those used in Fig. 1.22. The figure is adapted from ref. [33].

functionality was first implemented [9] in the capacitively coupled version of the electronic dimer scatterer shown in the inset of Fig.1.24. It was shown that the two-port $\mathcal{PTS}$ dimer can behave simultaneously as a perfect absorber and as an amplifier, a property which can be explored using an overall output coefficient Θ defined as

$$\Theta = \frac{\left|V_R^+\right|^2 + \left|V_L^-\right|^2}{\left|V_L^+\right|^2 + \left|V_R^-\right|^2} \tag{1.38}$$

where $V_{L,R}^+$ and $V_{L,R}^-$ represent the forward and the backward wave amplitudes.

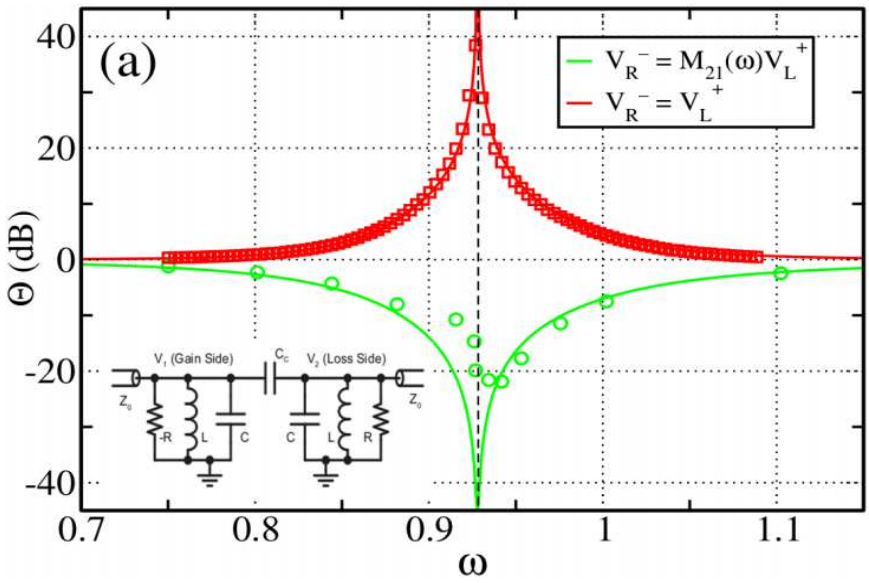

Figure 1.24: (a)The overall output coefficient $\Theta(\omega)$ versus frequency ω near the amplification/attenuation frequency ω_J (vertical dashed line). The $\mathcal{PTS}$ electronic circuit is coupled to two ports and has $\eta = 0.110$; $\gamma = 0.186$; $c = 0.161$. At $\omega = \omega_J$ the system acts as a perfect absorber when the input signal satisfies the coherent attenuation relation $V_R^- = \mathcal{M}_{21}(\omega) V_L^+$. For any other incident signal (e.g. see the blue line corresponding to $V_R^- = V_L^+$) the system acts as an amplifier. The dots are experimental values while the lines are numerical results. The figure is adapted from ref. [9].

In the optics framework as well, the authors in [121, 137] have suggested that a two-port $\mathcal{PT}$-symmetric cavity can act as a simultaneous coherent perfect absorber (CPA)-laser. They have shown that an optical medium that satisfies the $\mathcal{PT}$ symmetry condition $\epsilon(-r) = \epsilon^*(r)$ can behave simultaneously as a laser oscillator, emitting outgoing coherent waves, and as a coherent perfect absorber, fully absorbing incoming coherent waves with appropriate amplitudes and phases.

Conclusion

In this chapter, after providing a state of the art on the notions of Hermiticity and $\mathcal{PT}$ symmetry, a particular attention was paid on giving the generalities on the mechanical systems more precisely on the $\mathcal{PT}$ symmetric mechanical systems. The concepts of resonance and scattering were also introduced. The next chapter will be devoted to mathematical models of the studied system and methodology used to obtain the results.

Chapter 2

Material and methods

Introduction

Many areas of physics are concerned by nonlinearity problems, which generally appear as nonlinear terms in the equations governing the dynamics of the system. The solution of these equations may require a number of methods, both analytical and numerical. Although the analytical method is considered to be the most suitable to explain the behaviour of the system, it has its limitations. On the other hand, numerical integration has almost no limitations whatever the nature of the equations, since the solution takes into account the previous information, such as the initial conditions or previous data, unlike the analytical solution which requires a functional relationship. In this chapter we present the methodology used to solve the problem in this thesis. To achieve our objective, the study starts with the description and modelling of the nonlinear $\mathcal{PT}$-symmetric mechanical system under consideration, followed by the modelling and dynamic analysis of the associated mechanical scattering system. Finally, the different mathematical and numerical methods for the solution of the resulting equations are presented.

2.1 Design, description and mathematical modelling of the $\mathcal{PT}$-symmetric mechanical system

2.1.1 Design and description

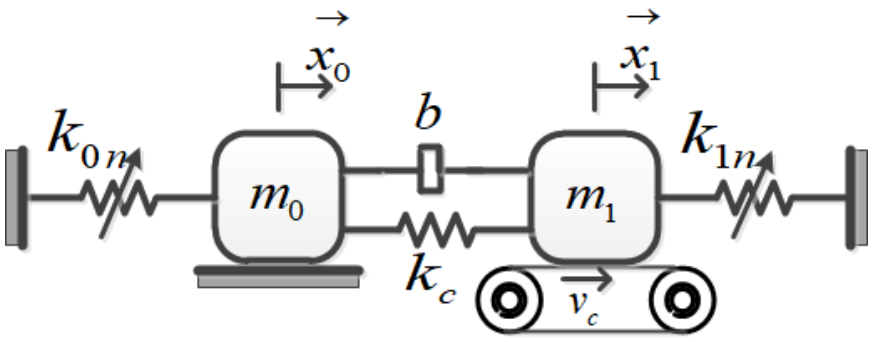

Figure 2.1: $\mathcal{PT}$-symmetric or non-Hermitian mechanical system model.

The system under investigation is a two damped and linearly coupled mass-spring devices as illustrated in Fig.2.1. The coupling between the two masses is realised through two mechanical elements: the spring of stiffness k_c and the inerter of inertance coefficient b, which provide the elastic and inertial connection respectively between the two masses. The first mass (m_0) is subjected to liquid/air natural frictional force proportional to its velocity $\dot{x_0}$ (for sufficiently small velocities to allow friction linearisation). This friction introduces energy loss and thus hinders the mass m_0 motion. Masses m_0 and m_1 are connected on their left and right sides to springs of nonlinear stiffness k_{0n} and k_{1n} respectively, which are attached to a fixed support. The second mass (m_1) is placed on a conveyor, which moves with constant velocity v_c. The conveyor, subjected to roll in a defined direction (along the $\vec{x}$ axis), drags the mass m_1 whose displacement will compress the spring of nonlinear stiffness k_{1n}. When the spring tension is greater than the static frictional force exerted by the conveyor surface on the mass m_1 [138], the latter will slip and return to its initial position for a new cycle. The conveyor thus acts as a reservoir that supply the mass m_1 with energy gain. It is said that mass m_1 is subjected to anti-friction or negative friction [18, 131]. If the positive and negative frictions are balanced, the coupled masses m_0 and m_1 form a $\mathcal{PT}$-symmetric system. And, in linear regime, the model presented in Fig.2.1 is similar to the ones described in [8, 10, 11, 13, 15, 16].

2.1.2 Modelling of the $\mathcal{PT}$-symmetric mechanical system.

Since the two masses m_0 and m_1 are constrained to move along the horizontal axis $\vec{x}$, their respective displacements are denoted by the variables x_0 and x_1. In the mechanical model shown in Fig.2.1, nonlinear terms is introduced by considering only the nonlinear character of the springs at the ends.

When the system is excited, the energies brought into play are :

- **Potential energy of the system**

Assume that the potential involved in the springs k_{0n} and k_{1n} is a ϕ^6 potential, the total potential energy of the system is in the form :

$$V = V_1 + V_2 + \frac{1}{2}k_c(x_0 - x_1)^2 \tag{2.1}$$

with

$$V_i = \frac{1}{2}k_{i0}x_i^2 - \frac{1}{4}k_{i1}x_i^4 + \frac{1}{6}k_{i2}x_i^6 \ ; \ i \in \{0,\ 1\} \ ;$$

where k_c is the stiffness of the coupling spring while k_{i0}, k_{i1} and k_{i2} are the stiffness coefficients of the quadratic, quartic and sixtic terms respectively. This potential with nonlinear terms of order greater than 4 is called the ϕ^6 potential.

- **Kinetic energy of the system**

The total kinetic energy of the system is expressed as follows:

$$T = \frac{1}{2}m_0\dot{x}_0^2 + \frac{1}{2}m_1\dot{x}_1^2 + \frac{1}{2}b(\dot{x}_1 - \dot{x}_0)^2, \tag{2.2}$$

where m_0, m_1 represent the masses of the oscillators 0 and 1 respectively, and b is the inertance coefficient of the inerter.

- **Dissipation and amplification energy of the system**

For the oscillator (m_0): As described in the previous section, the frictional force experienced by mass m_0 is proportional to its velocity $\dot{x}_0$ and it is therefore given by the following equation

$$f_0 = -\lambda_0\dot{x}_0, \tag{2.3}$$

For the oscillator (m_1): The resultant of the dissipative forces acting on the mass m_1 is given by :

$$f_1 = -\lambda\dot{x}_1 + F\left(\dot{x}_1 - v_c\right), \tag{2.4}$$

where $F\left(v_c - \dot{x}_1\right)$ is the friction force of the conveyor on the mass m_1. It depends on both $\dot{x}_1$ and v_c, and proportional to the first order of $\dot{x}_1$. For small velocities ($\dot{x}_1 << v_c$), one can expand $F\left(v_c - \dot{x}_1\right) \approx F(v_c) - F'(v_c)\dot{x}_1$. The constant force $F(v_c)$ results in a shift of stationary position for x_1, whereas the second term $F'(v_c)\dot{x}_1$ results in modification of the dissipation parameter.

$$f_1 = \left(-\lambda - F'(v_c)\right)\dot{x}_1 + F(v_c) \tag{2.5}$$

With this consideration, the linear model of the system is given by :

$$\begin{cases} (m_0 + b)\ddot{x}_0 + b\ddot{x}_1 + \lambda_0\dot{x}_0 + (k_{00} + k_c)x_0 - k_c x_1 = 0 \\ (m_1 + b)\ddot{x}_1 - b\ddot{x}_0 + (\lambda + F'(v_c))\dot{x}_1 + (k_{10} + k_c)x_1 - k_c x_0 = F(v_c) \end{cases} \tag{2.6}$$

Thus, a negative dissipation parameter can be achieved if the coefficient $F'(v_c)$ is chosen appropriately so that, $\lambda + F'(v_c) = \lambda_1 < 0$ (see section **1.2.3.2** in chapter 1).

The positions $x_{00} = 0$ (for the first oscillator) and $x_{01} = \frac{F(v_c)}{k_{10}+k_c}$ (for the second oscillator) correspond respectively to $\ddot{x}_0 = \dot{x}_0 = 0$ and $\ddot{x}_1 = \dot{x}_1 = 0$, i.e. these are the positions of equilibrium. Replacing x_0 by $x_{00}+x_0$ and x_1 by $x_{01}+x_1$ amounts to measuring the displacements from the positions of equilibrium and puts Eq.(2.6) in the form:

$$\begin{cases} (m_0 + b)\ddot{x}_0 + b\ddot{x}_1 + \lambda_0\dot{x}_0 + (k_{00} + k_c)x_0 - k_c x_1 = 0 \\ (m_1 + b)\ddot{x}_1 - b\ddot{x}_0 + \lambda_1\dot{x}_1 + (k_{10} + k_c)x_1 - k_c x_0 = 0 \end{cases} \tag{2.7}$$

Now taking all of the energies (kinetic and potential given in Eqs.(2.1) and (2.2)) into account, and applying the Lagrange formalism, the model is described by the following system of differential equations

$$\begin{cases} (m_0+b)\ddot{x}_0 + b\ddot{x}_1 + \lambda_0\dot{x}_0 + (k_{00}+k_c)x_0 - k_{01}x_0^3 + k_{02}x_0^5 - k_c x_1 = 0 \\ (m_1+b)\ddot{x}_1 - b\ddot{x}_0 + \lambda_1\dot{x}_1 + (k_{10}+k_c)x_1 - k_{11}x_1^3 + k_{12}x_1^5 - k_c x_0 = 0 \end{cases}, \tag{2.8}$$

The system (2.8) is that of a self-sustained nonlinear mechanical system of the Duffing type with elastic and inertial coupling, which, after a suitable normalisation, can be rewritten as

$$\begin{cases} (1+\mu_0)\ddot{X}_0 - \mu_0\ddot{X}_1 + 2\gamma_0\dot{X}_0 + X_0 - \alpha_0 X_0^3 + \eta_0 X_0^5 - \kappa_0 X_1 = 0 \\ (1+\mu_1)\ddot{X}_1 - \mu_1\ddot{X}_0 - 2\gamma_1\omega_0\dot{X}_1 + \omega_0^2 X_1 - \alpha_1\omega_0^2 X_1^3 + \eta_1\omega_0^2 X_1^5 - \kappa_1\omega_0^2 X_0 = 0 \end{cases} \tag{2.9}$$

where, $\tau = \omega_{0c}t$ represents the dimensionless time; $X_0 = \frac{x_0}{l_0}$ and $X_1 = \frac{x_1}{l_0}$ are the dimensionless variables of each oscillator. The following coefficients : $\mu_0 = \frac{b}{m_0}$, $\mu_1 = \frac{b}{m_1}$, $\gamma_0 = \frac{\lambda_0}{2m_0\omega_{0c}}$, $\gamma_1 = \frac{\lambda_1}{2m_1\omega_{1c}}$, $\alpha_0 = \frac{k_{03}l_0^2}{m_0\omega_{0c}^2}$, $\alpha_1 = \frac{k_{13}l_0^2}{m_1\omega_{1c}^2}$, $\eta_0 = \frac{k_{05}l_0^4}{m_0\omega_{0c}^2}$, $\eta_1 = \frac{k_{15}l_0^4}{m_1\omega_{1c}^2}$, $\kappa_0 = \frac{k_c}{m_0\omega_{0c}^2}$, $\kappa_1 = \frac{k_c}{m_1\omega_{1c}^2}$, $\omega_{0c}^2 = \frac{k_{01}+k_c}{m_0}$, $\omega_{1c}^2 = \frac{k_{11}+k_c}{m_1}$ and $\omega_0 = \frac{\omega_{1c}}{\omega_{0c}}$ denote the dimensionless parameters of inertial coupling, dissipation and amplification, cubic nonlinearity, quintic nonlinearity, elastic coupling, natural frequency in coupled regime and natural frequency ratio of the two oscillators respectively.

2.1.3 $\mathcal{PT}$-symmetry condition.

The system (2.9) is a more general form of two coupled nonlinear oscillators with both energy loss and gain. However, it cannot be immediately described as a $\mathcal{PT}$-symmetric system. To be a $\mathcal{PT}$-symmetric system, certain conditions must be satisfied. To obtain these conditions, the linear model in the system (2.10) have been considered

$$\begin{cases} (1+\mu_0)\ddot{X}_0 - \mu_0\ddot{X}_1 + 2\gamma_0\dot{X}_0 + X_0 - \kappa_0 X_1 = 0 \\ (1+\mu_1)\ddot{X}_1 - \mu_1\ddot{X}_0 + 2\gamma_1\omega_0\dot{X}_1 + \omega_0^2 X_1 - \kappa_1\omega_0^2 X_0 = 0 \end{cases} \tag{2.10}$$

Taking the solutions in the form $X_k = A_k e^{i\omega\tau}$, the characteristic equation below is obtained

$$\begin{aligned} &\left[(1+\mu_0)(1+\mu_1) - \mu_0\mu_1\right]\omega^4 + 2i\left[\omega_0(1+\mu_0)\gamma_1 + (1+\mu_1)\gamma_0\right]\omega^3 + \\ &\left[4\omega_0\gamma_0\gamma_1 - (1+\mu_0)\omega_0^2 - (1+\mu_1) + \kappa_0\mu_1 + \kappa_1\mu_0\omega_0^2\right]\omega^2 \\ &+2i\left[\omega_0^2\gamma_0 + \omega_0\gamma_1\right]\omega - \omega_0^2\kappa_0\kappa_1 = 0 \end{aligned} \tag{2.11}$$

In order for Eq.(2.11) to admit real eigenvalues, it is necessary for its imaginary part to be zero. It thus comes

$$\begin{cases} \omega_0(1+\mu_0)\gamma_1 + (1+\mu_1)\gamma_0 = 0 \\ \omega_0\gamma_0 + \gamma_1 = 0 \end{cases} \tag{2.12}$$

By setting $\omega_0^2 = 1$ (For the sake of simplicity), the following relations are found

$$\begin{cases} \gamma_0 = -\gamma_1 = \gamma \\ \mu_0 = \mu_1 = \mu \\ \kappa_0 = \kappa_1 = \kappa \end{cases} \tag{2.13}$$

So, when nonlinearity comes into play, we also get: $\alpha_0 = \alpha_1 = \alpha$ and $\eta_0 = \eta_1 = \eta$. Eq.(2.13) above defines the relations between the parameters of oscillator 0 and those of oscillator 1 so that the system is in the $\mathcal{PT}$ symmetry conditions. According to these relationships, to build a $\mathcal{PT}$-symmetric mechanical dimer, the two oscillators must be identical, i.e. the same masses ($m_0 = m_1$) and the same springs ($k_{00} = k_{10}$). Under these conditions, we can note that the rates of energy dissipation and amplification are the same and, the equations of motion are given by:

$$\begin{cases} (1+\mu)\ddot{X}_0 - \mu\ddot{X}_1 + 2\gamma\dot{X}_0 + X_0 - \alpha X_0^3 + \eta X_0^5 - \kappa X_1 = 0 \\ (1+\mu)\ddot{X}_1 - \mu\ddot{X}_0 - 2\gamma\dot{X}_1 + X_1 - \alpha X_1^3 + \eta X_1^5 - \kappa X_0 = 0 \end{cases} \tag{2.14}$$

On the other hand, if we interchange the variables X_0 and X_1, followed by inversion of time (under $\mathcal{PT}$ transformations, where $\mathcal{P}X_0 = X_1$, $\mathcal{P}X_1 = X_0$, $\mathcal{T}X_0(t) = X_0(-t)$ and $\mathcal{T}X_1(t) = X_1(-t)$), that system remains invariant with balance of dissipation and amplification rate.

The system in Eq.(2.14) above represent a set of two linearly coupled and damped extended Duffing oscillators (with ϕ^6 potential). The coupling here is bidirectional, and we can distinguish two types of coupling between the oscillators: elastic coupling and inertial coupling of respective coupling parameters κ and μ. The coefficient γ is the gain-loss rate of the X_i coordinate which describes the energy gain ($-\gamma < 0$) or loss ($+\gamma > 0$) in the system. α and η are the cubic and quintic nonlinearity parameters respectively. And, the $'dot'$ stands for the derivative with respect to time τ. In the linear limit, the Hamilton fonction assaociated to Eq.(2.14) can be derived as below:

$$H = \frac{\mu(1+\mu)(P_0^2+P_1^2)}{2(1+2\mu)} + \frac{(1+\mu)^2 P_0 P_1}{1+2\mu} - \frac{\gamma(X_0P_0+X_1P_1)}{1+\mu}$$
$$-\frac{\kappa(1+\mu)^2+\mu\gamma^2}{2(1+\mu)^3}(X_0^2+X_1^2) + \frac{(1+\mu)-\gamma^2}{(1+\mu)^2}X_0X_1$$

with the momenta given as follows: $P_0 = -\frac{\gamma}{1+\mu}(\frac{\mu}{1+\mu}X_0 + X_1) - \frac{\mu}{1+\mu}\dot{X}_0 + \dot{X}_1$ and $P_1 = \frac{\gamma}{1+\mu}(X_0 + \frac{\mu}{1+\mu}X_1) + \dot{X}_0 - \frac{\mu}{1+\mu}\dot{X}_1$. Interestingly, there are a number of symmetries that leave the system (2.14) invariant. These symmetries are listed in Table 2.1.

Symmetries (1) and (4) constitute the so-called spatial symmetry and time invariance making the nonlinear cubic-quintic Duffing (NCQD) equations a $\mathcal{PT}$-symmetric system.

2.1.4 Nonlinear characteristics and displacements.

Let us note that in the absence of coupling ($\kappa = \mu = 0$) the system in Eq.(2.14) reduces to two autonomous Duffing oscillators, one of which is an attenuator (the one with $+\gamma$ as

Table 2.1: Symmetries of system (2.14).

Symmetry 1	$(X_0,\, X_1) \to (-X_0,\, -X_1)$
Symmetry 2	$(X_0,\, \kappa) \to (-X_0,\, -\kappa)$
Symmetry 3	$(\kappa,\, X_1) \to (-\kappa,\, -X_1)$
Symmetry 4	$(t,\, \gamma) \to (-t,\, -\gamma)$
Symmetry 5	$(X_0,\, X_1,\, \gamma) \to (-X_1,\, -X_0,\, -\gamma)$
Symmetry 6	$(X_0,\, X_1,\, \alpha,\, \eta) \to \left(\delta X_0,\, \delta X_1,\, {}^{\alpha}/_{\delta^2},\, {}^{\eta}/_{\delta^4}\right)$

the damping coefficient) and the other an amplifier (the one with $-\gamma$ as the damping coefficient). In autonomous regime, the first produces damped vibrations, while the second shows amplification See Figs.1.18 and 1.20. But submitted to an external sinusoidal excitation, the classical cubic-quintic Duffing oscillator leads to various interesting phenomena like hysteresis, subharmonic and superharmonic oscillations, period-doubling, multistability, and transitions to chaos [140–142]. The Duffing equation in its various forms is used to approximate many nonlinear systems. The source of nonlinearity is the stiffness and depends on the type or landscape of the potential considered. This simply means that the force applied to the spring, and the resulting displacement X_i have a nonlinear relationship. In non-coupled mode, the dimensionless nonlinear potential in which each mass evolves has the form :

$$V(X) = \frac{1}{2}X^2 - \frac{1}{4}\alpha X^4 + \frac{1}{6}\eta X^6, \tag{2.15}$$

When there are these terms in the classical Duffing equation (with ϕ^4 potential), then the equation is called the extended equation of the Duffing oscillator. With this potential, it is possible to foresee the behaviour of systems when the amplitude of the oscillation is large. It gives rise to many configurations depending on the nature and the environment of the system in movement. These configurations can be classified into two groups as follow

- Hard spring systems: with these systems, when the amplitude of the external excitation increases, the system becomes tense and the natural frequency of free vibrations increases. Graphically, the displacement-force characteristic will show an upward-facing concavity. Such systems can have one, two or three potential wells depending on the values and signs of the parameters α and/or η.

- Soft spring systems: in these systems, the displacement-force characteristic has a downward facing concavity. The soft spring systems can be described by the ϕ^4 or ϕ^6 potential with one or two potential wells according to the consistence of the environment in which it is found.

In this work, due to the alternance between the signs of the potential terms, when the cubic term is positive (or negative), the spring is said to be softening (or hardening), whereas if the quintic term is positive (or negative) the spring is hardening (softening). In what follows, the force and potential versus deflection for different nonlinearity combinations are described. Two cases can be distinguished :

- **The ϕ^4 potential**

In the absence of the quintic nonlinear term ($\eta = 0$), the oscillator features the ϕ^4 potential characteristic. Fig.2.2(a) and 2.2(b) are plotted to illustrate the soft and hard cubic nonlinear characteristic of the spring, respectively. The case of the linear potential is plotted with the black colour.

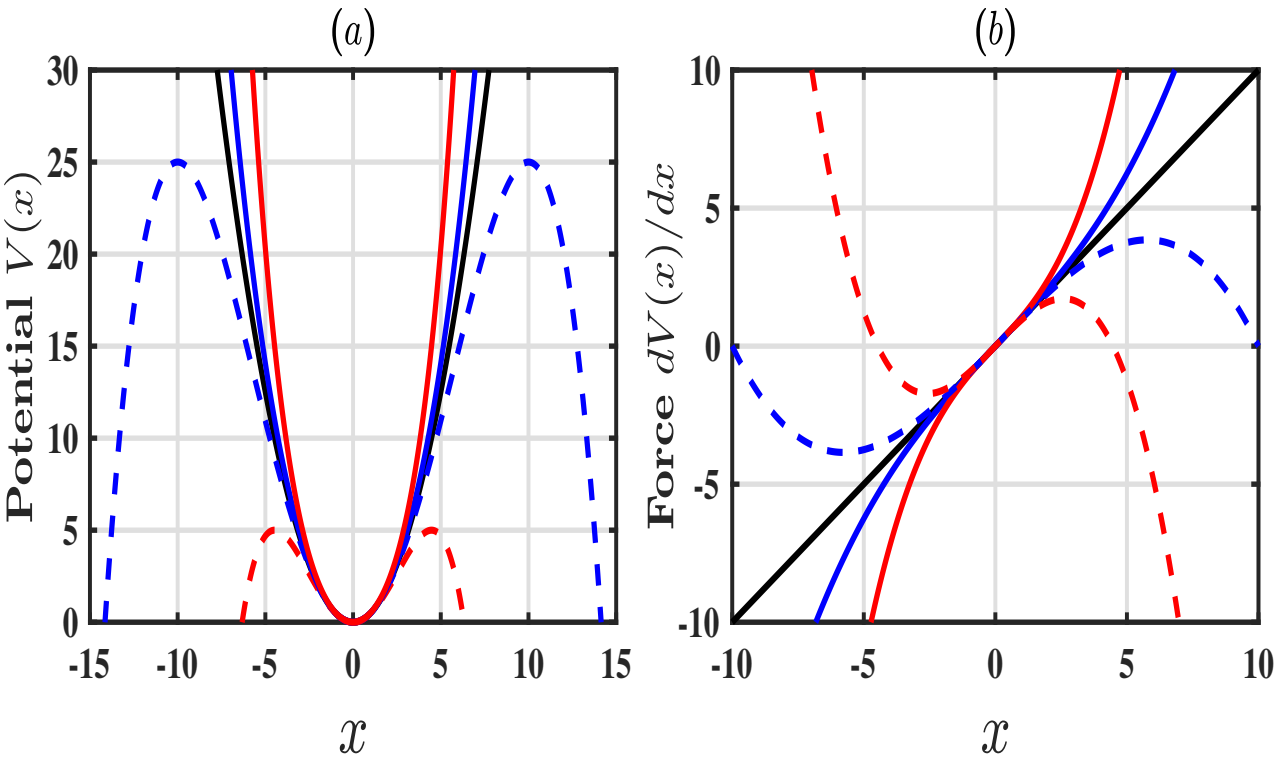

Figure 2.2: Potential (a) and Force (b) versus deflection. Linear spring is illustrated by black solid line. Nonlinear cubic hardening spring in solid for $\alpha = -0.01$ (in blue) and $\alpha = -0.05$ (in red) and, nonlinear cubic softening spring in dash line for $\alpha = 0.01$ (in blue) and $\alpha = 0.05$ (in red).

It can be observed that the three potentials are monostable and share a common ground state at $X = 0$. However, in these nonlinear hard potentials, oscillations can only exist about the ground state and there is no real possibility for energy explosion. This cubic hard potential is useful in modelling the atomic interaction in a diatomic chain with periodically distributed atoms, characteristic of optical media with spatially modulated refractive index [143]. These media exhibit two branches of the linear wave dispersion curve with opposite signs of dispersion and a gap between the branches. In particular, only heavy atoms can oscillate with frequencies inside the gap and this hard nonlinear potential is studied to localize modes inside the gap of the linear wave spectrum, the so-called gap breathers [144]. In contrast, the soft potential, in addition to the above-mentioned ground state, exhibits a metastable equilibrium state and becomes unbounded beyond its maximum point at $Xm = \sqrt{1/\alpha}$, corresponding to maximal energy of $V_m = 1/4\alpha$. For instance, this soft cubic potential may correspond to the hydrogen-bridge bond between nucleotides [145, 146]. It has been successfully used to study the energy-localization mechanisms in DNA molecules [147] and, also to modelling a variety of physical

phenomena such as the rolling motion of a ship, Josehpson oscillators, Foucoult's pendulum, etc [148]. On the other hand, When the nonlinear cubic term is increased, the well deepens for the hard potential while it is reduced for the soft potential. These analyses agree well with the force deflection which becomes important at $X \geq \sqrt{1/3\alpha}$.

- **The ϕ^6 potential**

On the other hand, quintic or ϕ^6 nonlinear terms deserve careful investigations as an extension of the cubic nonlinear Duffing oscillator. This is an example of a bounded (with one well, two or three wells), catastrophic monostable or multi-stable potential, depending on the cubic and quintic parameters combinations. To simplify the analysis, the parameter $\eta = \varepsilon\alpha^2$ is introduced, ε being a real constant parameter and thus the sign of ε is that of η. The nonlinear cubic-quintic potential (NCQP) characteristic for different stiffness combinations is considered in Fig.2.3, in dash for quintic softening (negative value of ε) and solid for quintic hardening (positive value of ε). The potential and the force versus deflection are represented for positive and negative values of cubic term respectively.

In top row, when $\alpha = 0.05$ (cubic softening), curves are plotted for $\varepsilon = -0.05$ (dash red), $\varepsilon = -1.0$ (dash blue) and $\varepsilon = -5.0$ (dash green). A single well and two metastable states are exhibited just as in the case of the soft cubic potential. The greater the ε (in negative direction), the softener the potential gets as compared to the cubic one. The nonlinear cubic-quintic potential (NCQP) deflects faster and stronger from the linear one. This potential is extensively used in the modelling of a strongly nonlinear beam with articulated ends under axial excitations mostly used in civil and mechanical engineering to study the action of seismic waves [149, 150]. However, when $\varepsilon = 0.1$ (solid green), $\varepsilon = 0.2$ (solid blue) and $\varepsilon = 0.3$ (solid red), the potential evolves from a tri-stable to a monostable, depending on the intensity of ε. Such potentials have found numerous applications in the study of cold atoms quantum tunnelling dynamics with trends atomic diodes and transistors [151,152] and for laser monitoring and control [153] of tunnelling transport in order to create new types of devices.

In bottom row, for $\alpha = -0.05$ (cubic hardening), we have: $\varepsilon = -0.1$ (dash blue), $\varepsilon = -0.2$ (dash green) and $\varepsilon = -0.5$ (dash red). The smaller the ε, the harder the potential gets as compared to the cubic one. This symmetric potential is monostable, with a zero energy centre ground state. It is also observed that the potential and force versus deflection curves are similar to the ones shown in Fig.2.2 in the case of the simple nonlinear cubic potential. This means that the negative quintic term strengthens the softening of the system. The quintic term action is to harden the initially soft potential. The potential and force versus deflection are also represented for positive values of ε with $\varepsilon = 0.05$ (solid blue), $\varepsilon = 1.0$ (solid green) and $\varepsilon = 5.0$ (solid red). From Figs.2.3(c) and (d), it can be seen that the single-well characteristic associated with a cubic soft or hard potential is similar to the what presented in Figs.2.2(a) and (b).

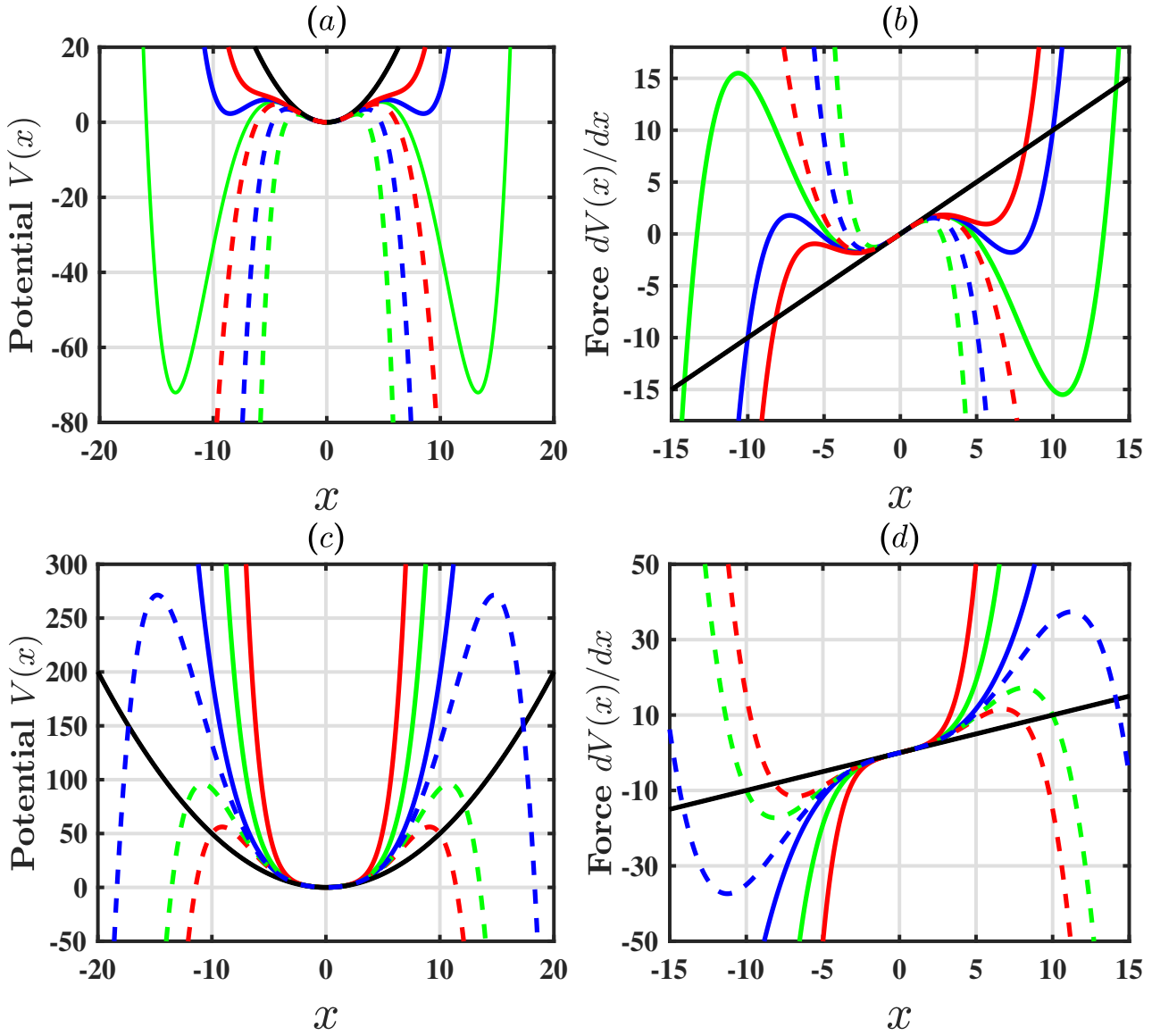

Figure 2.3: Potentials ((*a*) and (*c*) panels) and forces ((*b*) and (*d*) panels) versus deflection with nonlinear cubic-quintic term. The linear case is represented in black colour. The top row is obtained with $\alpha = 0.05$, for $\varepsilon = -0.05, -1.0, -5.0$ respectively in dash red, blue and red colour, and for $\varepsilon = 0.1, 0.2, 0.3$ respectively in solid green, blue and red colour. The bottom row, $\alpha = -0.05$ and the curves are plotted for $\varepsilon = -0.1, -0.2, -0.3$ in dash blue, green and red colour, and for $\varepsilon = 0.05, 1.0, 5.0$ in solid blue, green and red colour respectively.

2.2 Scattering properties in a mechanical dimer

2.2.1 Scattering formalism

The intention here is to investigate the wave propagation phenomenon through a one-dimensional transmission ($1D$) line assumed to be ideal. The wave scattering process has already been explored in several other fields, such as optics, acoustics and electronics [10, 24]. And since the process of wave scattering is basically the same from one branch to another, it can also be applied to mechanics. Here, the same principles applied in [10, 24] to explore this

phenomenon are also used in the framework of mechanics. To achieve this purpose, a linear mechanical dimer coupled to two identical TLs as shown in Fig.2.4 are considered. In this arrangement, the dimer acts as a defect, breaking the continuity of the mechanical signal coming from either side of the conservative TL.

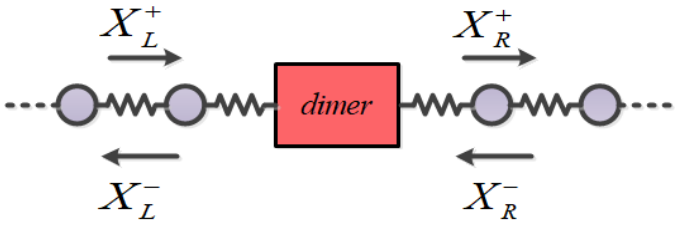

Figure 2.4: Schematic of a generic one-dimensional mechanical scattering system.

Considering that the incident signal is in the form of a plane wave and by taking into account the standard oscillating linearity, the scattering problem can be generalised by linear combination of the basic solutions. To describe the scattering, we introduce the concept of transmission and reflection, and due to the linearity, we can express the outputs X_L^- and X_R^+ according to the input terms by:

$$\begin{cases} X_R^+ = t_L X_L^+ + r_R X_R^- \\ X_L^- = r_L X_L^+ + t_R X_R^- \end{cases} \tag{2.16}$$

where t_L, r_L, t_R and r_R are the left and right transmission and reflection coefficients respectively. The scattering properties can therefore be characterised by defining a scattering matrix $\mathcal{S}$ which relates the incoming wave amplitudes to the outgoing ones:

$$\begin{pmatrix} X_R^+ \\ X_L^- \end{pmatrix} = \mathcal{S} \begin{pmatrix} X_L^+ \\ X_R^- \end{pmatrix}, \tag{2.17}$$

where the scattering matrix elements $\mathcal{S}$, representing reflection and transmission coefficients, are arranged as follows:

$$\mathcal{S} = \begin{pmatrix} t_L & r_R \\ r_L & t_R \end{pmatrix}. \tag{2.18}$$

Another useful quantity is the transfer matrix $\mathcal{M}$, which relates the wave amplitudes on the right to those on the left:

$$\begin{pmatrix} X_R^+ \\ X_R^- \end{pmatrix} = \mathcal{M} \begin{pmatrix} X_L^+ \\ X_L^- \end{pmatrix}, \tag{2.19}$$

with

$$\mathcal{M} = \begin{pmatrix} \mathcal{M}_{11} & \mathcal{M}_{12} \\ \mathcal{M}_{21} & \mathcal{M}_{22} \end{pmatrix}. \tag{2.20}$$

The elements of the $\mathcal{M}$ and $\mathcal{S}$ matrices are correlated according to the following relation-

ships:

$$t_L = \frac{\det \mathcal{M}}{\mathcal{M}_{22}} \; ; \; r_L = -\frac{\mathcal{M}_{21}}{\mathcal{M}_{22}} \; ; \; t_R = \frac{1}{\mathcal{M}_{22}} \; ; \; r_R = \frac{\mathcal{M}_{12}}{\mathcal{M}_{22}}. \tag{2.21}$$

The transmission and reflection amplitudes established above may, in general, be complex. An alternative representation is their exponential form which highlights the distinct phases. In this manner it follows that:

$$t_L = |t_L|\, e^{j\phi_{TL}} \; ; \; r_L = |r_L|\, e^{j\phi_{RL}} \; ; \; t_R = |t_L|\, e^{j\phi_{TR}} \; ; \; r_R = |r_R|\, e^{j\phi_{RR}}. \tag{2.22}$$

Therefore, in the following the transmission T and the reflection R are defined in terms of dimensionless normalized power.

$$T_L = |t_L|^2 \; ; \; R_L = |r_L|^2 \; ; \; T_R = |t_R|^2 \; ; \; R_R = |r_R|^2. \tag{2.23}$$

2.2.2 Description and modelling of the mechanical transmission line

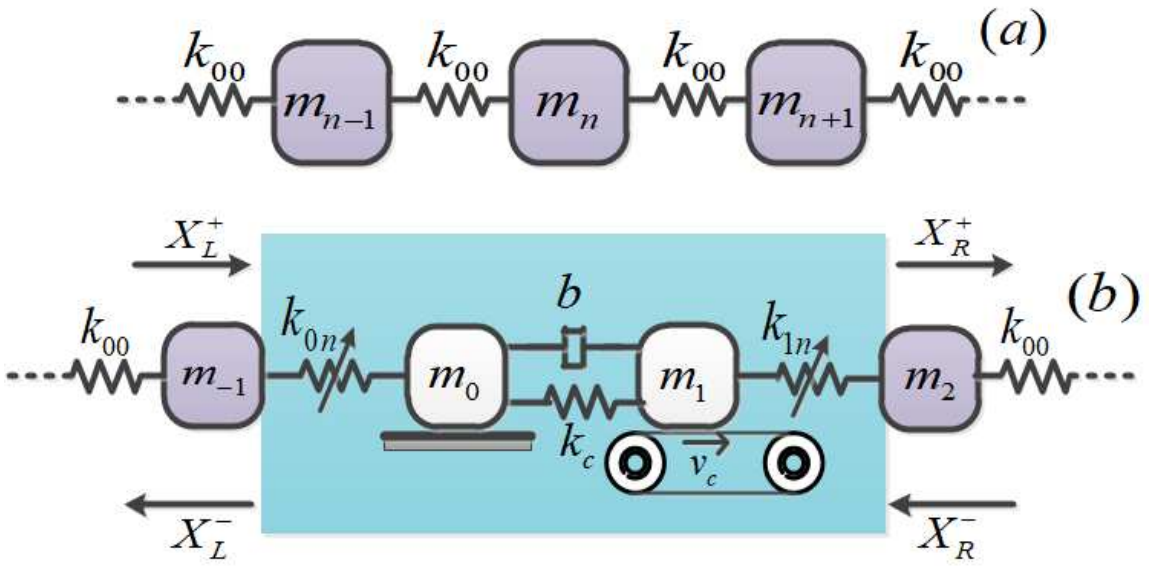

Figure 2.5: The Hermitian mechanical transmission line (a) and the scattering system when the dimer is incorporated as defect in the transmission line (b).

Let us consider a conservative and infinite mechanical chain consisting of a series of particles of identical mass m connected by identical springs of linear stiffness k_{00}, as shown in Fig.2.5(a). It is assumed that the constant term of the stiffness of the nonlinear spring (k_{0n} or k_{1n}) is equal to the stiffness k_{00} of the linear spring. This conservative mechanical chain will subsequently be referred to as the Hermitian mechanical transmission line (MTL). Now, by inserting the mechanical device presented in Fig.2.1 at any node n in the Hermitian MTL, we obtain the mechanical scattering system as illustrated in Fig.2.5(b). The Transmission Line (TL) is connected to the loss oscillator on the left hand side and to the gain gscillator on the right hand side. The index n indicates the position of the particle in the Hermitian MTL. The

presence of the $\mathcal{PT}$-symmetric mechanical dimer in this Hermitian MTL constitutes a defect (see the blue colour block of Fig.2.5(b)).

2.2.3 Modelling of the mechanical scattering system

- **Case of a linear mechanical dimer taken as a defect in the Hermitian MTL**

Consider the dimer shown in the blue block in the above Fig.2.5(b). By replacing the nonlinear springs k_{0n} and k_{1n} at the ends with identical linear springs of stiffness k_{00}, the dimer will thus be linearly coupled on its left and right sides to the Hermitian MTL. The potential and kinetic energies between particles of indices 0 and 1 are expressed by:

$$\begin{cases} T = \dfrac{1}{2}m_0\dot{x}_0^2 + \dfrac{1}{2}m_1\dot{x}_1^2 + \dfrac{1}{2}b(\dot{x}_0 - \dot{x}_1)^2 \\ V = \dfrac{1}{2}k_{00}(x_0 - x_{-1})^2 + \dfrac{1}{2}k_C(x_1 - x_0)^2 + \dfrac{1}{2}k_{00}(x_2 - x_1)^2 \end{cases} \tag{2.24}$$

Applying the Lagrangian formalism, the dimensionless equations governing the dynamics can be written in the form:

$$\begin{cases} (1+\mu)\,\ddot{X}_0 - \mu\ddot{X}_1 + 2\gamma\dot{X}_0 + X_0 - \kappa X_1 - \vartheta X_{-1} = 0 \\ (1+\mu)\,\ddot{X}_1 - \mu\ddot{X}_0 - 2\gamma\dot{X}_1 + X_1 - \kappa X_0 - \vartheta X_2 = 0 \\ \ddot{X}_n + 2\vartheta X_n - \vartheta X_{n-1} - \vartheta X_{n+1} = 0 \quad for \quad n \neq 0,\, 1 \end{cases} \tag{2.25}$$

where $\vartheta = \frac{k_0}{m\omega_{0c}^2}$ is the coupling coefficient with close neighbours. Note that, far away from the dimer in the MTL, the dispersion relation is obtained by substituting in the third equation of the system in Eq.(2.25) the following expressions of solution:

$$\begin{cases} X_n = Ae^{i(nk-\omega t)} \\ X_{n\pm1} = Ae^{i((n\pm1)k-\omega t)} \end{cases} \tag{2.26}$$

where k is the wavenumber of the incident wave. Doing so, we derive the dispersion relation expressed as:

$$\omega^2 = 4\vartheta \sin^2\left(\frac{k}{2}\right) \tag{2.27}$$

The Eq.(2.27) reveals that the MTL considered in Fig.2.5(a) admits two cut-off frequencies $f_1 = 0$ and $f_2 = \sqrt{\vartheta}/\pi$ for wavenumbers $k = 0$ and $k = \pi$ respectively. f_1 and f_2 represent the lower and upper cut-off frequencies of the band respectively.

Now, in order to investigate the possibilities of transmission in the presence of the dimer which constitutes a defect, the new form of the solutions, if the incident wave comes from left-hand side, is defined as:

$$\begin{cases} X_n = Ie^{i(nk-\omega\, t)} + R_l e^{i(-nk-\omega\, t)} & n \leqslant 0 \\ X_n = T_l e^{i(nk-\omega\, t)} & n \geqslant 1 \end{cases} \tag{2.28}$$

and if the incident wave instead originates from the right-hand side, then the solution takes the form :

$$\begin{cases} X_n = Ie^{-i(nk-\omega\, t)} + R_g e^{i(-nk-\omega\, t)} & n \geqslant 1 \\ X_n = T_g e^{-i(nk-\omega\, t)} & n \leqslant 0 \end{cases} \tag{2.29}$$

where I, R_l, R_g, and T are respectively the incident, reflected coefficients from the loss and gain side, and transmitted coefficients. The determination of the reflection and transmission coefficients for a given incidence from the gain/loss side is performed by substituting Eq.(2.28) and Eq.(2.29) into Eq.(2.25). After the resolution, the scattering coefficients are expressed as:

$$\begin{cases} R_l = \dfrac{B^2 - \left(A - \vartheta e^{ik}\right)\left(A^* - \vartheta e^{-ik}\right)}{\left(A - \vartheta e^{ik}\right)\left(A^* - \vartheta e^{ik}\right) - B^2} I \\ R_g = \dfrac{\left[B^2 - \left(A - \vartheta e^{-ik}\right)\left(A^* - \vartheta e^{ik}\right)\right] e^{-2ik}}{\left(A - \vartheta e^{ik}\right)\left(A^* - \vartheta e^{ik}\right) - B^2} I \\ T = \dfrac{2i\vartheta B \sin\left(k\right) e^{-ik}}{\left(A - \vartheta e^{ik}\right)\left(A^* - \vartheta e^{ik}\right) - B^2} I \end{cases} \tag{2.30}$$

with $A = 1 - (1+\mu)\omega^2 + 2i\omega\gamma$ and $B = \mu\omega^2 - \kappa$. Due to the reciprocity of transmission for any linear, stationary and non-magnetic medium, the right and left hand propagation of an incident wave coincide ($T_g = T_l = T$) [154]. Therefore, the reflection coefficients are non-reciprocal ($R_g \neq R_l$), and the corresponding scattering signals must satisfy the generalized unitary conservation relation $\left||T^2| - 1\right| = \left|R_l.R_g^*\right|$, which reveals the underlying symmetries of the scattering $\mathcal{PTS}$ defect. It can be seen that these three coefficients share a common denominator defined as:

$$D = \left(A - \vartheta e^{ik}\right)\left(A^* - \vartheta e^{ik}\right) - B^2. \tag{2.31}$$

When the denominator D turns to zero, the lasing gain/loss parameter γ_r and the critical wavenumber k_r are found .

$$\begin{cases} \cos k_r = \dfrac{-1 + 2\vartheta(1+\mu)}{(1+2\mu)\vartheta} \\ \gamma_r = \dfrac{1}{2\omega}\sqrt{B^2 + \vartheta^2 \sin^2 k_r} \end{cases} \tag{2.32}$$

- **Case 2: the nonlinear dimer taken as defect**

Now, consider the model shown in Fig.2.5(b). The system consists of a linear chain with a nonlinear defect represented here by the nonlinear dimer (in the blue block). With this configuration, the potential and kinetic energies linking the particles of indices -1, 0, 1 and 2 are found as:

$$\begin{cases} T = \frac{1}{2}m_{-1}\dot{x}_{-1}^2 + \frac{1}{2}m_0\dot{x}_0^2 + \frac{1}{2}m_1\dot{x}_1^2 + \frac{1}{2}m_2\dot{x}_2^2 + \frac{1}{2}b(\dot{x}_1 - \dot{x}_0)^2 \\ V = \frac{1}{2}k_0(x_{-1} - x_{-2})^2 + \frac{1}{2}k_{nl}(x_0 - x_{-1})^2 + \frac{1}{2}k_C(x_1 - x_0)^2 \\ \qquad\qquad + \frac{1}{2}k_{nl}(x_2 - x_1)^2 + \frac{1}{2}k_0(x_3 - x_2)^2 \end{cases} \tag{2.33}$$

with $k_{nl} = k_0 - \frac{1}{2}k_3(x_j - x_i)^2 + \frac{1}{3}k_5(x_j - x_i)^4$. The resulting equations after applying Lagrange formalism and a suitable normalisation can be written as follows

$$\begin{cases} \ddot{X}_{-1} + 2\vartheta X_{-1} - \vartheta X_{-2} - \vartheta X_0 - \alpha(X_{-1} - X_0)^3 + \eta(X_{-1} - X_0)^5 = 0 \\ (1+\mu)\ddot{X}_0 - \mu\ddot{X}_1 + 2\gamma\dot{X}_0 + X_0 - \vartheta X_{-1} - \alpha(X_0 - X_{-1})^3 + \eta(X_0 - X_{-1})^5 - \kappa X_1 = 0 \\ (1+\mu)\ddot{X}_1 - \mu\ddot{X}_0 - 2\gamma\dot{X}_1 + X_1 - \vartheta X_2 - \alpha(X_1 - X_2)^3 + \eta(X_1 - X_2)^5 - \kappa X_0 = 0 \\ \ddot{X}_2 + 2\vartheta X_2 - \vartheta X_1 - \vartheta X_3 - \alpha(X_2 - X_1)^3 + \eta(X_2 - X_1)^5 = 0 \\ \ddot{X}_n + 2\vartheta X_n - \vartheta X_{n-1} - \vartheta X_{n+1} = 0 \qquad\qquad for \quad n \neq -1,\, 0,\, 1 \; and \; 2 \end{cases} \tag{2.34}$$

The system (2.34) are those of the nonlinear scattering mechanical system (NSMS). In the absence of nonlinearities terms, Eq.(2.34) is reduced to Eq.(2.25).

2.3 Analytical and numerical methods

Once the mathematical modelling of the physical system under study has been completed, it would be interesting to extract the various pieces of information hidden in these equations. In this section, the analytical developments used to study the dynamic system in this thesis are discussed.

2.3.1 Analytical methods

2.3.1.1 Overview on analytical methods

Mathematicians and physicists have developed a number of perturbational techniques to deal with analytical solutions of nonlinear differential equations. Although Poisson was the first to use perturbation techniques, modern perturbation theory is attributed to Poincare. With the advent of low cost digital computational facilities, perturbation techniques have become one of the most powerful methods to solve nonlinear differential equations. Perturbational techniques approximate the solution of nonlinear governing system equations by considering only the first few terms of an asymptotic expansion. One can get more accurate solutions if more terms of the perturbation expansions are included. There are several methods commonly used in these techniques:

- (1) The straight-forward (or pedestrian) asymptotic expansion method [166];
- (2) The Lindstedt-Poincare Method [155].

- (3) The method of harmonic balance [155, 156].
- (4) The averaging method [155, 157]
- (5) The method of multiple scales [139, 159].

All these methods are different in their approaches, but they are similar in their basic idea. Some are valid only in a limited region, e.g., the straight-forward expansion method cannot have uniform expansion when time, increases to [155, 160]. Some need to have a tedious formulation, especially for a multi-degree-of-freedom system, e.g., the harmonic balance method needs to carry enough terms in the solution or an inaccurate approximation might be obtained. The averaging method can have valid results, but Mahaffey [161] showed that inconsistency between this and other techniques might possibly exist. Cheung and Lau [162, 163] developed an incremental harmonic balance (IHB) method, and generalized it to multiple time-scales. This is a new approach of a combination of methods (3) and (5). In this thesis, averaging method is chosen to tackle analytical solutions of our models.

2.3.1.2 Linear dynamic: exact solutions

In a linear regime or in the absence of any non-linearity ($\alpha = 0$ and $\eta = 0$), the nonlinear equations given in Eq.(2.14) can be reduced to Eq.(2.35), by setting $\dot{X}_i = Y_i$.

$$\begin{cases} \dot{X}_0 = Y_0 \\ (1+\mu)\,\dot{Y}_0 = \mu\dot{Y}_1 - 2\gamma Y_0 - X_0 + \kappa X_1 \\ \dot{X}_1 = Y_1 \\ (1+\mu)\,\dot{Y}_1 = \mu\dot{Y}_0 + 2\gamma Y_1 - X_1 + \kappa X_0 \end{cases} \tag{2.35}$$

In the matrix form, and after a few suitable transformations, the above equations become

$$\begin{pmatrix} \dot{X}_0 \\ \dot{Y}_0 \\ \dot{X}_1 \\ \dot{Y}_1 \end{pmatrix} = \begin{bmatrix} 0 & 1 & 0 & 0 \\ -\frac{1+\mu(1-\kappa)}{1+2\mu} & -\frac{2\gamma(1+\mu)}{1+2\mu} & -\frac{\mu(1-\kappa)-\kappa}{1+2\mu} & \frac{2\gamma\mu}{1+2\mu} \\ 0 & 0 & 0 & 1 \\ -\frac{\mu(1-\kappa)-\kappa}{1+2\mu} & -\frac{2\gamma\mu}{1+2\mu} & -\frac{1+\mu(1-\kappa)}{1+2\mu} & \frac{2\gamma(1+\mu)}{1+2\mu} \end{bmatrix} \begin{pmatrix} X_0 \\ Y_0 \\ X_1 \\ Y_1 \end{pmatrix}. \tag{2.36}$$

Eq.(2.36) can be put into Schrödinger form as

$$i\frac{d\psi}{d\tau} = H\psi \tag{2.37}$$

with $H = i \begin{bmatrix} 0 & 1 & 0 & 0 \\ -\frac{1+\mu(1-\kappa)}{1+2\mu} & -\frac{2\gamma(1+\mu)}{1+2\mu} & -\frac{\mu(1-\kappa)-\kappa}{1+2\mu} & \frac{2\gamma\mu}{1+2\mu} \\ 0 & 0 & 0 & 1 \\ -\frac{\mu(1-\kappa)-\kappa}{1+2\mu} & -\frac{2\gamma\mu}{1+2\mu} & -\frac{1+\mu(1-\kappa)}{1+2\mu} & \frac{2\gamma(1+\mu)}{1+2\mu} \end{bmatrix}$ and $\psi = \begin{pmatrix} X_0 \\ Y_0 \\ X_1 \\ Y_1 \end{pmatrix}$.

From the matrix form given in Eq.(2.37), the Jordan canonical form [164] can be used to find time-dependent analytical solutions as

$$X_k = \sum_{n=1}^{4} c_k v_{kn} e^{i\omega_n t}, \quad (1 \leq k \leq 4) \tag{2.38}$$

where c_k, ω_n and v_{kn} are the constant of integrations, eigenvalues and eigenvectors, respectively. The eigenvalues are expressed as

$$\omega_n = \pm\sqrt{\frac{1 - 2\gamma^2 + \mu(1-\kappa) \pm \sqrt{\gamma^2 - \gamma_{TH}^2}}{1 + 2\mu}} \tag{2.39}$$

From Eq.(2.39), the exceptional points (EP) are deduced and given by

$$\gamma_{TH_{1,2}} = \sqrt{\frac{1}{2}\left(1 + \mu(1-\kappa) \mp \sqrt{(1-\kappa^2)\,(1+2\mu)}\right)} \tag{2.40}$$

2.3.1.3 Nonlinear dynamic: mathematical approaches

In this thesis, two approximation methods, have been used to characterise the nonlinear dynamics of the system described by the recovered nonlinear differential equations. The aim here is to study the harmonic oscillatory behaviour of the nonlinear dimer in order to derive, as far as possible, an analytical expression of the threshold in the nonlinear regime, which would allow to explain the different dynamic bifurcations.

a) The method of multiple scales (MMS)

- **Nonlinear Schrödinger dimer**

Several methods have been proposed in the literature to approximate the analytical solutions of coupled systems described by nonlinear differential equations. Among them, there is the method of multiple scales, which is one of the highly applicable perturbation-based approaches [165–167]. This method consists of looking for a solution in the form of asymptotic development in multiple time scales considered as independent variables and defined as

$$T_n = \epsilon^n \tau \quad for \quad n = 0,\, 1,\, 2,\, ... \tag{2.41}$$

Let's take $X(\tau)$ to be a function of two independent variables or time scales T_0 and T_1. T_0 is a fast scale and $T_1 = \epsilon\tau$ is a slow scale characterising the modulation in the amplitude and phase caused by the nonlinearity, damping, resonances and coupling. Thus $X_i(\tau)$ can be written in the form

$$\begin{cases} X_0(\tau,\, \epsilon) = x_{00}(T_0,\, T_1) + \epsilon x_{01}(T_0,\, T_1) + ... \\ X_1(\tau,\, \epsilon) = x_{10}(T_0,\, T_1) + \epsilon x_{11}(T_0,\, T_1) + ... \end{cases} \tag{2.42}$$

The derivative operators are defined as follow

$$\begin{cases} \frac{d}{d\tau} = D_0 + \varepsilon D_1 \\ \frac{d^2}{d\tau^2} = D_0^2 + 2\varepsilon D_0 D_1 \end{cases} \tag{2.43}$$

where $D_n^m = \frac{\partial^m}{\partial T_n^m}$.

Substituting Eq.(2.42) into Eq.(2.14) and equating coefficients like powers of ϵ, we get

$$D_0 x_{00} + x_{00} = 0 \tag{2.44a}$$

$$D_0 x_{10} + x_{10} = 0 \tag{2.44b}$$

$$D_0^2 x_{01} + x_{01} + (2D_0 D_1 + 2\gamma D_0)x_{00} - \alpha x_{00}^3 + \eta x_{00}^5 - \kappa x_{10} = 0 \tag{2.44c}$$

$$D_0^2 x_{11} + x_{11} + (2D_0 D_1 - 2\gamma D_0)x_{10} - \alpha x_{10}^3 + \eta x_{10}^5 - \kappa x_{00} = 0 \tag{2.44d}$$

The general solutions of Eqs.(2.44a) and (2.44b) can be expressed in the following form

$$x_{00}(T_0, T_1) = \phi_0(T_1)e^{iT_0} + c.c. \tag{2.45a}$$

$$x_{10}(T_0, T_1) = \phi_1(T_1)e^{iT_0} + c.c. \tag{2.45b}$$

where *c.c.* stands for the complex conjugate of each preceding term. The quantities $\phi_0(T_1)$ and $\phi_1(T_1)$ are arbitrary, complex functions which are determined from Eqs.(2.44c) and (2.44d) by imposing solvability or secular conditions. Substituting Eqs.(2.45a) and (2.45b) into Eqs.(2.44c) and (2.44d) respectively, we obtain the nonlinear Schrödinger dimer given by:

$$2i\dot{\phi}_0 = \left(3\alpha|\phi_0|^2 - 10\eta|\phi_0|^4 - 2i\gamma + \mu\right)\phi_0 + (\kappa - \mu)\,\phi_1 \tag{2.46a}$$

$$2i\dot{\phi}_1 = \left(3\alpha|\phi_1|^2 - 10\eta|\phi_1|^4 + 2i\gamma + \mu\right)\phi_1 + (\kappa - \mu)\,\phi_0 \tag{2.46b}$$

- **Stationary solutions and stability**

Eqs.(2.46a) and (2.46b) are the secular terms whose resolution leads to the expected approximate solution. To do this, it is necessary to determine the stationary states and study their stability. Thus, the search of stationary solutions may be carried out by setting:

$$\phi_0(\tau) = a_0 e^{-i\nu\tau} \tag{2.47a}$$

$$\phi_1(\tau) = a_1 e^{-i\nu\tau} \tag{2.47b}$$

where ν is a real constant, a_0 and a_1 are two complex unknowns and τ the time. After substitution Eqs.(2.47a) and (2.47ab) into Eqs.(2.46a) and (2.46b), we get

$$-\nu a_0 = i\gamma a_0 - \frac{\mu}{2}a_0 - \frac{3\alpha}{2}|a_0|^2 a_0 + 5\eta|a_0|^4 a_0 + \frac{\mu - \kappa}{2}a_1 \tag{2.48a}$$

$$-\nu a_1 = -i\gamma a_1 - \frac{\mu}{2}a_1 - \frac{3\alpha}{2}|a_1|^2 a_1 + 5\eta|a_1|^4 a_1 + \frac{\mu - \kappa}{2}a_0 \tag{2.48b}$$

Taking the polar representation of the two sites $a_k = A_k e^{i\theta_k}$, $k = 0, 1$ we obtain the steady-states expressions given as

$$(A_0^{(\pm)})^2 = (A_1^{(\pm)})^2 = \frac{-2\nu - \mu \pm \sqrt{(\mu - \kappa)^2 - 4\gamma^2}}{3\alpha} \tag{2.49}$$

for the cubic system and,

$$(A_0^{(\pm)})^2 = (A_1^{(\pm)})^2 = \frac{3\alpha \mp \sqrt{9\alpha^2 - 40\varepsilon\alpha^2\left(-2\nu - \mu \pm \sqrt{(\mu-\kappa)^2 - 4\gamma^2}\right)}}{20\varepsilon\alpha^2} \tag{2.50}$$

for the cubic-quintic system. The superscript $(\pm)$ in the expression for stationary solutions refers to the sign of the second radical $\sqrt{(\mu-\kappa)^2 - 4\gamma^2}$. The $(+)$ sign indicates the first branch, and the $(-)$ sign the second. The stability can be studied by linearising Eqs.(2.46a) and (2.46b) around these stationary solutions. Considering the perturbed form of the solutions given by Eq.(2.51) :

$$\phi(\tau) = e^{i\nu\tau}\left[\phi_0 + \delta\left(e^{\lambda\tau}\mathbf{r} + e^{\lambda^*\tau}\mathbf{s}\right)\right] + O(\delta^2), \tag{2.51}$$

(here, the star denotes the conjugate, $\mathbf{r}$ and $\mathbf{s}$ are eigenvectors whereas λ corresponds to the eigenvalues). $\phi(\tau)$ is the time-dependent solution, ϕ_0 the base (unperturbed) solution representing the equilibrium or stationary state of the system before perturbation, ν is the real frequency of the fundamental oscillation, δ a small parameter ($\delta << 1$), used to expand the solution perturbatively. substituting them into Eqs.(2.46a) and (2.46b), the following Jacobian matrix J is :

$$J = \begin{pmatrix} J_1 & J_2 \\ -J_2^* & -J_1^* \end{pmatrix} \tag{2.52}$$

where $J_1 = \begin{pmatrix} -\nu - i\gamma + \frac{\mu}{2} + 3\alpha|a_0|^2 - 15\varepsilon\alpha^2|a_0|^4 & -\frac{\mu-\kappa}{2} \\ -\frac{\mu-\kappa}{2} & -\nu + i\gamma + \frac{\mu}{2} + 3\alpha|a_1|^2 - 15\varepsilon\alpha^2|a_1|^4 \end{pmatrix}$

and

$J_2 = \begin{pmatrix} \frac{3\alpha}{2}a_0^2 - 10\varepsilon\alpha^2|a_0|^2a_0^2 & 0 \\ 0 & \frac{3\alpha}{2}a_1^2 - 10\varepsilon\alpha^2|a_1|^2a_1^2 \end{pmatrix}$

– Cubic system

According to Eq.(2.50), the stationary solutions in the absence of the inertial coefficient are given by

$$(A_0^{(\pm)})^2 = (A_1^{(\pm)})^2 = \frac{2\nu \pm \sqrt{\kappa^2 - 4\gamma^2}}{3\alpha} \tag{2.53}$$

Eq.(2.53) above expresses the square of the stationary solutions for the cubic nonlinear system. And in order to make sure that these quantities are always positive, the coefficients ν and α have to be chosen very suitably. The study of the stability of these stationary solutions through the Jacobian matrix in Eq.(2.58) leads to obtain the eigenvalues given by Eq.(2.54) below.

$$\lambda^{(+)} = \pm i\sqrt{2}\sqrt{(\kappa^2 - 4\gamma^2) + \nu\sqrt{\kappa^2 - 4\gamma^2}} \tag{2.54a}$$

$$\lambda^{(-)} = \pm i\sqrt{2}\sqrt{(\kappa^2 - 4\gamma^2) - \nu\sqrt{\kappa^2 - 4\gamma^2}} \tag{2.54b}$$

$\lambda^{(+)}$ and $\lambda^{(-)}$ for the first and second branch respectively.

By a simple analysis of these nonzero eigenvalues pairs obtained by linearising the system around the branches given in Eq.(2.53), one can deduce that the stability occurs when their square are negative. It is easy to see that in the linear regime, the eigenvalues would be $\pm\sqrt{\kappa^2 - 4\gamma^2}$. And in this case, the phase is linear unbroken $\mathcal{PT}$ symmetric for $0 < \gamma < \frac{\kappa}{2}$. For $\gamma > \frac{\kappa}{2}$ the eigenvalues are in the linear $\mathcal{PT}$ broken phase [168]. If we assume ν to be positive, only the first branch $\lambda^{(+)}$ is always stable in the linear $\mathcal{PT}$ unbroken phase, whereas the second branch $\lambda^{(-)}$ is stable in a region of $\mathcal{PT}$ unbroken phase (for $\gamma \leq \gamma_c = \frac{\sqrt{\kappa^2-\nu^2}}{2}$, with $\nu < \kappa$).

The Fig.2.6 below presents the stability diagram of the two branches of stationary solutions for different values of ν. The curves are plotted for $\alpha > 0$ ($\alpha = 0.15$) despite the fact that the cubic nonlinearity do not affect the above eigenvalues. The cubic nonlinearity rather affects the stationary solutions by acting on their amplitude.

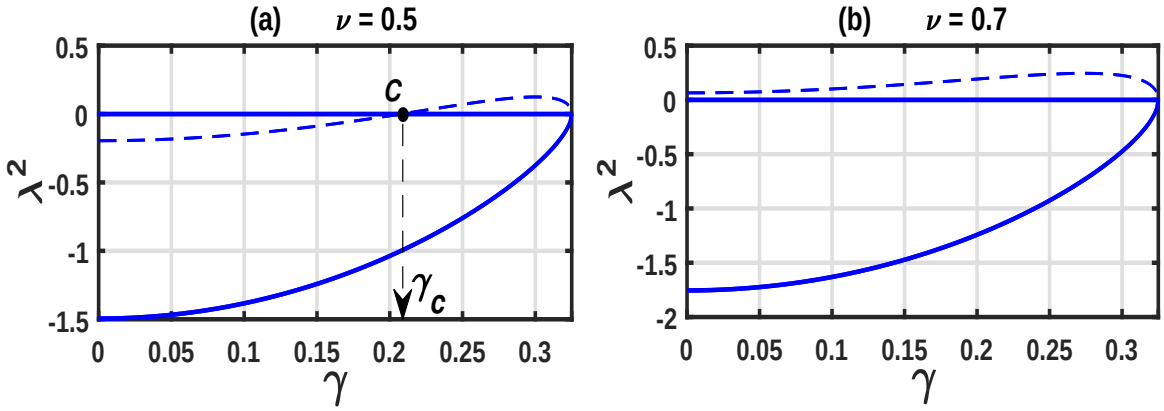

Figure 2.6: The squared eigenvalues of two branches. The solid blue line is for the first branch whereas the dashed blue line is for the second branch. In the dial (a), $\nu = 0.5$ while in the dial (b) $\nu = 0.7$. The parameters are $\kappa = 0.65$, $\alpha = 0.15$.

The Fig.2.6, shows that for $\gamma > 0.325$ (which corresponds to the transition threshold that separates the $\mathcal{PT}$ broken and unbroken phases) the two branches cancel. Furthermore, although it corresponds to the linear $\mathcal{PT}$ unbroken region, the second branch is unstable for $\gamma > \gamma_c$ (beyond the point C in Fig.2.6(a)), while the first branch is always stable. On the other hand, in Fig.2.6(b), when $\nu > \kappa$, only the first branch is stable, while the second branch is unstable in the linear $\mathcal{PT}$ unbroken phase. The Fig.2.7 below present the dynamic behaviours relative to the various branches of the dimer system given in Eq.(2.47) with $\eta = 0$. The plots are shown in Fig.2.7 below.

As observed on Fig.2.7, the first branch is always stable (Fig.2.7(a)) while the second branch is unstable (Fig.2.7(b)) for the chosen value of parameter γ in the linear $\mathcal{PT}$ unbroken phase. Indeed, this result is predicted in the Fig.2.6(a) for $\gamma = 0.30$. The asymmetric evolutions (unstable states) illustrated in the Fig.2.7(c) indicates that the linear $\mathcal{PT}$ symmetric threshold has been crossed.

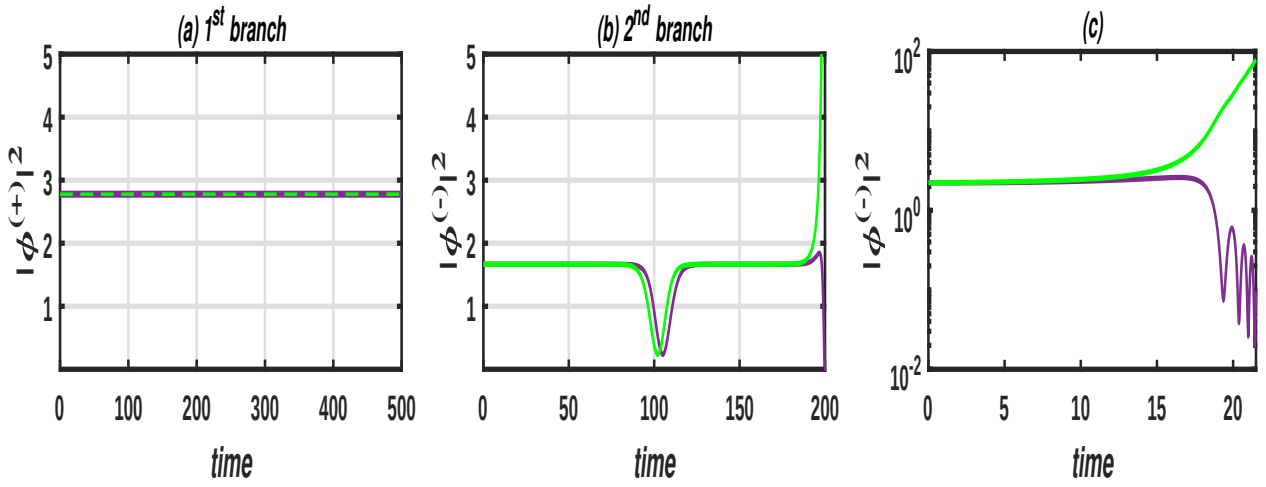

Figure 2.7: Dynamical evolutions of the dimer for the two branches. Green and purple colours indicate the dynamical behaviour of the gain and loss oscillators respectively. The dials (a) and (b) corresponding to the first and second branch respectively, are obtained in the $\mathcal{PT}$ unbroken phase with $\gamma = 0.30$. The dial (c) is plotted in semilog for $\gamma = 0.326$ in the $\mathcal{PT}$ broken phase. The parameters are $\kappa = 0.65$, $\alpha = 0.15$ and $\nu = 0.5$.

– Quintic system

In the presence of quintic coefficient, the expressions of the stationary solutions are :

$$(A_0^{(\pm)})^2 = (A_1^{(\pm)})^2 = \frac{3\alpha - \sqrt{9\alpha^2 - 40\varepsilon\alpha^2\left(2\nu \pm \sqrt{\kappa^2 - 4\gamma^2}\right)}}{20\varepsilon\alpha^2} \tag{2.55a}$$

$$(A_0^{(\pm)})^2 = (A_1^{(\pm)})^2 = \frac{3\alpha + \sqrt{9\alpha^2 - 40\varepsilon\alpha^2\left(2\nu \pm \sqrt{\kappa^2 - 4\gamma^2}\right)}}{20\varepsilon\alpha^2} \tag{2.55b}$$

The Eqs.(2.55a) and (2.55b) represent the two families of solutions obtained. For each family, corresponds two branches of solutions referred by the symbol $(\pm)$ in front of the square root $\sqrt{\kappa^2 - 4\gamma^2}$ in the expressions of stationary solutions. Thus, the non-zero eigenvalues pairs according to the first family of stationary solutions are :

$$\lambda_1^{(+)} = \pm i\sqrt{\frac{60\varepsilon\left(\kappa^2 - 4\gamma^2\right) - \sqrt{\kappa^2 - 4\gamma^2}\left(9 - 80\nu\varepsilon - 3\sqrt{9 - 40\varepsilon\left(2\nu + \sqrt{\kappa^2 - 4\gamma^2}\right)}\right)}{20\varepsilon}} \tag{2.56a}$$

$$\lambda_1^{(-)} = \pm i\sqrt{\frac{60\varepsilon\left(\kappa^2 - 4\gamma^2\right) + \sqrt{\kappa^2 - 4\gamma^2}\left(9 - 80\nu\varepsilon - 3\sqrt{9 - 40\varepsilon\left(2\nu - \sqrt{\kappa^2 - 4\gamma^2}\right)}\right)}{20\varepsilon}} \tag{2.56b}$$

and the the non-zero eigenvalues pairs according to the second family of stationary solutions are expressed as

$$\lambda_2^{(+)} = \pm i\sqrt{\frac{60\varepsilon\left(\kappa^2-4\gamma^2\right)-\sqrt{\kappa^2-4\gamma^2}\left(9-80\nu\varepsilon+3\sqrt{9-40\varepsilon\left(2\nu+\sqrt{\kappa^2-4\gamma^2}\right)}\right)}{20\varepsilon}} \tag{2.57a}$$

$$\lambda_2^{(-)} = \pm i\sqrt{\frac{60\varepsilon\left(\kappa^2-4\gamma^2\right)+\sqrt{\kappa^2-4\gamma^2}\left(9-80\nu\varepsilon+3\sqrt{9-40\varepsilon\left(2\nu-\sqrt{\kappa^2-4\gamma^2}\right)}\right)}{20\varepsilon}} \tag{2.57b}$$

Like in the cubic case, Eqs.(2.56a) and (2.56b) and Eqs.(2.57a) and (2.57b) suggest that the stability will occurs in the system when the square of those eigenvalues is negative. We will be interested here only the branches of the first family to illustrate or show the different behaviours which can be observed in the quintic case. The Fig.2.8 present the diagram of stability represented in the form of map of stability.

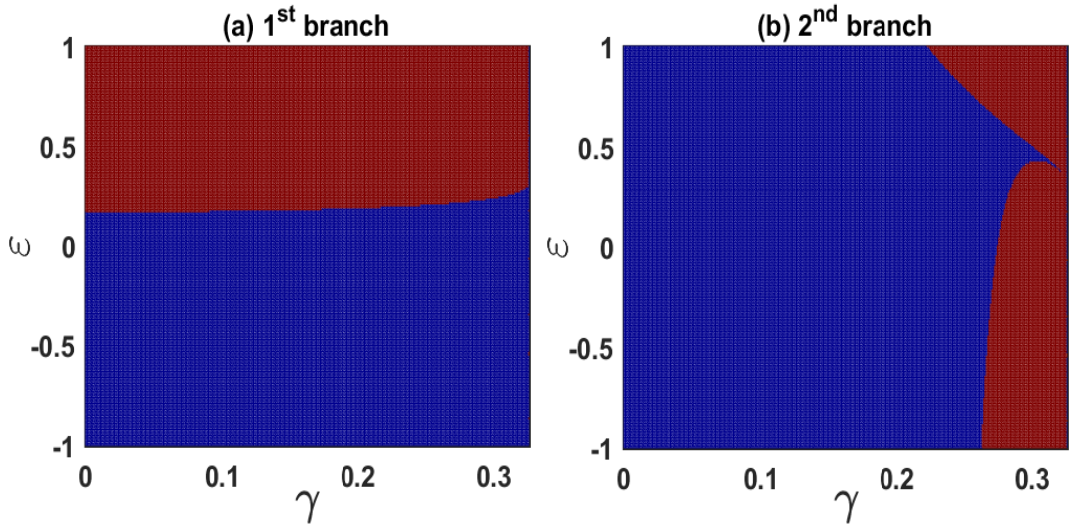

Figure 2.8: Map of stability of the first family of stationary solutions in the (γ,ε) space. (a) and (b) show the stability regions of the first and second branch respectively. Blue and red colours represent stable and unstable regions respectively. The parameters are $\kappa = 0.65$, $\alpha = 1.0$ and $\nu = 0.35$.

Note that, these maps are plotted taking the cubic parameter to be positive just for illustration. If the cubic parameter were negative, an another map of stability different from the one presented in Fig.2.8 would be obtained, but the analysis would remain the same. Thus, according to the quintic parameter sign, it is easy to predict from these maps the region where stability will occur. Indeed, the maps are also represented in the limit of linear unbroken $\mathcal{PT}$ phase. In this domain, two different regions of stability located by two different colours are distinguished. The red colour indicating the unstable region and, the blue colour indicating the stable region.

The Fig.2.9, shows the different dynamics of the two branches. The values of the parameters are defined as $\kappa = 0.65$, $\nu = 0.35$, $\alpha = 1.0$ and the couple $(\gamma, \varepsilon) = (-0.5, 0.3)$. For this latter couple of parameters, the first branch will always be stable (see Fig.2.9(a)) whereas the second branch is unstable (see Fig.2.9(b)). The Fig.2.9(c) exhibits the asymmetric evolutions (unstable

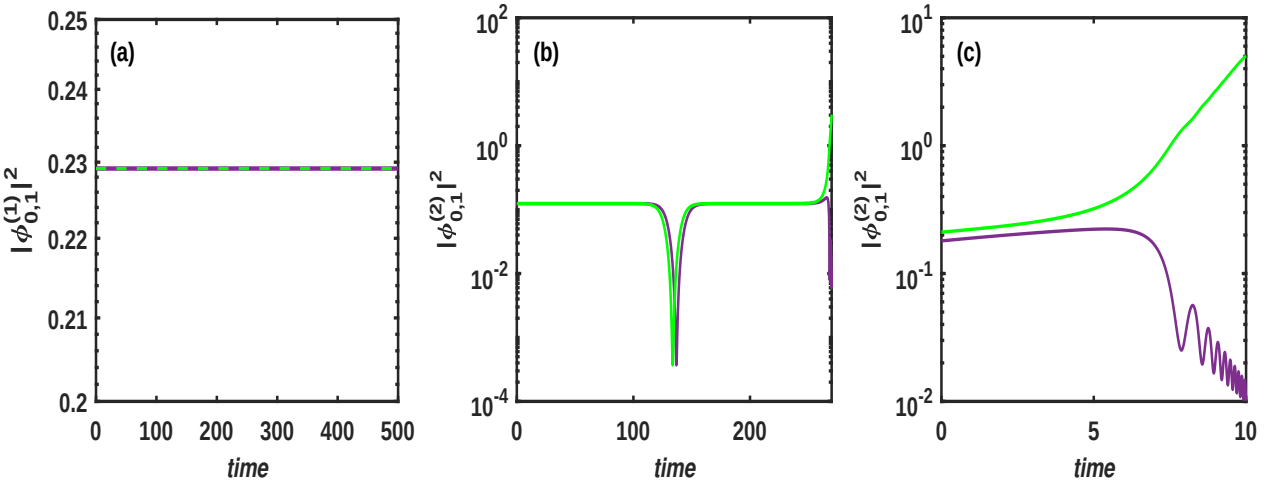

Figure 2.9: Dynamical evolutions of the dimer for the two branches. Green and purple colours indicate the dynamical behaviour of the gain and loss oscillators respectively. The dials (a) and (b) corresponding to the first and second branch respectively, are obtained in the $\mathcal{PT}$ unbroken phase with $\gamma = 0.30$. The dial (c) is plotted in semilog for $\gamma = 0.326$ in the $\mathcal{PT}$ broken phase. The parameters are $\kappa = 0.65$, $\alpha = 1.0$ and $\nu = 0.35$.

states) of the stationary solutions for $\gamma = 0.326$ belonging to the linear $\mathcal{PT}$ broken phase.

- **Stokes parameters formalism**

In order to understand the geometry of the phase space, the general coupled nonlinear Schrödinger-type $\mathcal{PT}$-symmetric dimer given in Eqs.(2.46a) and (2.46b) are reformulated in terms of the Stokes variables by :

$$S_0 = |\phi_0|^2 + |\phi_1|^2 \tag{2.58a}$$

$$S_1 = |\phi_0|^2 - |\phi_1|^2 \tag{2.58b}$$

$$S_2 = \phi_0^* \phi_1 + \phi_1^* \phi_0 = 2\mathrm{Re}\left(\phi_0^* \phi_1\right) \tag{2.58c}$$

$$S_3 = i\left(\phi_0^* \phi_1 - \phi_1^* \phi_0\right) = -2\mathrm{Im}\left(\phi_0^* \phi_1\right) \tag{2.58d}$$

which satisfy the constraint condition $S_0^2 = S_1^2 + S_2^2 + S_3^2$. By introducing methodically these Stokes parameters into the general expression of the dynamical system, the following equations are found :

$$\dot{S}_0 = -2\gamma S_1, \tag{2.59a}$$

$$\dot{S}_1 = -2\gamma S_0 - (\kappa - \mu) S_3, \tag{2.59b}$$

$$\dot{S}_2 = \frac{3\alpha}{2} S_1 S_3 - 5\eta S_0 S_1 S_3, \tag{2.59c}$$

$$\dot{S}_3 = (\kappa - \mu) S_1 - \frac{3\alpha}{2} S_1 S_2 + 5\eta S_0 S_1 S_2 \tag{2.59d}$$

In what follows, all the results are obtained in the absence of inertial parameter ($\mu = 0$). The Fig.2.10 illustrates the different solution trajectories of system (2.60) in distinguishing the

cubic system (Fig.2.10(a,b,c)) to quintic system (Fig.2.10(d)).

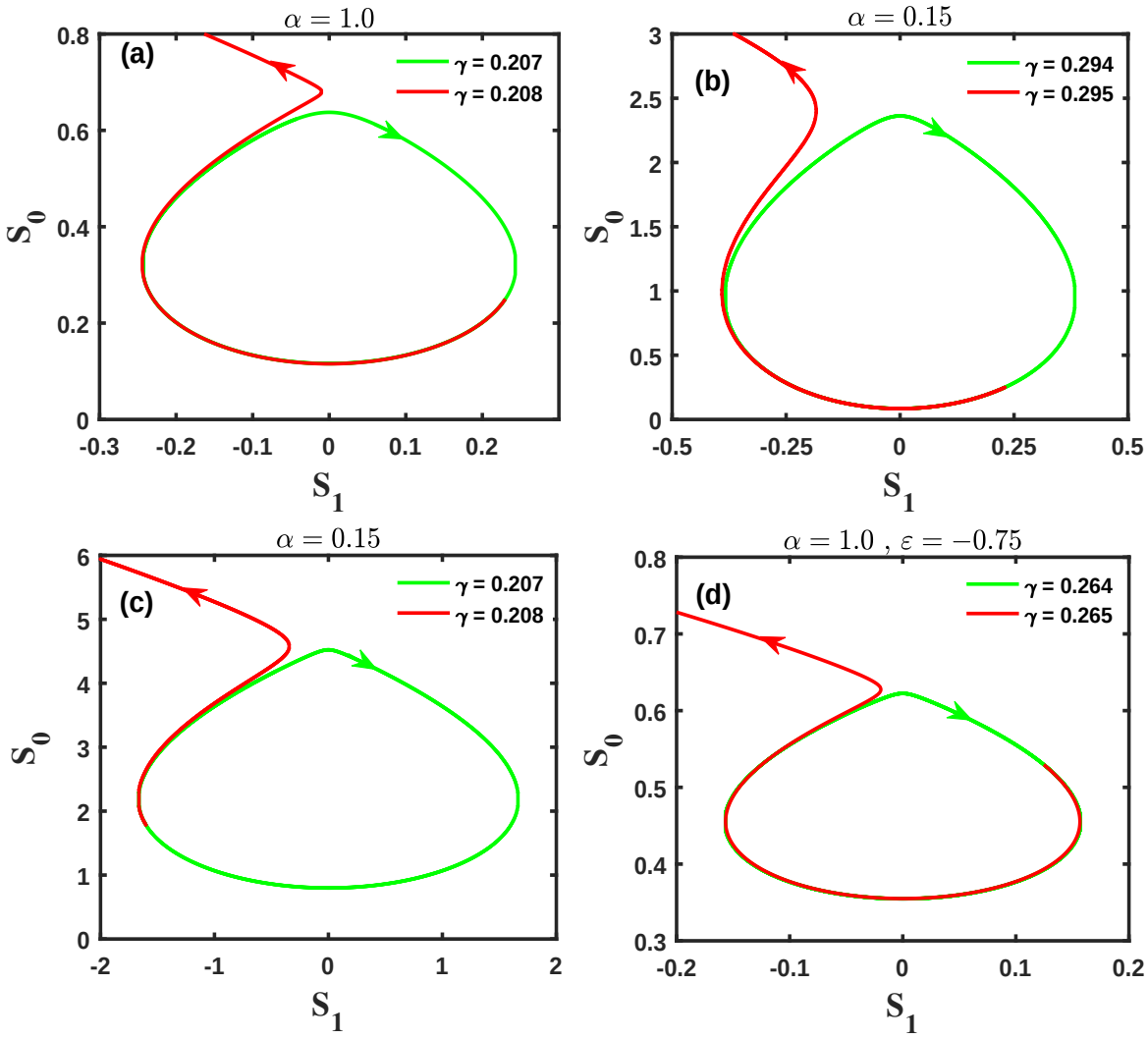

Figure 2.10: Dynamical evolutions of the system by Stokes parameters in the $(S_1;S_0)$ space. In (a) and (b), initial conditions are the same i.e., $\phi_1(0) = 0.49$ and $\phi_2(0) = 0.1i$. In (c), initial conditions are $\phi_1(0) = 0.3$ and $\phi_2(0) = 1.3i$. (d) is plotted with initial conditions $\phi_1(0) = 0.572$ and $\phi_2(0) = 0.45i$ for the quintic system. Cubic and quintic coefficients are given on the graph. $\kappa = 0.65$.

In each dial, the red curve which does not form a closed cycle, indicates that the exceptional point or the breaking point is reached. Below this threshold, trajectories are periodic and describe the stable limit cycles in the $(S_1;S_0)$ space. But when γ attains a critical value, an unsteady state analogous to that occurring in a $\mathcal{PT}$ broken phase, can be observed. In Fig.2.10(a), $\alpha = 1.0$ and initial conditions are $\phi_1(0) = 0.49$ and $\phi_2(0) = 0.1i$. With this initial condition, the breaking point occurs exactly at the predicted value shown in the Fig.2.6(a).

On the other hand, one can see in Fig.2.10 that initial conditions and nonlinearity affect the breaking point. Indeed, for the same initial conditions (Fig.2.10(a) and 2.10(b)), when nonlinearity varies, the breaking point varies at the same time. Likewise, for the same value of nonlinearity (see Fig.2.10(b) and Fig.2.10(c)) and different initial conditions, the breaking point is also modified. In addition, it can be observed that the breaking point value decreases

when nonlinearity increases. In other words, the increasing of nonlinearity reduces the $\mathcal{PT}$ unbroken region. These observations remain unchanged when the quintic system is considered, as it is shown in Fig.2.10(d).

Since the Hamiltonian for this case has not yet been found, it is important to note that the quintic system is not integrable. However, for the cubic system ($\eta = 0$) it is easy find the following motion constants, expressed as

$$\begin{aligned} C_1^2 &= \left(3\alpha S_2 - 2\left(\kappa - \mu\right)\right)^2 + \left(3\alpha S_3\right)^2 \\ C_2 &= S_0 - \frac{4\gamma}{3\alpha} tan^{-1}\left(\frac{3\alpha S_2 - 2\left(\kappa - \mu\right)}{S_3}\right) \end{aligned} \tag{2.60}$$

Proof that the cubic system is integrable is provided by the existence of these two constants of motion.

b) The averaging method

For dynamic systems described by nonlinear differential equations, the averaging method [147, 148] is one of the most useful mathematical techniques for finding analytical solutions. It applies not only to the study of periodic oscillations, but also to the study of transient oscillations where the amplitude and phase of the oscillations vary slowly with time. So, looking for oscillatory solutions of the system (2.14) around each fixed point, this last system can be rewritten in the general form as

$$\begin{cases} \ddot{X}_0 + \tilde{\omega} X_0 = \tilde{\gamma} F_1\left(X_0\,,\, \dot{X}_0\,,\, X_1\,,\, \dot{X}_1\right) \\ \ddot{X}_1 + \tilde{\omega} X_1 = \tilde{\gamma} F_2\left(X_0\,,\, \dot{X}_0\,,\, X_1\,,\, \dot{X}_1\right). \end{cases} \tag{2.61}$$

The solutions will be taken in the form:

$$\begin{cases} X_0(\tau) = x_{00} + a_0(\tau)\cos\left(\omega\tau + \theta_0(\tau)\right) \\ X_1(\tau) = x_{10} + a_1(\tau)\cos\left(\omega\tau + \theta_1(\tau)\right) \end{cases} \tag{2.62}$$

with $a_i(\tau)$, $\theta_i(\tau)$, x_{i0} (with $x_{00}^2 = x_{10}^2$) and ω are respectively the amplitude, phase, fixed points and frequency of oscillations of the oscillator i ($i = 0, 1$). The functions F_1 and F_2 are expressed in the equations below:

$$F_1 = -2(1+\mu)\tilde{\gamma}\dot{X}_0 + 2\mu\tilde{\gamma}\dot{X}_1 + (1+\mu)\tilde{\alpha}X_0^3 + \mu\tilde{\alpha}X_1^3 - (1+\mu)\tilde{\eta}X_0^5 - \mu\tilde{\eta}X_1^5 + \tilde{\kappa}X_1, \tag{2.63a}$$

$$F_2 = 2(1+\mu)\tilde{\gamma}\dot{X}_1 - 2\mu\tilde{\gamma}\dot{X}_0 + (1+\mu)\tilde{\alpha}X_1^3 + \mu\tilde{\alpha}X_0^3 - (1+\mu)\tilde{\eta}X_1^5 - \mu\tilde{\eta}X_0^5 + \tilde{\kappa}X_0 \tag{2.63b}$$

with $\tilde{\omega} = \frac{1+\mu(1-\kappa)}{1+2\mu}$, $\tilde{\gamma} = \frac{\gamma}{1+2\mu}$, $\tilde{\alpha} = \frac{\alpha}{1+2\mu}$, $\tilde{\eta} = \frac{\eta}{1+2\mu}$ and $\tilde{\kappa} = \frac{\kappa-\mu(1-\kappa)}{1+2\mu}$

The averaging method requires the amplitudes and phases to be the solutions of the system

$$\dot{a}_0 = -\frac{\tilde{\gamma}\omega}{2\pi}\int_0^{2\pi} F_1.\sin(\omega t+\theta_0)dt \tag{2.64a}$$

$$\dot{a}_1 = -\frac{\tilde{\gamma}\omega}{2\pi}\int_0^{2\pi} F_2.\sin(\omega t+\theta_1)dt \tag{2.64b}$$

$$\dot{\theta}_0 = \frac{\tilde{\gamma}\omega}{2\pi a_0}\int_0^{2\pi} F_1.\cos(\omega t+\theta_0)dt \tag{2.64c}$$

$$\dot{\theta}_1 = \frac{\tilde{\gamma}\omega}{2\pi a_1}\int_0^{2\pi} F_2.\cos(\omega t+\theta_1)dt \tag{2.64d}$$

Substituting the functions F_1 and F_2 into the Eqs.(2.64a),(2.64b), (2.64c) and (2.64d), we obtain the following first-order differential equations for the amplitudes and phases:

$$\begin{aligned}
&\dot{\theta}_0 = \tfrac{1}{16\tilde{\omega}}(5\mu\tilde{\eta}a_1^5 + 6\mu(10\tilde{\eta}x_{10}^2 - \tilde{\alpha})a_1^3 + 8\mu(5\tilde{\eta}x_{10}^2 - 3\tilde{\alpha})x_{10}^2 a_1 - 8\tilde{\kappa}a_1)\sin(\theta) + \\
&\mu\tilde{\gamma}a_1\cos(\theta) - \tilde{\gamma}(1+\mu)a_0 \\
&\\
&\dot{a}_0 = \tfrac{1}{16\tilde{\omega}}(5\mu\tilde{\eta}a_1^5 + 6\mu(10\tilde{\eta}x_{10}^2 - \tilde{\alpha})a_1^3 + 8\mu(5\tilde{\eta}x_{10}^2 - 3\tilde{\alpha})a_1 - 8\tilde{\kappa}a_1)\cos(\theta) \\
&-\mu\tilde{\gamma}a_1\sin(\theta) + \tfrac{1}{16\tilde{\omega}}(5\tilde{\eta}(1+\mu)a_0^5 + 60\tilde{\eta}(1+\mu)x_{00}^2 a_0^3 - 6\tilde{\alpha}(1+\mu)a_0^3 + \\
&40\tilde{\eta}(1+\mu)x_{00}^4 a_0 - 24\tilde{\alpha}(1+\mu)x_{00}^2 a_0) \\
&\dot{\theta}_1 = \tfrac{1}{16\tilde{\omega}}(-5\mu\tilde{\eta}a_0^5 - 6\mu(10\tilde{\eta}x_{00}^2 - \tilde{\alpha})a_0^3 - 8\mu(5\tilde{\eta}x_{00}^2 - 3\tilde{\alpha})x_{00}^2 a_1 + 8\tilde{\kappa}a_0)\sin(\theta) \\
&-\mu\tilde{\gamma}a_0\cos(\theta) + \tilde{\gamma}(1+\mu)a_1 \\
&\\
&\dot{a}_1 = \tfrac{1}{16\tilde{\omega}}(5\mu\tilde{\eta}a_0^5 + 6\mu(10\tilde{\eta}x_{00}^2 - \tilde{\alpha})a_0^3 + 8\mu(5\tilde{\eta}x_{00}^2 - 3\tilde{\alpha})a_0 - 8\tilde{\kappa}a_0)\cos(\theta) \\
&-\mu\tilde{\gamma}a_0\sin(\theta) + \tfrac{1}{16\tilde{\omega}}(5\tilde{\eta}(1+\mu)a_1^5 + 60\tilde{\eta}(1+\mu)x_{10}^2 a_1^3 - 6\tilde{\alpha}(1+\mu)a_1^3 + \\
&40\tilde{\eta}(1+\mu)x_{10}^4 a_1 - 24\tilde{\alpha}(1+\mu)x_{10}^2 a_1)
\end{aligned} \tag{2.65}$$

where $\theta = \theta_0 - \theta_1$.

The equilibrium states $a_0 = A_{00}$, $a_1 = A_{01}$ and $\theta = \theta_0$ of Eq.(2.65) are defined by the following nonlinear algebraic equation in A_{00} (θ_0 can be obtained after substitution of A_{00} and A_{01} into the first and third relations in Eq.(2.65)).

$$c_8 A_{00}^8 + c_6 A_{00}^6 + c_4 A_{00}^4 + c_2 A_{00}^2 + c_0 = 0 \tag{2.66}$$

The amplitudes are related by

$$A_{01}^2 = A_{00}^2. \tag{2.67}$$

and the coefficients c_i are defined as follows:

$$c_8 = \frac{25}{32}\mu\tilde{\eta}^2 + \frac{25}{64}\tilde{\eta}^2 \tag{2.68}$$

$$c_6 = -\frac{15}{8}\mu\tilde{\alpha}\tilde{\eta} - \frac{75}{8}\mu^2\tilde{\eta}^2x_{10}^2 + \frac{75}{8}\mu^2\tilde{\eta}^2x_{00}^2 + \frac{75}{8}\mu\tilde{\eta}^2x_{00}^2 - \frac{15}{16}\tilde{\alpha}\tilde{\eta} + \frac{75}{8}\tilde{\eta}^2x_{00}^2 \tag{2.69}$$

$$\begin{aligned} c_4 = {} & 15\mu^2\tilde{\alpha}\tilde{\eta}x_{10}^2 - 15\mu^2\tilde{\alpha}\tilde{\eta}x_{00}^2 - 30\mu\tilde{\alpha}\tilde{\eta}x_{00}^2 - \tfrac{5}{4}\mu\tilde{\eta}\omega^2 + \tfrac{5}{4}\mu\tilde{\eta}\tilde{\omega}^2 - 15\tilde{\alpha}\tilde{\eta}x_{00}^2 - \tfrac{125}{2}\mu^2\tilde{\eta}^2x_{10}^5 \\ & + \tfrac{5}{4}\mu\tilde{\eta}\tilde{\kappa} + \tfrac{125}{2}\mu^2\tilde{\eta}^2x_{00}^4 + 125\mu\tilde{\eta}^2x_{00}^4 - \tfrac{5}{4}\tilde{\eta}\omega^2 + \tfrac{9}{8}\mu\tilde{\alpha}^2 + \tfrac{5}{4}\tilde{\eta}\tilde{\omega}^2 + \tfrac{9}{16}\tilde{\alpha}^2 + \tfrac{125}{2}\tilde{\eta}^2x_{00}^4 \end{aligned} \tag{2.70}$$

$$\begin{aligned} c_2 = {} & \tfrac{105}{2}\mu^2\tilde{\alpha}\tilde{\eta}x_{10}^4 + 15\mu\tilde{\eta}\tilde{\kappa}x_{10}^2 - \tfrac{105}{2}\mu^2\tilde{\alpha}\tilde{\eta}x_{00}^4 - 105\mu\tilde{\alpha}\tilde{\eta}x_{00}^4 - 15\mu\tilde{\eta}\omega^2x_{00}^2 + 15\mu\tilde{\eta}\tilde{\omega}^2x_{00}^2 \\ & + 9\mu^2\tilde{\alpha}^2x_{00}^2 - \tfrac{105}{2}\tilde{\alpha}\tilde{\eta}x_{00}^4 + 9\mu\tilde{\alpha}^2\tilde{\eta}x_{00}^2 - 15\tilde{\eta}\omega^2x_{00}^2 + 15\tilde{\eta}\tilde{\omega}^2x_{00}^2 + \tfrac{3}{2}\mu\tilde{\alpha}\omega^2 - \tfrac{3}{2}\mu\tilde{\alpha}\tilde{\omega}^2 \\ & - 75\mu^2\tilde{\eta}^2x_{10}^6 - \tfrac{9}{2}\mu^2\tilde{\alpha}^2x_{10}^2 - \tfrac{3}{2}\mu\tilde{\alpha}\tilde{\kappa}x_{10}^2 + 75\mu^2\tilde{\eta}^2x_{00}^6 + 150\mu\tilde{\eta}^2x_{00}^6 + \tfrac{3}{2}\tilde{\alpha}\omega^2 + \tfrac{9}{2}\tilde{\alpha}^2x_{00}^2 \\ & + 75\tilde{\eta}^2x_{00}^6 - \tfrac{3}{2}\tilde{\alpha}\tilde{\omega}^2 \end{aligned} \tag{2.71}$$

$$\begin{aligned} c_0 = {} & 25\mu^2\tilde{\eta}^2x_{00}^8 - 25\mu^2\tilde{\eta}^2x_{10}^8 + 50\mu\tilde{\eta}^2x_{00}^8 - 30\mu^2\tilde{\alpha}\tilde{\eta}x_{00}^6 + 30\mu^2\tilde{\alpha}\tilde{\eta}x_{10}^6 + 25\tilde{\eta}^2x_{00}^8 \\ & - 60\mu\tilde{\alpha}\tilde{\eta}x_{00}^6 + 9\mu^2\tilde{\alpha}^2x_{00}^4 - 9\mu^2\tilde{\alpha}^2x_{10}^4 - 10\mu\tilde{\eta}\omega^2x_{00}^4 + 10\mu\tilde{\eta}\tilde{\omega}^2x_{00}^4 - 30\tilde{\alpha}\tilde{\eta}x_{00}^6 \\ & + 18\mu\tilde{\alpha}^2x_{00}^4 + 10\mu\tilde{\eta}\tilde{\kappa}x_{10}^4 - 10\tilde{\eta}\omega^2x_{00}^4 + 10\tilde{\eta}\tilde{\omega}^2x_{00}^4 + 6\mu\tilde{\alpha}\omega^2x_{00}^2 - 6\mu\tilde{\alpha}\tilde{\omega}^2x_{00}^2 \\ & + 9\tilde{\alpha}x_{00}^4 + 8\mu\tilde{\gamma}\omega^2 - 6\mu\tilde{\alpha}\tilde{\kappa}x_{10}^2 + 6\tilde{\alpha}\omega^2x_{00}^2 - 6\tilde{\alpha}\tilde{\omega}^2x_{00}^2 + \omega^4 + (4\tilde{\gamma}^2 - \tilde{\omega}^2)\omega^2 + \tilde{\omega}^4 - \tilde{\kappa}^2 \end{aligned} \tag{2.72}$$

The polynomial of variable A_{00} shown in Eq.(2.66) can be solved by means of the Newton-Raphson algorithm.

2.3.2 Numerical methods

When it comes to solving non-linear differential equations, analytical methods have limitations, i.e. they do not have exact analytical solutions or, under certain conditions, allow approximate solutions. In order to overcome these difficulties, numerical methods are generally used to solve such equations. In this thesis, the fourth-order Runge-Kutta algorithm (RK4) is applied to integrate the differential equations describing the dynamics of the system under study. Other techniques are also utilised to solve certain equations. These include the Newton-Raphson method and dichotomy. The main computational softwares applied are Matlab and occasionally Maple. Thereafter, the iterative schemes of the RK4 algorithm and the other numerical methods for system dynamics analysis are presented.

2.3.2.1 Fourth-order Runge-Kutta algorithm: Iterative scheme

The use of numerical tools is of great interest in ordinary differential equation analysis. They provide more accurate solutions than analytical ones, as well as validation of experimental results. This method is named after two of its pioneers: Carle Runge, who first developed the method in 1894, and Martin W. Kutta, who improved it a few years later in 1901. This method widely used and very stable, combines two numerical integration methods: the trapezoidal method and the Simpson method. Thus, if the equation to solve is a second-order differential

equation, it can be decomposed into a first-order vector system like

$$\dot{X} = \frac{dX}{dt} = F(t,\ X(t)) \tag{2.73}$$

with initial conditions $X(t_0) = X_0$, X and F being vectors. The aim is to find the solutions $x_{k,m}$ at any given time as a function of the previous ones. To solve the problem, the method is based on the following sequence of instructions:

$$\begin{aligned}
t_k &= t_0 + kh \\
x_{0,m} &= x_m(t_0) \\
L_{1,m} &= f_m\left(t_k,\ x_{k,m}\right) \\
L_{2,m} &= f_m\left(t_k + \frac{h}{2},\ x_{k,m} + \frac{L_{1,m}}{2}\right) \\
L_{3,m} &= f_m\left(t_k + \frac{h}{2},\ x_{k,m} + \frac{L_{2,m}}{2}\right) \\
L_{4,m} &= f_m\left(t_k + h,\ x_{k,m} + L_{3,m}\right) \\
x_{k+1,m} &= x_{k,m} + \frac{1}{6}\left(L_{1,m} + 2L_{2,m} + 2L_{3,m} + L_{4,m}\right)
\end{aligned} \tag{2.74}$$

where k represents the time incrementation and m labels their components related to $L_{1,j}$, $L_{2,m}$, $L_{3,m}$,$L_{4,m}$ are intermediate variables and h is the time step.

2.3.2.2 Newton-Raphson method

The most often method to numerically solve the polynomial equations is the Newton-Raphson algorithm. This method use an iterative technique for finding roots of an equation or the system of nonlinear equations. The principle of the Newton-Raphson method is described as follows :

Consider a one-variable equation of the form

$$f(x) = 0 \tag{2.75}$$

Let $f \in C^2\left[a,\, b\right]$, i.e. f and f' are continuous functions on $[a,\, b]$. Let also x_n be a sequence of approximate roots for f such that: $f'(x_n) \neq 0$ and $|x_n - \alpha| < \varepsilon\ \forall n$, where α is the exact root for $f(x) = 0$. By using Taylor expansion for f around x_n, as defined below

$$f(x) = f(x_n) + (x - x_n)f'(x_n) + \frac{(x - x_n)^2}{2!}f(x_n) + O(x) \tag{2.76}$$

setting $\alpha = x = x_{n+1}$, the iterative method is

$$x_{n+1} = x_n - \frac{f(x_n)}{f'(x_n)} \tag{2.77}$$

In order to guarantee that, the iterative process is convergent, the initial root, x_0, should be chosen close to the exact root α which means

$$|x_0 - \alpha| < \varepsilon \tag{2.78}$$

2.3.2.3 Dichotomy method

Newton's method is a popular technique for the solution of nonlinear equations, but alternative methods exist which may be preferable in certain situations. The Dichotomy method is yet another technique for finding a solution to the nonlinear equation $f(x) = 0$, which can be used provided that the function f is continuous. The motivation for this technique is drawn from Bolzano's theorem for continuous functions:

Theorem: If the function f(x) is continuous in [a, b] and $f(a).f(b) < 0$ (i.e. the function f has values with different signs at a and b), then a value $c \in (a, b)$ exists such that $f(c) = 0$.

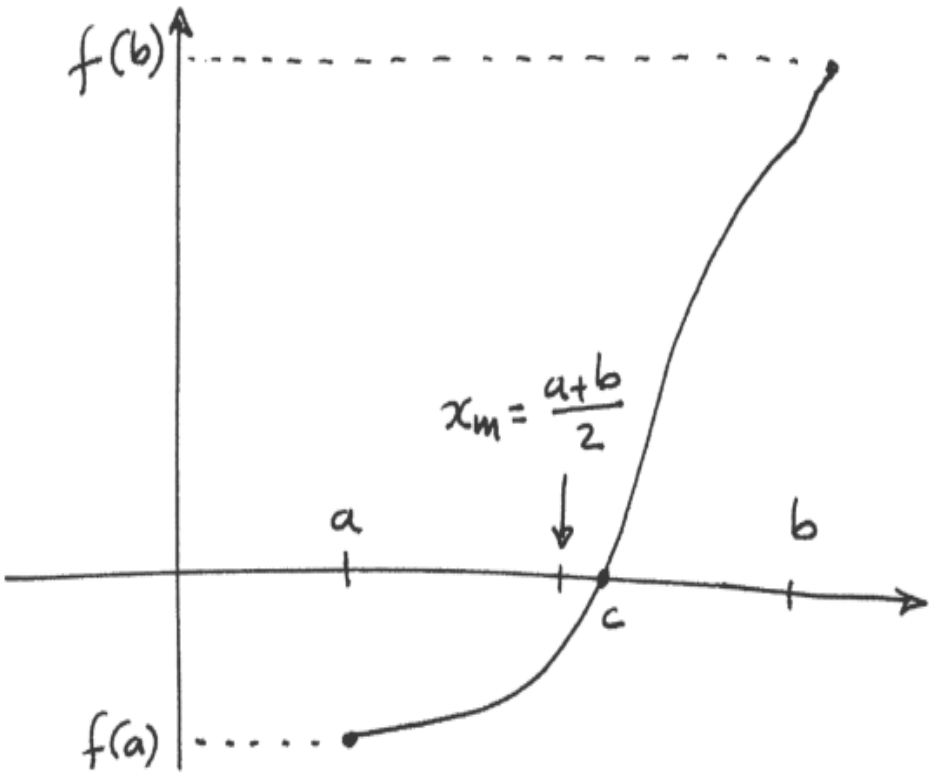

Figure 2.11: Graphic illustration of Dichotomy method.

The Dichotomy algorithm attempts to locate the value c where the plot of f crosses over zero, by checking whether it belongs to either of the two sub-intervals [a, x_m] , [x_m, b], where x_m is the midpoint

$$x_m = \frac{a+b}{2} \tag{2.79}$$

The algorithm proceeds as follows:

- If $f(x_m) = 0$, we have our solution (x_m) and the algorithm terminates.;

- In the much more likely case that $f(x_m) \neq 0$ we observe that $f(x_m)$ must have the opposite sign than one of $f(a)$ or $f(b)$ (since they have opposite signs themselves). Thus
  - Either $f(a).f(x_m) < 0$, or
  - $f(x_m).f(b) < 0$.

We pick whichever of these 2 intervals satisfies this condition, and continue the bisection process with it.

Convergence Let us conventionally define the "approximation" at x_k after the $k-th$ iteration as the midpoint

$$x_k = \frac{a_k + b_k}{2} \tag{2.80}$$

of I_k. Since the actual solution $f(a) = 0$ satisfies $a \in I_k$, then

$$|x_k - a| \leq \frac{1}{2} |I_k| \tag{2.81}$$

where $|I_k|$ symbolises the length of the interval I_k.

2.4 Hardware and software

The main computer tool used to perform all the calculations in this thesis is a laptop running Windows 10pro operating system. Microsoft Visio has been used for the design of the physical systems to be modelled, Maple to perform the integral calculations and Matlab for the analysis of the data.

Conclusion

The purpose of this chapter has been to establish the differential equations governing the dynamics of a system of coupled nonlinear $\mathcal{PT}$-symmetry mechanical oscillators, both in isolation and when introduced as a defect into a Hermitian conservative mechanical transmission line. We also presented the different analytical and numerical methods used to study our system's dynamics. The next chapter deals with the found results and discussion.

Chapter 3

Results and Discussion

Introduction

In this present chapter, the results from analytical and numerical analyses carried out in the previous chapter are presented and discussed. The structure of this chapter is as follows: In section 3.1, the linear dynamics of the mechanical system under influence of both inertial and elastic couplings are studied in its generality. In section 3.2, the nonlinear dynamics of our studied $\mathcal{PT}$-Symmetric mechanical system is investigated. The stability, breaking point in nonlinear regime and influence of the inerter parameter are analysed. In section 3.3, the scattering properties of the mechanical dimer (linear one only) is also investigated when it is inserted as a defect in a Hermitian mechanical transmission line (MTL). The last paragraph of this chapter is devoted to the conclusion.

3.1 Linear dynamics of the $\mathcal{PT}$-symmetric mechanical dimer

This section deals only with the dynamics of $\mathcal{PT}$-symmetric mechanical systems in the linear regime. In fact, knowledge of the system's behaviour in its simplest state i.e., in the absence of any non-linearity, is decisive in characterising its dynamics. In this respect, it is interesting to study the influence of certain parameters on the dynamic behaviour of the mechanical dimer.

3.1.1 Normal modes and breaking points

Let's look at the model described in Fig.2.1 of the previous chapter and assume that the springs at the ends are identical and have constant stiffness k_{00}. Consider the relations: (2.39) and (2.40), which denote the normal modes and the breaking points respectively, and expresssed by

$$\omega_n = \pm\sqrt{\frac{1-2\gamma^2+\mu(1-\kappa)\pm\sqrt{\gamma^2-\gamma_{TH}^2}}{1+2\mu}}$$

$$\gamma_{TH_{1,2}} = \sqrt{\frac{1}{2}\left(1+\mu(1-\kappa)\mp\sqrt{(1-\kappa^2)\,(1+2\mu)}\right)}$$

A quick analysis shows that these two couplings can vary independently. This indicates that they do not affect the dynamics in the same way. Furthermore, the expression of the eigenfrequencies ω_n (Eq.(2.39)) reveals two dynamic transition points at the thresholds of the gain-loss parameters $\gamma = \gamma_{th_1}$ and $\gamma = \gamma_{th_2}$. γ_{th_1} and γ_{th_2} are the transition points, also known as exceptional points (EPs). In other words, as the γ parameter evolves, the nature of the eigenfrequencies changes from real to complex and then from complex to pure imaginary. Obviously, these changes in the nature of the eigenfrequencies have consequences for the dynamic behaviour of the dimer.

On the other hand, by observing the expressions of the breaking points γ_{th_1} and γ_{th_2}, it is easy to see that for $0 < \kappa < 1$ and $\mu > 0$ the latter remain real. However, if the condition given by Eq.(3.1) is satisfied, γ_{th_2} always exists while $\gamma_{th_1} = 0$.

$$\kappa_{THL} = \frac{\mu}{1+\mu} \tag{3.1}$$

Thus, for a given combination of different couplings, we can distinguish two categories of dimers: threshold ($\gamma_{th_1} \neq 0$) dimers and thresholdless ($\gamma_{th_1} = 0$) dimers.

When $\gamma_{th_1} = 0$, the exact phase disappear and the eigenmodes of the system switch directly from the complex domain the pure imaginary domain. This property is characteristic of $\mathcal{PTS}$ systems that exhibits the THL phenomenon. Similar results in the field of electronics have already been demonstrated [11].

- **TH dimer**

In Fig.3.1, gives the positive normal modes with respect to the elastic coupling parameter κ at $\mu = 0$. One can see that, the system faithfully reflects the characteristics of a $\mathcal{PTS}$ TH-dimer at this value (see Figs.3.1(a) and 3.1(b), for $0 < \kappa < 1$). When for $0 < \gamma < \gamma_{th_1}$, all normal modes are entirely in the exact phase and the system has an oscillatory motion in this realm during which its total energy is conserved. However, at the value $\gamma = \gamma_{th_1}$, called the exceptional point (EP), the state oscillatory of the system becomes uncontrollable because the amplitude increases indefinitely with time. This behaviour reflects a spontaneous symmetry breaking. As a result, the previously conservative energy suddenly becomes non-conservative. When this EP is crossed, the eigenvalues are said to coalesce and their imaginary parts are degenerated. For $\gamma_{th_1} < \gamma < \gamma_{th_2}$ the system is in the so-called broken phase. The eigenvalues are complex and the system oscillates with a non-conservative energy and the system is no longer $\mathcal{PT}$-symmetric. Finally, for $\gamma > \gamma_{th_2}$ the eigenvalues are all imaginary, and this has the effect of not producing any oscillations in the system.

If one of the couplings is fixed at zero, the γ_{th_1} transition point will increase with the control coupling, extending the region of the exact phase. However, the broken phase gap between γ_{th_2} and γ_{th_1} can either decrease or remain constant as the active coupling evolves. In the Fig.3.1, the solid dark line (which represents the difference between γ_{th_2} and γ_{th_1}) accurately reflects this phenomenon. Thus, when the active coupling is κ (Figs.3.1(a) and 3.1(b)), the solid dark line curve decreases before stabilising at the value 0 when $\kappa > 1$. In other words, beyond this

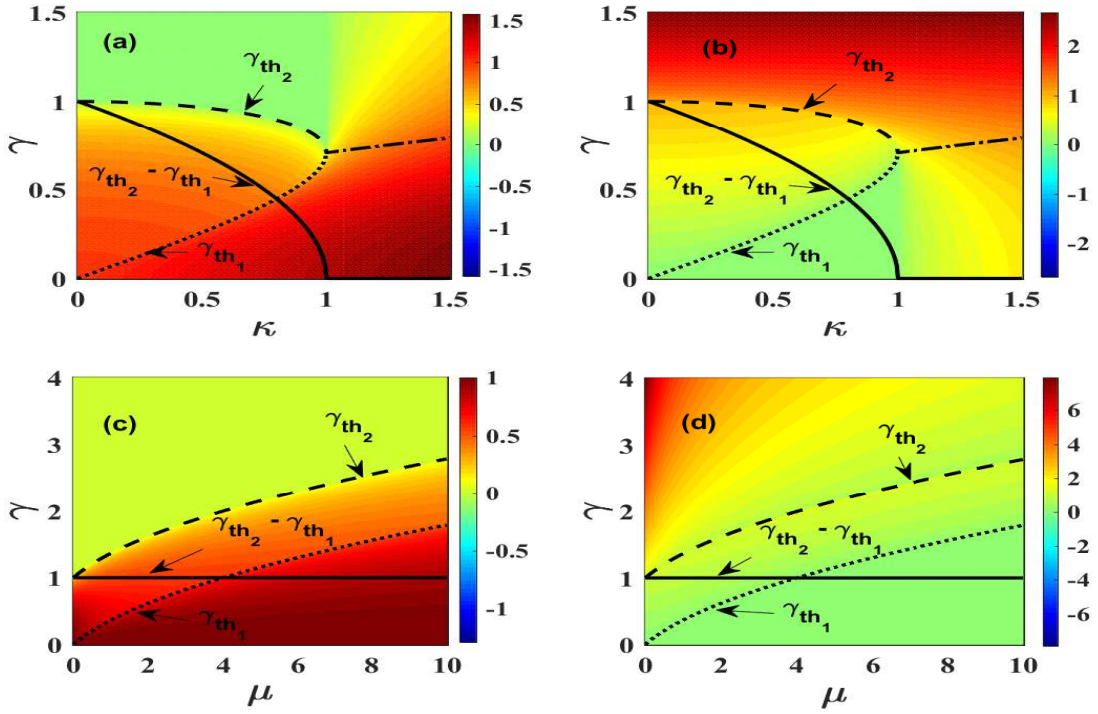

Figure 3.1: Eigenmodes and threshold evolutions of $\mathcal{PTS}$ dimer. First and second column represent the real and imaginary parts respectively. (a) and (b) show the elastic coupling effect when $\mu = 0$ whereas, (c) and (d) display the inertial coupling effect when $\kappa = 0$. The transition curves are indicated as γ_{th_1} and γ_{th_2} in the dotted and dashed dark lines respectively, while their relative difference is plotted in a plain dark line.

value, the exact phase region disappears and so the normal modes become complex.

In Figs.3.1(c) and 3.1(d) (when μ is the active coupling), the solid dark line remains constant and fixed at the value 1 indefinitely according to μ. This means that the exact phase region will exist whatever the value of μ.

- **Thresholdless dimer**

In the particular case where $\kappa = \kappa_{THL} = \mu/(1+\mu)$, corresponding to $\gamma_{th_1} = 0$, the normal modes move directly in the broken phase. As defined in [13], it is the point where normal modes coalesce along the controlling coupling constant. For this combination of coupling parameters, the transition point is zero without the active coupling being zero, which is unique to THL dimers. With the TH dimers, it would inevitably lead to the decoupling of the two oscillators. So, THL will only occur if there is at least two types of coupling in the system. The mechanical dimer model studied here has two types of coupling: elastic and inertial, controlled by the parameters κ and μ respectively.

The Fig.3.2 shows both THL and TH behaviours of the normal modes for each coupling type. In each case, one of the coupling parameters is active while the other one is defined constant. The critical value of the active coupling for which the THL ($\gamma_{th_1} = 0$) is realised, corresponds to a nonzero fixed passive coupling. In Fig.3.2(a), μ is the active coupling, and, at $\mu_{THL} = 4.0$ which correspond to the fixed value of $\kappa = 0.8$, the THL behaviour is achieved. Likewise, in Fig.3.2(c), the active coupling is now κ, and for $\mu = 1.0$, the same behaviour is

realised at $\kappa_{THL} = 0.5$.

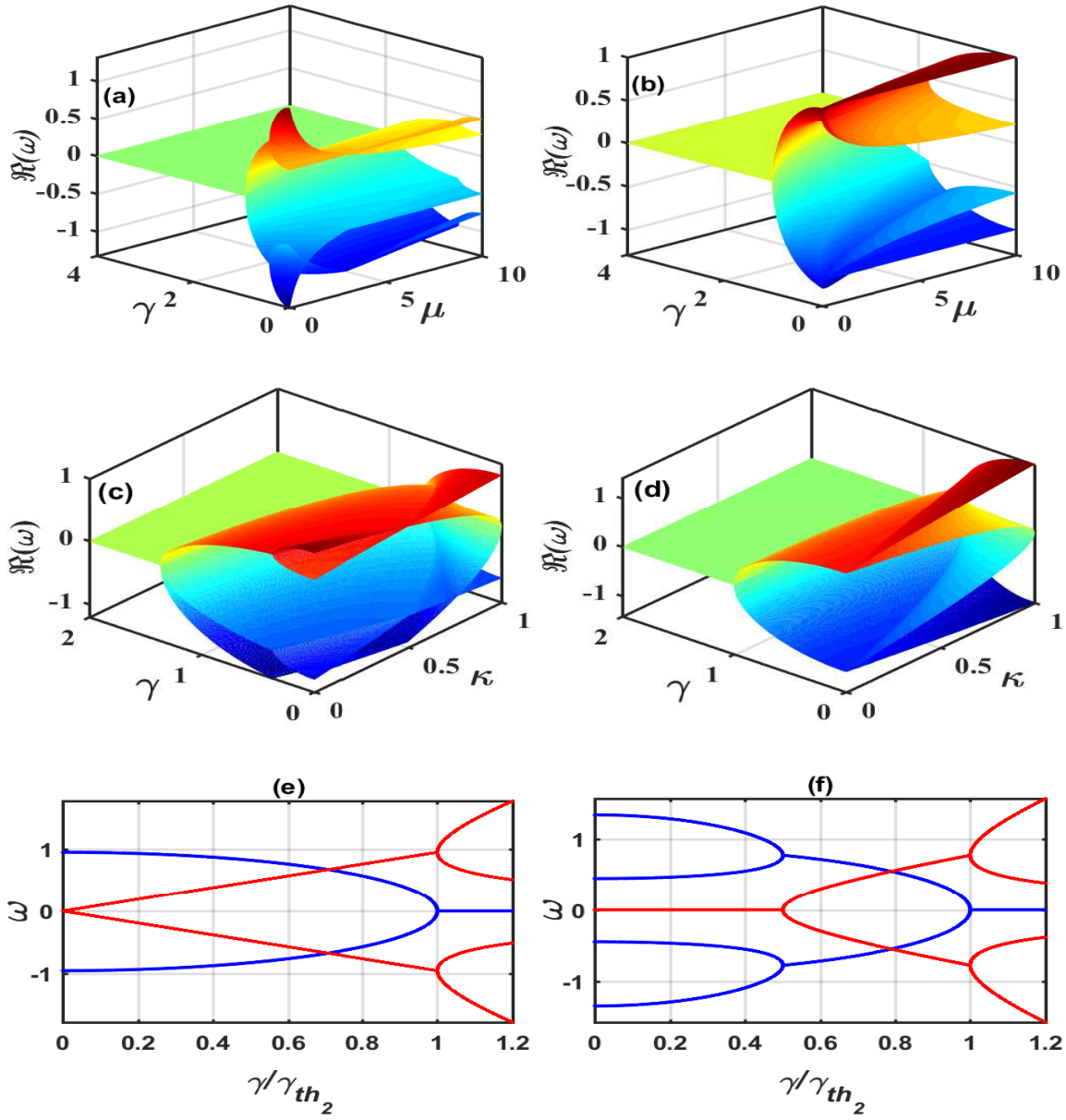

Figure 3.2: Eigenmodes evolution as a function of μ (a) and (b), and as a function of κ (c) and (d). (a) and (c) show the THL behaviour whereas (b) and (d) display the TH one. (e) shows a section of (a) and (c) at THL points. Likewise, (f) presents a section of (b) and (d) at any value of coupling (TH case). Real and imaginary parts are depicted by the blue and red colour, respectively. $\kappa = \mu/(1+\mu)$ (in (a)) and (c), $\mu = 0.1$ at $\gamma_{th_1} = 0$ when $\kappa = \mu/(1+\mu)$. For TH dimer (b), $\mu = 0$ and $\kappa = 0.8$.

In addition, one can note that around the thresholdless point (THLP) i.e., $\mu < \mu_{THL}$ and $\mu > \mu_{THL}$ in Fig.3.2(a) or $\kappa < \kappa_{THL}$ and $\kappa_{THL} < \kappa < 1$ in Fig.3.2(c), the exact phase region evolves in the opposite manner. Indeed, when $\kappa < \kappa_{THL}$ or $\mu < \mu_{THL}$, the exact phase decreases until desapears at the THLP whereas, beyond the THLP, the exact phase increases indefinitely with the coupling if the active coupling is μ. If the active coupling is κ, the exact phase region stops to widen and to exist when $\kappa = 1$. Consequently, before the THLP, the range of stable oscillatory regime is reduced as the coupling parameter increases. And after this THLP, the range of stable oscillations widens. Figs.3.2(e) and 3.2(f) give a simplified representation in the

(γ, ω) plane of the behaviour of the eigenfrequencies as a function of the normalised gain-loss parameter γ, at the THL point and outside, respectively. From this point of view, the absence of the first transition point ($\gamma_{th_1} = 0$), when the THL condition is satisfied, can be better appreciated (Fig.3.2(e)). However, when $0 < \gamma < 1$, the eigenfrequency field is complex. In this interval, which corresponds to the so-called broken phase region, the energy of the dimer cannot be conserved as it evolves indefinitely over time. On the other hand, in Fig.3.2(f) clearly shows the existence of the two exceptional points which distinctly delimit the different types of nature of the eigenfrequencies, namely real, complex and purely imaginary.

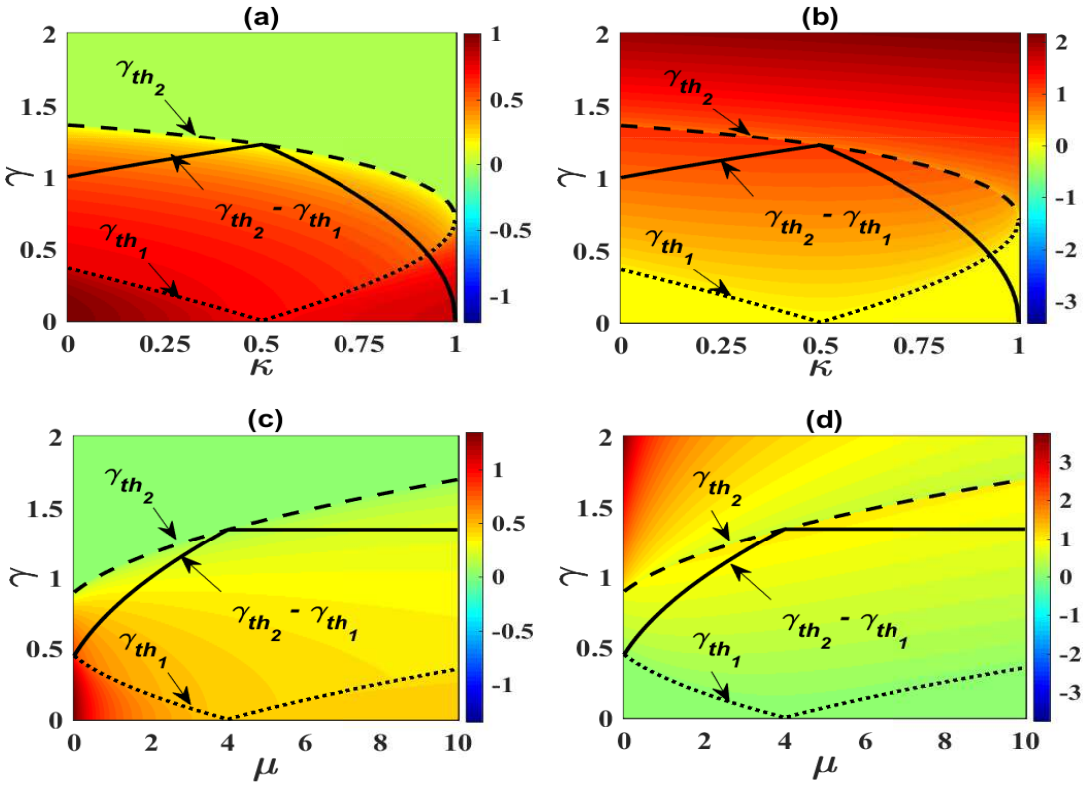

Figure 3.3: Normal modes and thresholds evolution of $\mathcal{PTS}$ THL-dimer. First and second column represent respectively the real and imaginary parts of the normal modes. In (a) and (b), $\mu = 1.0$ whereas in (c) and (d) $\kappa = 0.8$. The transitions values curves are indicated as γ_{th_1} and γ_{th_2} in the dotted and dashed dark lines respectively, while their relative difference is plotted in a solid dark line.

Fig.3.3, also show the behaviour of the eigenmodes for an active coupling parameter when the other one is non-zero and fixed exactly at the value for which the THL condition is satisfied. Compared to Fig.3.2, the exact phase regions gradually shrink until they reach the THL point ($\gamma_{th_1} = 0$), and then widen. When κ is active (Figs.3.3(a) and 3.3(b)), the exact phase range stops when κ becomes 1. In fact, κ cannot take on values greater than 1, because beyond that point the exact phase region disappears (see the solid dark line). However, When μ is active (Fig.3.3(c) and 3.3(d)), the dark line remains constant after the THL point, which means that the exact phase region will continue to enlarge indefinitely.

In order to show their flexibility with respect to the different coupling coefficients involved, the dynamics of the breaking points are studied. The dynamics of the normal modes (see

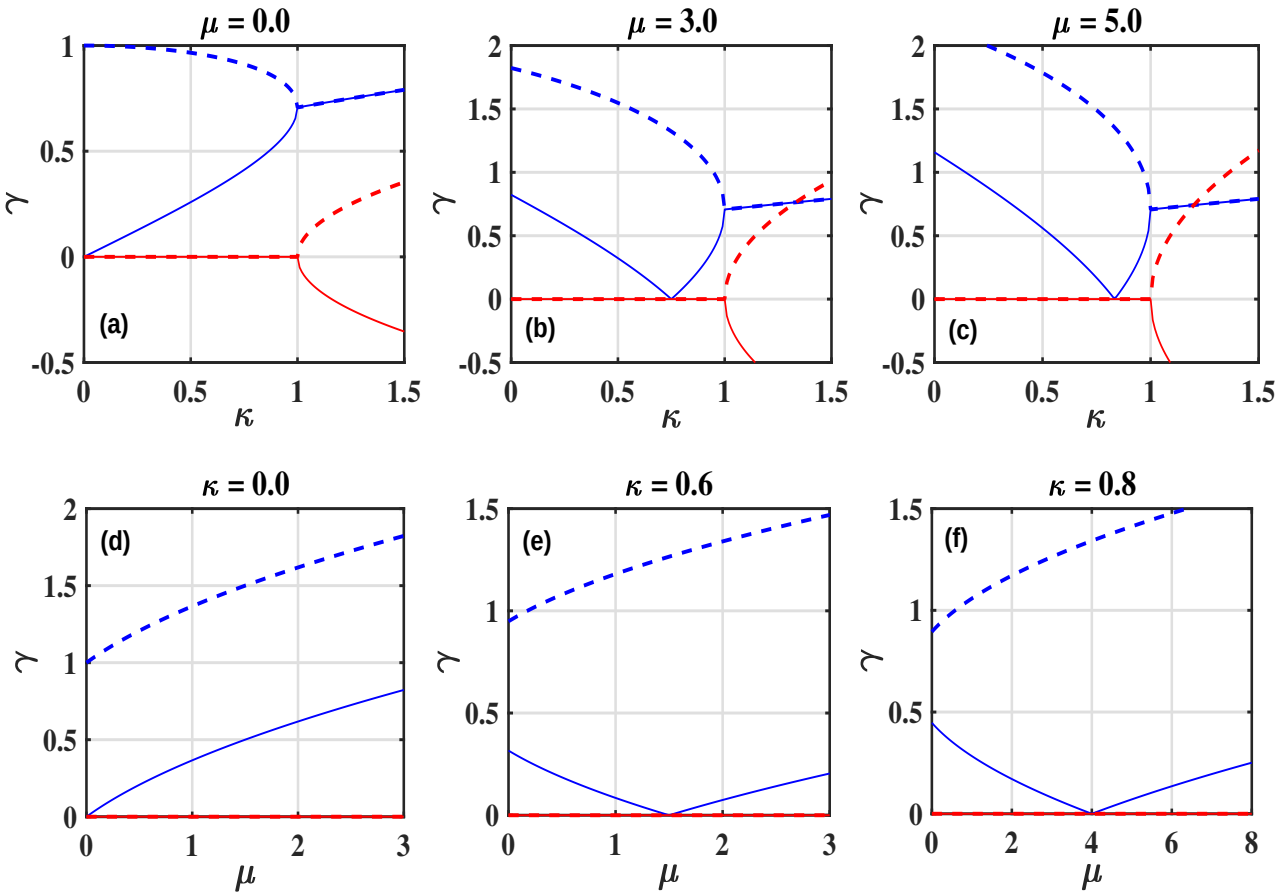

Figure 3.4: Breaking points dynamics as a function of coupling. (a, b, c): The active coupling is κ whereas μ is constant and its value is specified in the graphs. (c, d, e): The active coupling is μ, while κ is fixed and specified in the graphs. On all the dials, the colours blue and red indicate the real and imaginary parts respectively. Likewise, solid and dashed lines reflect the evolution of γ_{th_1} and γ_{th_2}.

Fig.3.2(f)) seen above showed that when the gain-loss parameter γ is before the first threshold ($\gamma < \gamma_{th_1}$), the eigenmodes are all real. The advantage of these eigenmodes being real is that the energy in the system is conserved making the system stable. This stability depends on the value of the elastic coupling κ.

Fig.3.4 also shows the diagram of the stability according to which coupling is active and for different values of the other one. The stability area lies below the first threshold γ_{th_1} (solid blue line). However, for $0 < \kappa < 1$ or for $\mu > 0$, two branches of breaking points (γ_{th_1} precisely) and also the zero breaking point when $\kappa = \kappa_{THL}$, are observed ($\mu = \mu_{THL}$ respectively).

3.1.2 Temporal evolutions

Consider the physical model shown in Fig.2.1 of the previous chapter in linear limit. The system consists of two coupled oscillators, one with loss and the other with equal gain. The preliminary study carried out in the previous sections on the eigenmodes of vibration and the breaking points has provided us with the necessary elements for predicting the dynamic

behaviour of such a system. In the following, the system's behaviour will be examine under the influence of the various parameters involved in its dynamics.

3.1.2.1 Threshold dimer

Let's distinguish two regions: the exact and broken phases. Three configurations of initial conditions will be taken into account. Notice that, in all the figures illustrating temporal evolution below, the green colour is used for the oscillator governed by the displacement X_1 (gain) and purple colour for the one governed by X_0 (loss). In Figs.3.5, 3.6 and 3.7, the top and bottom rows are obtained with $\kappa = 0.1$ and $\kappa = 0.65$ respectively. The first, second and third columns are plotted for $\gamma = 0.25\gamma_{th_1}$, $\gamma = 0.75\gamma_{th_1}$ $\gamma = 0.99\gamma_{th_1}$ respectively.

In the $\mathcal{PT}$ exact phase

- **Elastic coupling effect (with $\kappa \neq 0$ when $\mu = 0$):**

– Initial conditions on the loss oscillator: $(X_0\ \dot{X}_0,\ X_1,\ \dot{X}_1) = (1,\ 0,\ 0, 0)$

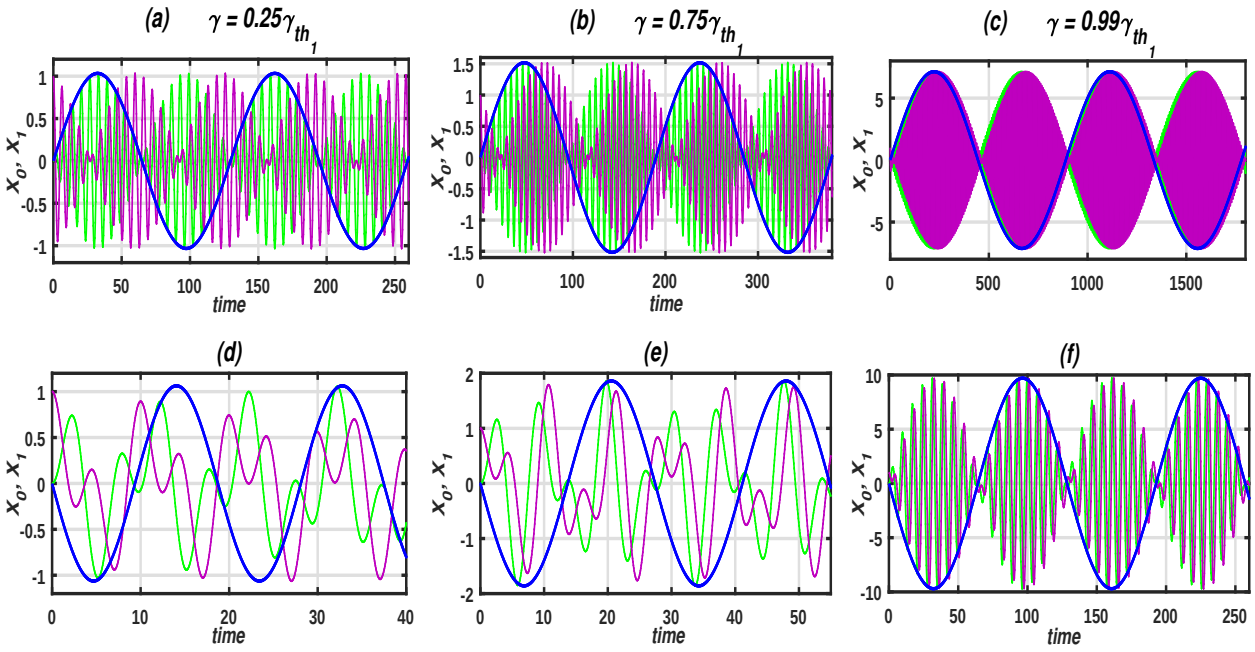

Figure 3.5: Temporal evolutions in linear limit of system (2.14). When initial conditions are fixed on the loss oscillator. On the top row $\kappa = 0.1$ (panels (a), (b) and (c)) and on the bottom row $\kappa = 0.65$ (panels (d), (e) and (f)). From the left column to the right column, the gain-loss parameters are respectively $\gamma = 0.25\gamma_{th_1}$, $\gamma = 0.75\gamma_{th_1}$ $\gamma = 0.99\gamma_{th_1}$.

All these figures are represented for two Rabi periods of frequency $\Omega_{Rabi} = |\omega_1 - \omega_2|/2$ in blue line colour. In Fig.3.5 (Fig.3.6 respectively), the initial conditions are fixed on the loss oscillator (on the gain oscillator respectively) as follows, $(X_0\ \dot{X}_0,\ X_1,\ \dot{X}_1) = (1,\ 0,\ 0, 0)$ $((X_0,\ \dot{X}_0,\ X_1,\ \dot{X}_1) = (0,\ 0,\ 1,\ 0)$ respectively). In Fig.3.7, the initial conditions are equally distributed between the two oscillators so that, $(X_0,\ \dot{X}_0,\ X_1,\ \dot{X}_1) = (\frac{\sqrt{2}}{2},\ 0,\ \frac{\sqrt{2}}{2},\ 0)$.

The dynamics of the system remains unchanged whether the initial excitation is defined entirely on the loss oscillator or on the gain oscillator (Fig.3.5 and Fig.3.6). For these two

– Initial conditions on the gain oscillator: $(X_0\ \dot{X}_0,\ X_1,\ \dot{X}_1) = (0,\ 0,\ 1, 0)$

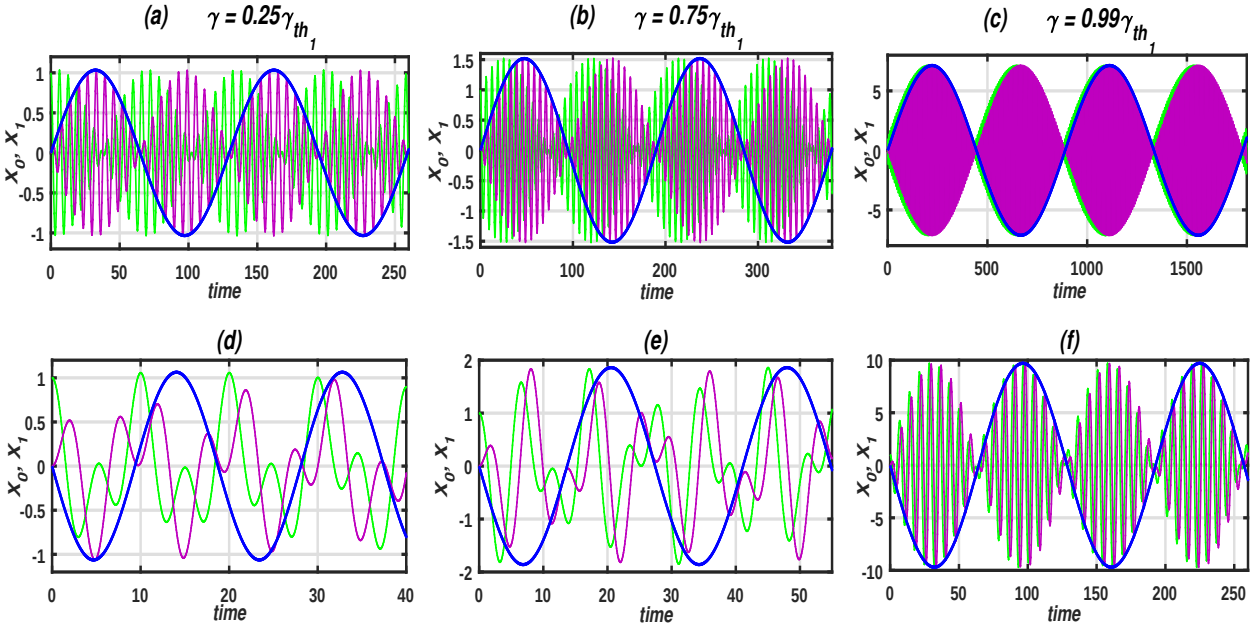

Figure 3.6: Temporal evolutions in linear limit of system (2.14). When initial conditions are fixed on the gain oscillator. On the top row $\kappa = 0.1$ (panels (a), (b) and (c)) and on the bottom row $\kappa = 0.65$ (panels (d), (e) and (f)). From the left column to the right column, the gain-loss parameters are respectively $\gamma = 0.25\gamma_{th_1}$, $\gamma = 0.75\gamma_{th_1}$ $\gamma = 0.99\gamma_{th_1}$.

– Initial conditions on both oscillators: $(X_0,\ \dot{X}_0,\ X_1,\ \dot{X}_1) = (\frac{\sqrt{2}}{2},\ 0,\ \frac{\sqrt{2}}{2},\ 0)$

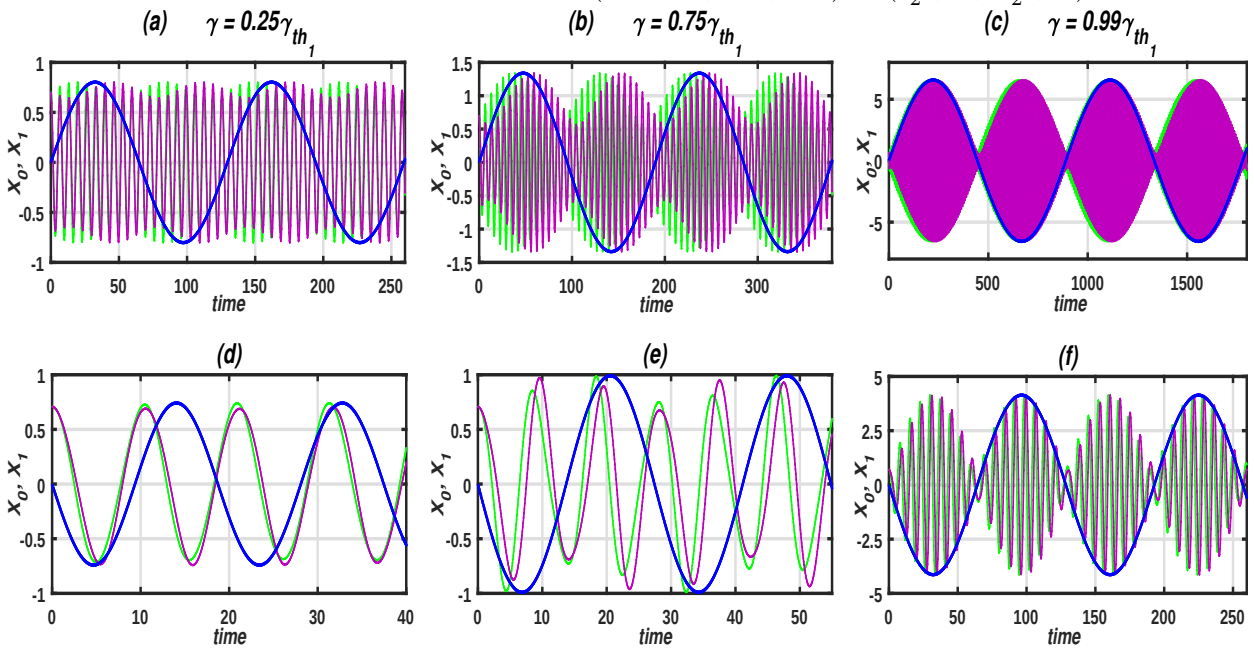

Figure 3.7: Temporal evolutions in linear limit of system (2.14). When initial conditions are fixed on both oscillators. On the top row $\kappa = 0.1$ (panels (a), (b) and (c)) and on the bottom row $\kappa = 0.65$ (panels (d), (e) and (f)). From the left column to the right column, the gain-loss parameters are respectively $\gamma = 0.25\gamma_{th_1}$, $\gamma = 0.75\gamma_{th_1}$ $\gamma = 0.99\gamma_{th_1}$.

configurations of initial conditions and for the same values of parameters, the dynamics have the same profile. However, when the initial excitation is balanced between the two oscillators (see Fig.3.7), a slightly different behaviour compared to the other two configurations is observed. The difference lies firstly in the shape of the oscillations (when the gain-loss parameter is weak) and secondly in the fact that the amplitude of the oscillations evolves in the opposite direction as the active coupling increases (Fig.3.5 and Fig.3.6). In addition, the energy of the system is greater for one side excitation than for both sides excitation (see for example Fig.3.5(f) or Fig.3.6(f) and Fig.3.7(f)). Another point to note is the time delay observed between the two signals when the coupling and the gain-loss ratio are low.

- **Inertial coupling effect (with $\mu \neq 0$ when $\kappa = 0$):**

  – Initial conditions on the loss oscillator: $(X_0,\ \dot{X}_0,\ X_1,\ \dot{X}_1) = (1,\ 0,\ 0,\ 0)$

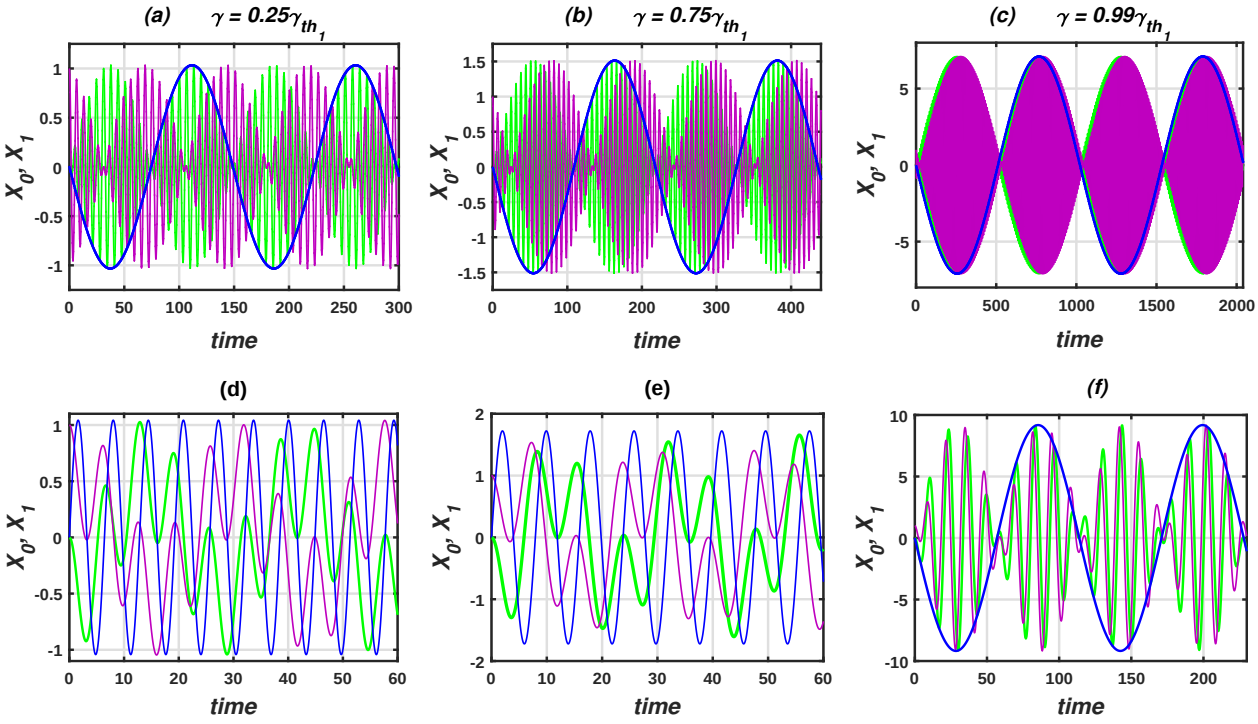

Figure 3.8: Temporal evolutions in linear limit of system (2.14). When initial conditions are fixed on the loss oscillator. On the top row $\mu = 0.1$ (panels (a), (b) and (c)) and on the bottom row $\mu = 10.0$ (panels (d), (e) and (f)). From the left column to the right column, the gain-loss parameters are respectively $\gamma = 0.25\gamma_{th_1}$, $\gamma = 0.75\gamma_{th_1}$ $\gamma = 0.99\gamma_{th_1}$.

The time evolutions depicting the effect of inertial coupling, as well as those illustrating the effect of elastic coupling, were obtained for identical configurations of initial conditions and the same values of the gain-loss parameter. For each figure, the first and second lines are obtained for $\mu = 0.1$ and $\mu = 10.0$ respectively. The behaviour is identical to that shown in the analysis of the effect of elastic coupling as the breaking point is approached. An important observation is that the inertial coupling can affect the energy of the system (or the amplitude of the oscillations) as well as the period of the oscillations. For instance, a comparison between

– Initial conditions on the gain oscillator: $(X_0,\ \dot{X}_0,\ X_1,\ \dot{X}_1) = (0,\ 0,\ 1,\ 0)$

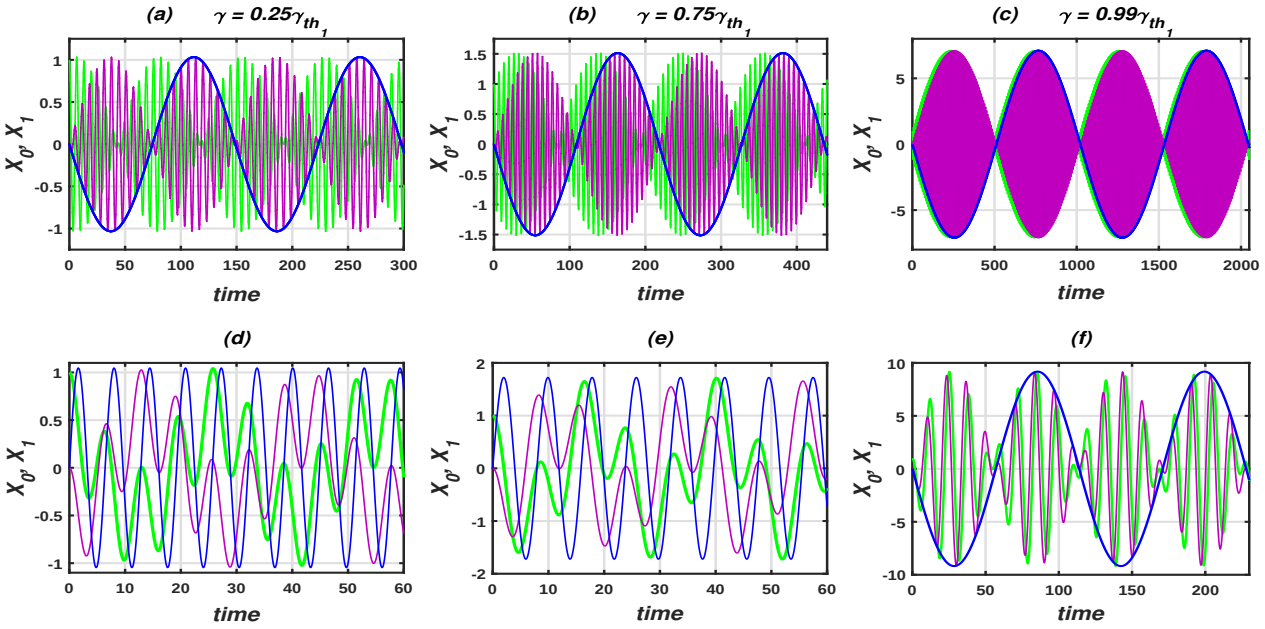

Figure 3.9: Temporal evolutions in linear limit of system (2.14). When initial conditions are fixed on the gain oscillator. On the top row $\mu = 0.1$ (panels (a), (b) and (c)) and on the bottom row $\mu = 10.0$ (panels (d), (e) and (f)). From the left column to the right column, the gain-loss parameters are respectively $\gamma = 0.25\gamma_{th_1}$, $\gamma = 0.75\gamma_{th_1}$ $\gamma = 0.99\gamma_{th_1}$.

– Initial conditions on both oscillators: $(X_0,\ \dot{X}_0,\ X_1,\ \dot{X}_1) = (\frac{\sqrt{2}}{2},\ 0,\ \frac{\sqrt{2}}{2},\ 0)$

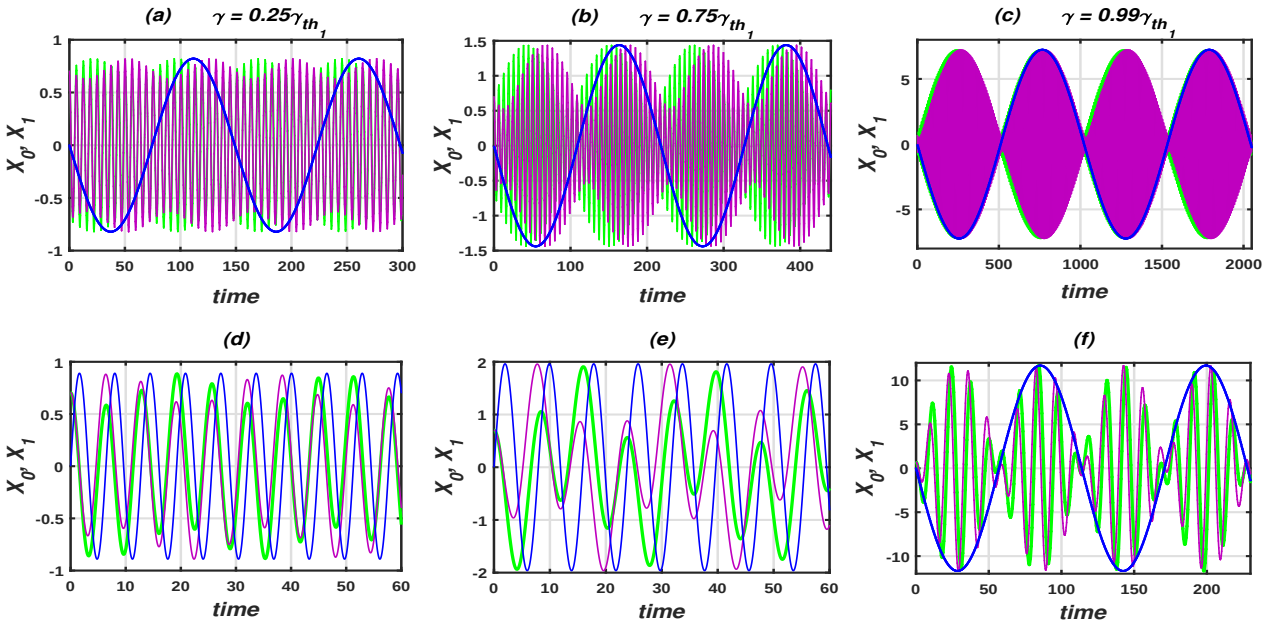

Figure 3.10: Temporal evolutions in linear limit of system (2.14). When initial conditions are fixed on both oscillators. On the top row $\mu = 0.1$ (panels (a), (b) and (c)) and on the bottom row $\mu = 10.0$ (panels (d), (e) and (f)). From the left column to the right column, the gain-loss parameters are respectively $\gamma = 0.25\gamma_{th_1}$, $\gamma = 0.75\gamma_{th_1}$ $\gamma = 0.99\gamma_{th_1}$.

Fig.3.10(f) and Fig.3.10(c) reveals that, for large values of μ, the amplitude and the period of the oscillations have significantly changed, irrespective of the configuration of the initial conditions.

In the $\mathcal{PT}$ broken phase

When the threshold is crossed or when $\gamma > \gamma_{th_1}$, the eigenvalues of the system become complex and the system enters in the $\mathcal{PT}$ broken phase. In this region, whatever the initial conditions, the oscillations blow up as the time is increasing, like an exponential growth. In other words, the system is no longer in equilibrium. So, in Figs.3.11(a) and 3.11(b) below, the Rabi oscillations are ceased and consequently, the system energy is no longer conserved.

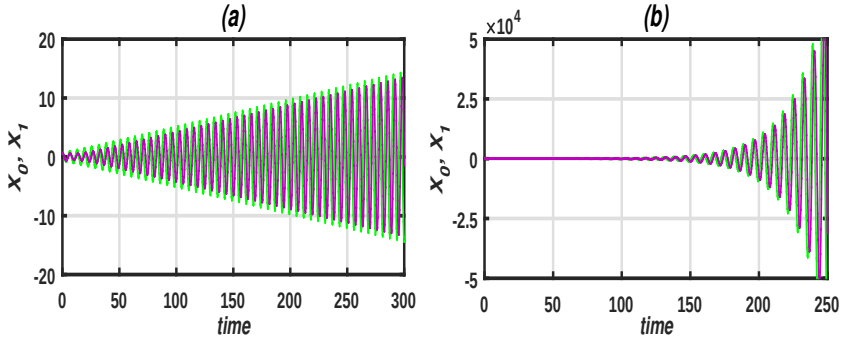

Figure 3.11: Temporal evolutions in linear limit of system (2.14) in the $\mathcal{PT}$ broken phase: in (a), $\gamma = \gamma_{th_1}$ and in (b), $\gamma = 1.05\gamma_{th_1}$.

In the context of optics and electronics, the $\mathcal{PT}$ transition phase has been observed experimentally. In optics for example, the experiment was carried out on two [39] coupled microwave cavities and also on a pair of [28, 36] coupled waveguides, one of which has the gain and the other the loss. The experiment revealed that, depending on whether the coupling is well adjusted or not, the system can either be in equilibrium and Rabi oscillations can be observed or it can no longer be in equilibrium and Rabi oscillations cease.When the $\mathcal{PT}$ phase transition was observed, there was an exponential increase in power in one waveguide and an exponential decrease in power in the other. With one difference in the studied system, when the $\mathcal{PT}$ phase transition is crossed, an exponential decay of the power in the two oscillators are observed.

3.1.2.2 Thresholdless dimer

Now, let's consider the case where both types of coupling affect the system's dynamic behaviour simultaneously. In this subsection, only the case where initial conditions are set in the gain oscillator to obtain the temporal evolution curves are considered.

In the vicinity of the thresholdless point ($\kappa \neq 0$ and $\mu \neq 0$)

Let's now consider the situation where the two coupling parameters are competing in the dynamics of the system, but around the THL point. This means that the coefficients κ and μ are all non-zero, and that the THL condition is not satisfied.

In Fig.3.12, both couplings are active at the same time. Two values of elastic coupling (one per row, 0.1 and 0.65 for the first and second rows respectively) and three values of inertial coupling (one per column) have been used to plot these curves. In all of these these curves, the gain-loss parameter is set to $0.99\gamma_{th_1}$.

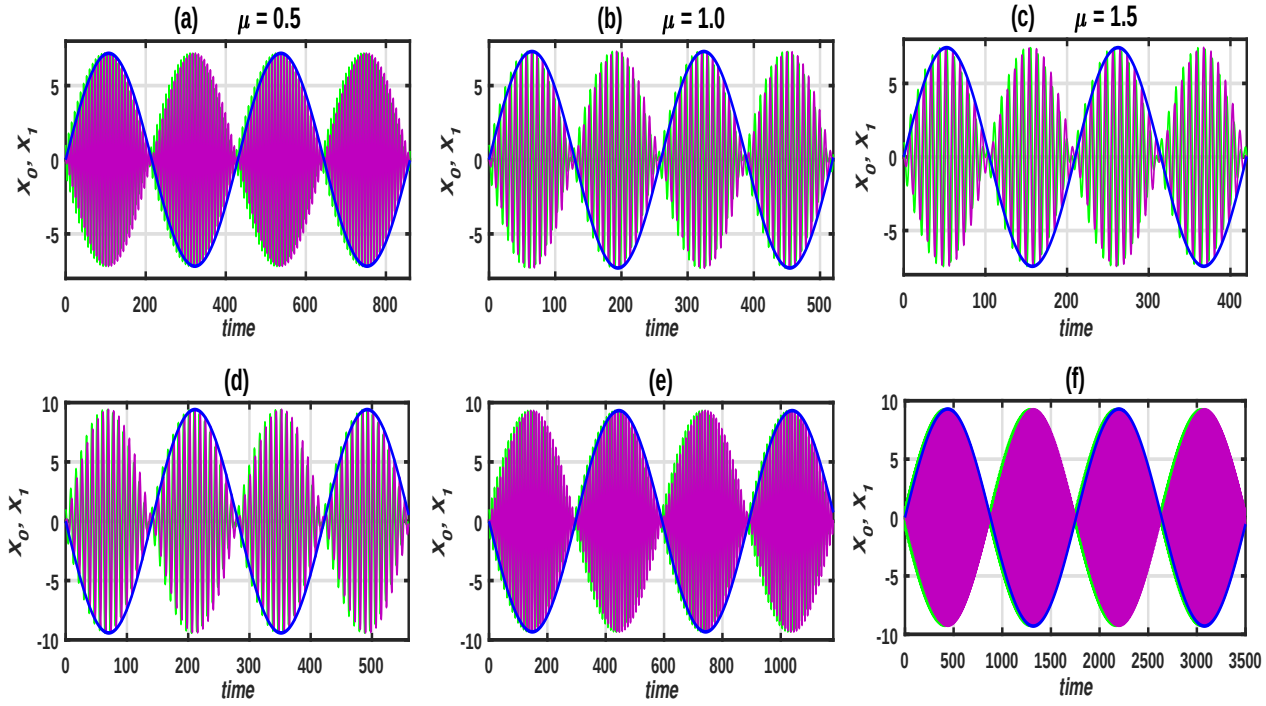

Figure 3.12: Temporal evolutions of the THL dimer in linear limit. Initial conditions are fixed on the gain oscillator. The top (panels (a), (b) and (c)) and bottom (panels (d), (e) and (f)) rows are plotted for $\kappa = 0.1$ and $\kappa = 0.65$ respectively. The inertial coupling values used for each column are mentioned in the figure.

Looking at all the figure profiles shown in Fig.3.12, it can be seen clearly that the effects of each of the couplings involved. On the one hand, with a constant elastic coupling, the oscillations have almost the same amplitude for different values of the inertial coefficient (Fig.3.12(a, b, c) or Fig.3.12(d, e, f)). On the other hand, when this time the inertial coupling is constant, it is rather the period of the oscillations that varies (Fig.3.12(a, d), Fig.3.12(b, e) or Fig.3.12(c, f)). This leads us to conclude that κ and μ affect the amplitude and frequency of the oscillations respectively.

In addition, the oscillation times, represented for two Rabi periods, are all different from each other. When $\kappa = 0.1$, the time oscillation decreases, i.e. the Rabi frequency increases. But for $\kappa = 0.65$, the opposite occurs. Knowing that, for a given value of μ there corresponds a precise value of κ_{THL}, a simple analysis shows that when $\kappa < \kappa_{THL}$, the Rabi frequency increases with μ and at the same simultaneously, the duration of the oscillations decreases (see Fig.3.12(a, b, c)). However, the opposite phenomenon is observed when $\kappa > \kappa_{THL}$ (see Fig.3.12(d, e, f)). If we evaluate κ_{THL} for values of $\mu = 0.5$, 1.0 and 1.5, we get $\kappa_{THL} = 0.33$, $\kappa_{THL} = 0.5$ and $\kappa_{THL} = 0.60$ respectively. So in the dials (a), (b) and (c) of Fig.3.12, plotted for $\kappa = 0.1$ and where $\kappa < \kappa_{THL}$, the intensity of the Rabi oscillations decreases when μ moves

away from the THL point. On the other hand, if $\kappa > \kappa_{THL}$, as is the case for dials (d), (e) and (f), the intensity of the Rabi oscillations increases when μ approaches the THL point.

At the thresholdless point ($\kappa = \kappa_{THL}$)

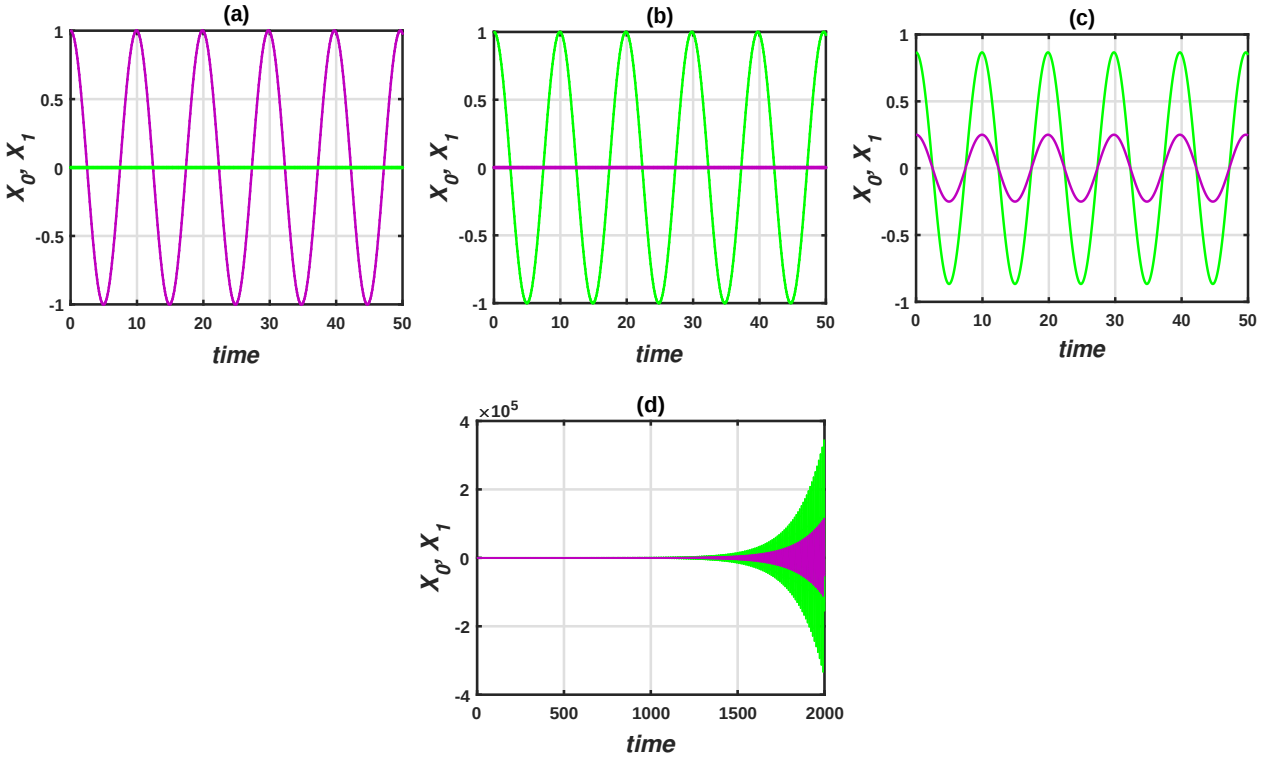

Figure 3.13: Temporal evolutions of the THL dimer in linear limit at the THL point. Initial conditions are fixed on the loss oscillator (a), on the gain oscillator (b) and on both oscillators (c) (obtained by assigning initial conditions of different magnitudes to the two oscillators). The dial in (d) reveals how the system behaves once symmetry is broken. All curves are plotted for $\mu = 1.5$ with $\kappa = \kappa_{THL} = 0.6$.

In Fig.3.13(a) initial conditions are set on the loss oscillator, in Fig.3.13(b) on the gain oscillator and in Fig.3.13(c) on both oscillators. When the initial excitation is fixed on the loss oscillator, then only this oscillates, while the gain oscillator remains fixed at 0. And, conversely, the same observation is made when the initial excitation is fixed on the gain oscillator. Morever, if the configuration of the initial excitation is such that the two oscillators are excited simultaneously, then the oscillations in the two oscillators will be observed. Recall that for a combination of non-zero coupling parameters, the threshold is zero ($\gamma = \gamma_{th_1} = 0$) at the THL point. However, upon examining the curves in Figs.3.13(a, b, c), it appears that the two oscillators are decoupled and independent of each other. In other words, the system does not seem to be sensitive to the coupling when the THL condition is fulfilled. Consequently, thresholdless phenomena are characterised by this feature. The Fig.3.13(d) is plotted for $\gamma = 0.01\gamma_{th_2}$. It simply shows that nothing significant can be observed in the broken phase, even though the THL conditions are respected. The exponential growth behaviour of the oscillations is the same as for the TH dimer.

3.2 Nonlinear dynamics of the $\mathcal{PT}$ symmetric mechanical dimer

In this section, the nonlinear dynamic of the studied $\mathcal{PT}$-symmetric mechanical dimer is investigated. The main objective is to characterise the breaking point in the nonlinear regime. This will enable to predict the state of stability. For the sake of simplicity, it will be first removed the inertial effect on the dynamics ($\mu = 0$). In other words, only the elastic coupling is considered in this study. However, a further section is devoted to studying the effect of inertial coupling on the stability and nonlinear dynamics of the dimer.

3.2.1 Some temporal evolutions: behaviours at the $\mathcal{PT}$ broken phase

Let's start by looking at the dynamics of the system for some given parameter values, when nonlinearity comes into play. But first, remember that in the absence of inertial coupling, Eq.(2.14) is reduced to the following Eq.(3.2)

$$\begin{cases} \ddot{X}_0 + 2\gamma\dot{X}_0 + X_0 - \alpha X_0^3 + \eta X_0^5 - \kappa X_1 = 0 \\ \ddot{X}_1 - 2\gamma\dot{X}_1 + X_1 - \alpha X_1^3 + \eta X_1^5 - \kappa X_0 = 0 \end{cases} \tag{3.2}$$

with $\eta = \varepsilon\alpha^2$.

This system of equations is solved numerically using the RK4 algorithm. The Figs.3.14 and 3.15 below are obtained for the cubic system case. Figs.3.14(a) and 3.14(b) show for different values of nonlinear cubic coefficient α, the shapes of catastrophic and bounded potentials respectively. The potential curves in Fig.3.14(a) obtained for $\alpha = 0.014$ (in black), $\alpha = 0.15$ (in blue) and $\alpha = 0.35$ (in red) correspond to the temporal evolutions in Figs.3.15(a), 3.15(b) and 3.15(c) respectively. Likewise, the potenial curves in Fig.3.14(b) obtained for $\alpha = -0.1$ (in black), $\alpha = -0.5$ (in blue) and $\alpha = -1.5$ (in red) correspond to the temporal evolutions in Figs.3.15(d), 3.15(e) and 3.15(f) respectively. In each case, all the dials are obtained at the breaking point. It is observed that, the behaviour at the breaking point is different depending on the nature of the potential involved. Indeed, in the presence of a catastrophic potential, it is observed that the oscillations cease after a transient time. An another observation is that, the oscillations can only occur within the width of the corresponding potential well before leaving it (see the potential curves in Fig.3.14(a)). However, when the potential involved is bounded, the oscillations persist though in this case, the gain oscillator has increased to a limiting amplitude, while the loss oscillator practically dies down to a limiting amplitude around the trivial fixed point.

On the other hand, when each row is carefully observed on the Fig.3.15, it is obvious that the nonlinearity can shift the threshold. Indeed, for the catastrophic potential for example (top row of Fig.3.15), the breaking point is obtained at $\gamma_{th_n} = 0.98\gamma_{th_1}$ for $\alpha = 0.014$ in (a), at $\gamma_{th_n} = 0.49\gamma_{th_1}$ for $\alpha = 0.15$ in (b) and at $\gamma_{th_n} = 0.29\gamma_{th_1}$ for $\alpha = 0.35$ in (c). In addition, the system vibrates with a smaller amplitude the greater the nonlinearity. This can be explained

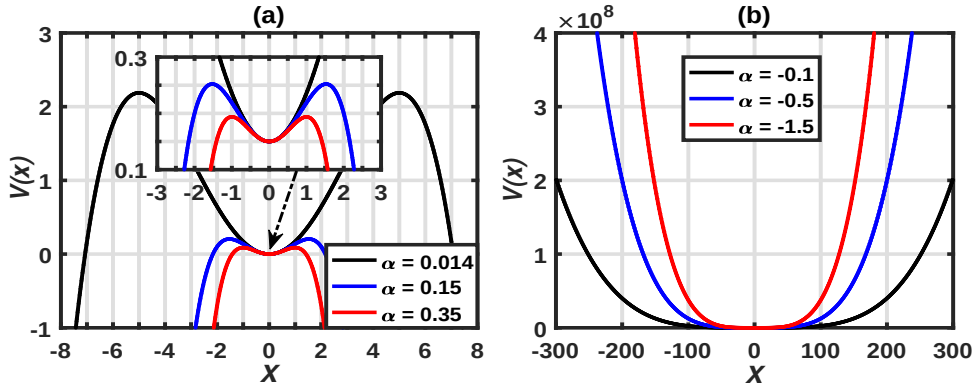

Figure 3.14: The catastrophic (a) and bounded (b) potentials for the cubic system. The catastrophic one is obtained for $\alpha = 0.014$ (in black), $\alpha = 0.15$ (in blue) and $\alpha = 0.35$ (in red) while the bounded potential is plotted for $\alpha = -0.1$ (in black), $\alpha = -0.5$ (in blue) and $\alpha = -1.5$ (in red).

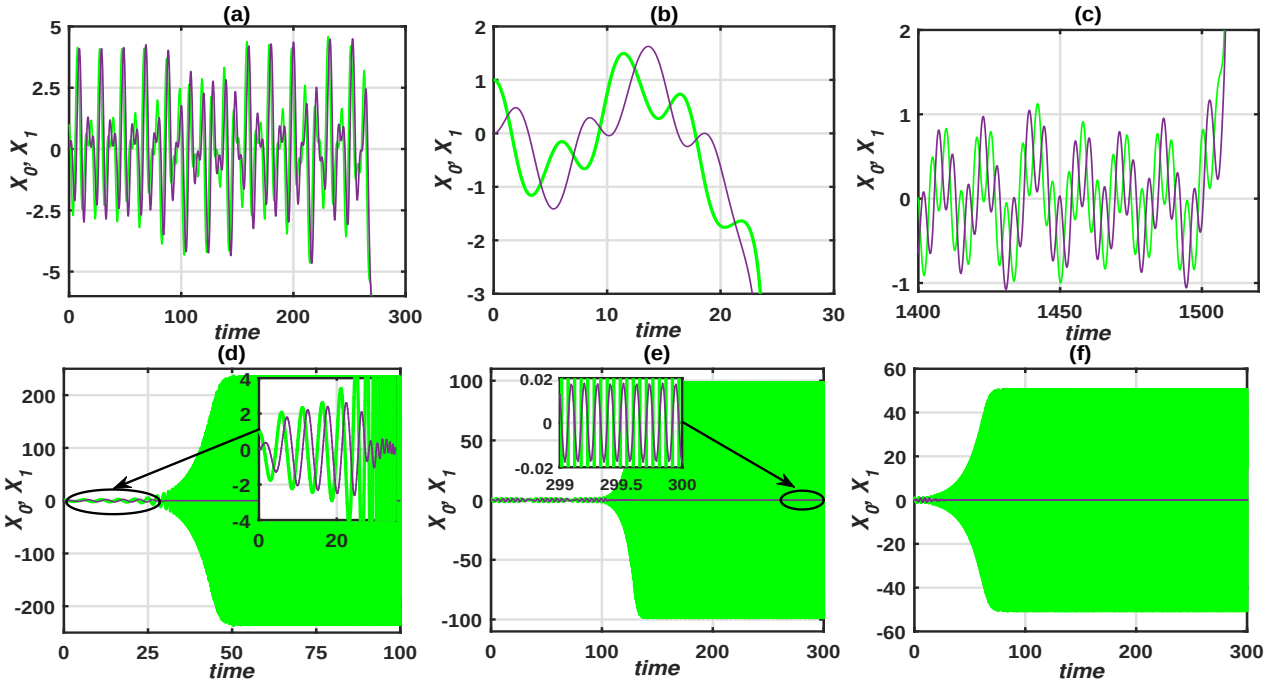

Figure 3.15: Dynamical evolutions of the nonlinear cubic systems around the trivial fixed point. Green and purple colours represent the responses of the gain and loss oscillators respectively. In the top row: (a) $\gamma_{th_n} = 0.98\gamma_{th_1}$ for $\alpha = 0.014$, (b) $\gamma_{th_n} = 0.49\gamma_{th_1}$ for $\alpha = 0.15$ and (c) $\gamma_{th_n} = 0.29\gamma_{th_1}$ for $\alpha = 0.35$. In the bottom row: (d) $\gamma_{th_n} = 0.77\gamma_{th_1}$ for $\alpha = -0.1$, (e) $\gamma_{th_n} = 0.55\gamma_{th_1}$ for $\alpha = -0.5$ and (f) $\gamma_{th_n} = 0.29\gamma_{th_1}$ for $\alpha = -1.5$. For each panel, $\kappa = 0.65$.

simply by the fact that the greater the nonlinearity, the smaller the width of the corresponding potential well and so, the system can't extend beyond the width of the well. If this is the case, a change in the behaviour will be noticed (either an abrupt increasing of amplitude or a energy transfer from one oscillator to another)

As in the case of the cubic system, the Figs.3.16 and 3.18 showing the potential curves corresponding to the temporal evolutions of the Figs.3.17 and 3.19 respectively, have been obtained for the quintic system case. For the Figs.3.16 and 3.17, $\alpha = 0.15$ and for the Figs.3.18 and 3.19, $\alpha = -0.5$. In each case, the curves are plotted at the breaking point and it is clear

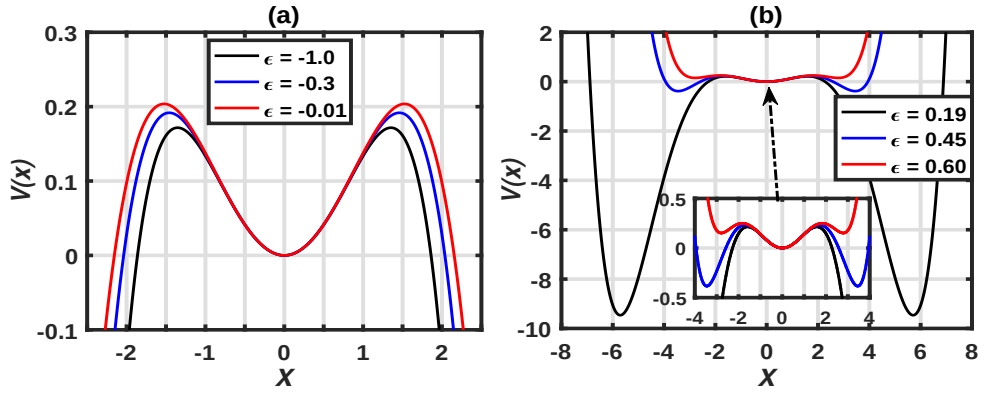

Figure 3.16: The catastrophic (a) and bounded (b) potentials for the quintic system when $\alpha = 0.15$. The catastrophic one is obtained for $\varepsilon = -0.19$ (in black), $\varepsilon = -0.3$ (in blue) and $\varepsilon = -0.01$ (in red) while the bounded potential is plotted for $\varepsilon = 0.19$ (in black), $\varepsilon = 0.45$ (in blue) and $\varepsilon = 0.60$ (in red).

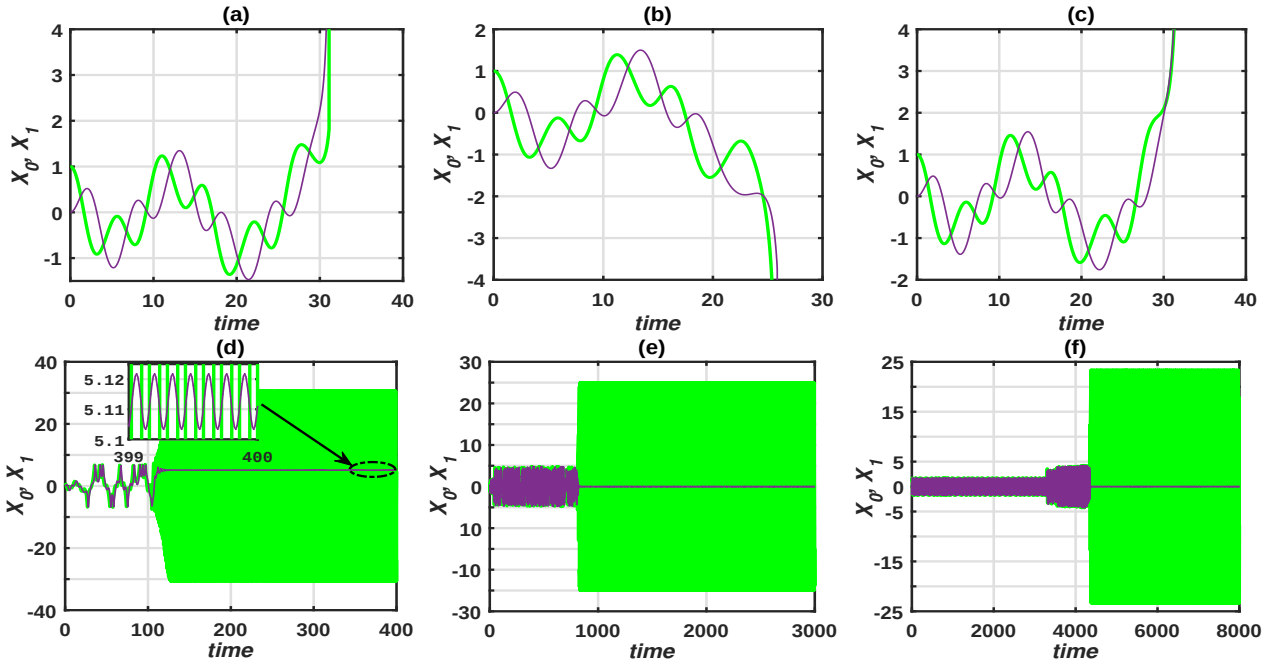

Figure 3.17: Dynamical evolutions of the nonlinear quintic systems around the trivial fixed point when $\alpha = 0.15$. Green and purple colours represent the responses of the gain and loss oscillators respectively. In the top row: (a) $\gamma_{th_n} = 0.38\gamma_{th_1}$ for $\varepsilon = -1.0$, (b) $\gamma_{th_n} = 0.45\gamma_{th_1}$ for $\varepsilon = -0.3$ and (c) $\gamma_{th_n} = 0.48\gamma_{th_1}$ for $\varepsilon = -0.01$. In the bottom row: (d) $\gamma_{th_n} = 0.51\gamma_{th_1}$ for $\varepsilon = 0.19$, (e) $\gamma_{th_n} = 0.55\gamma_{th_1}$ for $\varepsilon = 0.45$ and (f) $\gamma_{th_n} = 0.58\gamma_{th_1}$ for $\varepsilon = 0.60$. For each panel, $\kappa = 0.65$.

that the behaviour remains unchanged from that of the cubic system. However, depending on the nature of the potential of cubic system, two behaviours of the threshold are distinguished. From the catastrophic cubic system, the adding of the quintic term extends the $\mathcal{PT}$ exact phase (see for example Figs.3.17(d, e, f) with $\gamma_{th_n} = 0.51\gamma_{th_1}$ for $\varepsilon = 0.19$, $\gamma_{th_n} = 0.55\gamma_{th_1}$ for $\varepsilon = 0.45$ and $\gamma_{th_n} = 0.58\gamma_{th_1}$ for $\varepsilon = 0.60$ respectively). In the opposite, from the bounded cubic system, the adding the quintic term reduces the $\mathcal{PT}$ exact phase (see for example Figs.3.19(d, e, f) with $\gamma_{th_n} = 0.54\gamma_{th_1}$ for $\varepsilon = 0.1$, $\gamma_{th_n} = 0.49\gamma_{th_1}$ for $\varepsilon = 0.5$ and $\gamma_{th_n} = 0.45\gamma_{th_1}$ for $\varepsilon = 0.9$

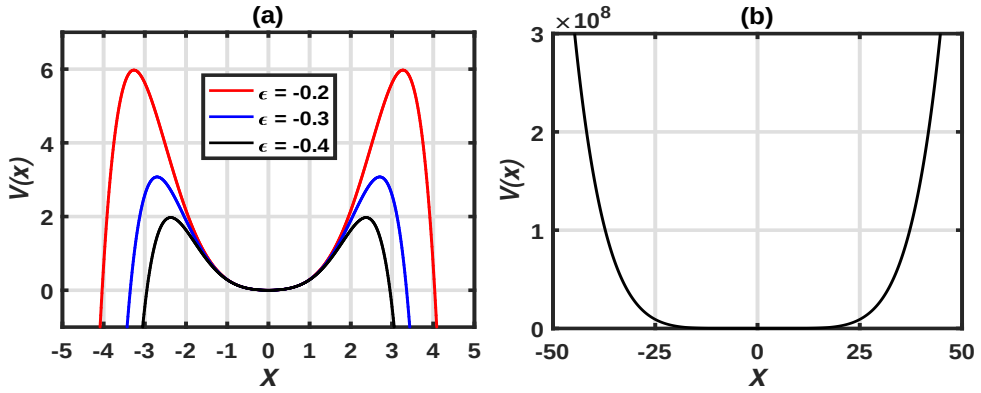

Figure 3.18: The catastrophic (a) and bounded (b) potentials for the quintic system when $\alpha = -0.5$. The catastrophic one is obtained for $\varepsilon = -0.4$ (in black), $\varepsilon = -0.3$ (in blue) and $\varepsilon = -0.2$ (in red) while the bounded potential is showned in the dial (c) for any value of ε.

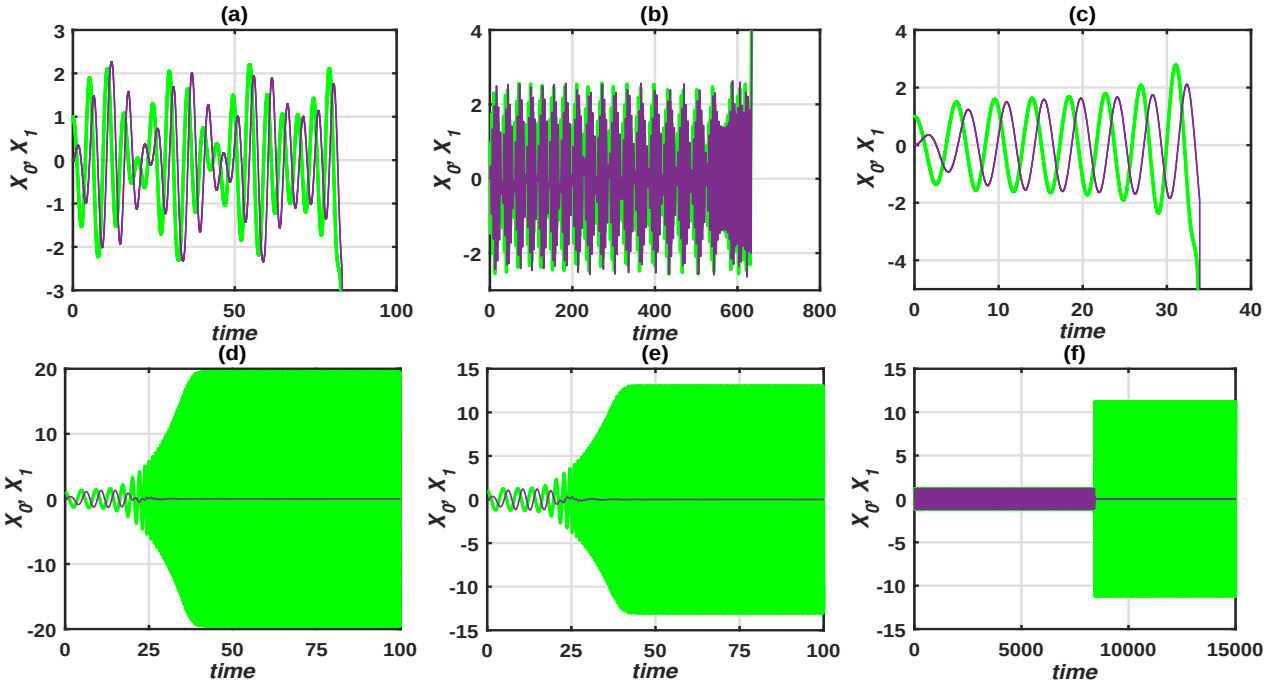

Figure 3.19: Dynamical evolutions of the nonlinear quintic systems around the trivial fixed point when $\alpha = -0.5$. Green and purple colours represent the responses of the gain and loss oscillators respectively. In the top row: (a) $\gamma_{th_n} = 0.69\gamma_{th_1}$ for $\varepsilon = -0.4$, (b) $\gamma_{th_n} = 0.66\gamma_{th_1}$ for $\varepsilon = -0.3$ and (c) $\gamma_{th_n} = 0.59\gamma_{th_1}$ for $\varepsilon = -0.2$. In the bottom row: (d) $\gamma_{th_n} = 0.54\gamma_{th_1}$ for $\varepsilon = 0.1$, (e) $\gamma_{th_n} = 0.49\gamma_{th_1}$ for $\varepsilon = 0.5$ and (f) $\gamma_{th_n} = 0.45\gamma_{th_1}$ for $\varepsilon = 0.9$. For each panel, $\kappa = 0.65$..

respectively).

3.2.2 Nonlinear dynamics investigations

3.2.2.1 Fixed points and their stability

The Fixed points and their stability can be investigated by transforming the system (2.14) into a system of differential equations of order 1 given by :

$$\begin{cases} \dot{X}_0 = Y_0 \\ (1+\mu)\,\dot{Y}_0 = \mu\dot{Y}_1 - 2\gamma Y_0 - X_0 + \alpha X_0^3 - \varepsilon\alpha^2 X_0^5 + \kappa X_1 \\ \dot{X}_1 = Y_1 \\ (1+\mu)\,\dot{Y}_1 = \mu\dot{Y}_0 + 2\gamma Y_1 - X_1 + \alpha X_1^3 - \varepsilon\alpha^2 X_1^5 + \kappa X_0 \end{cases} \tag{3.3}$$

Equilibrium points are found by setting all the first derivatives of the system to zero. Recall that the coefficients κ and γ are positive and, $\kappa < 1$. Two cases are distinguished:

- **Cubic system: (ε=0)**

So, from Eqs.(2.42), when $\alpha > 0$, three fixed points are found: FP0 (0, 0, 0, 0), FP1 ($\pm a_1$, 0, $\pm a_1$, 0), $a_1 = \sqrt{(1-\kappa)/\alpha}$ and FP2 ($\pm a_2$, 0, $\mp a_2$, 0), with $a_2 = \sqrt{(1+\kappa)/\alpha}$. For $\alpha < 0$, there is a single fixed point PF0. FP0 is the trivial fixed point; FP1 represents the symmetric branch of the fixed points, whereas FP2 stands for anti-symmetric branch solution.

- **Quintic system: ($\varepsilon \neq 0$)**

When $\varepsilon \neq 0$, the system admits one, three or five fixed points, depending on the signs of α and ε.

– For $\alpha > 0$, we distinguish four cases:

Case 1: $0 < \varepsilon < \frac{1}{4(1-\kappa)}$, there are five symmetric fixed points FP0 and FP3 ($\pm q_1^{(\pm)}, 0$, $\pm q_1^{(\pm)}, 0$) with $q_1^{(\pm)} = \sqrt{\frac{\alpha \pm \sqrt{\alpha^2 - 4\varepsilon\alpha^2(1-\kappa)}}{2\varepsilon\alpha^2}}$.

Case 2: $0 < \varepsilon < \frac{1}{4(1+\kappa)}$, there are also five anti-symmtric fixed points FP0 and FP4 ($\pm q_2^{(\pm)}, 0,\ \mp q_2^{(\pm)}, 0$) with $q_2^{(\pm)} = \sqrt{\frac{\alpha \pm \sqrt{\alpha^2 - 4\varepsilon\alpha^2(1+\kappa)}}{2\varepsilon\alpha^2}}$

Case 3: $\varepsilon > \frac{1}{4(1-\kappa)}$ or $\varepsilon > \frac{1}{4(1+\kappa)}$, there is only the trivial fixed point FP0.

Case 4: $\varepsilon < 0$, there are three fixed points FP0 and ($\pm q_1^{(-)}$, 0, $\pm q_1^{(-)}$, 0) or ($\pm q_2^{(-)}$, 0, $\pm q_2^{(-)}$, 0).

– For $\alpha < 0$, there are two cases.

Case 1: $\varepsilon > 0$, there is only the trivial fixed point FP0.

Case 2: $\varepsilon < 0$, there are three fixed points FP0 and ($\pm q_1^{(-)}$, 0, $\pm q_1^{(-)}$,0) or ($\pm q_2^{(-)}$, 0, $\pm q_2^{(-)}$, 0).

Now, the local stability of these fixed points is investigated. From Eq.(3.3), the Jacobian matrix is obtained below

$$J = \begin{pmatrix} 0 & 1 & 0 & 0 \\ f_1(x_i) & -\frac{2\gamma(1+\mu)}{1+2\mu} & f_2(x_i) & \frac{2\gamma\mu}{1+2\mu} \\ 0 & 0 & 1 & 0 \\ f_2(x_i) & -\frac{2\gamma\mu}{1+2\mu} & f_1(x_i) & \frac{2\gamma(1+\mu)}{1+2\mu} \end{pmatrix}. \tag{3.4}$$

with

$$f_1(x_i) = \frac{1}{1+2\mu}\left(-1-\mu(1-\kappa)+3\alpha(1+\mu)x_i^2-5\eta(1+\mu)x_i^4\right)$$
$$f_2(x_i) = \frac{1}{1+2\mu}\left(\kappa-\mu(1-\kappa)+3\alpha\mu x_i^2-5\eta\mu x_i^4\right) \tag{3.5}$$

where x_i is the considered fixed point.

Assuming the normalised gain/loss ratio γ/γ_{th} as control parameter, the study of the stability of each fixed points can be done by finding the eigenvalues of the Jacobian matrix J. Lyapunov stability states that, a fixed point is stable if all the eigenvalues of J are negative real parts. But if only one eigenvalue is positive real part, the fixed point is unstable. Moreover, if a fixed point admits a pair of purely imaginary conjugate eigenvalues, then it is a Hopf bifurcation point, which leads to a quasi-periodic response. According to the nonlinear coefficients, the fixed points $x_i = \left(a_1,\, a_2,\, q_1^{(-)},\, q_2^{(-)}\right)$ give pure imaginary values. Consequently, they do not lead to a bifurcation or transition point. So, only the stability of the three fixed points FP0, FP3 which is defined by $q_1^{(+)}$ and FP4 by $q_2^{(+)}$ will be analysed.

The Fig.3.20 shows the real (a) and imaginary (b) parts of eigenvalues of the linearized system in Eq.(3.3) with respect to the ratio γ/γ_{th_1}. γ_{th_1} being the first transition point obtained in the linear regime. At the vicinity of FP0 (green colour), the plot is made for any values of ε and α. However, around FP3 (yellow curve), the plot is obtained with $\alpha = 0.01$ and $\varepsilon = 0.71$, whereas for FP4 (red curve) it is obtained for $\alpha = 0.01$ and $\varepsilon = 0.14$.

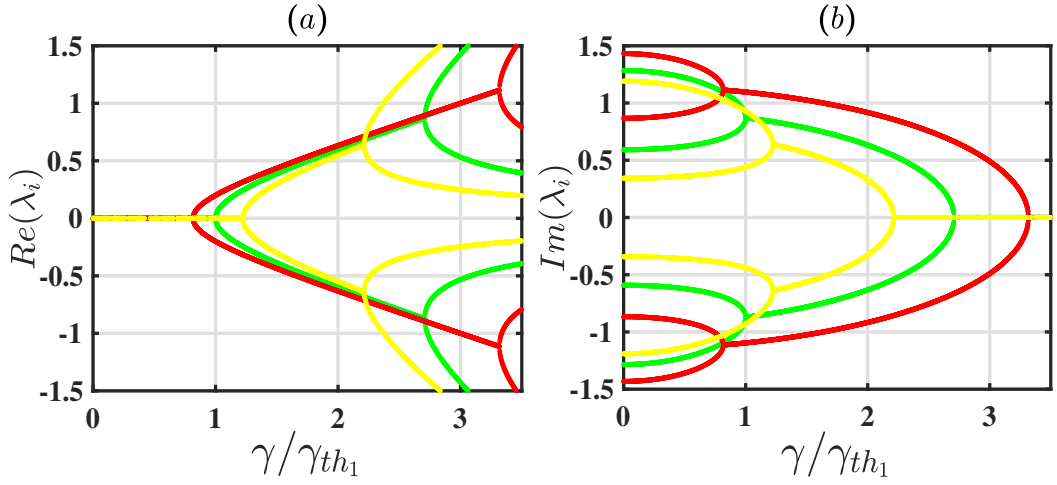

Figure 3.20: Real (a) and imaginary (b) parts of the eigenvalues around trivial fixed points. Green curve is for the trivial fixed point. Yellow curve is for the symmetric fixed points $q_1^{(+)}$ obtained with $\alpha = 0.01$ and $\varepsilon = 0.71$, and red curve is for anti-symmetric fixed points $q_2^{(+)}$ obtained with $\alpha = 0.01$ and $\varepsilon = 0.14$. $\kappa = 0.65$.

From the figure, it is noticed that FP0, FP3 and FP4 represent the Hopf bifurcation points. All the considered fixed points display two breaking transition points. For FP3 the first breaking point is above 1 ($\gamma/\gamma_{th_1} > 1$) and, for FP4 the first transition point is before 1 ($\gamma/\gamma_{th_1} < 1$) for the chosen parameters. Remarkably, for the FP0 fixed point, the first transition coincides with the first breaking point in the linear regime, that is ($\gamma/\gamma_{th_1} = 1$), whatever α and ε are. One can easily see from the green curve that whatever the kind of nonlinearity (cubic or quintic

systems), our system exhibits qualitatively the same stability around the trivial fixed point, since the phase transition occurs at $\gamma/\gamma_{th_1} = 1$. This last observation suggests that around the trivial fixed point, the system is indifferent to the effects of nonlinearity and consequently presents an oscillatory regime identical to that obtained in the linear regime. The trivial fixed point serves as reference point. The following shows that the breaking point around the fixed point doesn't only depend on the nonlinearity parameters, but also on the initial conditions.

3.2.2.2 Numerical nonlinear threshold analysis

To show the influence of the initial conditions on the breaking point, numerical investigations on the normalised gain/loss parameter have been done. For this purpose, the dichotomy and fourth-order Runge Kutta methods have been combined to obtain the evolution of the normalised gain/loss (γ/γ_{th_1}) as a function of the nonlinearity parameters of the system. Figs.3.21(a, b, c, d) illustrate this evolution in the cubic soft ($\alpha > 0$), cubic hard ($\alpha < 0$), quintic hard ($\varepsilon > 0$) and quintic soft ($\varepsilon < 0$)cases, respectively. In the cubic case (Fig.3.21(a, b)), the initial conditions ($X_k(0)$=X_{0k}, $Y_k(0)$=Y_{0k} with $k = 1, 2$) are imposed on the gain oscillator: $X_{01} = 0.0$, $Y_{01} = 0.0$, $X_{02} = 1.0$, $Y_{02} = 0.0$ (green colour), on the loss oscillator: $X_{01} = 1.0$, $Y_{01} = 0.0$, $X_{02} = 0.0$, $Y_{02} = 0.0$ (red colour) and on both oscillators: $X_{01} = \frac{\sqrt{2}}{2}$, $Y_{01} = 0.0$, $X_{02} = \frac{\sqrt{2}}{2}$, $Y_{02} = 0.0$ (blue colour).

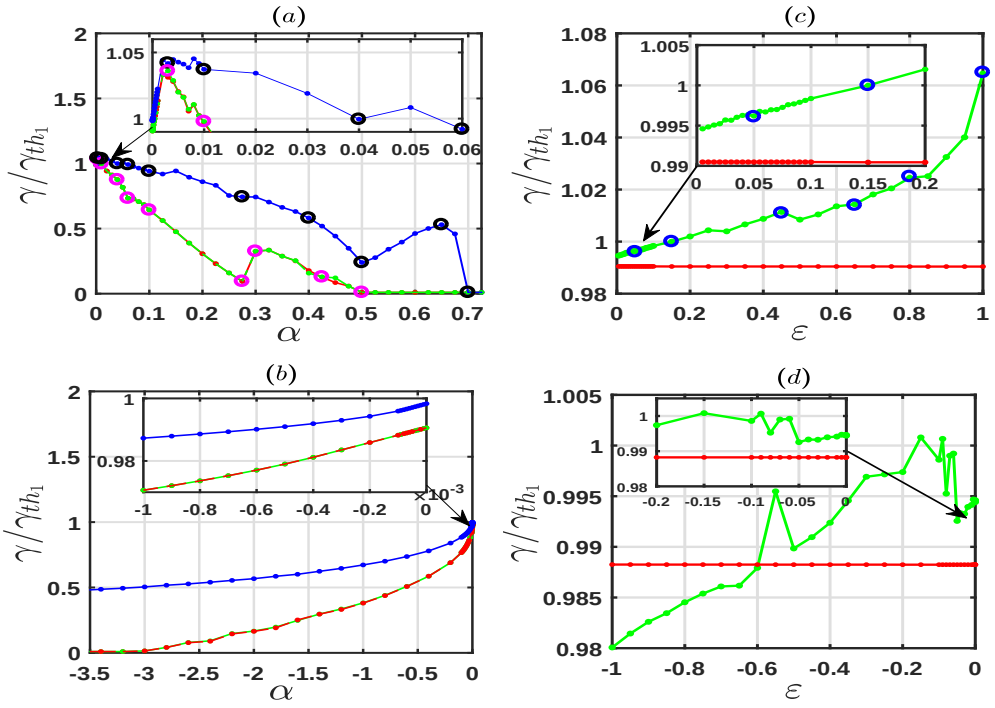

Figure 3.21: Effects of cubic and quintic parameters on the stability of the system. For all curves, κ is equal to 0.65. (a) and (b) curves are for soft and hard cubic systems, when $\varepsilon = 0$. (c) and (d) curves are for the quintic system, obtained with $\alpha = -10^{-4}$ in red colour and $\alpha = 0.01$ in green colour.

However, in the quintic case (Fig.3.21(c, d)), the initial conditions have been imposed on the gain oscillator for $\alpha = 0.01 > 0$ (green colour) and for $\alpha = -0.0001 < 0$ (red colour). But, in the cubic cases (Fig.3.21(a, b)), the oscillatory domain decreases in general when absolute

value of nonlinear cubic parameter is increased which indicates that, the threshold in nonlinear regime is lower as compared to the critical value found in linear regime (γ_{th_1}). On the other hand, in the quintic case, the dynamics of normalised gain-loss parameter as a function of ε in the both soft and hard cases are presented. The curve Fig.3.21(c) (quintic hard case) shows that, for the considered range of ε, this transition increases with the nonlinearity when α is set to 0.01. But for $\alpha = -0.0001$, one can see that quintic nonlinearity re-establishes the transition point of the linear regime. This can be also seen in Fig.3.21(d) for quintic soft case. The only difference between quintic soft and quintic hard is located on the fact that, quintic soft does not boost the oscillatory regime of the system like quintic hard. An example it that, the green curves in Figs.3.21(c), corresponding to the quintic hard, has exceeded the linear threshold value ($\gamma/\gamma_{th_1} = 1$), unlike that one in 3.21(d), which corresponds to the quintic soft case.

The lower part of each curve corresponds to the $\mathcal{PT}$ exact phase where the energy and symmetric properties of the system remain conserved. The upper part corresponds to the broken phase in which the oscillations will not persist (system with soft nonlinearity) in the time and where asymmetric behaviours can be observed (with hard nonlinearity). In opposition to what have seen in the previous section, it is important to highlight the effect of the initial conditions of the system. In fact, the curves make it possible to understand that perturbing the system around the trivial fixed point FP0 would correspond to taking a precise value of the cubic stiffness parameter α. For example, in Fig.3.21(a), when excitation is fixed on the gain or on the loss oscillators (green and red curve), the only value of α for which the system would be perturbed around the trivial fixed point is equal to 0.01, where the ratio γ/γ_{th_1} is closest to 1 in default. If the excitation is fixed on both oscillators simultaneously (blue curve), the value of α to obtain the linear threshold is 0.06. In other words, if for these initial conditions the value of α is taken differently from the previous ones, then, the system is perturbed around a point different from FP0. Interestingly, the nonlinearity can boost a system around the trivial fixed point by expanding its oscillatory regime as it is observed in the inset plots (Fig.3.21(a,c)), where $\gamma/\gamma_{th_1} > 1$.

To consolidate the previous results, let's see again some temporal evolutions of the system of Figs.3.15 and 3.17. For different values of the nonlinearity: $\alpha = 0.01$ (Figs.3.15(a,d)), $\alpha = -10^{-4}$ (Figs.3.15(b,e)) and $\alpha = 0.01$, $\varepsilon = 0.09$ (Fig.3.15(c) and Fig.3.17(a)). The green colour represents the response of the gain oscillator while the purple colour is for the loss oscillator. In the top row, the behaviour is illustrated for the normalised gain/loss ratio $\gamma/\gamma_{th_1} = 0.99 < 1$ ($\mathcal{PT}$ exact phase), whereas for the bottom row $\gamma/\gamma_{th_1} = 1$ (PT broken phase). As we can see, in the $\mathcal{PT}$ exact phase, the system exhibits Rabi oscillations (Fig.3.15(a,b,c)).

However, in the $\mathcal{PT}$ broken region, the oscillations may either disappear (for soft nonlinear system) after a transient time (Fig.3.15(d) for example) or persist (for hard nonlinear system) during a transient time. In this latter case, the gain oscillator has increased to a limiting amplitude. The loss oscillator practically dies down to a limiting amplitude around the trivial fixed point (Fig.3.15(e)) or around an another equilibrium point (Fig.3.17(a)). This last result indicates that in the $\mathcal{PT}$ broken phase, the system is perturbed around the equilibrium which

is not necessarily the trivial fixed point for both oscillators. The nonlinearity has transformed the Rabi oscillations, a formal characteristic of the exact phase, into a robust stable periodic oscillations with constant amplitude.

3.2.2.3 Analytical treatment

Using the Newton-Raphson algorithm to numerically solve Eq.(2.66), the amplitude of oscillations of the system, when certain parameters are varying, have been determined. The response curves of the amplitudes are shown in Fig.3.22. The cubic soft system ($\alpha > 0$) is represented on the top row, while the cubic hard system ($\alpha < 0$) is shown on the bottom row. Thus, the Figs.3.22(a_1,a_2) display the frequency-response shapes for three given values of γ and two fixed values of α. In addition, in Figs.3.22(b_1,b_2), as well as in Figs.3.22(a_1,a_2), the amplitude depicts the curves function of the gain/loss parameters for the same three given values of α and two fixed values of ω. Moreover, in Figs.3.22(c_1,c_2), the nonlinear-response curves are presented for three fixed values of γ and two fixed values of ω.

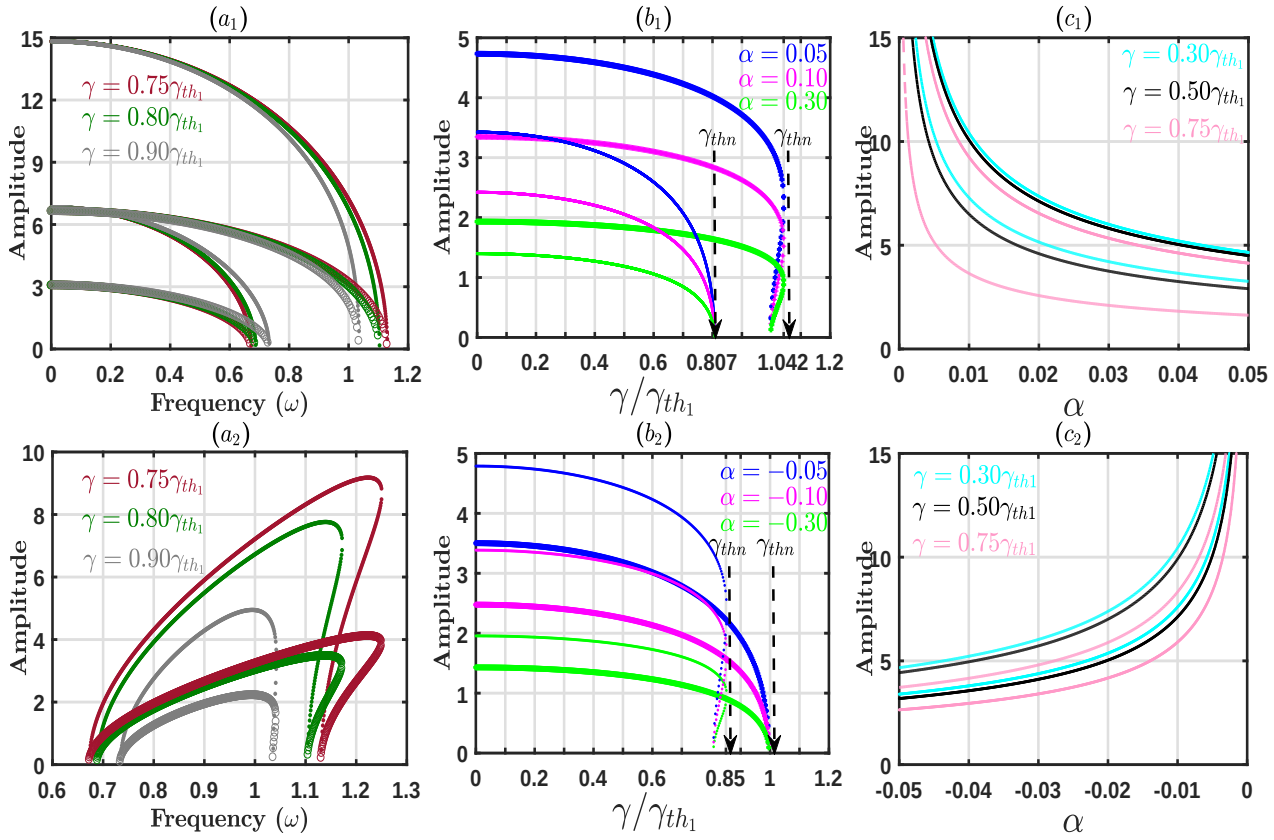

Figure 3.22: Analytical response curves for the cubic system. The cubic soft and hard systems are represented respectively in the top and bottom row. In (a_1) and (a_2), the *dot* is for $|\alpha| = 0.01$ and the *circle* is for $|\alpha| = 0.05$. In (b_1) and (b_2), the *star* is $\omega = 0.9$ when the *dot* is $\omega = 1.1$. Finally, (c_1) and (c_2) are obtained with $\omega = 0.9$ in *star* and $\omega = 1.1$ in *dot*.

In Figs.3.22(a_1,a_2) that, for a chosen value of the nonlinearity, the amplitude decreases when γ increases. The figure presents three different regions: one region with two amplitudes, another with one amplitude and the last region without amplitude which delimits the zone where the

response of the system to an initial excitation does not exists. From a qualitative point of view, these curve responses can describe the hysteresis phenomenon. Indeed, for each type of system, we have two branches of solutions. The first branch is linked to the lowest value of the two eigenmodes of the linear system (values at small amplitudes) and the second branch is related to the uppest value.

In the cubic soft system, i.e. in Fig.3.22(a_1), if the initial conditions force the system to evolve on the first branch, the amplitude jump phenomenon will be observed when the frequency reaches the first eigenmode of the linear system. But, if the conditions constrain the system to move on the second branch, there will be no jump phenomenon even when ω decreases. In the cubic hard system (see Fig.3.22(a_2)), as ω increases, the amplitude will evolve along the first branch (highest branch) until it reaches a certain value corresponding to a critical frequency beyond which there are no longer solutions. However, when ω decreases, it will be possible, depending on the initial conditions of the system, that the amplitude follows the first branch or the second branch. In the case where the amplitude follows the second branch, a jump phenomenon will be observed when ω will attain the largest value of the eigenmodes of the linear system. In particular, it can be seen that soft and hard systems have opposite behaviours when ω varies. Indeed, in the soft case, when ω increases the amplitude decreases and when ω decreases, the amplitude increases. But in the hard case, the opposite takes place.

Figs.3.22(b_1,b_2) represent the behaviour of the amplitude of oscillations according to the normalised parameter γ/γ_{th_1}. Although for some parameter values one can observe regions with or without amplitudes, these curves simply show where the threshold is located. As it is illustrated, when the normalised parameter γ/γ_{th_1} increases, the amplitude decreases until an extreme value of γ/γ_{th_1} from which there is no amplitude. Thus, this extreme value of γ/γ_{th_1} (as represented on panels (b_1) and (b_2) by the dashed arrows) designates the threshold of the system in the nonlinear regime, which we will define as the nonlinear breaking point. The reason for referring to this extreme value as the nonlinear breaking point is simply that it depends on the nonlinearity coefficients. Indeed, the curve obtained numerically (Fig.3.21), shows that there is a correlation between the normalised gain-loss parameter and the nonlinear coefficient. For instance, when $\omega = 0.9$ (star curve), there are no longer solutions beyond the extreme value of the normalised gain-loss parameter (at $\gamma/\gamma_{th_1} = 1.042$ in Fig.3.22(b_1)) or (at $\gamma/\gamma_{th_1} = 1.0$ in Fig.3.22(b_2)). These extreme values correspond precisely to the threshold values obtained numerically for $\alpha = 0.003$ when the system is initially excited in equal proportions on both oscillators. On the other hand, we can see that the increasing of the nonlinearity reduces the amplitude without moving the nonlinear breaking point; this seems intriguing in the light of the numerical curves obtained in Fig.3.21 which prove the opposite. However, regardless of α, there is a single value of the frequency that corresponds to the breaking point. This means analytically that the nonlinear breaking point depends explicitly on the frequency. Thus, as we have predicted, from Figs.3.22(c_1,c_2), we can see that the amplitude of oscillations decreases as the absolute value of the nonlinearity is increasing and the normalised gain/loss parameter decreases.

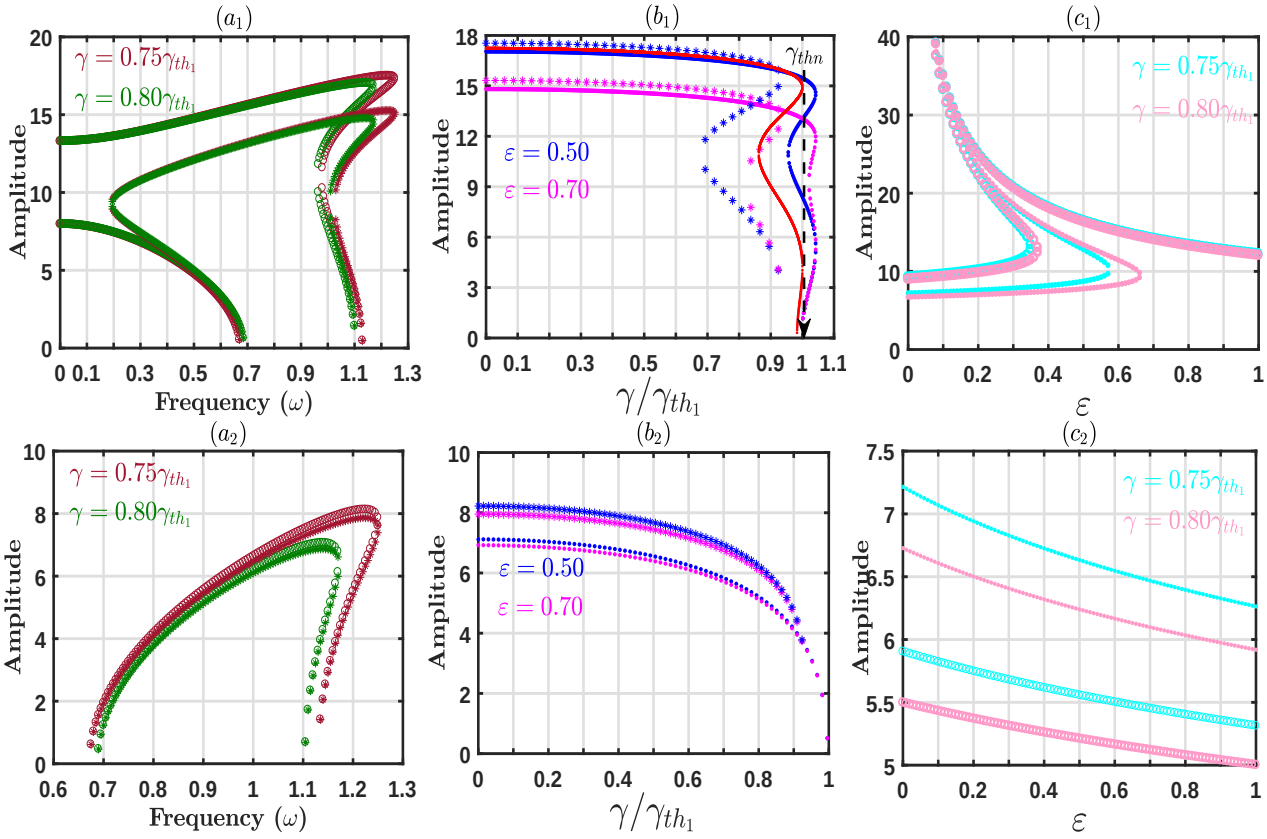

Figure 3.23: Analytical response curves for the quintic hard system ($\varepsilon > 0$). In the top row, the nonlinearity cubic parameter is $\alpha = 0.01$ while, in the bottom row, it is $\alpha = -0.01$. (a_1) and (a_2) present the frequency-responses plotted for $\varepsilon = 0.5$ in *circle* and for $\varepsilon = 0.7$ in *star*. (b_1) and (b_2) show the normalised gain/loss parameter response obtained with $\omega = 0.9$ in *dot* and $\omega = 1.0$ in *star*. (c_1) and (c_2) displayed the quintic coefficient responses plotted with $\omega = 0.9$ in *circle* and $\omega = 1.0$ in *dot*.

With the quintic system ($\varepsilon \neq 0$), the results obtained seem identical to those found in the cubic system. The Fig.3.23 and Fig.3.24 also show the behaviour of the oscillations amplitude under the influence of the system's parameters (ω, γ/γ_{th_1} and ε), at α fixed. In Fig.3.23, the curves are plotted with $+\varepsilon$ while in Fig.3.24, they are obtained with $-\varepsilon$. In each panels of the Fig.3.23 and Fig.3.24, the top row is realised with $\alpha = 0.01$ and the bottom row with $\alpha = -0.01$. In Figs.3.23 and 3.24, the panels (a_1) and (a_2) show the frequency response, (b_1) and (b_2) exhibit the normalised parameter amplitude characteristic and (c_1) and (c_2) display the effect of the quintic term on the amplitude. The panels Figs.3.23(a_2,b_2) and the panels Figs.3.24(a_2,b_2) are very similar to ones of Figs.3.22(a_2,b_2), the Figs.3.22(a_1,b_1), respectively, of the cubic case. Indeed, this result is due to the same nature of the nonlinear cubic and quintic parameters (i.e. $\alpha_{soft}/\varepsilon_{soft}$ or $\alpha_{hard}/\varepsilon_{hard}$). However, when they are different in nature, the amplitude-response curves are slightly different as is the case the Figs.3.23(a_1,b_1), and in Figs.3.24(a_1,b_1). This difference is reflected by the existence of a third branch of solutions in a certain region. In Figs.3.23(c_1,c_2) and 3.24(c_1,c_2), we provide the amplitude-response curves as a function of the quintic nonlinearity parameter ε for two fixed values of γ and ω. As expected, the curves show that the amplitude of the oscillations decreases with the nonlinearity. In particular, in

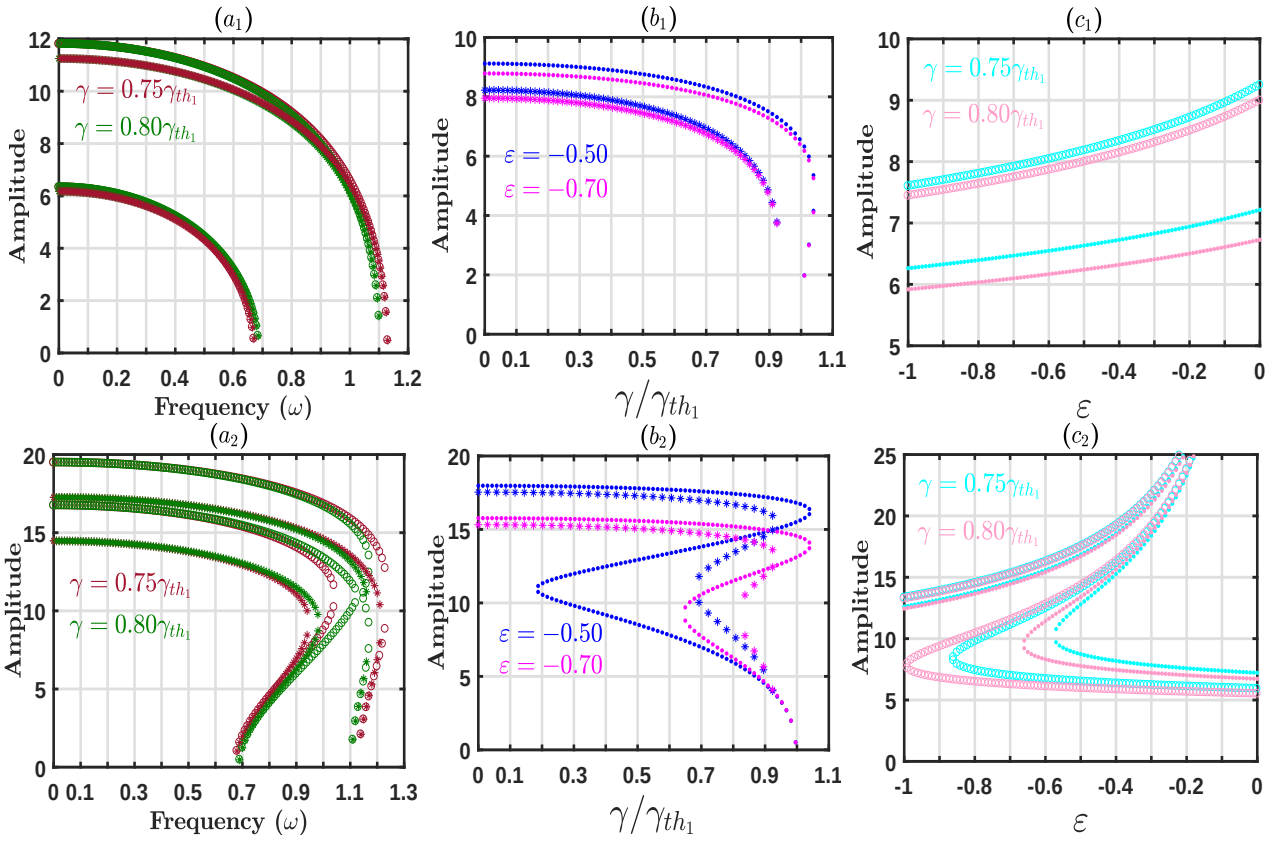

Figure 3.24: Analytical response curves for the quintic soft system ($\varepsilon < 0$). In the top row, $\alpha = 0.01$ and in the bottom row, $\alpha = -0.01$. (a_1) and (a_2) present the frequency-responses curves obtained for $\varepsilon = -0.5$ in *circle* and for $\varepsilon = -0.7$ in *star*. (b_1) and (b_2) displayed the normalised gain/loss parameter responses plotted for $\omega = 0.9$ in *dot* and $\omega = 1.0$ in *star*. In (c_1) and (c_2), the quintic coefficient responses are represented for $\omega = 0.9$ in *circle* and $\omega = 1.0$ in *star*.

Fig.3.23(c_1) and Fig.3.24(c_2), it is observed the existence of two regions: one with three values and the other with a single value of amplitude. This simply indicates that, depending on the region, the system's potential is either three-well stable or one-well stable.

From the foregoing, while the order of the nonlinearity increases, the characterisation procedure of the nonlinear threshold remains unaffected i.e., by looking for the extreme value of the ratio γ/γ_{th_1} given by the curve $A(\gamma/\gamma_{th_1})$. In order to conciliate the analytical results with the numerical ones in the following, we perform a simple analysis which consists in showing the interdependence between the frequency ω and the gain-loss parameter γ in nonlinear regime for some values of the nonlinearities. Indeed, for each nonlinearity value (cubic and/or quintic), there is a unique value of the threshold transition associated with a given frequency. In Table 3.1 and Table 3.2 the relation between cubic/quintic nonlinearity, frequency and threshold respectively for the cubic soft (one and both side excitations), and for the quintic hard with $\alpha = 0.01$ (one side excitation) are presented. Each pair of points (α, γ/γ_{th_1}) and (ε, γ/γ_{th_1}) taken from Table 3.1 and Table 3.2, respectively, have been represented by blue, magenta and black circles on the same graphs obtained numerically (see Fig.3.21). Thus, in Fig.3.21 a very good matching between some analytically chosen points and the numerical results can be observed.

Table 3.1: Correspondance between the frequency of oscillations and numerical breaking point in the cubic soft system

One side excitation			**Both sides excitation**		
ω	γ/γ_{th_1}	α	ω	γ/γ_{th_1}	α
0.905000	1.03600	0.003	**0.900000**	1.0420	0.003
0.940000	0.99780	0.010	**0.905000**	1.0370	0.010
1.055000	0.87530	0.040	**0.938400**	0.9995	0.040
1.138500	0.73350	0.060	**0.945500**	0.9920	0.060
1.176600	0.64290	0.100	**0.997000**	0.9408	0.100
1.282370	0.09499	0.275	**1.133500**	0.7439	0.275
1.258790	0.32590	0.300	**1.198100**	0.5811	0.400
1.280570	0.12890	0.425	**1.270750**	0.2395	0.500
1.284499	0.01000	0.500	**1.213600**	0.5302	0.650
			1.284499	0.0100	0.700

Table 3.2: Correspondance between the frequency of oscillations and numerical breaking point in the quintic hard system for $\alpha = 0.01$

One side excitation					
ω	**0.9415**	**0.9379**	**0.9300**	**0.9210**	**0.8809**
γ/γ_{th_1}	0.9961	1.0000	1.0080	1.0180	1.0650
ε	0.05	0.150	0.500	0.700	1.000

3.2.2.4 Effect of the inerter on the system stability

In the linear regime, it has been showed that the inertial parameter mainly acts on the oscillations frequency of the system. Now, in order to have a good understanding of the inertial parameter effect's on the stability, we will first proceed to analyse some temporal evolutions of the system in nonlinear regime before plotting his diagram of stability for different values of μ.

In Fig.3.25, the first and second rows show the dynamics of the cubic system whereas the third and fourth rows present the ones of the quintic system. In the first row $\alpha = 0.01$ and for this value, the threshold occurs at $\gamma = \gamma_{th_1}$ when $\mu = 0$. If we observe Figs.3.25(a_1, b_1, c_1), it can be noted that the threshold moves away far as the inertial parameter is incereasing. When $\mu = 0.1$, 0.5 and 1.0, the threshold is located respectively at $\gamma = 1.02\gamma_{th_1}$, $1.07\gamma_{th_1}$ and $1.25\gamma_{th_1}$. By observing the duration of oscillations, we can also note that the parameter μ improves the time of stability in the system.

It is already known that in the cubic or quintic hard system and, in the absence of inertial parameter, the gain oscillator increases to a limiting amplitude whereas the loss oscillator practically dies down to a limiting amplitude around the trivial fixed point. However, when the inertial parameter comes into play, ($\mu \neq 0$), as we can see in Figs.3.25(a_2, b_2, c_2), the phenomenon of energy absorption by the gain oscillator gradually disappears when the inertial parameter μ increases. The second row of Fig.3.25 has been obtained with $\alpha = -0.5$. For this

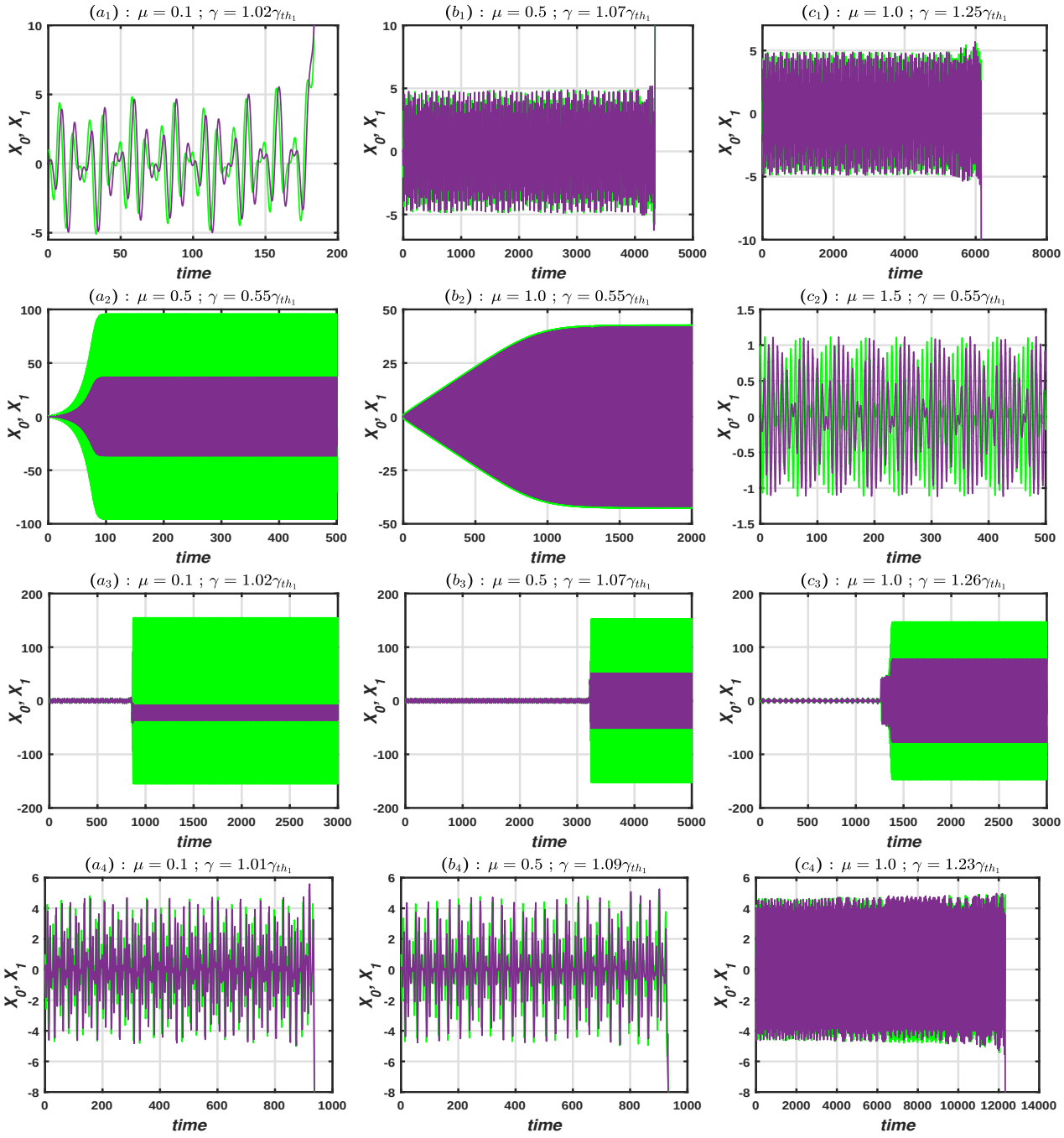

Figure 3.25: Effect of the inertial parameter on the dynamics in the cubic nonlinear regime. In the first row (a_1, b_1, c_1), $\alpha = 0.01$ (cubic soft) and in the second row (a_2, b_2, c_2), $\alpha = -0.5$ (cubic hard). Likewise, nonlinear coefficients in the third (a_3, b_3, c_3, quintic hard) and fourth (a_4, b_4, c_4, quintic soft) rows are ($\alpha = 0.01$, $\varepsilon = 0.09$) and ($\alpha = 0.01$, $\varepsilon = -0.4$) respectively. The used values of gain-loss and inertial parameters are displayed in each dial. Green and purple colours denote the dynamics of gain and loss oscillators respectively.

value, when μ is equal to 0, the transition point occurs at $\gamma = 0.55\gamma_{th_1}$. But, when μ begins acting in the system, a progressive growth in the amplitude of oscillations of the loss oscillator can be observed. Moreover, as μ increases, the amplitudes of the gain and loss oscillators tend to balance (Fig.3.25(b_2)) with a drop in amplitude of the oscillations. The same obversations also occur when it comes to quintic system (Figs.3.25(a_3, b_3, c_3) and Figs.3.25(a_4, b_4, c_4)). All the

figures in the cubic hard system (the 2^{nd} row) have been plotted for the same value of gain-loss parameter ($\gamma = 0.55\gamma_{th_1}$) in order to show that when μ increases and reaches a sufficiently large value, one can remark that the system still generates the Rabi oscillations (Fig.3.25(c_2)). In other words, this means that the transition point has been shifted and the linear $\mathcal{PT}$ unbroken region has been also extended. We can observe it in Figs.3.25(c_1) and 3.25(c_4) when the system is soften.

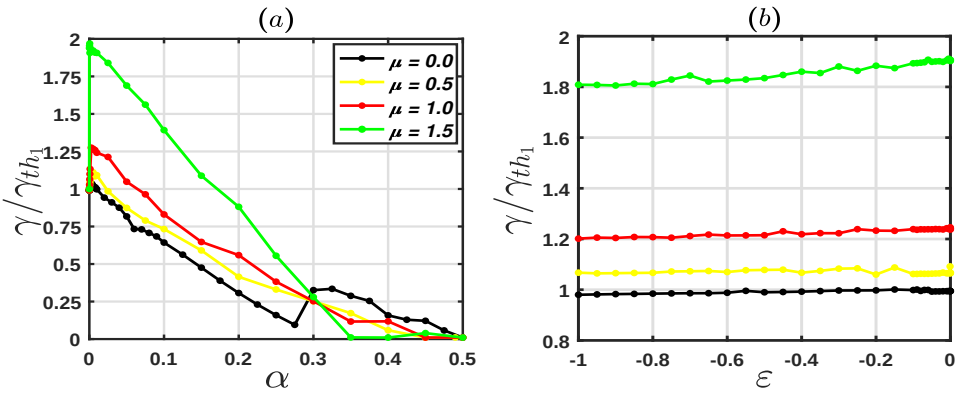

Figure 3.26: Influence of inertial parameter on the system stability. (a) and (b) are for the cubic soft and quintic soft systems respectively. The black colour curve shows the threshold when $\mu = 0$. The yellow, red and green colours display the threshold for $\mu = 0.5$, $\mu = 1.0$ and $\mu = 1.5$ respectively. In (b), the plots are obtained for $\alpha = 0.01$. The coupling parameter is $\kappa = 0.65$.

In each panel of the above Fig.3.26, the black curve refers to the case where the effect of inertial parameter does not exist. Fig.3.26(a) presents the normalised gain-loss parameter evolution according to α (for the cubic soft sytem i.e., $\eta = \varepsilon = 0$), whereas Fig.3.26(b) displays the one of the quintic soft system plotted as a function of ε for $\alpha = 0.01$. In each of both cases, one can see that the presence of inertial term in the system modifies the $\mathcal{PT}$ unbroken region. We can also affirm that the inertial parameter boosts the oscillatory regime of the system. Indeed, more the intensity of inertial coupling increases, more the domain of stable oscillations extends. On the other hand, whatever intensity of the inertial parameter, it is clear that for the cubic soft system (see Fig.3.26(a)), the nonlinear breaking point (threshold) has a decreasing dynamic when the cubic coefficient increases. A simple observation of these bifurcation frontier show that they converge to a specific value ($\alpha = 0.3$ in Fig.3.26(a)). And beyond this specific value, the normalised gain-loss dynamic is reversed. This means that, for values of the cubic coefficient greater than 0.3, the inertial parameter reduces the domain of stable oscillations. However, for the quintic soft system (Fig.3.26(b)), plotted for $\alpha = 0.01$, there is no convergent point for all these curves, but, we can easy observe that the transition threshold is practically constant along ε.

3.3 Scattering properties of a non-Hermitian mechanical dimer

The achievement of scattering will consist here, to insert into the Hermitian MTL in Fig.2.5(a), the studied non-Hermitian $\mathcal{PT}$ symmetric dimer presented in Fig.2.1, taken as a defect. Once the defect is introduced, the problem will now be summarised to study the transmission and reflection phenomena of a wave propagating in the Hermitian TL and arriving on this defect.

To achieve this investigation, we will consider that linear dimer is taken as defect and inserted in the Hermitian MTL as presented in Eq.(2.25). It is already known that, the TH or THL characteristic of the dimer plays an interesting role in the scattering features like lasing modes, unidirectional transparency, mirror-like behavior, etc. The lasing modes properties of the mechanical dimer are investigated by analyzing the lasing gain/loss parameter γ_r and critical wavenumber k_r given in Eq.(2.32).

The spectra of these lasing modes are represented in Fig.3.27 below. From Eq.(2.32a), we derive the boundaries F_1 and F_2 given by Eq.(3.6), which represents the domain of validity of the wavenumber.

$$\frac{1}{3+4\mu} \leq \vartheta\,, \quad \text{for } F_1 \tag{3.6a}$$

$$\vartheta \leq 1\,, \quad \text{for } F_2 \tag{3.6b}$$

The frontiers F_1 and F_2 define the separation line between the regions I and II, and the regions II and III respectively. A simple observation of Figs.3.27(a) and 3.27(b), show that the lasing parameter γ_r can be either purely imaginary (region I-1) or real (region I-2). In region I, which is the lower forbidden gap, the wavenumbers k is complex with a constant and positive real part equal to π, while his imaginary part is a varying negative value ($k = \pi - ib$). Morever, it is the region for which $cos(k) < -1$, the frequencies ω are real and, if the lasing parameter γ_r is real (see region I-2), then the lasing mode will occur. But in region I-1, the lasing mode cannot be observed. Region III is an another forbidden bandgap for which $cos(k) > 1$ and the wavenumbers are purely imaginary ($k = +ib$). Likewise, the frequencies are also purely imaginary. In region II, the wavenumbers and frequencies are purely real and positive values. It also corresponds to the allowed frequencies from the TL dispersion relation in which the lasing mode occurs when γ_r is real.

The THL dimer allows control of real, complex, and imaginary propagation wavenumbers. The existence of region I-2 implies that lasing modes can occur for for real values of the lasing parameter γ_r and for complex values of k_r.

Now,the transmission and reflection phenomena through the scattering coefficients given by Eq.(2.30), in each of these regions will be investigated. Depending on the k spectrum of the dimer in which a region is observed, the behaviour is imposed by the related scattering coefficients. The Figs.3.28 and 3.28 below display the spectral singularities of zero-width resonances

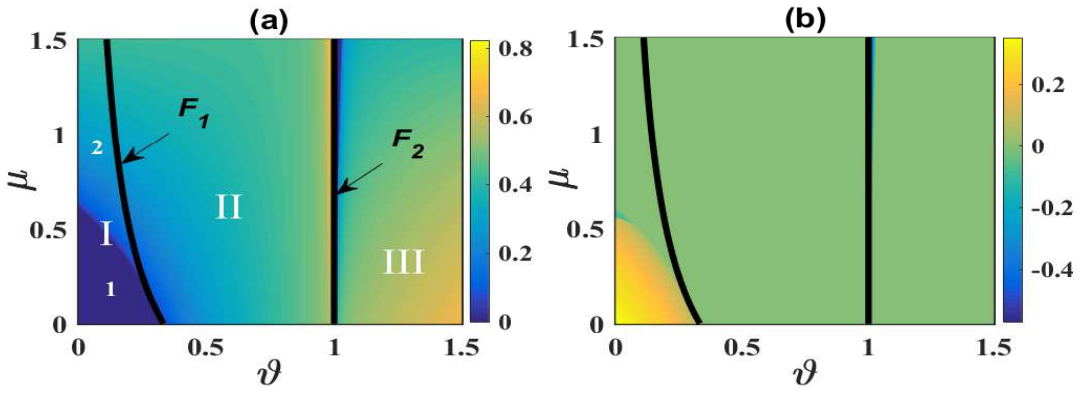

Figure 3.27: Spectra of γ_r of the THL dimer for which $D = 0$. (a) and (b) represent the real and imaginary parts respectively. F_1 and F_2 define the frontiers of regions I (complex k), II (real k), and III (purely imaginary k).

$(D = 0)$ [78] corresponding to intense scattering coefficients amplifications $(T_{g,l} = R_{g,l} = \infty)$ in all the propagation regions. However, at the frontiers, the phenomenon of wave reflections are observed $(T_{g,l} = 0$ and $R_{g,l} = 1)$. It is due to the presence of these spectral singularities that the system exhibits the lasing modes k_r at γ_r. Let's now observe in what follows the different features of the scattering coefficients in each region.

Depending on the nature of the wavenumber k, we have in region I (see the first column of Fig.3.28), two possible cases. The first case (region I-1) is the region where γ_r is purely imaginary and the second case (region I-2) is where γ_r is real. Whatever the subregion, the wavenumbers are complex (see Fig.3.28(a, b)). However, for purely imaginary γ_r i.e., in region I-1, no resonant modes can not be observed as we can see in Fig.3.28(a). The reflection scatterings are constants (with $R_l = 1$ and $R_l > R_g$) after a precise value of gain-loss parameter $(\gamma = 0.2)$ while the transmission is vanishing and before that point, (with $R_l > 1$ and $R_l > R_g$). On the other hand, for real γ_r i.e., in region I-2, there is a resonant mode at $\gamma_r = 0.294$ where $R_l > T > R_g$ and beyond that value of γ, transmission is suddendly attenuated, loss reflection is unity and gain reflection stabilises at a very low value (on the order of 10^{-4}). In the region I, only in the gain direction, the dimer behaves like an absorber far away the resonant mode, since for this direction the transmission is vanished and reflection is attenuated and very small than 1. But, in the loss side, the dimer will behave as a perfect mirror.

In region II (the second column), the wavenumbers are all real and positive. This region represents the region of the allowed frequencies. In Fig.3.28(c), we can observe two EPs: one from the gain side at $\gamma_g = 0.260$ $(R_g = 0$ and $R_l \neq 0)$ and the other from the loss side at $\gamma_l = 0.495$ $(R_g \neq 0$ and $R_l = 0)$. For each of these points, the transmission is unity i.e., $T_{g,l} = 1$. Moreover, these points correspond to regions of unidirectional invisibility [26, 169] from gain and loss side, respectively. Between these points (i.e., $\gamma_g < \gamma < \gamma_l$), the transmission is superunitary $(T > 1)$ and outside this range, the transmission is subunitary $(T < 1)$. This unitary transmission feature is specific to any $\mathcal{PTS}$ scattering system. These characteristics were of great technological interest since it allowed one-way designing of linear optical devices [26, 169, 170]. It was also demonstrated that in $\mathcal{PTS}$ systems, the transition from the $\mathcal{PTS}$

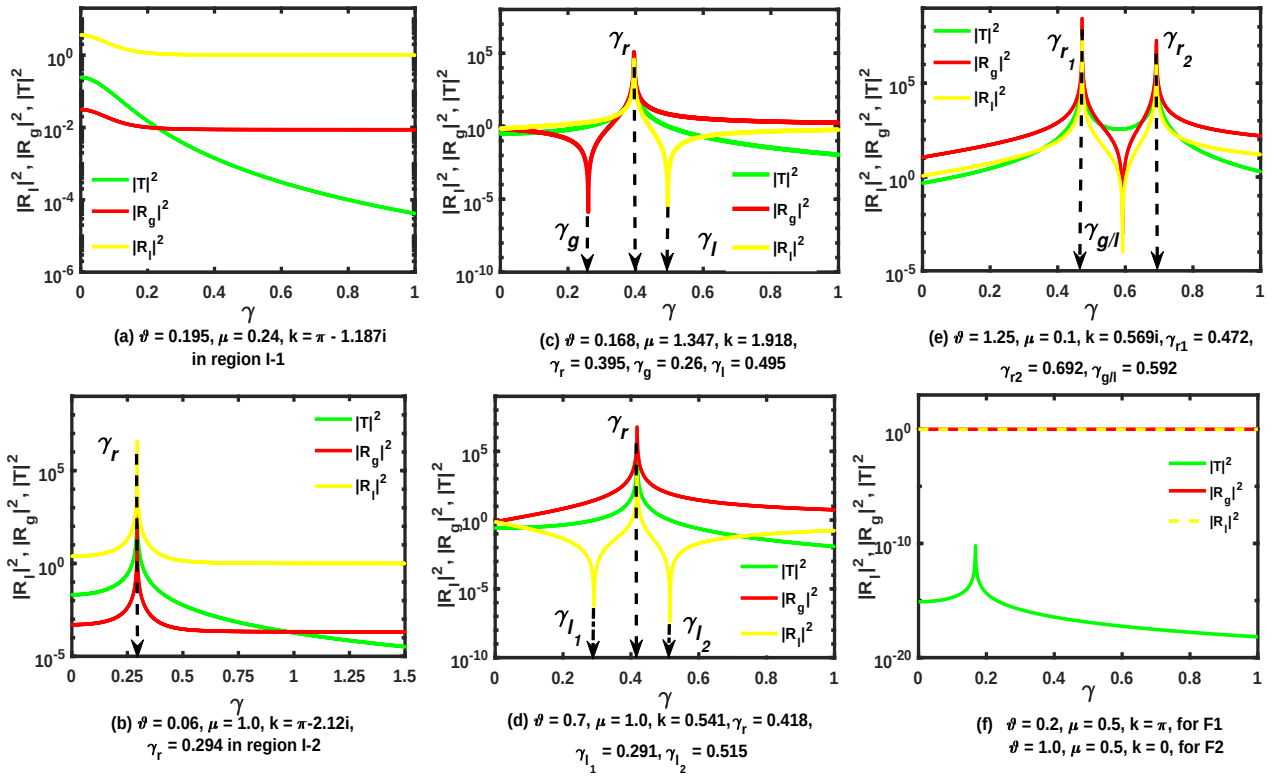

Figure 3.28: Scattering normalised coefficient T and $R_{g,l}$ of the THL dimer versus the gain-loss parameter. The first column represents the obtained plots in the region I. So, (a) region I-1, $\vartheta = 0.195$,$\mu = 0.24$ and k is complex but γ is purely imaginary. There is no lasing mode in this region.The transmission vanishes completely while the reflection scatterings are constants ($T = 0$, $R_l = 1$ and $R_l > R_g$). (b) region I-2, $\vartheta = 0.06$,$\mu = 1.0$, k is always complex but γ is real. Lasing mode is observed at $\gamma_r = 0.294$. The transmission vanishes completely $T = 0$ and $R_l = 1$ with $R_l > R_g$. (c) region II, k and γ are real, EPs occur for the gain and the loss incidences ($\gamma_g = 0.260$ and $\gamma_l = 0.495$) while in (d), EPs occur only for the loss incidence at two points ($\gamma_{l_1} = 0.291$ and $\gamma_{l_2} = 0.515$). Lasing mode are observed between the EPs. (e) region III, k is purely imaginary and γ is real. EPs for the gain and loss incidences occur at the same value of $\gamma = \gamma_{g/l}$. Lasing modes are observed twice for each reflections scattering at $\gamma_{r_1} = 0.472$ and $\gamma_{r_2} = 0.692$. (f) at the frontiers $F1$ with $\vartheta = 0.2$, $\mu = 0.5$, $k = \pi$ for $F1$ and $\vartheta = 1.0$, $\mu = 0.5$, $k = 0$ for $F2$.

phase to the $\mathcal{PTS}$ broken phase is imposed by the unitary related transmission [78, 171, 172].

On the other hand, still in region II, we can get particular case where the reflection scattering coefficient from the gain side does not vanish any longer, whereas the loss reflection vanishes at two different values of γ ($\gamma_{l_1} = 0.291$ and $\gamma_{l_2} = 0.515$) in Fig.3.28(d). These EPs are located on either side of the lasing mode ($\gamma_r = 0.418$). These two can be obtained by solving equation $R_l = 0$. This scenario occurs ϑ exceeds a certain critical value in this region. For $\mu = 1.0$ the calculated critical value is $\vartheta_c = 0.358$. We have plotted the Fig.3.28(d) with $\vartheta = 0.7 > \vartheta_c$ and as we can see, the plot exhibits two EPs at γ_{l_1} and γ_{l_2} for which $T = 1$ when $R_l = 0$. We can also note that the gain reflection is always greater than the transmission. Far away the EPs points, the transmission tends to vanish from the gain and loss sides when both reflections tend to unity ($R_{g,l} \to 1$ when $T \to 0$).

In region III, wavenumbers and frequencies are purely imaginary and this it also corresponds to the forbidden region. In this region, γ_r is completely real. However, this region admits two

resonant modes indicated in Fig.3.28(f) by γ_{r_1} and γ_{r_2}, and one EPs emerges for the same gain-loss value ($\gamma_{g,l} = 0.592$) at which the gain and loss reflections waves are vanished (i.e., $R_g = R_l = 0$), when the transmission is amplified ($T > 1$). for this value of the modulation parameter, the incident wave coming from either the gain or loss side is totally transmitted with a slight amplification without being reflected. This point may represent a point of bidirectional invisibility, compared to unidirectional invisibility, where this only occurs in one direction. This is a rather interesting case because, as known, it has never been encountered in the literature. Far away from the second resonant mode γ_{r_2}, the transmission is vanished, and only the loss reflection tends to unity while the gain reflection is amplified ($T \to 0$, $R_l \to 1$ and $R_g > R_l$).

Fig.3.28(f) illustrates the behaviour at the two frontiers F1 and F2 respectively. We can see that, the transmission vanishes while the gain and loss reflections remain constants and equal to 1 throughout the γ range ($T = 0$, and $R_g = R_l = 1$). This means that, the defect completely returns or reflects any signal arriving at it, on both gain and loss directions like a perfect mirror. The curves are obtained for $\vartheta = 0.2$, $\mu = 0.5$, $k = \pi$ for $F1$ and $\vartheta = 1.0$, $\mu = 0.5$, $k = 0$ for $F2$.

Conclusion

The results obtained on the study of the dynamical behaviour of $\mathcal{PT}$-Symmetric mechanical system described in the previous chapter have been presented and discussed throughout this chapter. Here, a devotion has been mainly made on the characterisation of the $\mathcal{PT}$ breaking point in nonlinear regime after having investigated it in the linear regime. It emerges that under effect of nonlinear parameters, the $\mathcal{PT}$ unbroken region can either extend or contract depending on the strength of nonlinearity. the scattering properties of $\mathcal{PTS}$ mechanical dimer, when it is inserted as an impurity in a Hermitian conservative MTL have also investigated.

General Conclusion

1- Main results of the Thesis

As stated in the objectives, the work presented in this dissertation has two main contributions. The first main contribution of this work was to show how the phase transition point (EP) is modified in a $\mathcal{PT}$-symmetric nonlinear system. To do this, we considered a physical system consisting of two coupled nonlinear mechanical oscillators respecting $\mathcal{PT}$ symmetry, i.e. one with gain and the other with equal and opposite loss, whose dynamics in the nonlinear regime were characterised. The second contribution was to study the scattering properties of the linear $\mathcal{PT}$ dimer incorporated as a defect in a Hermitian mechanical transmission line.

The first chapter reviewed the literature on the concepts of Hermitian theory and $\mathcal{PT}$ symmetry in order to understand their applicability to different physical systems. We also discussed the generalities of mechanical systems and presented the different types of coupling, as well as the sources of nonlinearity in mechanical systems. We then presented the techniques for designing a $\mathcal{PT}$-symmetric mechanical system. Finally, an overview of scattering properties was presented.

The second chapter was devoted to the modelling and the methodological framework. We described the mechanical system model and derived mathematical equations which govern its dynamics, and then we described the analytical and numerical methods used within dissertation.

The third and last chapter was devoted to results and discussions. Here, we provided our various findings and comments, which are summarised below.

$\star$ Firstly, in order to understand the character of the phase transition point, a linear regime study was carried out on the system. The aim of this study was to find analytical expressions for the eigenvalues and the transition point, taking into account both types of coupling (elastic and inertial). This study shows that the effects of each type of coupling on the amplitude of the oscillations (elastic coupling) and on the frequency of the oscillations (inertial coupling) are clearly visible in the dynamics of the system. On the other hand, the range of values of the inertial coupling is very large, while that of the elastic coupling is limited, which restricts the exact phase region $\mathcal{PT}$. However, when the hermiticity parameter reaches a threshold value (EP), the system adopts an unstable behaviour, characterised by an exponential growth of the oscillation amplitude with time. In addition, the simultaneous action or presence of the two couplings makes it possible to obtain a combination between these two parameters for which the exact phase $\mathcal{PT}$ disappears, even though neither of the two couplings is zero. As a result, the system is no longer conservative, because the spectrum of the system's eigenvalues will

switch directly from complex to pure imaginary values. Indeed, at this point, the absence of the exact phase region $\mathcal{PT}$ will cause an exponential amplification of the system's energy and could therefore lead to its destruction.

⋆ Secondly, concerning the study of the dynamics of the system in the nonlinear regime, we first focused on the study of the system in the absence of inertial effects (without inertial coupling) and then studied its effect on the dynamics. From the study of the nonlinear dynamics of the system (where only elastic coupling is involved), which mainly consisted in characterising the transition point, we found, using numerical tools, that the latter depends on the distribution of the initial perturbation of the system. In other words, the transition point in the nonlinear regime varies as a function of the initial conditions. Thus, if the intensity of the initial excitation is completely fixed on either the gain or the loss oscillator, the behaviour of the transition point as a function of the nonlinearity is identical, unlike the case where the initial excitation is equally distributed between the two oscillators. The result is that when the initial excitation is split between the two oscillators, the exact phase region $\mathcal{PT}$ is much larger than when the initial excitation is fixed to a single oscillator. This study also showed that nonlinearity reduces the $\mathcal{PT}$ exact phase region regardless of the nature of the potential involved, i.e. whether the nonlinearity is soft or hard. However, especially in the soft system, the low values of the nonlinearity extend the $\mathcal{PT}$ exact phase region than in the linear case. The analysis of the time evolution around the phase transition point in the nonlinear regime shows two different features. In the presence of soft nonlinearity, the nonlinear system exhibits the same behaviour as in the linear regime, i.e. an infinite growth of the amplitude of the oscillations when the transition point is reached, or a cessation of the oscillations after the passage of time. On the other hand, in the presence of a hard nonlinearity, the breaking point marks a transition to stable oscillations in the system with, in particular, a transfer of energy from the loss oscillator to the gain oscillator. This is because the gain oscillator oscillates at a very high amplitude, while the loss oscillator oscillates at a very low amplitude. We have also shown that for small cubic nonlinearities, the quintic order has the effect of restoring the linear breaking point, thereby extending the oscillatory regime of the system.

⋆ Thirdly, from the study of the effect of inertial coupling on the dynamics of the system around the transition threshold, when the nonlinearity of the system involved is soft, we found that increasing the value of the inertial coupling parameter increases the period of the oscillations or, alternatively, prolongs the time of the oscillations for the same fixed values of the gain-loss parameter. As a result, the exact phase range is extended. In the presence of a hard nonlinearity, increasing the value of the inertial coupling parameter tends to rebalance the energy between the two oscillators. As a result, the phenomenon of energy absorption by the gain oscillator observed in the absence of the inertial coupling parameter gradually disappears. The energies in the two oscillators compensate, bringing the system back into the exact phase region $\mathcal{PT}$ and moving the transition point further away.

⋆ In the framework of the investigation of the scattering properties in a conservative mechanical line, in which the dimer is inserted as a defect, we found that:

– When the PTS dimer scattering system propagates a real wavenumber, it undergoes a spontaneous symmetry breaking around the EPs, where the transmission is superunitary inside ($T > 1$) and subunitary outside ($T < 1$). Furthermore, when the coupling parameter of the Hermitian line exceeds a certain critical value, the $\mathcal{PTS}$ dimer system becomes unidirectional only) from the loss input. Consequently, unidirectional invisibility from the gain input is suppressed.

– We also noticed that when the $\mathcal{PTS}$ dimer scattering system propagates a complex wavenumber, the resonant mode is only observed for real values of the gain-loss parameter. However, for purely imaginary values of the gain-loss modulation parameter, the system behaves as an absorber only on the gain side and as a perfect mirror on the loss side.

– The study also showed that when the $\mathcal{PTS}$ dimer scattering system generates the purely imaginary wave numbers corresponding to the real values of the gain-loss parameter, it exhibits two resonant modes for a single EP on the gain and loss sides. This could be interpreted as bidirectional invisibility.

2- Open problems and future directions

The work carried out in this dissertation and the results so far obtained are a source of encouragement for studies. Other points of interest may be solved in the future.

- It would be interesting to characterise the chaotic behaviour of the $\mathcal{PTS}$ mechanical system by studying its Lyapunov exponent and bifurcation diagram. For this type of system, it would be interesting to know whether Melnikov's or Shilnikov's theory can be used to predict the parameters that generate chaos.

- It would be interesting to study the scattering properties by considering the $\mathcal{PTS}$ nonlinear dimer as a defect embedded in a hermitian mechanical transmission line. This study will be done numerically in order to compare the new results with those obtained with the $\mathcal{PTS}$ linear dimer.

- It would also be interesting to analyse the behaviour of the dimer in the mechanical transmission line when the wave passes through it.

Bibliography

[1] C. M. Bender and S. Boettcher, *Phys. Rev. Lett.*, **80**, 5243 (1998).

[2] C. M. Bender, S. Boettcher and P. N. Meisinger, *J. Math. Phys*, **40**, 2201 (1999).

[3] C. M. Bender, M. V.Berry and A. Mandilara, *J. Phys. A*, **35**, L467 (2002).

[4] X. Zhu, H. Ramezani, C. Shi, J. Zhu and X. Zhang, *Phys. Rev. X*, **4**, 031042 (2014).

[5] R. Fleury, D. Sounas and A. Alu, *Nat. Commun.*, **6**, 5905 (2015).

[6] M. Hiller, T. Kottos, and A. Ossipov, *Phys. Rev. A*, **73**, 063625 (2006).

[7] K. G. Makris, R. El-Ganainy, D. N. Christodoulides, and Z. H. Musslimani, *Phys. Rev. Lett.*, **100**, 103904 (2008).

[8] C. M. Bender, M. Gianfreda, S. K. Özdemir, B. Peng, and L. Yang, *Phys. Rev. A*, **88**, 062111 (2013).

[9] J. Schindler, Z. Lin, J. M. Lee, H. Ramezani, F. M. Ellis, and T. Kottos, *J. Phys. A: Math. Theor.*, **45**, 444029 (2012).

[10] J. Schindler, A. Li, M. C. Zheng, F. M. Ellis, T. Kottos, *Phys. Rev. A.*, **84(4)**, 040101 (2011).

[11] F. Fotsa-Ngaffo, S. B. Tabeu, S. Tagouegni and A. Kenfack-Jiotsa, *J. Opt. Soc. Am. B.*, **34(3)**, 658-667 (2017).

[12] S. Assawaworrarit, X. Yu, S. Fan, *Nature*, **546**, 387 (2017).

[13] C. M. Bender, B. K. Berntson, D. Parker, E. Samuel, *Am. J. Phys.*, **81**, 173 (2013).

[14] X. -W. Xu, Y. -X. Liu, C. -P. Sun, and Y. Li, *Phys. Rev. A*, **92**, 013852 (2015).

[15] E. D. Tsoy, *Phys. Lett. A*, **381**, 462-466 (2017).

[16] C. M. Bender, M. Gianfreda, S. P. Klevansky, *Phys. Rev. A.*, **90**, 022114 (2014).

[17] K. Bertoldi, V. Vitelli, J. Christensen and M. van Hecke, *Nat. Rev. Mater.*, **2**, 17066 (2017).

[18] I.V. Barashenkov, M. Gianfreda, *J. Phys. A.*, **47**, 282001 (2014).

[19] X.-Y. Lü, H. Jing, J.-Y. Ma, Y. Wu, *Phys. Rev. Lett.*, **114**, 253601 (2015).

[20] J. Cuevas, P. G. Kevrekidis, A. Saxena, A. Khare, *Phys. Rev. A.*, **88**, 032108 (2013).

[21] K. V. Kepesidis, T. J. Milburn, J. Huber, K. G. Makris, S. Rotter, P. Rabl, *New J. Phys.*, **18**, 095003 (2016).

[22] G. Barton, Introduction to Advanced Field Theory, *John Wiley and Sons, New York*, (1963).

[23] Z. H. Musslimani, K. G. Makris, R. El-Ganainy, D. N. Christodoulides, *Phys. Rev. Lett.*, **100**, 030402 (2008).

[24] R. El-Ganainy, K. G. Makris, D. N. Christodoulides, Z. H. Musslimani, *Opt. Lett.*, **32(17)**, 2632–2634 (2007).

[25] R. El-Ganainy, K. G. Makris, M. Khajavikhan, Z. H. Musslimani, S. Rotter, D. N. Christodoulides, *Nat. Phys.*, **14**, 11–19 (2018).

[26] Z. Lin, H. Ramezani, T. Eichelkraut, T. Kottos, H. Cao, D. N. Christodoulides, *Phys. Rev. Lett.*, **106**, 213901 (2011).

[27] S. V. Suchkov, F. Fotsa-Ngaffo, A. Kenfack-Jiotsa, A. D. Tikeng, T. C. Kofane, Y. S. Kivshar, A. A. Sukhorukov, *New J. Phys.*, **18**, 065005 (2016).

[28] C. E. Rüter, K. G. Makris, R. El-Ganainy, D. N. Christodoulides, M. Segev, D. Kip, *Nat. Phys.*, **6**, 192 (2010).

[29] S. V. Suchkov, A. A. Sukhorukov, J. Huang, S.V. Dmitriev, C. Lee, Y.S. Kivshar, *Laser Photonics Rev.*, **10**, 177 (2016).

[30] B. Peng, et al., *Proc. Natl. Acad. Sci. USA*, **113**, 6845–6850 (2016).

[31] B. Peng, et al., *Science*, **346**, 328–332 (2014).

[32] W. Chen, S.K. Özdemir, G. Zhao, J. Wiersig, L. Yang, *Nature*, **548**, 192–196 (2017).

[33] Z. Lin, J. Schindler, F. M. Ellis, and T. Kottos, *Phys. Rev. A*, **85**, 050101 (2012).

[34] M. C. Smith, *IEEE Trans. Aut. Cont.*, **47(10)**, 1648-1662 (2002).

[35] J. Rubinstein, P. Sternberg, and Q. Ma, *Phys. Rev. Lett.*, **99**, 167003 (2007).

[36] A. Guo, G. J. Salamo, D. Duchesne, R. Morandotti, M. Volatier-Ravat, V. Aimez, G. A. Siviloglou, and D. N. Christodoulides, *Phys. Rev. Lett.*, **103**, 093902 (2009).

[37] K. F. Zhao, M. Schaden, and Z. Wu, *Phys. Rev. A*, **81**, 042903 (2010).

[38] L. Feng, M. Ayache, J. Huang, Y.-L. Xu, M.-H. Lu, Y.- F. Chen, Y. Fainman, and A. Scherer, *Science*, **333**, 729 (2011).

[39] S. Bittner, B. Dietz, U. Günther, H. L. Harney, M. MiskiOglu, A. Richter, and F. Schäfer, *Phys. Rev. Lett.*, **108**, 024101 (2012).

[40] J. Zhang, B. Peng, S. K. Özdemir, K. Pichler, D. O. Krimer, G. Zhao, F. Nori, Yu-xi Liu, S. Rotter and L. Yang, *Nat. Photon.*, **12**, 479-484 (2018).

[41] H. Lü, C. Wang, L. Yang and H. Jing, *Phys. Rev. A*, **10**, 014006 (2018).

[42] A. E. Miroshnichenko, B. A. Malomed and Y. S. Kivshar, *Phys. Rev. A*, **84**, 012123 (2011).

[43] H. Ramezani and T. Kottos, *Phys. Rev. A*, **82**, 043803 (2010).

[44] S. V. Suchkov, B. A. Malomed, S. V. Dmitriev and Y. S. Kivshar, *Phys. Rev. E*, **84**, 046609 (2011).

[45] W. Walasik, C. Ma and N. M. Litchinitser *Optics Letters*, **40**, 5327-5330 (2015).

[46] Y. Lumer, Y. Plotnik, M. C. Rechtsman, and M. Segev, *Phys. Rev. Lett.*, **111**, 263901 (2013).

[47] F. Strocchi, *Eur. Phys. J. Plus*, **127**, (2012).

[48] N. Dunford, and J. T. Schwartz, Linear operators II : Spectral theory : self adjoint operators in Hilbert Space eng. isbn: 0471226386 (Wiley-Intersience, New York, 1963).

[49] B. Khantoul, La Pseudo hermiticité et sa généralisation aux systèmes dépendants du temps, archives.umc.edu.dz, (2010).

[50] N. Moiseyev, Non-Hermitian Quantum Mechanics, (2011).

[51] D. J. Griffiths, Introduction to quantum mechanics, (2010).

[52] T. Wu, *Phys. Rev.*, **115**, 1390 (1959).

[53] R. Haydock and M. J. Kelly, *Phys. C : Solid State Physics.*, **8**, 197 (1975).

[54] C.M. Bender, *Rep. Prog. Phys.*, **70**, 947, (2007).

[55] C. M. Bender, D. C. Brody, and H. F. Jones, *Phys. Rev. Lett.* **89**, 270401 (2002). Erratum *Phys. Rev. Lett.*, **92**, 119902 (2004).

[56] C. M. Bender, The complex pendulum, Physics Reports, **315**, 27 (1999).

[57] C. M. Bender, S. Boettcher, and V. M. Savage, *J. Math. Phys.*, **41**, 6381 (2000).

[58] C. M. Bender and Q. Wang, *J. Phys. A.*, **34**, 3325 (2001).

[59] C. M. Bender, S. Boettcher, P. N. Meisinger and Q. Wang, *Phys. Lett. A.*, **302**, 286 (2002).

[60] C. M. Bender, D. C. Brody and H. F. Jones, *Am. J. Phys.*, **71**, 1905 (2003).

[61] C. M. Bender and H. F. Jones, *Phys. Lett. A*, **328**, 102 (2004).

[62] B. Khantoul, Mémoire de magister, Université des Frères Mentouri, Constantine (2010).

[63] W. D. Heiss, *J. Phys. A: Math. Gen.*, **37**, 2455 (2004).

[64] M. V. Berry, *Czechoslov. J. Phys.*, **54**, 1039-1047 (2004).

[65] S. Klaiman, U. Günther, N. Moiseyev, *Phys. Rev. Lett.*, **101**, 080402 (2008).

[66] P. M. Morse, H. Feshbach, Methods of Theoretical Physics McGraw-Hill, New York, 1953.

[67] J. Schnabel, H. Cartarius, J. Main, G. Wunner, W. D. Heiss, *Phys. Rev. A.*, **95**, 053868 (2017).

[68] B. Peng, S. K. Özdemir, F. Lei, F. Monifi, M. Gianfreda, G. L. Long, S. Fan, F. Nori, C. M. Bender, L. Yang, *Nat. Phys.*, **10**, 394 (2014).

[69] Y.-L. Liu, R. Wu, J. Zhang, S. K. Özdemir, L. Yang, F. Nori, Y. Liu, *Phys. Rev. A*, **95**, 013843 (2017).

[70] E.-M. Graefe, *J. Phys. A*, **45**, 444015 (2012).

[71] H. Xu, D. Mason, L. Jiang and J. G. E. Harris, *Nature*, **80**, 537 (2016).

[72] A. Alù and N. Engheta, *Phys. Rev. Lett.*, **103**, 143902 (2009).

[73] H. Alaeian and J. A. Dionne, *Phys. Rev. A.*, **89**, 033829 (2014).

[74] A. Baev, P. N. Prasad, H. Agren, M. Samoć and M. Wegener, *Phys. Rep.*, **594**, 1 (2015).

[75] P. Tassin, L. Zhang, T. Koschny, E. N. Economou and C. M. Soukoulis, *Phys. Rev. Lett.*, **102**, (2009).

[76] H. Benisty, A. Degiron, A. Lupu, A. D. Lustrac, S. Forget, M. Besbes, G. Barbillon, A. Bruyant, S. Blaize and G. Lerondel, *Opt. Expr.*, **19**, 3567 (2011).

[77] I. B. Njike-Njike, F. Fotsa-Ngaffo, S. B. Tabeu, A. Kenfack-Jiotsa. *Arab. J. Sci. Eng.*, **47**, 3659 (2022).

[78] A. Mostafazadeh, *Phys. Rev. Lett.*, **102**, 220402 (2009).

[79] H. Ramezani, H.-K. Li, Y. Wang and X. Zhang, *Phys. Rev. Lett.*, **113**, 263905 (2014).

[80] A. A. Sukhorukov, Z. Y. Xu and Y. S. Kivshar, *Phys. Rev. A.*, **82**, 043818 (2010).

[81] S. Longhi, *Phys. Rev. A*, **82**, 031801 (2010).

[82] L. Ge and A. D. Stone, *Phys. Rev. X*, **4**, 031011 (2014).

[83] V. A. Vysloukh and Y. V. Kartashov, *Opt. Lett.*, **39**, 5933 (2014).

[84] C. T. West, T. Kottos and T. Prosen, *Phys. Rev. Lett.*, **104**, 054102 (2010).

[85] L. Rayleigh, The Theory of Sound. 2nd edn. Dover Publications, New York, 1945.

[86] D. M. Chandler, R. I. Waller and W. G. Adam, *West Greenland. Ann. Glaciol.*, **42**, 67-70 (2005).

[87] W. Pauli, *Rev. Mod. Phys.*, **15**, 175 (1943).

[88] S. N. Gupta, *Phys. Rev.* **77**, 294 (1950) and *Proc. Phys. Soc. London*, **63**, 681 (1950).

[89] K. Bleuler, Helv. *Phys. Act.*, **23**, 567 (1950).

[90] E. C. G. Sudarshan, *Phys. Rev.*, **123**, 2183 (1961).

[91] T. D. Lee and G. C. Wick, *Nucl. Phys. B*, **9**, 209 (1969).

[92] A. Mostafazadeh, *J. Math. Phys.*, **43**, 205 (2002).

[93] A. Mostafazadeh, *J. Math. Phys.*, **43**, 2814 (2002).

[94] A. Mostafazadeh, *J. Math. Phys.*, **43**, 3944 (2002).

[95] S. Phang, Theory and Numerical Modelling of Parity-Time Symmetric Structures for Photonics, *Thesis*, *University of Nottingham* (2016).

[96] J. C. Schindler, $\mathcal{PT}$-Symmetric Electronics, *Thesis*, *Wesleyan University* (2013).

[97] L. Chang, X. Jiang, S. Hua, C. Yang, J. Wen, L. Jiang, G. Li, G. Wang, and M. Xiao, *Nat. Photonics*, **8**, 524–529 (2014).

[98] A. Regensburger, C. Bersch, M.-A. Miri, G. Onishchukov, D. N. Christodoulides, and U. Peschel, *Nature*, **488**, 167–71 (2012).

[99] S. Longhi, *J. Phys. A Math. Theor.*, **44**, 485302 (2011).

[100] H. F. Jones, *J. Phys. A Math. Theor.*, **45**, 135306 (2012).

[101] M. Kulishov, J. M. Laniel, N. Bélanger, J. Azana, and D. V. Plant, *Opt. Express*, **13**, 3068–78 (2005).

[102] J. Ctyroký, V. Kuzmiak, and S. Eyderman, *Opt. Express*, **18**, 21585–21593 (2010).

[103] L. Razzari and R. Morandotti, *Nature*, pp. 8–9 (2012).

[104] F. Nazari, M. Nazari, and M. K. Moravvej-Farshi, *Opt. Lett.*, **36**, 4368–70 (2011).

[105] Y. N. Joglekar, C. Thompson, D. D. Scott, and G. Vemuri, *Eur. Phys. J. Appl. Phys.*, **63**, 30001 (2013).

[106] F. Bagarello and G. Pantano, *Int. J. Theor. Phys.*, **52**, 4507–4518 (2013).

[107] J. Schindler, *$\mathcal{PT}$-Symmetric Electronics*, honor thesis, Wesleyan University, (2013)

[108] M. C. Zheng, *Non-Hermitian Dynamics*, Master's thesis, Wesleyan University High Honors Thesis, (2009).

[109] Z. Lin, *Exploiting Wave Transp ort in $\mathcal{PT}$-Symmetric Media, Thesis*, *Wesleyan University* (2012).

[110] N. Bender, *Asymmetric Transp ort Using Nonlinear Parity-Time Symmetric Structures, Thesis*, *Wesleyan University* (2014).

[111] I. I. Rabi, *Phys. Rev.*, **51**, 652 (1937).

[112] https://en.wikipedia.org/wiki/pendulum ($accessedonthe08June2017$).

[113] https://www.teachengineering.org/view lesson.php?url= collection/cub /lessons/cub pend lesson01.xml (accessed on the 08 June 2017).

[114] https://shanesettle.weebly.com/uploads/9/0/5/3/9053419/2pendulum-introductionframing.pdf (accessed on the 08 June 2017).

[115] https://www.math24.net/double-pendulum.html (accessed on the 02 September 2016).

[116] T. Shinbrot and et al, *American Journal of Physics*, **60**, 491-499 (1992).

[117] T. C. Huang, *Journal of Applied Mechanics*, **22**, 107–110 (1955).

[118] C. M. Bender, *Time and Science*, **3**, 285-310 (2023).

[119] B. R. Nana Nbendjo, *Dynamique et contrôle actif avec délai de la dynamique des structures mécaniques à potentiel ϕ^6 monostable non bornés, Thèse*, *Université de Yaoundé 1* (2004).

[120] A.O. Gilchrist, *International Journal of Mechanical Science*, **3**, 286–311 (1961).

[121] G.J. Efstathiades, *Journal of Sound and Vibration*, **34**, 379–397 (1974).

[122] G. Chen, *Journal of Sound and Vibration*, **119**, 225–242 (1987).

[123] Y.V. Ladygina, A.I. Manevich, *Journal of Applied Mathematics and Mechanics*, **57**, 257–266 (1993).

[124] L. Cveticanin, *Journal of Sound and Vibration*, **252**, 361–369 (2002).

[125] L. Cveticanin, *Journal of Sound and Vibration*, **247**, 279–292 (2001).

[126] F.V. Alexander, H.R. Richard, *International Journal of Non-linear Mechanics*, **39**, 1079–1091 (2004).

[127] A. D. Dimarogonas, S. Haddad, *Vibration for Engineers*, Prentice-Hall, Englewood Cliffs, New Jersey, 1992.

[128] G. Lewis, F. Monasa, *Int. J. Non-Linear Mech.*, **17**, 1 (1982).

[129] H. W. Haslach, *Int. J. Non-Linear Mech.*, **20**, 53 (1985).

[130] M. Z. Q. Chen, C. Papageorgiou, F. Scheibe, F.C. Wang, M.C. Smith, *IEEE Circuits and Systems Magazine*, **9**, 10–26 (2009).

[131] A.A. Andronov, A. A. Vitt, S. E. Khaikin, *Theory of Oscillators, Dover Books on Elet Eng*, (2011).

[132] F. Bloch, W. W. Hansen and M. Packard, *Phys. Rev.*, **70**, 474-485 (1946).

[133] F. Bloch, *Phys. Rev.*, **70**, 460–474 (1946).

[134] E. M. Purcell, H. C. Torrey and R. V. pound, *Phys. Rev.*, **69**, 37-38 (1946).

[135] R. Damadian, *Science*, **19**, 1151-1153 (1971).

[136] H. Ramezani, J. Schindler, F. M. Ellis, U. Guenther and T. Kottos, *Phys. Rev. A*, **85**, 062122 (2012).

[137] Y. D. Chong, L. Ge, A. D. Stone, *Phys. Rev. Lett.*, **106**, 093902 (2011).

[138] G. Djuidjé Kenmoé, A. Kenfack Jiotsa, T.C. Kofané, *Phys. D*, **191**, 31-48 (2004).

[139] A. H. Nayfeh and D. T. Mook, *Nonlinear Oscillations Wiley, New York*, (1979).

[140] C. Hayashi, *Nonlinear Oscillations in Physical Systems, McGraw-Hill, New York*, (1964).

[141] J. Guckenheimer and P. J. Holmes, *Nonlinear Oscillations, Dynamical Systems and Bifurcations of Vector Fields, Springer, New York*, (1983).

[142] A. V. Gorbach, M. Johansson, *Phys. Rev. E*, **67**, 066608 (2003).

[143] S. Flach, C. R. Willis, *Phys. Lett. A*, **181**, 232-238 (1993).

[144] T. Dauxois, M. Peyrard, C. R. Willis, *Phys. D*, **57**, 267-282 (1992).

[145] Y. S. Kivshar, M. Peyrard, *Phys. Rev. A*, **46**, 3198 (1992).

[146] V. Achilleos, A. Alvarez, J. Cuevas, D. J. Frantzeskakis, N. I. Karachalios, P. G. Kevrekidis, B. Sanchez-Rey, *Phys. D*, **244**, 1-24 (2013).

[147] P. Holmes, *Philos-trans. R. Soc. London ser*, **282**, 419 (1979)

[148] R. Tchoukuegno, P. Woafo, *Phys. D*, **167**, 86-100 (2002).

[149] S. Lenci, G. Menditto, A. M. Tarantino, *Int. J. Non-Linear Mech.*, **34**, 615-632 (1999).

[150] B. T. Seaman, M. Krämer, D. Z. Anderson, M. J. Holland, *Phys. Rev. A*, **75**, 023615 (2007).

[151] A. Ruschhaupt, J. G. Muga, *Phys. Rev. A*, **76**, 013619 (2007).

[152] T. F. Viscondi, K. Furuya, *J. Phys. A*, **44**, 175301 (2011).

[153] A Mostafazadeh, *Phys. Rev. A*, **87**, 012103 (2013).

[154] S.H. Weintraub, *Jordan canonical form: Application to differential equations, Synth. Lect. Math. Stat. 1*, **1**, 1–85 (2008).

[155] A. H. Nayfeh, *Nonlinear oscillations, Wiley Interscience applied Maths*, (1979).

[156] H. Hatwall, A. K. Mallik, A. Ghosh, *J. Appl. Mech.*, **50**, 657-662 (1983).

[157] P. R. Aethna, K. R. Meyer, A. K. Bajaj, *J. Appl. Maths*, **45**, 343-359 (1985).

[158] A. H. Nayfeh, D. T. Mook, D. W. Lobtitz, *AIAA*, **12**, 1222-1228 (1974).

[159] A. H. Nayfeh, D. T. Mook, Sridhar, *J. Accoust. Soci. Am.*, **55**, 281-291 (1974).

[160] J. D. Murray, *Asymptotic analysis, Springger-Verlag*, (1984).

[161] R. A. Mahaffeh, *Phys. fluids*, **19**, 1387-1391 (1976).

[162] Y. K. Cheung, S. L. Lau, *J. Appl. Mech.*, *48*, 959-964 (1981).

[163] Y. K. Cheung, S. L. Lau, *J. Appl. Mech.*, **50**, 65-73 (1983).

[164] A. H. Nayfeh, *Introduction to perturbation techniques*, Wiley, (1981).

[165] A. H. Nayfeh and D. T. Mook, *Nonlinear Oscillations*, Wiley-VCH Verlag GmbH, (1995).

[166] A. H. Nayfeh, *Perturbation methods*, Wiley, (1973).

[167] M. H. Holmes, *Introduction to perturbation methods*. Springer, New York, (2013).

[168] K. Li and P. G. Kevrekidis, *Phys. Rev. E*, **83**, 066608 (2011).

[169] A. Mostafazadeh, *Phys. Rev. A.*, **90**, 023833 (2014).

[170] L. Feng, Y.-L. Xu, W. S. Fegasolli, M.-H. Lu, J. E. B. Oliveira, V. R. Almeida, Y.-F. Chen and A. Scherer, *Nat. Mater.*, **12**, 108 (2012).

[171] L. Ge, Y. D. Chong and A. D. Stone, *Phys. Rev. A.*, **85**, 023802 (2012).

[172] Y. Fu, Y. Xu and H. Chen, *Opt. Expr.*, **24**, 1648 (2016).

List of Publications

Publications in International Refereed Journals

1- **Ibrahim Azeghap-Simo**, Fernande Fotsa-Ngaffo, Aurélien Kenfack-Jiotsa, Dynamics of cubic-quintic nonlinear $\mathcal{PT}$-symmetry mechanical oscillators. *Physica D*, **449**, 133750 (2023)

Physica D 449 (2023) 133750

Contents lists available at ScienceDirect

Physica D

journal homepage: www.elsevier.com/locate/physd

Dynamics of cubic–quintic nonlinear $\mathcal{PT}$-symmetry mechanical oscillators

Ibrahim Azeghap-Simo [a,b,*], Fernande Fotsa-Ngaffo [c], Aurélien Kenfack-Jiotsa [b,d]

[a] Laboratory of Mechanics, Materials and Structures, Department of Physics, Faculty of Science, University of Yaoundé I, P.O. Box 812, Yaoundé, Cameroon
[b] Nonlinear and Complex Systems Physics Group, Department of Physics, The Higher Teachers' Training College, University of Yaoundé I, P.O. Box 47, Yaoundé, Cameroon
[c] Institute of Wood Technologies, University of Yaoundé I, P.O. Box 306, Mbalmayo, Cameroon
[d] Department of physics, Higher Teachers' Training College, University of Yaoundé I, P.O. Box 47, Yaoundé, Cameroon

ARTICLE INFO

Article history:
Received 16 September 2022
Received in revised form 13 March 2023
Accepted 7 April 2023
Available online 14 April 2023
Communicated by T. Insperger

Keywords:
Parity-time symmetry
Cubic nonlinearity
Quintic nonlinearity
Fixed points stability
Nonlinear breaking point

ABSTRACT

In this paper, we investigate the dynamics of two mechanical coupled oscillators (MCO) with Parity-Time ($\mathcal{PT}$)-symmetry i.e., one has gain and the other has an equal and opposite amount of loss. In the linear case, the eigenmodes and breaking points were determined. In the nonlinear case, the breaking point for soft cubic or quintic potential obtained numerically was also found analytically with perfect agreement. However, instead of the breaking point, for the hard cubic or quintic potential, it is noted a transition toward a regime of periodic or quasi-periodic stable oscillation with energy transfer from the loss oscillator to the gain oscillator. This latter result suggests very important applications within the framework of the optical cavities and waveguides.

1. Introduction

Inspired by the relevance of the spatially symmetric harmonic oscillator, Bender et al. [1] demonstrated the weakness requirement of the essentially self-adjoint Hamiltonian as the unique possibility for the operator associated to have a real observable. Thus, the axiom of hermiticity has been replaced by the $\mathcal{PT}$-symmetry condition for which the Hamiltonian must simultaneously commutes with the parity inversion ($\mathcal{P}$: $x \rightarrow$ -x, p $\rightarrow$ -p) and time reversal ($\mathcal{T}$: p $\rightarrow$ -p, i $\rightarrow$ -i) operators. Here, p and x are the momentum and the position operators, respectively. Under the $\mathcal{PT}$-symmetry condition, the non-Hermitian Hamiltonian share the same eigenfunctions with the $\mathcal{PT}$ operator. In addition, this Hamiltonian exhibits at least a region in which all the eigenvalues are completely real and then the energy is conserved. However, there exists a critical parameter so-called exceptional point (EP) [2], also referenced as a branch point singularity [3–5] at which all the eigenvalues and their corresponding eigenvectors coalesce (i.e., modes become completely non-orthogonal or parallel). This EP makes the Hamiltonian describing the system non-Hermitian [6,7] likewise EPs exist only in non-Hermitian Hamiltonians. Above the EP, some of the Hamiltonian eigenvalues become complex and the system symmetry is broken, i.e., the Hamiltonian still commutes with the $\mathcal{PT}$ operator but no longer shares the same eigenfunctions.

Thanks to the isomorphism between the quantum Schrödinger and the paraxial optical wave equation in which the refractive index plays the role of the potential, the optics field has provided valuable insights into this initial fairly abstract mathematical demonstration. It is now understood that the $\mathcal{PT}$-symmetry phase is the results of a net compensation between the losses (attenuation or dissipation) and the gain (amplification) in the dynamic of a coupled system [8–15]. This balanced gain and loss condition and the symmetry breaking phase appear under more general non-$\mathcal{PT}$ symmetric systems [3,4,13] called pseudo-Hermitian systems. At the EP, many unconventional properties such as unidirectional invisibility [10,12], non-reciprocal Bloch oscillations [14], chiral behaviour [16], mode selection in lasers [17] and enhanced sensor [18] have been realised.

This flurry of achievements in the realm of the self-consistent quantum theory has boosted the explorations of phase transition at the classical level, where $\mathcal{PT}$-symmetry effective Hamiltonians can be derived. Major thrusts include electronic [19–21], whispery gallery micro cavities [22] as well as phonon laser [23–26] and mechanical coupled oscillators [27–34]. In such systems, intriguing EP effect such as robust wireless power transfer [21], laser linewidth broadening [23], ultralow $\mathcal{PT}$ breaking

* Corresponding author at: Laboratory of Mechanics, Materials and Structures, Department of Physics, Faculty of Science, University of Yaoundé I, P.O. Box 812, Yaoundé, Cameroon.
E-mail address: ibrahima.simo@yahoo.com (I. Azeghap-Simo).

https://doi.org/10.1016/j.physd.2023.133750
0167-2789/

chaos [32], reduced fluctuations due to nonlinear saturation effects and quantum noise combination [33], slow to fast light switching modulation [24] have been successfully predicted. Interestingly, distinctive phenomena arise when nonlinearity comes into play [32,34–36]. For example, it was reported that integrable $\mathcal{PT}$-symmetric Kerr nonlinear structures involving a balanced gain–loss can act as unidirectional optical valves above a critical value of the nonlinearity strength [37]. It was also mentioned that solitons evolving in a $\mathcal{PT}$-symmetric nonlinear chain develop an instability, leading to blow-up when their amplitudes exceed a critical value [38]. On the other hand, it was rather demonstrated that cubic nonlinear terms can soften the $\mathcal{PT}$-symmetry transition and, thus, enable the existence of stable periodic and/or quasi-periodic states at any arbitrary value of the gain–loss parameter γ [31,32,34].

However, as the nonlinearity increases, non-cubic nonlinear terms come into play and give rise to unexpected phenomena whose effects are seldom considered [39]. Depending on the landscape of the potential energy which may have multiple minima, energy exchange between the adjacent minima may exist and play a critical role in the system dynamics and stability [40–42]. Nowadays, there is a lack of investigation on the effect of the fifth power nonlinearity on the dynamics of coupled $\mathcal{PT}$-symmetric systems. This particular nonlinearity seems intriguing and has already found applications in non-coupled cubic–quintic systems such as the propagation of a short electromagnetic pulse in a nonlinear medium [43], the generalised Pochhammer–Chree (PC) problem [44], the Korteweg–de Vries (KdV) nonlinear wave systems [45], and the modelling of free vibration of a restrained uniform beam carrying intermediate lumped mass [46]. From the foregoing, further predictions and understanding of the expected (or not) structural stability of $\mathcal{PT}$-symmetric nonlinear cubic–quintic coupled system remain in progress. The physical model considered in the present work is inspired from [30], where the regions of stable dynamics of the systems were investigated. Our model takes into account the soft and/or hard cubic and quintic nonlinearities. We aim to investigate how the nonlinearity and initial conditions act on the stability region of the mechanical coupled system. Our study provides a better characterisation of the breaking point in nonlinear $\mathcal{PT}$-symmetric systems.

The paper is organised as follows. In Section 2, we provide the general model equations and discuss their symmetries, nonlinear characteristics and displacements will be presented and the dynamics of the system in linear regime will be analysed. In Section 3, we study the nonlinear dynamics of the system in all its generality. Fixed points and their stability are investigated and numerical characterisation of the nonlinear threshold are carried out. Section 4 is devoted to the analytical treatment. We elaborate a characterisation procedure of the nonlinear threshold via averaging method to consolidate the numerical results. We conclude our work in Section 5.

2. Mechanical model

2.1. Equations of motion

The system under investigation is a two damped and linearly coupled mass–spring devices as illustrated in Fig. 1. The first mass (m_1) is subjected to liquid/air natural frictional force proportional to its velocity $\dot{X}_1$ (for sufficiently small velocities to allow friction linearisation). This friction introduces energy loss and thus hinders the mass m_1 motion. The second mass (m_2) is placed on a conveyor, which moves with constant velocity V_c. The conveyor, subjected to roll in a defined direction, drags the mass m_2 whose displacement will compress the spring of stiffness k_n

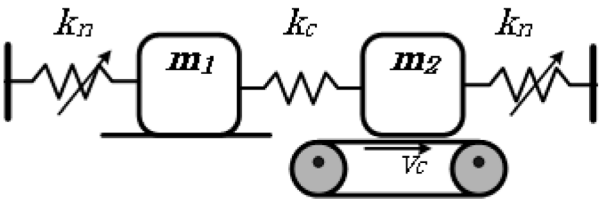

Fig. 1. $\mathcal{PT}$-symmetric mechanical system model.

Table 1
Symmetries of system (2).

Symmetry 1	$(X_1, X_2) \to (-X_1, -X_2)$
Symmetry 2	$(X_1, \kappa) \to (-X_1, -\kappa)$
Symmetry 3	$(\kappa, X_2) \to (-\kappa, -X_2)$
Symmetry 4	$(t, \gamma) \to (-t, -\gamma)$
Symmetry 5	$(X_1, X_2, \gamma) \to (\pm X_1, \pm X_2, -\gamma)$
Symmetry 6	$(X_1, X_2, \alpha, \eta) \to \left(\delta X_1, \delta X_2, {}^{\alpha}/_{\delta^2}, {}^{\eta}/_{\delta^4}\right)$

attached to a fixed support. When the spring tension is greater than the static frictional force exerted by the conveyor surface on the mass m_2 [47], the latter will slip and return to its initial position for a new cycle. The conveyor thus acts as a reservoir that supply the mass m_2 with energy gain. It is said that mass m_2 is subjected to anti-friction or negative friction [30,35]. If the positive and negative frictions are balanced, the coupled masses m_1 and m_2 form a linear $\mathcal{PT}$-symmetric system similar to the ones described in [19,20,27–30]. For the purpose of convenience, we shall assume identical masses $m_1 = m_2 = m$.

Considering that each mass evolves within a nonlinear onsite potential in the form:

$$V(X) = \frac{1}{2}X^2 - \frac{1}{4}\alpha X^4 + \frac{1}{6}\eta X^6, \tag{1}$$

where α and η are real constant parameters representing the cubic and quintic nonlinear terms, respectively. From the Lagrange formalism we obtain the dimensionless coupled damped cubic–quintic Duffing oscillators. Thus, the general equations of motion are described by displacements X_i ($i = 1, 2$) as follows:

$$\begin{cases} \ddot{X}_1 + 2\gamma\dot{X}_1 + X_1 - \alpha X_1^3 + \eta X_1^5 - \kappa X_2 = 0 \\ \ddot{X}_2 - 2\gamma\dot{X}_2 + X_2 - \alpha X_2^3 + \eta X_2^5 - \kappa X_1 = 0 \end{cases}. \tag{2}$$

Here, the coefficient γ is the gain/loss rate of the X_i coordinate which describes its energy gain ($-\gamma < 0$) or loss ($+\gamma > 0$). The parameter κ is the coupling between the masses and the '*dot*' stands for the derivative with respect to time t. Interestingly, there are a number of symmetries that leave the system (2) invariant. These symmetries are listed in Table 1.

Symmetries (1) and (4) constitute the so-called spatial symmetry and time invariance making the nonlinear cubic–quintic Duffing (NCQD) equations a $\mathcal{PT}$-symmetric system.

2.2. Nonlinear characteristics and displacements

The Duffing equation in its various forms is used to approximate many nonlinear systems. The source of nonlinearity is the stiffness and depends on the type or landscape of the potential considered. This simply means that the force applied to the spring, and the resulting displacement X_i have a nonlinear relationship. In this work, when the cubic term is positive (or negative), the spring is said to be softening (or hardening), whereas if the quintic term is positive (or negative) the spring is hardening (softening). In what follows, the force and potential versus deflection for different nonlinearity combinations are described. In the absence of the quintic nonlinear term ($\eta = 0$),

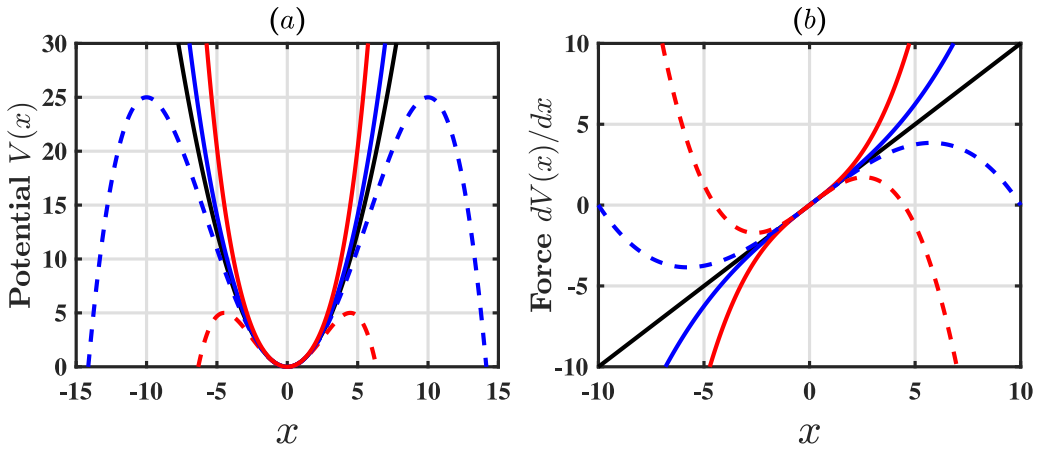

Fig. 2. Potential (a) and Force (b) versus deflection. Linear spring is illustrated by black solid line. Nonlinear cubic hardening spring in solid for $\alpha = -0.01$ (in blue) and $\alpha = -0.05$ (in red) and, nonlinear cubic softening spring in dash line for $\alpha = 0.01$ (in blue) and $\alpha = 0.05$ (in red).

the oscillator features the ϕ^4 potential characteristic. Fig. 2(a) and (b) are plotted to illustrate the soft and hard cubic nonlinear characteristic of the spring, respectively. The case of the linear potential is plotted with the black colour.

It can be observed that the three potentials are monostable and share a common ground state at $X = 0$. However, in these nonlinear hard potentials, oscillations can only exist about the ground state and there is no real possibility for energy explosion. This cubic hard potential is useful in modelling the atomic interaction in a diatomic chain with periodically distributed atoms, characteristic of optical media with spatially modulated refractive index [48]. These media exhibit two branches of the linear wave dispersion curve with opposite signs of dispersion and a gap between the branches. In particular, only heavy atoms can oscillate with frequencies inside the gap and this hard nonlinear potential is studied to localise modes inside the gap of the linear wave spectrum, the so-called gap breathers [49]. In contrast, the soft potential, in addition to the above-mentioned ground state, exhibits a metastable equilibrium state and becomes unbounded beyond its maximum point at $Xm = \sqrt{1/\alpha}$, corresponding to maximal energy of $V_m = 1/4\alpha$. For instance, this soft cubic potential may correspond to the hydrogen-bridge bond between nucleotides [50,51]. It has been successfully used to study the energy-localisation mechanisms in DNA molecules [52]. When the nonlinear cubic term is increased, the well deepens for the hard potential while it is reduced for the soft potential. These analyses agree well with the force deflection which becomes important at $X \geq \sqrt{1/3\alpha}$.

On the other hand, quintic or ϕ^6 nonlinear terms deserve careful investigations as an extension of the cubic nonlinear Duffing oscillator. This is an example of a bounded, catastrophic monostable or multi-stable potential, depending on the cubic and quintic parameters combinations. To simplify the analysis, we introduce the parameter $\eta = \varepsilon\alpha^2$, ε being a real constant parameter and thus the sign of ε is that of η. The nonlinear cubic–quintic potential (NCQP) characteristic for different stiffness combinations is considered in Fig. 3, in dash for quintic softening (negative value of ε) and solid for quintic hardening (positive value of ε). The potential and the force versus deflection are represented for positive and negative values of cubic term respectively.

In top row, when $\alpha = 0.05$ (cubic softening), curves are plotted for $\varepsilon = -0.05$ (dash red), $\varepsilon = -1.0$ (dash blue) and $\varepsilon = -5.0$ (dash green). A single well and two metastable states are exhibited just as in the case of the soft cubic potential. The greater the ε (in negative direction), the softener the potential gets as compared to the cubic one. The nonlinear cubic–quintic potential (NCQP) deflects faster and stronger from the linear one. This potential is extensively used in the modelling of a strongly nonlinear beam with articulated ends under axial excitations mostly used in civil and mechanical engineering to study the action of seismic waves [39,53]. However, when $\varepsilon = 0.1$ (solid green), $\varepsilon = 0.2$ (solid blue) and $\varepsilon = 0.3$ (solid red), the potential evolves from a tri-stable to a monostable, depending on the intensity of ε. Such potentials have found numerous applications in the study of cold atoms quantum tunnelling dynamics with trends atomic diodes and transistors [54,55] and for laser monitoring and control [56] of tunnelling transport in order to create new types of devices.

In bottom row, for $\alpha = -0.05$ (cubic hardening), we have: $\varepsilon = -0.1$ (dash blue), $\varepsilon = -0.2$ (dash green) and $\varepsilon = -0.5$ (dash red). The smaller the ε, the harder the potential gets as compared to the cubic one. This symmetric potential is monostable, with a zero energy centre ground state. It is also observed that the potential and force versus deflection curves are similar to the ones shown in Fig. 2 in the case of the simple nonlinear cubic potential. This means that the negative quintic term strengthens the softening of the system. The quintic term action is to harden the initially soft potential. The potential and force versus deflection are also represented for positive values of ε with $\varepsilon = 0.05$ (solid blue), $\varepsilon = 1.0$ (solid green) and $\varepsilon = 5.0$ (solid red). From Figs. 3(c) and (d), it can be seen that the single-well characteristic associated with a cubic soft or hard potential is similar to the what presented in Figs. 2(a) and (b).

2.3. Linear dynamic

In this regime, $\alpha = 0$ and $\eta = \varepsilon = 0$. The two coupled particles are subjected to a single well bounded potential. Assuming a dynamical solution in the form $X_k = A_k e^{i\omega_k t}$, with A_k being the amplitude, the normal modes are given by Eq. (3)

$$\omega_k = \pm\sqrt{\left(1 - 2\gamma^2\right) \pm \sqrt{\gamma^2 - \gamma_{th}^2}}, \tag{3}$$

where

$$\gamma_{th_{1,2}} = \sqrt{\frac{1}{2}\left(1 \pm \sqrt{1 - \kappa^2}\right)}. \tag{4}$$

$\gamma_{th_{1,2}}$ represents the breaking points. In Fig. 4(a), the real (blue) and the imaginary (red) parts of the normal modes evolution are shown as a function of the gain/loss parameter γ/γ_{th_1} for the coupling parameter $\kappa = 0.65$. This value remains constant

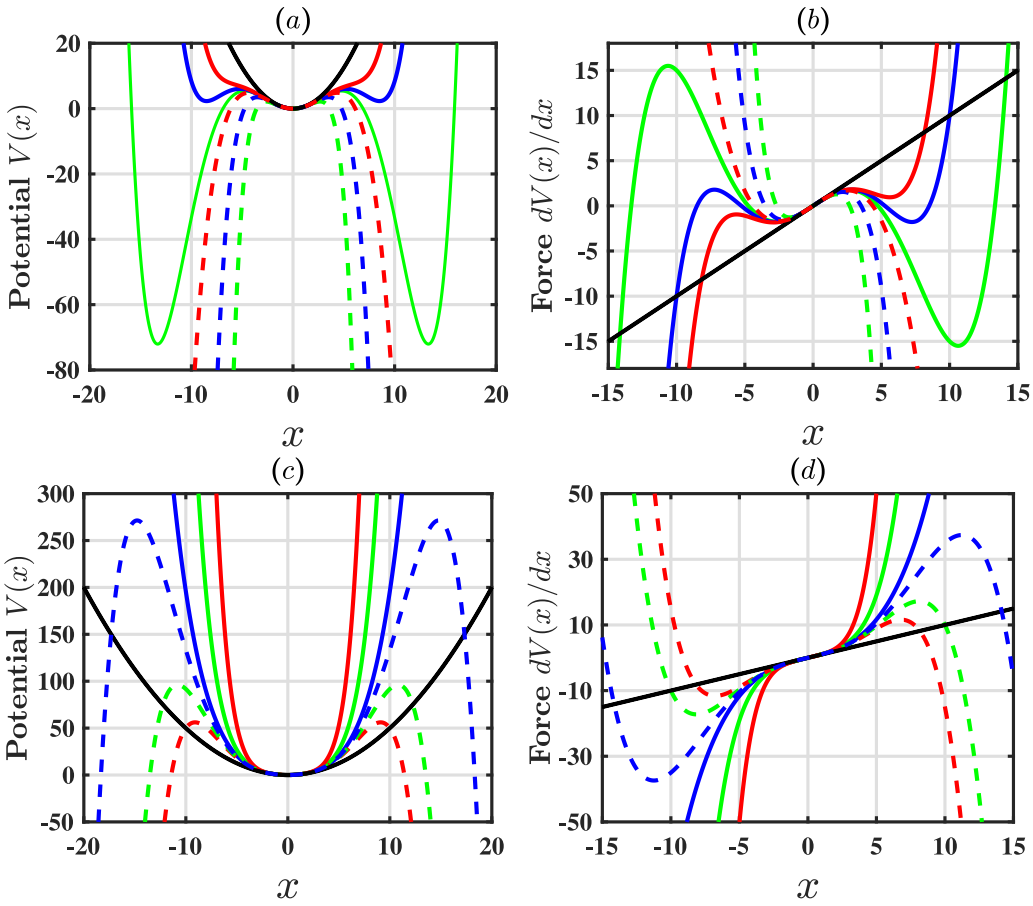

Fig. 3. Potential and force versus deflection with nonlinear cubic–quintic term. The linear case is represented in black colour. The top row is obtained with $\alpha = 0.05$, for $\varepsilon = -0.05, -1.0, -5.0$ respectively in dash red, blue and red colour, and for $\varepsilon = 0.1, 0.2, 0.3$ respectively in solid green, blue and red colour. The bottom row, $\alpha = -0.05$ and the curves are plotted for $\varepsilon = -0.1, -0.2, -0.3$ in dash blue, green and red colour, and for $\varepsilon = 0.05, 1.0, 5.0$ in solid blue, green and red colour respectively.

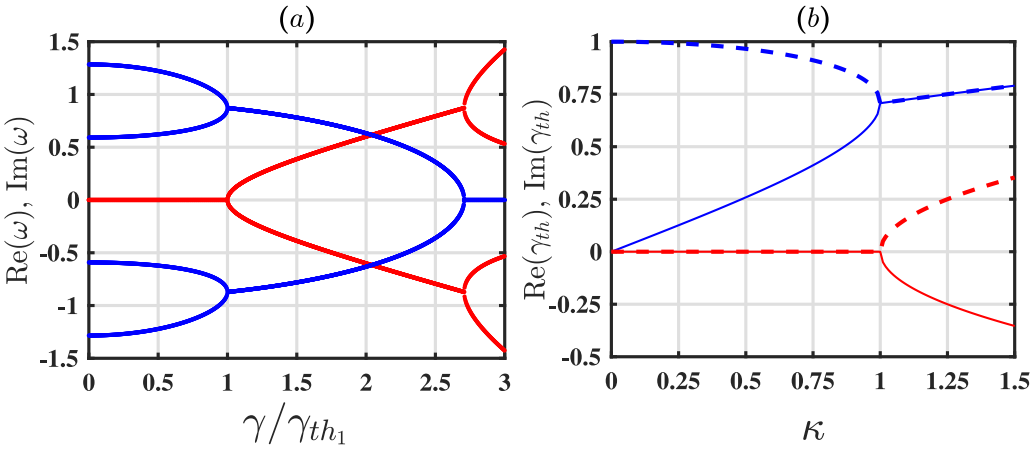

Fig. 4. (a) Normal modes evolution as a function of the normalised gain/loss parameter γ/γ_{th_1} for $\kappa = 0.65$. (b) Breaking point evolution as a function of κ. In both figures, blue colour represents the real part and red colour the imaginary part. In (b), solid line is for γ_{th_1} whereas dashed line corresponds to γ_{th_2}.

throughout the paper. As it can be observed when $\gamma < \gamma_{th_1}$, the symmetric normal modes are purely real as their imaginary part is zero. This region represents the PT exact phase. However, in the region $\gamma_{th_1} < \gamma < \gamma_{th_2}$, corresponding to the PT broken phase (BP), the normal modes are complex and the energy is no longer conserved. Beyond $\gamma = \gamma_{th_2}$, all of the eigenvalues are purely imaginary. Fig. 4(b) depicts the dependence of the real (blue) and imaginary (red) parts of γ_{th} as a function of κ. The first transition γ_{th_1} is represented in solid line whereas the second γ_{th_2} is plotted with the dashed line. As can be seen, γ_{th} is real in the region $\kappa < 1$. Remarkably, γ_{th_1} increases with the coupling, which indicates the broadening of the domain of periodic solutions.

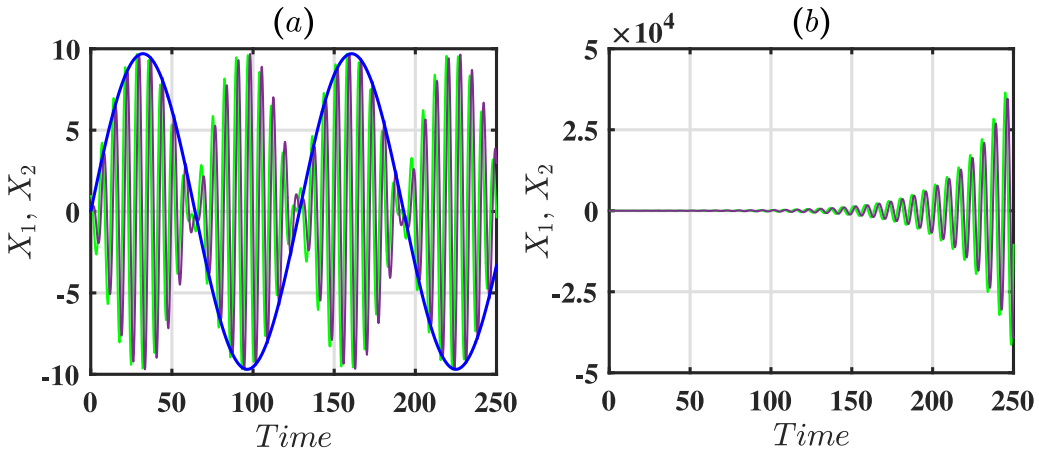

Fig. 5. Temporal evolution in linear limit of system (2). Green colour for the oscillator governed by the displacement X_2 (gain) and purple colour for the one governed by X_1 (loss). (a): in the $\mathcal{PT}$ exact phase. (b): in $\mathcal{PT}$ broken phase.

The exact solutions for the linear system are found using the Jordan canonical form [57] as

$$X_k = \sum_{n=1}^{4} c_k v_{kn} e^{i\omega_n t}, \quad (1 \le k \le 4) \tag{5}$$

where c_k and v_{kn} are constant of integrations and eigenvectors, respectively.

Using the initial conditions on the gain oscillator as: $X_1(0) = 0.0$, $Y_1(0) = 0.0$, $X_2(0) = 1.0$, $Y_2(0) = 0.0$, the temporal evolution of these solutions is represented in Fig. 5. As we can note, when the system is in the PT exact phase for example when $\gamma = 0.99\gamma_{th1}$ (Fig. 5(a)), it exhibits Rabi oscillations [28] of frequency $\Omega_{Rabi} = |\omega_1 - \omega_2|/2$ in blue line colour.

However, when the system is in the broken phase for example for $\gamma = 1.05\gamma_{th_1}$ (see Fig. 5(b)), the oscillations blow up as the time is increasing.

3. Nonlinear dynamics investigation

3.1. Fixed points and their stability

The nonlinear equation given in Eq. (2) can be rewritten in the following way by setting $\dot{X}_i = Y_i$

$$\begin{cases} \dot{X}_1 = Y_1 \\ \dot{Y}_1 = -2\gamma Y_1 - X_1 + \alpha X_1^3 - \varepsilon\alpha^2 X_1^5 + \kappa X_2 \\ \dot{X}_2 = Y_2 \\ \dot{Y}_2 = 2\gamma Y_2 - X_2 + \alpha X_2^3 - \varepsilon\alpha^2 X_2^5 + \kappa X_1 \end{cases}. \tag{6}$$

In what follows, we set κ and γ to be positive with $\kappa < 1$. Let us first analyse the case $\varepsilon = 0$. So, from Eqs. (6), we find for $\alpha > 0$, three fixed points: FP0 $(0,\ 0,\ 0,\ 0)$, FP1 $(\pm a_1,\ 0,\ \pm a_1,\ 0)$, $a_1 = \sqrt{(1-\kappa)/\alpha}$ and FP2 $(\pm a_2,\ 0,\ \mp a_2,\ 0)$, with $a_2 = \sqrt{(1+\kappa)/\alpha}$. For $\alpha < 0$, there is a single fixed point PF0. FP0 is the trivial fixed point; FP1 represents the symmetric branch of the fixed points, whereas FP2 stands for anti-symmetric branch solution.

When $\varepsilon \neq 0$, the system admits one, three or five fixed points, depending on the signs of α and ε.

• For $\alpha > 0$, we distinguish four cases:

Case 1: $0 < \varepsilon < \frac{1}{4(1-\kappa)}$, there are five symmetric fixed points FP0 and FP3 $(\pm q_1^{(\pm)},\ 0,\ \pm q_1^{(\pm)},\ 0)$ with $q_1^{(\pm)} = \sqrt{\frac{\alpha \pm \sqrt{\alpha^2 - 4\varepsilon\alpha^2(1-\kappa)}}{2\varepsilon\alpha^2}}$.

Case 2: $0 < \varepsilon < \frac{1}{4(1+\kappa)}$, there are also five anti-symmetric fixed points FP0 and FP4 $(\pm q_2^{(\pm)},\ 0,\ \mp q_2^{(\pm)},\ 0)$ with $q_2^{(\pm)} = \sqrt{\frac{\alpha \pm \sqrt{\alpha^2 - 4\varepsilon\alpha^2(1+\kappa)}}{2\varepsilon\alpha^2}}$

Case 3: $\varepsilon > \frac{1}{4(1-\kappa)}$ or $\varepsilon > \frac{1}{4(1+\kappa)}$, there is only the trivial fixed point FP0.

Case 4: $\varepsilon < 0$, there are three fixed points FP0 and $(\pm q_1^{(-)},\ 0,\ \pm q_1^{(-)},\ 0)$ or $(\pm q_2^{(-)},\ 0,\ \pm q_2^{(-)},\ 0)$.

• For $\alpha < 0$, there are two cases.

Case 1: $\varepsilon > 0$, there is only the trivial fixed point FP0.

Case 2: $\varepsilon < 0$, there are three fixed points FP0 and $(\pm q_1^{(-)},\ 0,\ \pm q_1^{(-)},0)$ or $(\pm q_2^{(-)},\ 0,\ \pm q_2^{(-)},\ 0)$.

Now, let us investigate the local stability of these fixed points. From Eq. (6), we get the Jacobian matrix below

$$J = \begin{pmatrix} 0 & 1 & 0 & 0 \\ f(x_i) & -2\gamma & \kappa & 0 \\ 0 & 0 & 0 & 1 \\ \kappa & 0 & f(x_i) & 2\gamma \end{pmatrix}. \tag{7}$$

with $f(x_i) = -1 + 3\alpha x_i^2 - 5\varepsilon\alpha^2 x_i^4$, where x_i is the considered fixed point.

Assuming the normalised gain/loss ratio γ/γ_{th} as control parameter, the study of the stability of each fixed point can be done by finding the eigenvalues of the Jacobian matrix J. These eigenvalues are numerically obtained using the Matlab's *eig* function. From the classical local analysis of Lyapunov, a fixed point is stable if all the eigenvalues of J are negative real parts. But if only one eigenvalue is positive real part, the fixed point is unstable. Moreover, if a fixed point admits a pair of purely imaginary conjugate eigenvalues, then it is a Hopf bifurcation point, which leads to a quasi-periodic response. In this study, we will not focus on the fixed points $x_i = \left(a_1,\ a_2,\ q_1^{(-)},\ q_2^{(-)}\right)$ because either they give purely imaginary values according to the nonlinear coefficients, or they do not lead to a bifurcation point. We will analyse the stability of the three fixed points FP0, FP3 which is defined by $q_1^{(+)}$ and FP4 by $q_2^{(+)}$.

Fig. 6 shows the real (a) and imaginary (b) parts of eigenvalues of the linearised system in Eq. (6) with respect to the ratio γ/γ_{th_1}. γ_{th_1} being the first transition point obtained in the linear regime. At the vicinity of FP0 (green colour), the plot is made for any values of ε and α. However, around FP3 (yellow curve), the plot is obtained with $\alpha = 0.01$ and $\varepsilon = 0.71$, whereas for FP4 (red curve) it is obtained for $\alpha = 0.01$ and $\varepsilon = 0.14$.

From the figure, it is noticed that FP0, FP3 and FP4 represent the Hopf bifurcation points. All the considered fixed points display two breaking transition points. For FP3 the first breaking point is above 1 $(\gamma/\gamma_{th_1} > 1)$ and, for FP4 the first transition point is before 1 $(\gamma/\gamma_{th_1} < 1)$ for the chosen parameters. Remarkably, for the FP0 fixed point, the first transition coincides with the

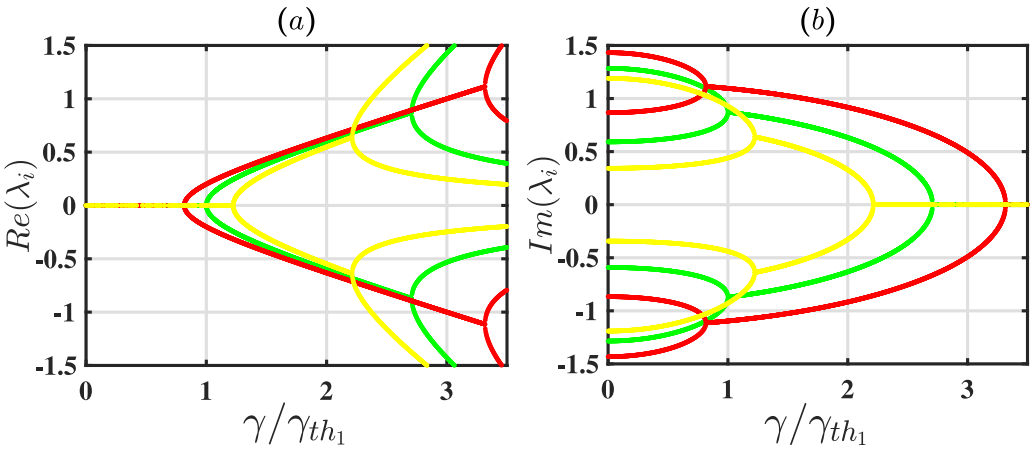

Fig. 6. Real and imaginary parts of the eigenvalues around trivial fixed points. Green curve is for the trivial fixed point. Yellow curve is for the symmetric fixed points $q_1^{(+)}$ obtained with $\alpha = 0.01$ and $\varepsilon = 0.71$, and red curve is for anti-symmetric fixed points $q_2^{(+)}$ obtained with $\alpha = 0.01$ and $\varepsilon = 0.14$. $\kappa = 0.65$.

first breaking point in the linear regime, that is ($\gamma/\gamma_{th_1} = 1$), whatever α and ε are. One can easily see from the green curve that whatever the kind of nonlinearity (cubic or quintic systems), our system exhibits qualitatively the same stability around the trivial fixed point, since the phase transition occurs at $\gamma/\gamma_{th_1} = 1$. This last observation suggests that around the trivial fixed point, the system is indifferent to the effects of nonlinearity and consequently presents an oscillatory regime identical to that obtained in the linear regime. The trivial fixed point serves as reference point. In the following, we show that the breaking point around the fixed point does not only depend on the nonlinearity parameters, but also on the initial conditions.

3.2. Numerical nonlinear threshold analysis

To show the influence of the initial conditions on the breaking point, we have numerically investigated the normalised gain/loss parameter. For this purpose, we have combined the dichotomy and fourth-order Runge Kutta methods and obtained the evolution of the normalised gain/loss (γ/γ_{th_1}) as a function of the nonlinearity parameters of the system. Fig. 7(a), (b) and (c) illustrate this evolution in the cubic soft ($\alpha > 0$), cubic hard ($\alpha < 0$) and quintic hard ($\varepsilon > 0$) cases, respectively. In the cubic case (Fig. 7(a), (b)), the initial conditions ($X_k(0) = X_{0k}$, $Y_k(0) = Y_{0k}$ with $k = 1, 2$) are imposed on the gain oscillator: $X_{01} = 0.0$, $Y_{01} = 0.0$, $X_{02} = 1.0$, $Y_{02} = 0.0$ (green colour), on the loss oscillator: $X_{01} = 1.0$, $Y_{01} = 0.0$, $X_{02} = 0.0$, $Y_{02} = 0.0$ (red colour) and on both oscillators: $X_{01} = \frac{\sqrt{2}}{2}$, $Y_{01} = 0.0$, $X_{02} = \frac{\sqrt{2}}{2}$, $Y_{02} = 0.0$ (blue colour).

However, in the quintic case (Fig. 7(c)), the initial conditions have been imposed on the gain oscillator for $\alpha = 0.01 > 0$ (green colour) and for $\alpha = -0.0001 < 0$ (red colour). As we can see in the cubic cases (Fig. 7(a) and (b)), the oscillatory domain decreases in general when absolute value of nonlinear cubic parameter is increased which indicates that, the threshold in nonlinear regime is lower as compared to the critical value found in linear regime (γ_{th_1}). On the other hand, in the quintic case, we restrict ourselves only to the quintic hard. The curve Fig. 7(c) shows that, for the considered range of ε, this transition increases with the nonlinearity, although it decreases from a certain value of ε (not shown in the figure).

The lower part of each curve corresponds to the $\mathcal{PT}$ exact phase where the energy and symmetric properties of the system remain conserved. The upper part corresponds to the broken phase in which the oscillations will not persist (system with soft nonlinearity) in the time and where asymmetric behaviours can be observed (with hard nonlinearity). In opposition to what we have seen in the previous section, it is important to highlight the effect of the initial conditions of the system. In fact, the curves make it possible to understand that perturbing the system around the trivial fixed point FP0 would correspond to taking a precise value of the cubic stiffness parameter α. For example, in Fig. 7(a), when excitation is fixed on the gain or on the loss oscillators (green and red curve), the only value of α for which the system would be perturbed around the trivial fixed point is equal to 0.01, where the ratio γ/γ_{th_1} is closest to 1 in default. If the excitation is fixed on both oscillators simultaneously (blue curve), the value of α to obtain the linear threshold is 0.06. In other words, if for these initial conditions the value of α is taken differently from the previous ones, then, the system is perturbed around a point different from FP0. Interestingly, the nonlinearity can boost a system around the trivial fixed point by expanding its oscillatory regime as we can observe in the inset plots (Fig. 7(a) and (c)), where $\gamma/\gamma_{th_1} > 1$.

To consolidate the previous results, we analyse in Fig. 8 the temporal evolutions of the system. For different values of the nonlinearity: $\alpha = 0.01$ ((a) and (b)), $\alpha = -10^{-4}$ ((c) and (d)) and $\alpha = 0.01$, $\varepsilon = 0.09$ ((e) and (f)). The green colour represents the response of the gain oscillator while the purple colour is for the loss oscillator. In the top row, the behaviour is illustrated for the normalised gain/loss ratio $\gamma/\gamma_{th_1} = 0.99 < 1$ ($\mathcal{PT}$ exact phase), whereas for the bottom row $\gamma/\gamma_{th_1} = 1$ (PT broken phase). As we can see, in the $\mathcal{PT}$ exact phase, the system exhibits Rabi oscillations (Fig. 8(a), (c) and (e)).

However, in the $\mathcal{PT}$ broken region, the oscillations may either disappear (for soft nonlinear system) after a transient time (Fig. 8(b) for example) or persist (for hard nonlinear system) during a transient time. In this latter case, the gain oscillator has increased to a limiting amplitude. The loss oscillator practically dies down to a limiting amplitude around the trivial fixed point (Fig. 8(d)) or around an another equilibrium point (Fig. 8(f)). This last result indicates that in the $\mathcal{PT}$ broken phase, the system is perturbed around the equilibrium which is not necessarily the trivial fixed point for both oscillators. The nonlinearity has transformed the Rabi oscillations, a formal characteristic of the exact phase, into a robust stable periodic oscillations with constant amplitude.

4. Analytical treatment

Using averaging method [58,59], we look for oscillatory solutions of Eqs. (2) around each fixed point. To do this, we can

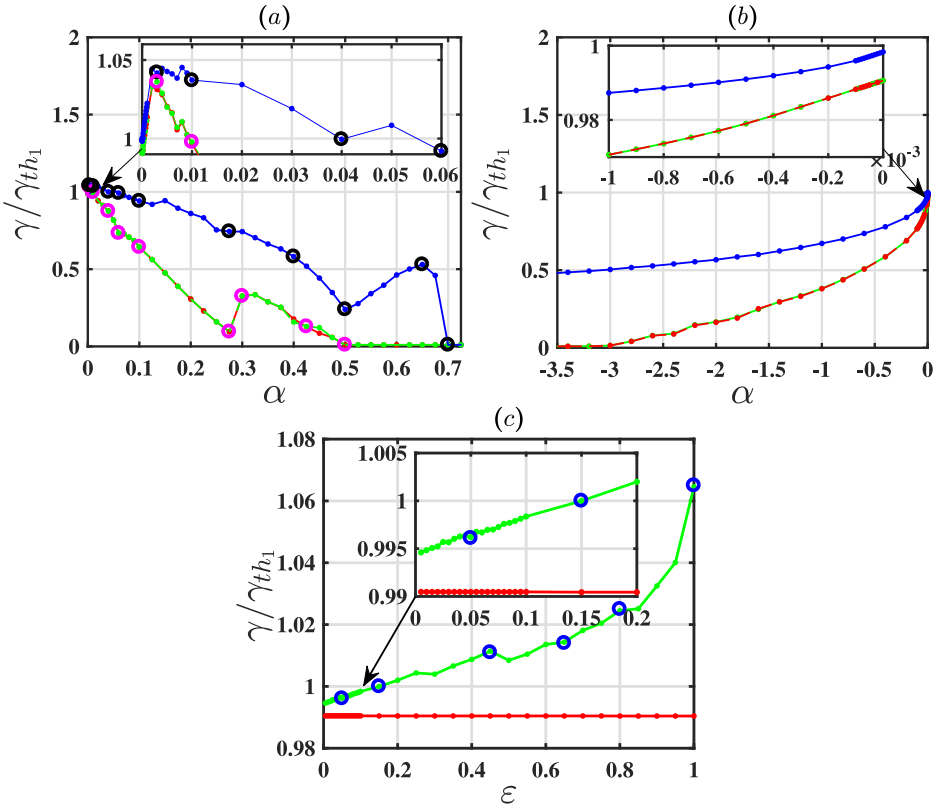

Fig. 7. Effects of cubic and quintic parameters on the stability of the system. For all curves, κ is equal to 0.65. (a) and (b) curves are for soft and hard cubic systems, when $\varepsilon = 0$. (c) curves are for the quintic system, obtained with $\alpha = -10^{-4}$ in red colour and 0.01 in green colour.

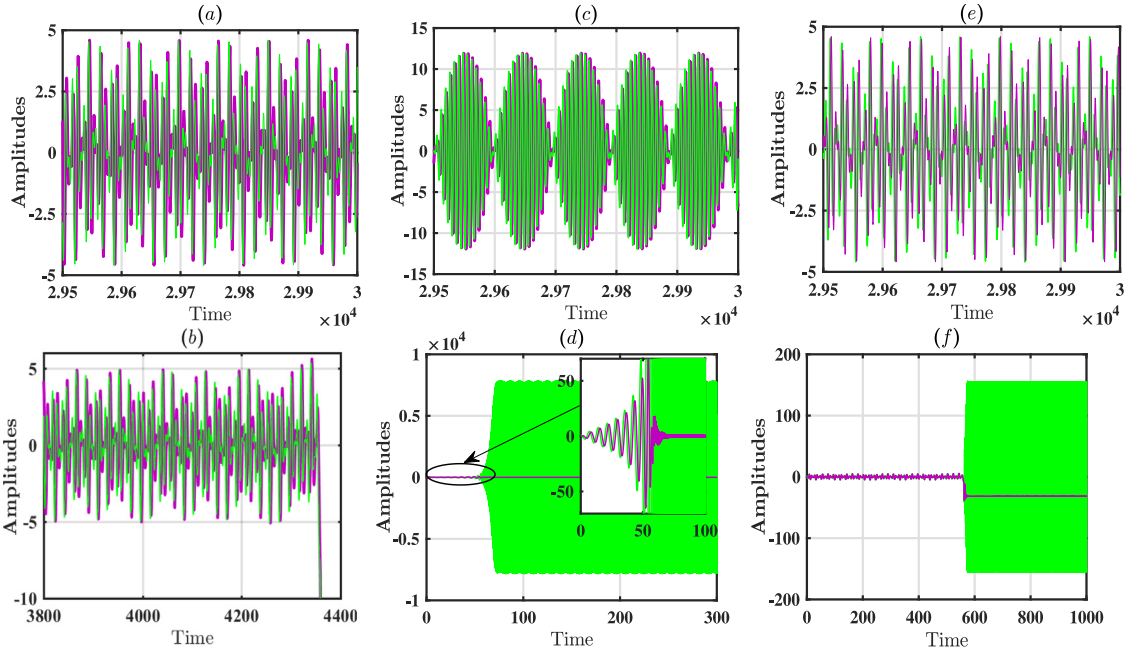

Fig. 8. Dynamical evolutions of the nonlinear cubic ((a), (b), (c) and (d)) and quintic ((e) and (f)) systems around the trivial fixed point. Green colour represents the response of the gain oscillator and purple colour is for the loss oscillator. (a) and (b) $\alpha = 0.01$, (c) and (d) $\alpha = -10^{-4}$ and, (e) and (f) $\alpha = 0.01$, $\varepsilon = 0.09$.

rewrite Eqs. (2) in the general form as

$$\begin{aligned} \ddot{X}_1 + X_1 &= \gamma F_1(X_1, \dot{X}_1, X_2, \dot{X}_2) \\ \ddot{X}_2 + X_2 &= \gamma F_2(X_1, \dot{X}_1, X_2, \dot{X}_2). \end{aligned} \tag{8}$$

we find the solutions in the form

$$\begin{aligned} X_1(t) &= x_{10} + a_1(t)\cos(\omega t + \theta_1(t)) \\ X_2(t) &= x_{20} + a_2(t)\cos(\omega t + \theta_2(t)), \end{aligned} \tag{9}$$

with $a_i(t)$, $\theta_i(t)$, x_{i0} (with $x_{10}^2 = x_{20}^2$) and ω are respectively the amplitude, phase, fixed points and frequency of oscillations of the oscillator i ($i = 1, 2$). The functions F_1 and F_2 become :

$$\begin{aligned}
F_1 &= \tfrac{1}{16\omega}(16(1-\omega^2)a_1 + (10\eta a_1^5 - 12\alpha a_1^3 \\
&\quad +120\eta x_{10}^2 a_1^3 + 80\eta x_{10}^4 a_1 \\
&\quad -48\alpha x_{10}^2 a_1)) \cos(\omega t + \theta_1) + \tfrac{1}{16\omega}(40\eta x_{10} a_1^4 \\
&\quad -24\alpha x_{10} a_1^2) \cos(2\omega t + 2\theta_1) \\
&\quad -2\gamma a_1 \sin(\omega t + \theta_1) + 80\eta x_{10}^3 a_1^2 + \tfrac{x_{10}}{\omega} + \tfrac{\eta a_1^5}{16\omega} \cos(5\omega t + 5\theta_1) + \\
&\quad \tfrac{5\eta x_{10} a_1^4}{8\omega} \cos(4\omega t + 4\theta_1) + \tfrac{(5\eta a_1^5 + 40\eta x_{10}^2 a_1^3 - 4\alpha a_1^3)}{16\omega} \cos(3\omega t + 3\theta_1) \\
&\quad -\tfrac{\kappa a_2}{\omega} \cos(\omega t + \theta_2) + \tfrac{1}{16\omega}(30\eta x_{10} a_1^4 \\
&\quad +80\eta x_{10}^3 a_1^2 + 16\eta x_{10}^5 - 24\alpha x_{10} a_1^2 \\
&\quad -16\alpha x_{10}^3 - 16\kappa x_{20}), \\
F_2 &= \tfrac{1}{16\omega}(16(1-\omega^2)a_2 + (10\eta a_2^5 - 12\alpha a_2^3 \\
&\quad +120\eta x_{20}^2 a_2^3 + 80\eta x_{20}^4 a_2 \\
&\quad -48\alpha x_{20}^2 a_2)) \cos(\omega t + \theta_2) + \tfrac{1}{16\omega}(40\eta x_{20} a_2^4 \\
&\quad -24\alpha x_{20} a_2^2) \cos(2\omega t + 2\theta_2) \\
&\quad +2\gamma a_2 \sin(\omega t + \theta_2) + 80\eta x_{20}^3 a_2^2 + \tfrac{x_{20}}{\omega} + \tfrac{\eta a_2^5}{16\omega} \cos(5\omega t + 5\theta_2) + \\
&\quad \tfrac{5\eta x_{20} a_2^4}{8\omega} \cos(4\omega t + 4\theta_2) + \tfrac{(5\eta a_2^5 + 40\eta x_{20}^2 a_2^3 - 4\alpha a_2^3)}{16\omega} \cos(3\omega t + 3\theta_2) \\
&\quad -\tfrac{\kappa a_1}{\omega} \cos(\omega t + \theta_1) + + \tfrac{1}{16\omega}(30\eta x_{20} a_2^4 + 80\eta x_{20}^3 a_2^2 \\
&\quad +16\eta x_{20}^5 - 24\alpha x_{20} a_2^2 \\
&\quad -16\alpha x_{20}^3 - 16\kappa x_{10}).
\end{aligned} \tag{10}$$

The averaging method requires the amplitudes and phases to be solutions of the system

$$\begin{aligned}
\dot{a}_1 &= \frac{-\gamma\omega}{2\pi} \int_0^{\frac{2\pi}{\omega}} F_1 . \sin(\omega t + \theta_1)\, dt, \\
\dot{\theta}_1 &= \frac{\gamma\omega}{2\pi a_1} \int_0^{\frac{2\pi}{\omega}} F_1 . \sin(\omega t + \theta_1)\, dt, \\
\dot{a}_2 &= \frac{-\gamma\omega}{2\pi} \int_0^{\frac{2\pi}{\omega}} F_2 . \sin(\omega t + \theta_2)\, dt, \\
\dot{\theta}_2 &= \frac{\gamma\omega}{2\pi a_2} \int_0^{\frac{2\pi}{\omega}} F_2 . \sin(\omega t + \theta_2)\, dt.
\end{aligned} \tag{11}$$

Substituting Eqs. (10) into Eqs. (11), we obtain the following first-order differential equations for the amplitudes and phases:

$$\begin{aligned}
\dot{\theta}_1 &= \tfrac{-\kappa a_2 \sin(\theta) - 2\gamma\omega a_1}{2\omega}, \\
\dot{a}_1 &= \tfrac{1}{16\omega}(8(1-\omega^2)a_1 - 8\kappa a_2 \cos(\theta) + 5\eta a_1^5 \\
&\quad +60\eta x_{10}^2 a_1^3 + 40\eta x_{10}^4 a_1 \\
&\quad -6\alpha a_1^3 - 24\alpha x_{10}^2 a_1), \\
\dot{\theta}_2 &= \tfrac{\kappa a_1 \sin(\theta) + 2\gamma\omega a_2}{2\omega}, \\
\dot{a}_2 &= \tfrac{1}{16\omega}(8(1-\omega^2)a_2 - 8\kappa a_1 \cos(\theta) + 5\eta a_2^5 \\
&\quad +60\eta x_{20}^2 a_2^3 + 40\eta x_{20}^4 a_2 \\
&\quad -6\alpha a_1^3 - 24\alpha x_{20}^2 a_2).
\end{aligned} \tag{12}$$

where $\theta = \theta_1 - \theta_2$.

The equilibrium states $a_1 = A_{01}$, $a_2 = A_{02}$ and $\theta = \theta_0$ of Eqs. (12) are defined by the following nonlinear algebraic equation in A_{01}. (θ_0 can be obtained after substitution of A_{01} and A_{02} into the first and third relations of Eqs. (12)).

$$\begin{aligned}
&\tfrac{25}{64}\eta^2 A_{01}^8 + (\tfrac{75}{8}\eta^2 x_{10}^2 - \tfrac{15}{16}\alpha\eta) A_{01}^6 + (\tfrac{125}{2}\eta^2 x_{10}^4 \\
&\quad -15\alpha\eta x_{10}^2 + \tfrac{9}{16}\alpha^2 - \tfrac{5}{4}\eta\omega^2 + \\
&\tfrac{5}{4}\eta) A_{01}^4 + (-\tfrac{105}{2}\alpha\eta x_{10}^4 - 15\eta x_{10}^2\omega^2 + 15\eta x_{10}^2 \\
&\quad -\tfrac{3}{2}\alpha + \tfrac{3}{2}\alpha\omega^2 + 75\eta^2 x_{10}^6 + \\
&\tfrac{9}{2}\alpha^2 x_{10}^2) A_{01}^2 + 25\eta^2 x_{10}^8 - 30\alpha\eta x_{10}^6 - 10\eta x_{10}^4\omega^2 \\
&\quad +9\alpha^2 x_{10}^4 + 6\alpha x_{10}^2\omega^2 + \\
&10\eta x_{10}^4 + 4\gamma^2\omega^2 + \omega^4 - 6\alpha x_{10}^2 - \kappa^2 - 2\omega^2 + 1 = 0.
\end{aligned} \tag{13}$$

The amplitudes are related by

$$A_{02}^2 = A_{01}^2. \tag{14}$$

Using the Newton–Raphson algorithm, we can determine the amplitude behaviour of the system when certain parameters are varied. The response curves of the amplitudes are shown in Fig. 9. The cubic soft system ($\alpha > 0$) is represented on the top row, while the cubic hard system ($\alpha < 0$) is shown on the bottom row. Thus, Figs. 9(a_1) and 9(a_2) display the frequency-response shapes for three given values of γ and two fixed values of α. In addition, in Figs. 9(b_1) and 9(b_2), as well as in Figs. 9(a_1) and 9(a_2), the amplitude depicts the curves function of the gain/loss parameters for the same three given values of α and two fixed values of ω. Moreover, in Figs. 9(c_1) and 9(c_2), the nonlinear-response curves are presented for three fixed values of γ and two fixed values of ω.

We can see in Figs. 9(a_1) and 9(a_2) that, for a chosen value of the nonlinearity, the amplitude decreases when γ increases. The figure presents three different regions: one region with two amplitudes, another with one amplitude and the last region without amplitude which delimits the zone where the response of the system to an initial excitation does not exist. From a qualitative point of view, these curve responses can describe the hysteresis phenomenon. Indeed, for each type of system, we have two branches of solutions. The first branch is linked to the lowest value of the two eigenmodes of the linear system (values at small amplitudes) and the second branch is related to the uppest value.

In the cubic soft system, i.e. in Fig. 9(a_1), if the initial conditions force the system to evolve on the first branch, the amplitude jump phenomenon will be observed when the frequency reaches the first eigenmode of the linear system. But, if the conditions constrain the system to move on the second branch, there will be no jump phenomenon even when ω decreases. In the cubic hard system (see Fig. 9(a_2)), as ω increases, the amplitude will evolve along the first branch (highest branch) until it reaches a certain value corresponding to a critical frequency beyond which there are no longer solutions. However, when ω decreases, it will be possible, depending on the initial conditions of the system, that the amplitude follows the first branch or the second branch. In the case where the amplitude follows the second branch, a jump phenomenon will be observed when ω will attain the largest value of the eigenmodes of the linear system. In particular, it can be seen that soft and hard systems have opposite behaviours when ω varies. Indeed, in the soft case, when ω increases the amplitude decreases and when ω decreases, the amplitude increases. But in the hard case, the opposite takes place.

Figs. 9(b_1) and 9(b_2) represent the behaviour of the amplitude of oscillations according to the normalised parameter γ/γ_{th_1}. Although for some parameter values one can observe regions with or without amplitudes, these curves simply show us where the threshold is located. As we can see, as the normalised parameter γ/γ_{th_1} increases, the amplitude decreases until an extreme value of γ/γ_{th_1} from which there is no amplitude. Thus, this extreme value of γ/γ_{th_1} (as represented on panels (b_1) and (b_2) by the

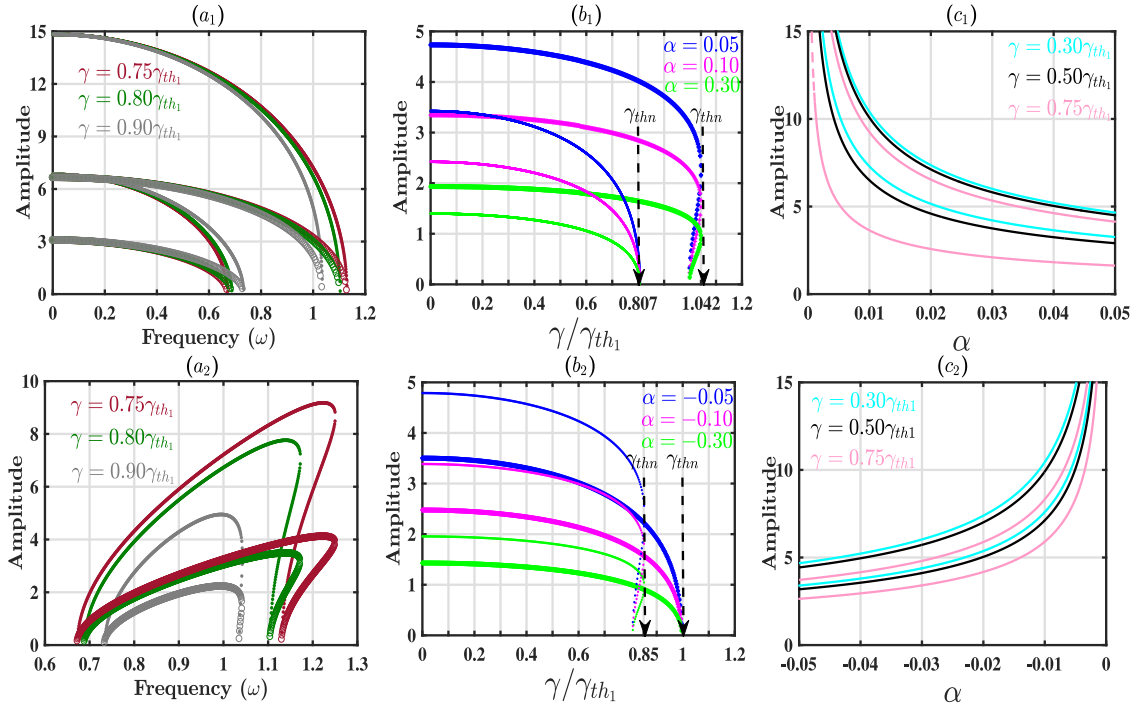

Fig. 9. Analytical response curves for the cubic system. The cubic soft and hard systems are represented respectively in the top and bottom row. In (a_1) and (a_2), the *dot* is for $|\alpha| = 0.01$ and the *circle* is for $|\alpha| = 0.05$. In (b_1) and (b_2), the *star* is $\omega = 0.9$ when the *dot* is $\omega = 1.1$. Finally, (c_1) and (c_2) are obtained with $\omega = 0.9$ in *star* and $\omega = 1.1$ in *dot*.

dashed arrows) designates the threshold of the system in the nonlinear regime, which we will define as the nonlinear breaking point. The reason for referring to this extreme value as the nonlinear breaking point is simply that it depends on the nonlinearity coefficients. Indeed, from the numerically obtained Fig. 7, we can see that there is a correlation between the normalised gain–loss parameter and the nonlinear coefficient. For instance, for $\omega = 0.9$ (star curve), we can see that beyond the extreme values $\gamma/\gamma_{th_1} = 1.042$ in Fig. 9(b_1) or $\gamma/\gamma_{th_1} = 1.0$ in Fig. 9(b_2), there are no longer solutions. These extreme values correspond precisely to the threshold values obtained numerically for $\alpha = 0.003$ when the system is initially excited in equal proportions on both oscillators. On the other hand, we can see that the increasing of the nonlinearity reduces the amplitude without moving the nonlinear breaking point; this seems intriguing in the light of the numerical curves obtained in Fig. 7 which prove the opposite. However, regardless of α, there is a single value of the frequency that corresponds to the breaking point. This means analytically that the nonlinear breaking point depends explicitly on the frequency. Thus, as we have predicted, from Figs. 9(c_1) and 9(c_2), we can see that the amplitude of oscillations decreases as the absolute value of the nonlinearity is increasing and the normalised gain/loss parameter decreases.

With the quintic system ($\varepsilon \neq 0$), the results obtained seem identical to those found in the cubic system. Fig. 10 and Fig. 11 also show the behaviour of the oscillations amplitude under the influence of the system's parameters (ω, γ/γ_{th_1} and ε), at α fixed. In Fig. 10, the curves are plotted with $+\varepsilon$ while in Fig. 11, they are obtained with $-\varepsilon$. In each panel of Fig. 10 and Fig. 11, the top row is realised with $\alpha = 0.01$ and the bottom row with $\alpha = -0.01$. In Figs. 10 and 11, the panels (a_1) and (a_2) show the frequency response, (b_1) and (b_2) exhibit the normalised parameter amplitude characteristic and (c_1) and (c_2) display the effect of the quintic term on the amplitude. The panels Figs. 10(a_2), (b_2) and the panels Figs. 11(a_2), (b_2) are very similar to ones of Figs. 9(a_2), (b_2), Figs. 9(a_1), (b_1), respectively, of the cubic case. Indeed, this result is due to the same nature of the nonlinear cubic and quintic parameters (i.e. $\alpha_{soft}/\varepsilon_{soft}$ or $\alpha_{hard}/\varepsilon_{hard}$). However, when they are different in nature, the amplitude-response curves are slightly different as is the case Figs. 10(a_1), (b_1), and in Figs. 11(a_1), (b_1). This difference is reflected by the existence of a third branch of solutions in a certain region. In Figs. 10(c_1), (c_2) and 11(c_1), (c_2), we provide the amplitude-response curves as a function of the quintic nonlinearity parameter ε for two fixed values of γ and ω. As expected, the curves show that the amplitude of the oscillations decreases with the nonlinearity. In particular, in Fig. 10(c_1) and Fig. 11(c_2), it is observed the existence of two regions: one with three values and the other with a single value of amplitude. This simply indicates that, depending on the region, the system's potential is either three-well stable or one-well stable.

From the foregoing, while the order of the nonlinearity increases, the characterisation procedure of the nonlinear threshold remains unaffected i.e., by looking for the extreme value of the ratio γ/γ_{th_1} given by the curve $A(\gamma/\gamma_{th_1})$. In order to conciliate the analytical results with the numerical ones in the following, we perform a simple analysis which consists in showing the interdependence between the frequency ω and the gain–loss parameter γ in nonlinear regime for some values of the nonlinearities. Indeed, for each nonlinearity value (cubic and/or quintic), there is a unique value of the threshold transition associated with a given frequency. We present in Tables 2 and 3 the relation between cubic/quintic nonlinearity, frequency and threshold respectively for the cubic soft (one and both side excitations), and for the quintic hard with $\alpha = 0.01$ (one side excitation). Each pair of points $(\alpha, \gamma/\gamma_{th_1})$ and $(\varepsilon, \gamma/\gamma_{th_1})$ taken from Tables 2 and 3, respectively, has been represented by blue, magenta and black circles on the same graphs obtained numerically (see Fig. 7). Thus, we notice in Fig. 7 a very good matching between some analytically chosen points and the numerical results.

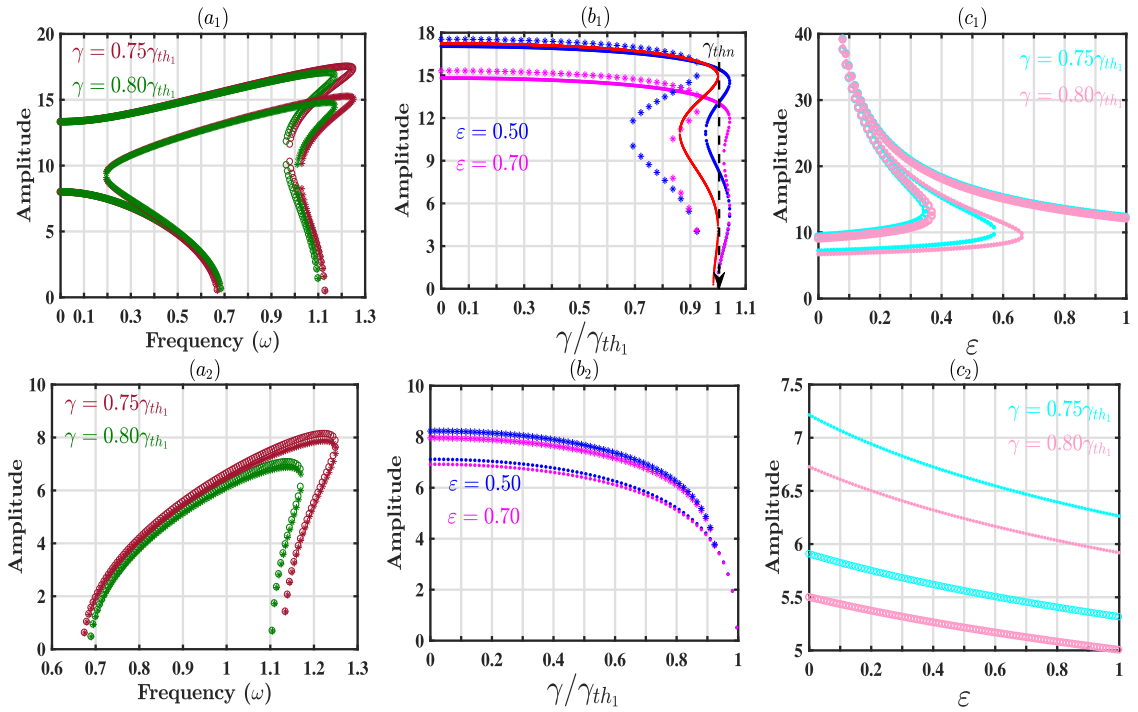

Fig. 10. Analytical response curves for the quintic hard system ($\varepsilon > 0$). In the top row, the nonlinearity cubic parameter is $\alpha = 0.01$ while, in the bottom row, it is $\alpha = -0.01$. (a_1) and (a_2) present the frequency-responses plotted for $\varepsilon = 0.5$ in *circle* and for $\varepsilon = 0.7$ in *star*. (b_1) and (b_2) show the normalised gain/loss parameter response obtained with $\omega = 0.9$ in *dot* and $\omega = 1.0$ in *star*. (c_1) and (c_2) displayed the quintic coefficient responses plotted with $\omega = 0.9$ in *circle* and $\omega = 1.0$ in *dot*.

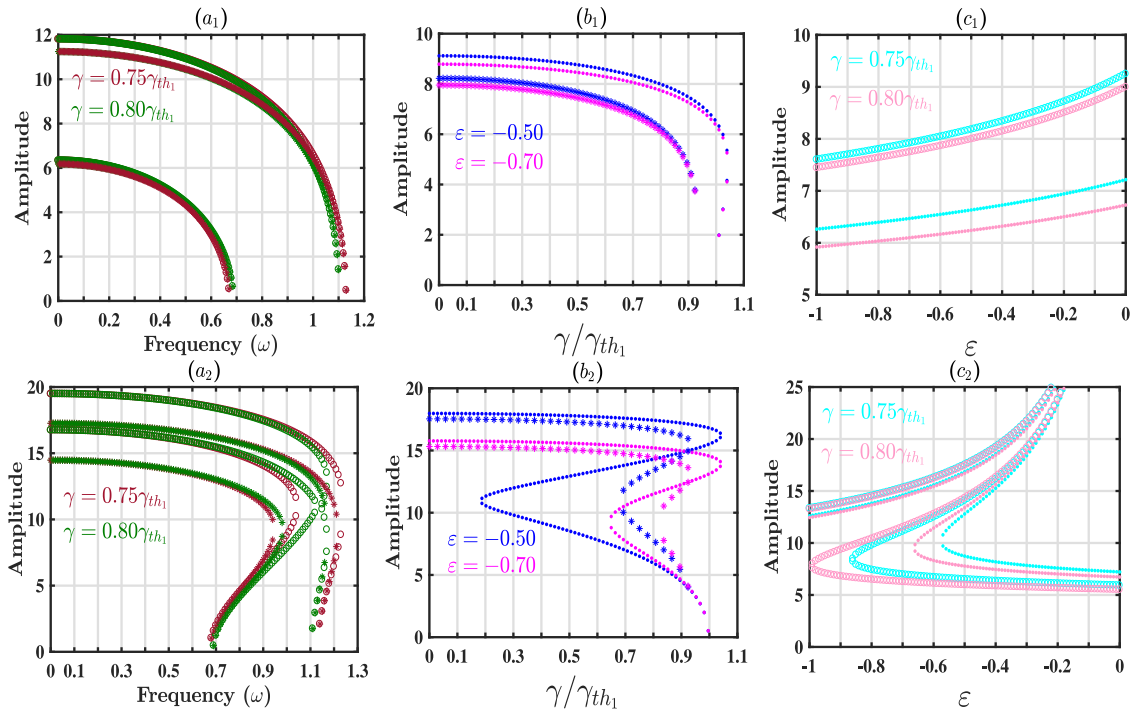

Fig. 11. Analytical response curves for the quintic soft system ($\varepsilon < 0$). In the top row, $\alpha = 0.01$ and in the bottom row, $\alpha = -0.01$. (a_1) and (a_2) present the frequency-responses curves obtained for $\varepsilon = -0.5$ in *circle* and for $\varepsilon = -0.7$ in *star*. (b_1) and (b_2) displayed the normalised gain/loss parameter responses plotted for $\omega = 0.9$ in *dot* and $\omega = 1.0$ in *star*. In (c_1) and (c_2), the quintic coefficient responses are represented for $\omega = 0.9$ in *circle* and $\omega = 1.0$ in *star*.

Table 2
Correspondence between the frequency of oscillations and numerical breaking point in the cubic soft system.

One side excitation			Both sides excitation		
ω	γ/γ_{th_1}	α	ω	γ/γ_{th_1}	α
0.905000	1.03600	0.003	**0.900000**	1.0420	0.003
0.940000	0.99780	0.010	**0.905000**	1.0370	0.010
1.055000	0.87530	0.040	**0.938400**	0.9995	0.040
1.138500	0.73350	0.060	**0.945500**	0.9920	0.060
1.176600	0.64290	0.100	**0.997000**	0.9408	0.100
1.282370	0.09499	0.275	**1.133500**	0.7439	0.275
1.258790	0.32590	0.300	**1.198100**	0.5811	0.400
1.280570	0.12890	0.425	**1.270750**	0.2395	0.500
1.284499	0.01000	0.500	**1.213600**	0.5302	0.650
			1.284499	0.0100	0.700

Table 3
Correspondence between the frequency of oscillations and numerical breaking point in the quintic hard system for $\alpha = 0.01$.

One side excitation					
ω	**0.9415**	**0.9379**	**0.9300**	**0.9210**	**0.8809**
γ/γ_{th_1}	0.9961	1.0000	1.0080	1.0180	1.0650
ε	0.05	0.150	0.500	0.700	1.000

5. Conclusion

We have studied two coupled $\mathcal{PT}$-symmetric nonlinear mechanical oscillators. In the linear case, we presented the eigenmodes and memory breaking. In the nonlinear case, a perfect agreement between numerical and analytical computations was determined while establishing the breaking point for soft cubic or quintic potential. It is important to note that the nonlinearity boosts the system by expanding its oscillatory regime. On one hand, the threshold in the nonlinear case could occur beyond the one obtained in the linear case. On the other hand, for hard cubic or quintic potentials, there is a transition toward a regime of stable oscillation (periodic or quasi-periodic) with energy transfer from one oscillator to another (from the lossy oscillator toward the gain one). This latter result suggests important applications in the field of coupled waveguides (data transmission), as well as optical cavities. We have also shown through numerical simulations that the nonlinear breaking point depends on the way energy is initially distributed between the two oscillators.

CRediT authorship contribution statement

Ibrahim Azeghap-Simo: Conceptualization, Data curation, Formal analysis, Methodology, Software, Writing – review & editing. **Fernande Fotsa-Ngaffo:** Project administration, Resources, Supervision, Validation, Visualization, Data curation, Formal analysis, Methodology, Software, Writing – original draft, Writing – review & editing. **Aurélien Kenfack-Jiotsa:** Project administration, Resources, Supervision, Validation, Visualization, Writing – review.

Declaration of competing interest

The authors declare that they have no known competing financial interests or personal relationships that could have appeared to influence the work reported in this paper.

Data availability

Data will be made available on request.

Acknowledgements

The authors would like to thanks Dr Emmanuel Fendzi Donfack and Dr Senghor Tagouegni for their fruitful discussions, and Professor Aloysius Nguefac for his help in improving the language.

References

[1] C.M. Bender, S. Boettcher, Real spectra in non-Hermitian Hamiltonians having $\mathcal{PT}$-symmetry, Phys. Rev. Lett. 80 (1998) 5243.
[2] C.M. Bender, B.K. Berntson, D. Parker, E. Samuel, Observation of $\mathcal{PT}$ phase transition in a simple mechanical system, Amer. J. Phys. 81 (2013) 173.
[3] W.D. Heiss, Exceptional points of non-Hermitian operators, J. Phys. A: Math. Gen. 37 (2004) 2455.
[4] M.V. Berry, Physics of non-Hermitian degeneracies, Czechoslov. J. Phys. 54 (2004) 1039–1047.
[5] S. Klaiman, U. Günther, N. Moiseyev, Visualization of branch points in $\mathcal{PT}$-symmetric waveguides, Phys. Rev. Lett. 101 (2008) 080402.
[6] P.M. Morse, H. Feshbach, Methods of Theoretical Physics, McGraw-Hill, New York, 1953.
[7] J. Schnabel, H. Cartarius, J. Main, G. Wunner, W.D. Heiss, $\mathcal{PT}$-Symmetric waveguide system with evidence of a third-order exceptional point, Phys. Rev. A 95 (2017) 053868.
[8] Z.H. Musslimani, K.G. Makris, R. El-Ganainy, D.N. Christodoulides, Optical solitons in $\mathcal{PT}$ periodic potentials, Phys. Rev. Lett. 100 (2008) 030402.
[9] K.G. Makris, El-Ganainy, D.N. Christodoulides, Z.H. Musslimani, Beam dynamics in $\mathcal{PT}$-symmetric optical lattices, Phys. Rev. Lett. 100 (2008) 103904.
[10] R. El-Ganainy, K.G. Makris, D.N. Christodoulides, Z.H. Musslimani, Theory of coupled optical $\mathcal{PT}$-symmetric structures, Opt. Lett. 32 (2007) 2632–2634.
[11] R. El-Ganainy, K.G. Makris, M. Khajavikhan, Z.H. Musslimani, S. Rotter, D.N. Christodoulides, Non-Hermitian physics and $\mathcal{PT}$-symmetry, Nat. Phys. 14 (2018) 11–19.
[12] Z. Lin, H. Ramezani, T. Eichelkraut, T. Kottos, H. Cao, D.N. Christodoulides, Unidirectional invisibility induced by $\mathcal{PT}$-symmetric periodic structures, Phys. Rev. Lett. 106 (2011) 213901.
[13] S.V. Suchkov, F. Fotsa-Ngaffo, A. Kenfack-Jiotsa, A.D. Tikeng, T.C. Kofane, Y.S. Kivshar, A.A. Sukhorukov, Non-Hermitian trimers: $\mathcal{PT}$-symmetry versus pseudo-hermiticity, New J. Phys. 18 (2016) 065005.
[14] C.E. Rüter, K.G. Makris, R. El-Ganainy, D.N. Christodoulides, M. Segev, D. Kip, Observation of parity-time symmetry in optics, Nat. Phys. 6 (2010) 192.
[15] S.V. Suchkov, A.A. Sukhorukov, J. Huang, S.V. Dmitriev, C. Lee, Y.S. Kivshar, Nonlinear switching and solitons in $\mathcal{PT}$-symmetric photonic systems, Laser Photonics Rev. 10 (2016) 177.
[16] B. Peng, et al., Chiral modes and directional lasing at exceptional points, Proc. Natl. Acad. Sci. USA 113 (2016) 6845–6850.
[17] B. Peng, et al., Loss-induced suppression and revival of lasing, Science 346 (2014) 328–332.
[18] W. Chen, S.K. Özdemir, G. Zhao, J. Wiersig, L. Yang, Exceptional points enhance sensing in an optical microcavity, Nature 548 (2017) 192–196.
[19] J. Schindler, A. Li, M.C. Zheng, F.M. Ellis, T. Kottos, Experimental study of active LRC circuits with $\mathcal{PT}$ symmetries, Phys. Rev. A 84 (2011) 040101.
[20] F. Fotsa-Ngaffo, S.B. Tabeu, S. Tagouegni, A. Kenfack-Jiotsa, Thresholdless characterization in space and time reflection symmetry electronic dimers, J. Opt. Soc. Amer. B 34 (3) (2017) 658–667.
[21] S. Assawaworrarit, X. Yu, S. Fan, Robust wireless power transfer using a nonlinear parity-time symmetric circuit, Nature 546 (2017) 387.
[22] B. Peng, S.K. Özdemir, F. Lei, F. Monifi, M. Gianfreda, G.L. Long, S. Fan, F. Nori, C.M. Bender, L. Yang, Parity-time symmetric whispering-gallery microcavities, Nat. Phys. 10 (2014) 394.
[23] J. Zhang, B. Peng, S.K. Özdemir, K. Pichler, D.O. Krimer, G. Zhao, F. Nori, Yu-xi. Liu, S. Rotter, L. Yang, A phonon laser operating at an exceptional point, Nature Photon. 12 (2018) 479–484.
[24] H. Lü, C. Wang, L. Yang, H. Jing, Optomechanically induced transparency at exceptional points, Phys. Rev. A 10 (2018) 014006.
[25] X.-W. Xu, Y. Liu, C.-P. Sun, Y. Li, Mechanical $\mathcal{PT}$-symmetry in coupled optomechanical systems, Phys. Rev. A 92 (2015) 013852.
[26] Y.-L. Liu, R. Wu, J. Zhang, S.K. Özdemir, L. Yang, F. Nori, Y. Liu, Controllable optical response by modifying the gain and loss of a mechanical resonator and cavity mode in an optomechanical system, Phys. Rev. A 95 (2017) 013843.
[27] C.M. Bender, B.K. Berntson, D. Parker, E. Samuel, Observation of $\mathcal{PT}$ phase transition in a simple mechanical system, Amer. J. Phys. 81 (2013) 173–179.
[28] C.M. Bender, M. Gianfreda, S.K. Özdemir, B. Peng, L. Yang, Twofold transition in $\mathcal{PT}$-symmetric coupled oscillators, Phys. Rev. A 88 (2013) 062111.

[29] C.M. Bender, M. Gianfreda, S.P. Klevansky, Systems of coupled $\mathcal{PT}$-symmetric oscillators, Phys. Rev. A 90 (2014) 022114.
[30] E.D. Tsoy, Coupled oscillators with parity-time symmetry, Phys. Lett. A 381 (2017) 462–466.
[31] I.V. Barashenkov, M. Gianfreda, An exactly solvable $\mathcal{PT}$-symmetric dimer from a Hamiltonian system of nonlinear oscillators with gain and loss, J. Phys. A 47 (2014) 282001.
[32] X.-Y. Lü, H. Jing, J.-Y. Ma, Y. Wu, $\mathcal{PT}$-Symmetry-breaking chaos in optomechanics, Phys. Rev. Lett. 114 (2015) 253601.
[33] J. Cuevas, P.G. Kevrekidis, A. Saxena, A. Khare, $\mathcal{PT}$-Symmetric dimer of coupled nonlinear oscillators, Phys. Rev. A 88 (2013) 032108.
[34] K.V. Kepesidis, T.J. Milburn, J. Huber, K.G. Makris, S. Rotter, P. Rabl, $\mathcal{PT}$-Symmetry breaking in the steady state of microscopic gain-loss systems, New J. Phys. 18 (2016) 095003.
[35] A.A. Andronov, A.A. Vitt, S.E. Khaikin, Theory of Oscillators, Dover Books on Elet Eng, 2011.
[36] A.E. Miroshnichenko, B.A. Malomed, Y.S. Kivshar, Nonlinearly-$\mathcal{PT}$-symmetric systems: Spontaneous symmetry breaking and transmission resonances, Phys. Rev. A 84 (2011) 012123.
[37] H. Ramezani, T. Kottos, Unidirectional nonlinear $\mathcal{PT}$-symmetric optical structures, Phys. Rev. A 82 (2010) 043803.
[38] S.V. Suchkov, B.A. Malomed, S.V. Dmitriev, Y.S. Kivshar, Solitons in a chain of parity-time-invariant dimers, Phys. Rev. E 84 (2011) 046609.
[39] R. Tchoukuegno, P. Woafo, Dynamics and active control of motion of a particle in a ϕ^6 potential with a parametric forcing, Physica D 167 (2002) 86–100.
[40] R. Tchoukuegno, B.R. Nana Nbendjo, P. Woafo, Linear feedback and parametric controls of vibration and chaotic escape in a ϕ^6 potential, Int. J. Non-Linear Mech. 38 (2003) 531–541.
[41] J. Argyris, V. Belubekian, N. Ovakimyan, M. Minasyan, Chaotic vibrations of a nonlinear viscoelastic beam, Chaos Solitons Fractals 7 (1996) 151–163.
[42] B.R. Nana Nbendjo, R. Tchoukuegno, P. Woafo, Active control with delay of vibration and chaos in a double-well Duffing oscillator, Chaos Solitons Fractals 18 (2003) 345–353.
[43] A.I. Maimistov, Propagation of an ultimately short electromagnetic pulse in a nonlinear medium described by the fifth-order Duffing model, Opt. Spectrosc. 94 (2003) 251–257.
[44] Z. Yan, A new sine-Gordon equation expansion algorithm to investigate some special nonlinear differential equations, Chaos Solitons Fractals 23 (2005) 767–775.
[45] D.J. Huang, H.Q. Zhang, Link between travelling waves and first order nonlinear ordinary differential equation with a sixth-degree nonlinear term, Chaos Solitons Fractals 29 (2006) 928–941.
[46] M.N. Hamdan, N.H. Shabaneh, On the large amplitude free vibrations of a restrained uniform beam carrying an intermediate lumped mass, J. Sound Vib. 199 (1997) 711–736.
[47] G. Djuidjé Kenmoé, A. Kenfack Jiotsa, T.C. Kofané, Physica D 191 (2004) 31–48.
[48] A.V. Gorbach, M. Johansson, Discrete gap breathers in a diatomic Klein–Gordon chain: Stability and mobility, Phys. Rev. E 67 (2003) 066608.
[49] S. Flach, C.R. Willis, Localized excitations in a discrete Klein–Gordon system, Phys. Lett. A 181 (1993) 232–238.
[50] T. Dauxois, M. Peyrard, C.R. Willis, Localized breather-like solution in a discrete Klein–Gordon model and application to DNA, Physica D 57 (1992) 267–282.
[51] Y.S. Kivshar, M. Peyrard, Modulational instabilities in discrete lattices, Phys. Rev. A 46 (1992) 3198.
[52] V. Achilleos, A. Alvarez, J. Cuevas, D.J. Frantzeskakis, N.I. Karachalios, P.G. Kevrekidis, B. Sanchez-Rey, Escape dynamics in the discrete repulsive ϕ^4 model, Physica D 244 (2013) 1–24.
[53] S. Lenci, G. Menditto, A.M. Tarantino, Homoclinic and heteroclinic bifurcation in the non-linear dynamics of beams resting on elastic substrate, Int. J. Non-Linear Mech. 34 (1999) 615–632.
[54] B.T. Seaman, M. Krämer, D.Z. Anderson, M.J. Holland, Atomtronics: Ultracold-atom analogs of electronic devices, Phys. Rev. A 75 (2007) 023615.
[55] A. Ruschhaupt, J.G. Muga, Three-dimensional effects in atom diodes: Atom-optical devices for one-way motion, Phys. Rev. A 76 (2007) 013619.
[56] T.F. Viscondi, K. Furuya, Dynamics of a Bose–Einstein condensate in a symmetric triple-well trap, J. Phys. A 44 (2011) 175301.
[57] S.H. Weintraub, Jordan canonical form: Application to differential equations, Synth. Lect. Math. Stat. 1 (1) (2008) 1–85.
[58] A.H. Nayfeh, D.T. Mook, Nonlinear Oscillations, Wiley, New York, 1979.
[59] C. Hayashi, Nonlinear Oscillations in Physical Systems, McGraw-Hill, New York, 1964.